CARBON MIGRATION ACROSS DISSIMILAR METAL WELDS, RELATED TO POWER PLANT

Dorothy Louise Elder
Hughes Hall, Cambridge

Department of Materials Science and Metallurgy
Pembroke Street
Cambridge
CB2 3QZ, UK

A dissertation submitted for the
degree of Doctor of Philosophy

August 2001

FOR CHRIS

Happiness is a warm puppy.

Charles M. Schulz

April 25th, 1960

Preface

This dissertation is submitted for the degree of Doctor of Philosophy in Natural Sciences at the University of Cambridge. The investigation described in this thesis was carried out under the supervision of Professor H. K. D. H. Bhadeshia at the Department of Materials Science and Metallurgy, Cambridge, between October 1997 to August 2001. Except where acknowledgement and reference to previous work has been made, this work is original and carried out without collaboration. Neither this, nor any substantially similar dissertation has been, or is being submitted for any degree, diploma or other qualification at this or any other university.

This dissertation contains less than 60 000 words.

Dorothy Elder

August 2001

Acknowledgements

The financial support for this project was provided in the form of an EPSRC / CASE award, with additional funding provided by The Welding Institute (TWI). I would like to thank Professor A. H. Windle and Mr P. Hart for the provision of laboratory facilities at the University of Cambridge and TWI, respectively.

Many thanks go to my academic supervisors Professor Harry Bhadeshia and Dr Rob Wallach, and also my industrial supervisors at TWI, Dr David Abson and Dr Trevor Gooch (deceased), for their support and assistance on all matters over the duration of this project. A special thank you also goes to Dr David Allen (Powertech) and Dr Stephen Brett (Innogy) for their provision of samples and *hands - on* knowledge of the project.

I would like to say a big thank - you to my friends in the Phase Transformations group, on the PTP-scheme and at TWI and university; Dr Dave Cole, Chris Downs, Miguel Gonzales, Dr L. S. Harsha, Gareth Hopkin, Hiroshi Matsuda, Fiona Smith, Thomas Sourmail and Dr Nick Tyas, Alan Bates, Richard Court, Rachel McCarthy, Dr Glen Parry and Dr Robin Preston, Glyn Hall, David Nicol and John Street.

Thank you mum, dad, Rose and Chris for being my family.

Abstract

This thesis deals with the changes in chemical composition and microstructure that occur when a joint between two different steels is heat treated for prolonged periods of time at a temperature below that at which austenite forms. Such joints are common place in power plant where components with different purpose are joined by welding.

The aim of the work was to characterise the changes that occur at the weld junction and to quantitatively model them such that the method has predictive power.

The temperatures involved are not high enough to permit the diffusion of substitutional solutes over significant length scales, but carbon diffuses readily as an interstitial atom in ferrite. The diffusion is driven by a discontinuity in the chemical potential of carbon that occurs at the dissimilar steel interface. Since the solubility of carbon in ferrite is very small, the diffusion process necessitates the dissolution of carbides on one side of the junction, matched by the precipitation of carbides on the other side.

In previous work, all the experiments designed to study the carbon partitioning have been conducted on actual welds, which have irregular interfaces together with some mixing between the different steels as a consequence of the melting associated with the welding process. It was decided, therefore, to create an experimental system in which different samples were pressure bonded at a high temperature and in a way that ensures a flat interface with a sharp composition discontinuity. At the same time, a series of welds of relevance to industry were studied for comparison purposes.

Metallographic analysis on dissimilar steel welds and bonds, heat-treated over a range of times and temperatures showed the ease of decarburised and carburised zone formation and their associated microstructures. In the low-alloy steel, rapid carbide dissolution close to the dissimilar interface leaves room for grain growth that forms a decarburised zone. In the associated carburised zone, precipitation and carbide coarsening occurred on grain boundaries and intragranularly due to the associated increase in carbon concentration. In vanadium-containing low-alloy steels, stable vanadium-alloy carbides were found to complicate carbon partitioning generating wider, shallower decarburised zones compared to the smaller, almost carbide-free ones in vanadium-free steels.

A model, developed for estimating the decarburised zone width in ferritic transition joints considers the carbon concentration as a function of distance from the dissimilar interface resulting from chemical potential gradients in the joint. Written in FORTRAN 77, the model uses the

Crank-Nicholson implicit finite difference solution of Fick's second law, and was found to accurately predict decarburised zone widths based on measurements taken from welds and bonds from a given series of tempering tests. The existence of substantial carbon chemical potential gradients in the transition joint causes carbides to dissolve in the low-alloy steel during heat-treatment, releasing carbon to diffuse across the dissimilar interface to form a corresponding carburised zone. Naturally, the temperature and time of the heat treatment influences carbon diffusion, but the particular alloy combination in the transition joint also affects the amount of carbon partitioning.

Nomenclature and Abbreviations

A_A	Activity of component A
Ac_1	Temperature of the start of transformation from ferrite to austenite, °C
Ac_3	Temperature of the end of transformation from ferrite to austenite, °C
a	The lattice parameter of the crystal structure of an element
BCC	Body-centred cubic lattice
C	A constant
C	Concentration, wt. %
$\overline{C}$	Average carbon concentration, wt. %
C_0	Initial concentration, wt. %
$C_{i,j}$	Carbon concentration at a grid point, (x,t)
C_α	Far field carbon concentration in the matrix on the low-alloy side of the dissimilar joint, wt. %
$C_{\alpha A}$	Carbon concentration in the matrix in equilibrium with the carbide on the low-alloy side, wt. %
$C_{A\alpha}$	Carbon concentration in the equilibrium carbide on the low-alloy side, wt. %
$C_{\alpha\beta}$	Equilibrium carbon concentration at the joint interface, on the low-alloy side, wt. %
C_β	Far field carbon concentration in the matrix on the high-alloy side of the dissimilar joint, wt. %
$C_{B\beta}$	Carbon concentration in the equilibrium carbide on the high-alloy side, wt. %
$C_{\beta B}$	Carbon concentration in the matrix in equilibrium with the carbide on the high-alloy side, wt. %
$C_{\beta\alpha}$	Equilibrium carbon concentration at the joint interface, on the high-alloy side, wt. %
c	The speed of light in a vacuum (2.99×10^{-8} m^2 s^{-1})
D_{weld}	Percentage dilution in a weld
D_{app}	Apparent diffusion coefficient, μm^2 s^{-1}
D_i	Diffusion coefficient of component i, μm^2 s^{-1}
D_b	Grain boundary diffusion coefficient, μm^2 s^{-1}
D_L	Diffusion coefficient through the lattice, μm^2 s^{-1}
D_0	Frequency factor of diffusion
D^{o-T-o}	The possible jumps of a solute from an octahedral site to another octahedral site via a tetrahedral site
D^{T-o-T}	The possible jumps of a solute from a tetrahedral site to another tetrahedral site via an octahedral site
D^{T-T}	The possible jumps of a solute from a tetrahedral site to another tetrahedral site

D1	Dimension of the block containing the carbide and matrix phases on the low-alloy side, μm
D2	Dimension of the carbide on the low-alloy side, μm
D3	Dimension of the matrix on the low-alloy side, μm
D4	Dimension of the block containing the carbide and matrix phases on the high-alloy side, μm
D5	Dimension of the carbide on the high-alloy side, μm
D6	Dimension of the matrix on the high-alloy side, μm
d	Crystallographic plane hkl spacing
d	Mean diagonal length of diamond hardness indentations, mm
d_t	Final grain size
d_0	Initial grain size
erf	The error function
erfc	The error function compliment, erfc(i) = 1 - erf(i)
e^-	Charge of an electron (1.602×10^{-19} coulomb)
f	The fraction of interstitial atoms on tetrahedral sites
FCC	Face - centred cubic lattice
G	The Gibbs free energy of a system
ΔG	The change in the Gibbs free energy
H	The enthalpy of a system
HAZ	Heat affected zone
h	Planck's constant (6.62×10^{-34} J s)
J	Flux of diffusing atoms (gradient of atoms per unit area per s)
k	A constant
k	Boltzmann's constant (1.38×10^{-23} J K^{-1})
$k^{(j)}_{cr(c)}$	Equivalence constant
k_p	Partition coefficient
L	Camera length, mm
L	Width of the block, μm
l	Width of the carbide, μm
MMA	Manual metal arc welding
m	The mass of an electron (9.10×10^{-25} kg)
$N_{cr(eq)}$	Thermodynamic equivalent of chromium in ferrite, at. %
n_A	A small quantity of component A, mol
P	Larson – Miller parameter
PWHT	Post-weld heat treatment
Q	Activation energy for diffusion
R	The Universal gas constant (8.314 J mol^{-1} K^{-1})
R_{hkl}	Distance between a transmitted and diffracted spot in the TEM
S	Entropy of a system
SEM	Scanning electron microscopy

T	Temperature, °C
T_{diss}	Dissolution temperature, °C
T_{m}	Melting temperature, °C
t	Time, s
TEM	Transmission electron microscopy
V	The accelerating voltage, kV
V_A	Volume fraction of carbide A
v	The interface velocity of the carbide, μm s^{-1}
X_A	Mole fraction of component A
x	Diffusion distance, μm
x_a	Diffusion distance in the low-alloy steel, μm
x	Diffusion distance in the high alloy steel, μm
α_1^*	Parameter for one-dimensional growth
γ_C	Activity coefficient of carbon
γ_C^α	The activity coefficient of carbon in the low-alloy steel
γ_C^β	The activity coefficient of carbon in the high-alloy steel
ϵ_j	Wagner interaction parameter
ε_c^j	Interaction coefficient of element j on carbon activity
ε_c^{cr}	Interaction coefficient of chromium on carbon activity
λ	Wavelength of an electron
μ_C	Chemical potential of carbon
ξ_α	Width of the decarburised zone, μm
ξ_β	Width of the carburised zone, μm
ϕ	The fraction of total interstitial atoms on sites in the lattice
Ω	Measure of the driving force for carbide dissolution, or the supersaturation parameter
$\overline{\omega}_c^{\text{cr}}$	Effective interaction coefficient of chromium on carbon activity

Contents

Chapter One

Introduction to Power Plant Steels

This chapter gives a background to the work presented in this thesis, including some relevant aspects of the power plant, an overview of the microstructural stability of power plant steels and features of ferritic dissimilar steel welds.

1.1 The power plant

In the power generation industry, electricity is generated by the indirect transformation of primary energy sources, such as coal and natural gas, into mechanical energy which is then converted into electrical energy.

Figure 1.1 illustrates the major features of such a power plant. The boiler heats up the water to produce steam at above 500 °C and at pressures over 30 MPa. This high temperature, high pressure (or *'superheated'*) steam then passes along pipes to the turbines which drive an alternator to generate electricity.

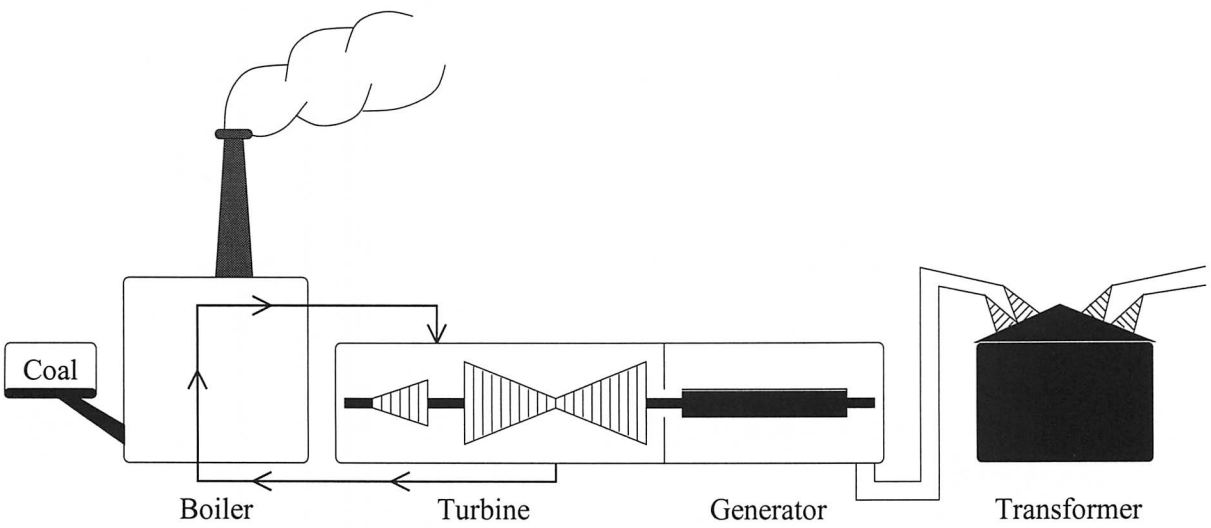

Figure 1.1 Major components of a fossil fuelled power plant (modified from Graham, 1975).

Improving the service life, to greater than 250,000 h, and increasing the steam temperatures from 500 to about 565 °C of typical power plant over the last half a century has necessitated the development of improved steels. World wide environmental concerns place limits on CO_2 emissions from power plant which are thought to contribute to global warming. Therefore

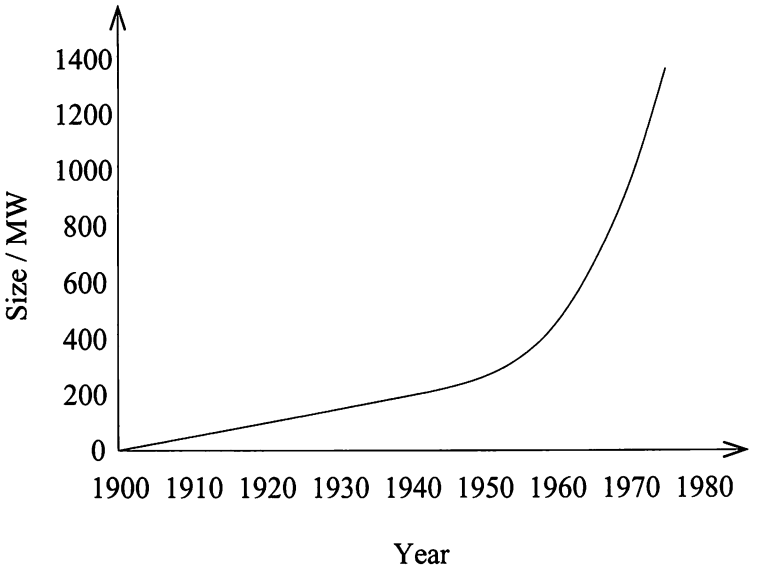

Figure 1.2 Historic growth of the power output of steam turbines (Seth, 1999).

strenuous efforts have been made throughout the world to improve the output efficiency of power generation by further increasing the operating temperature and pressure of the steam turbines (Schuster & Cerjack, 1995).

For example, an increase in turbine efficiency of 8 % is brought about by increasing the steam conditions from 538 °C at a pressure of 30 MPa to 650 °C at 40 MPa (Takeda & Masuyama, 1991). The overall efficiency of a conventional steam cycle is approximately 40 %. There are several process control measures that can improve operating efficiency, for example utilising the size of the turbines, and their reliability, and maintainability. All these factors have been used over the latter decades of last century to improve the output efficiency of the power plant; the increase in the power output of the steam turbine is illustrated in Figure 1.2.

1.1.1 Steels in the power plant

The steels used in the construction of power plant can be separated broadly into three classes. Firstly there are the mild and low-alloy steels. For a typical service life of 250,000 h, mild steels are limited to temperatures below 475 °C. Cr – Mo and Cr – Mo – V low-alloy steels can be selected for use at higher temperatures.

Chromium improves the steel's resistance to oxidation and along with molybdenum additions ameliorates the high temperature creep strength of the steels. Chromium and molybdenum together with the other elements in Table 1.1 improve the strength and hardenability of the steel, both by solid solution strengthening and by precipitation hardening (Irvine, 1975; Bailey, 1994; Honeycombe & Bhadeshia, 1995).

steel type	C	Cr	Mo	other elements
mild steel	0.20	0.04	0.015	0.76 Mn
$\frac{1}{2}$CrMoV	0.11	0.5	0.5	0.25 Si, 0.5 Mn, 0.25 V
2$\frac{1}{4}$Cr1Mo	0.12	2.25	1.0	0.25 Si, 0.5 Mn
9Cr1Mo	0.10	9.0	1.0	0.60 Si, 0.5 Mn
type 304	0.05	18.5	-	10 Ni, 1.3 Mn, 0.5 Si

Table 1.1 Typical compositions for some creep-resistant steels, wt. % (Evans & Wilshire, 1993).

The second class of steels includes the 9 to 12 wt. % chromium steels. These have been developed with the objective of extending the operating range of creep-resistant ferritic steels to temperatures above 600 °C (Brühl *et al.*, 1989a; Prader *et al.*, 1995).

Since the mid 1970's, considerable effort has been expended to develop 9 – 12 wt. % chromium steels to operate effectively at temperatures between 500 and 600 °C. This was to utilise the more favourable properties of ferritic steels over austenitic steels in this temperature range. Figure 1.3 shows the stress required at a given temperature to produce a lifetime to rupture of 10^5 h, for a variety of steels. An austenitic type 304 stainless steel (0.08 wt. % C, 18 wt. % Cr and 8 wt. % Ni) is also included on the diagram to show its performance compared to a 'modified' 9Cr1Mo steel. Several composition changes are made to standard 9Cr1Mo steels to increase their creep strength using vanadium and niobium modifications. The creep strength of modified 9Cr1Mo steel exceeds that of type 304 stainless steel up to 600 °C but falls away around 650 °C.

The final class of power plant steels include a variety of austenitic steels. From Figure 1.3, higher alloy ferritic steels and austenitic steels (for example type 304 steel) have the better creep resistance at high temperatures. However, these high chromium steels can be more expensive and have a high coefficient of thermal expansion, low thermal conductivity and a susceptibility to stress corrosion cracking (Evans & Wilshire, 1993).

The principal requirements for steels used in the steam heaters and pipeline in the power plant are creep rupture strength and ductility, adequate oxidation resistance, microstructural stability over long periods and good weldability and formability (Irvine, 1975). Hence at a cost of less than 250 per tonne (November, 2000) and with relative ease of manufacture, large-scale steel structures can be easily constructed.

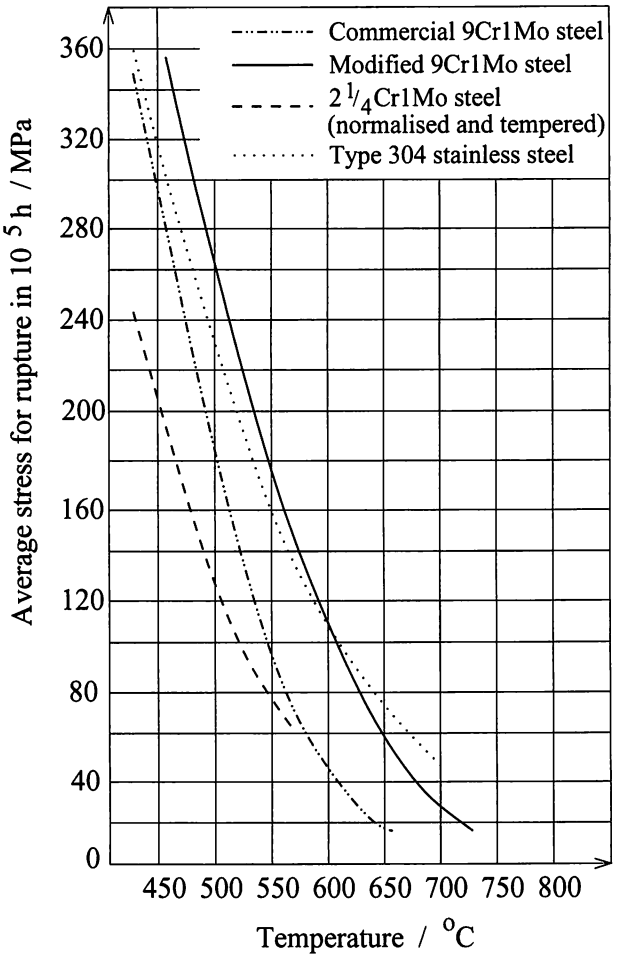

Figure 1.3 Creep rupture strength as a function of temperature, for $2\frac{1}{4}$Cr1Mo, standard and modified 9Cr1Mo steel and type austenitic 304 stainless steel. (modified from ASM Speciality Handbook, "Carbon and Low Alloy Steels", 1996).

At present, most of the high temperature pipework is made of either a $2\frac{1}{4}$Cr1Mo or CrMoV creep-resistant low-alloy steels. The principal failure mechanisms are circumferential or transverse cracking observed in either the pipe or in the weld metal. Some cracks can develop at the time of fabrication, others after thousands of hours service at temperatures in the range 540 to 570 °C. The cracking is attributed to the exhaustion of creep ductility. Better creep ductility is associated with a coarser grain size in the steel, in welds this can be achieved by controlling the welding process or by using preheats or a post-weld heat treatment (PWHT). The tendency for failure can be reduced by controlling the applied stress, however this defeats the purpose of good steel design.

1.1.2 Possible causes of premature degradation

The maximum temperature and pressure of the steam which drives the turbines is constrained by the performance of other parts in the power plant. As explained earlier, important components in the power plant are the boiler, the steam headers which connect the boiler to the steam pipes to carry the superheated steam, the main and steam reheating pipework, and the turbine and generator parts. The steam pipework in particular can sustain creep, weld cracking and thermal fatigue.

The service reliability of each component depends mainly on its creep, fatigue and oxidation resistance at elevated temperatures. To estimate the service life of a steel component within the power plant, the production conditions of the component and properties of the steel must be evaluated.

At the start of service, some components may become immediately susceptible to malfunction due to improper design, production and assembly (Pilious & Stránský, 1998). Material degradation shortens the later stages of life hence the structural stability of the steel is limited by its capacity to maintain its design properties. The damage processes are generally associated with the development of localised area of plastic deformation

1.1.3 Transition joints

Low-alloy ferritic steels are used extensively for many sections of the steam pipework in the power plant. In addition, the high temperatures and pressures associated with final steam conditions require higher alloy steels which possess more oxidation and creep resistance. Accordingly, transition weldments between these different kind of steels are unavoidable (Dooley *et al.*, 1982; Buchmayr 1989).

The constituent steels of a transition joint may be ferritic or austenitic in any combination. Disparate ferritic steels have to be joined even though they have different chemical compositions. Any variations in substitutional solute content alters the chemical potential, μ_C, of carbon to a form a gradient in μ_C at the dissimilar steel junction even though a carbon concentration gradient may not necessarily exist. Nevertheless, the gradient in chemical potential drives carbon in a direction that tends to reduce this gradient. This, in turn, leads to decarburisation of one steel and the carburisation of the other.

In the carburised zone there may be intense carbide precipitation. The dissolution of carbides in the decarburised side of the weld permits the ferrite grains there to coarsen. Both of these effects are confined to the proximity of the dissimilar steel interface and are detrimental to the

integrity of the welded structure (Emerson & Hutchinson, 1952).

The amount of carbon diffusion across a dissimilar steel weld is governed by time and temperature of heat treatment used, and of course the particular steel combination (Christoffel & Curran, 1956). The welding process and the cooling rate used inevitability introduces residual stresses, common to most welded joints, and complex stress/strain states into the dissimilar steel weld due to the different coefficients of thermal expansion of each steel (Kim *et al.*, 1992). A PWHT given to a dissimilar steel weld relaxes residual stresses within the weld, tempers any hard transformation products that may be present and will, in some cases, improve the fracture toughness of the weld as a whole. However this PWHT increases the likelihood and magnitude of carbon diffusion across the dissimilar steel weld; therefore, the region containing the weakened dissimilar steel junction may become more likely to suffer from premature failure.

Predictions of the measure of carbon migration help engineers to estimate the lifetime of a dissimilar steel weld operating at high temperatures. Precautions that limit the amount or the onset of carbon partitioning have been attempted with varying degrees of success. A common preventative method is to introduce a barrier between the steels, usually a layer of nickel – base alloy which has limited carbon solubility. This diffusion-barrier should also ensure that the coefficient of thermal expansion is between the welded steels thus enabling easy relaxation of any resultant stresses. The main parameter controlling the effectiveness of this diffusion-barrier is it's thickness. An alternative precaution is to modify or correct the chemical composition of either of the steels in the dissimilar steel weld. For example, the steel with the higher μ_C is alloyed with carbide forming elements that lower the chemical potential of carbon (Pilious & Stránský, 1998).

1.1.3.1 Filler metal selection

During the design and building of the power plant, high creep strength Mo – V or Cr – Mo – V steels were used for the high pressure components, but there were no suitable high creep strength welding electrodes available at that time (Toft & Yeldham, 1972). Instead, the power plant was constructed using inappropriate welding electrodes and though design and safety factors were considered, after 100 000 h of service long-term creep failures did occur.

It is good practice to select an electrode for welding which bests matches, in physical properties though not necessarily composition, the parent steels. This reduces the possibility of mechanical discontinuities and produces an overall improvement in life expectancy of the dissimilar steel weld.

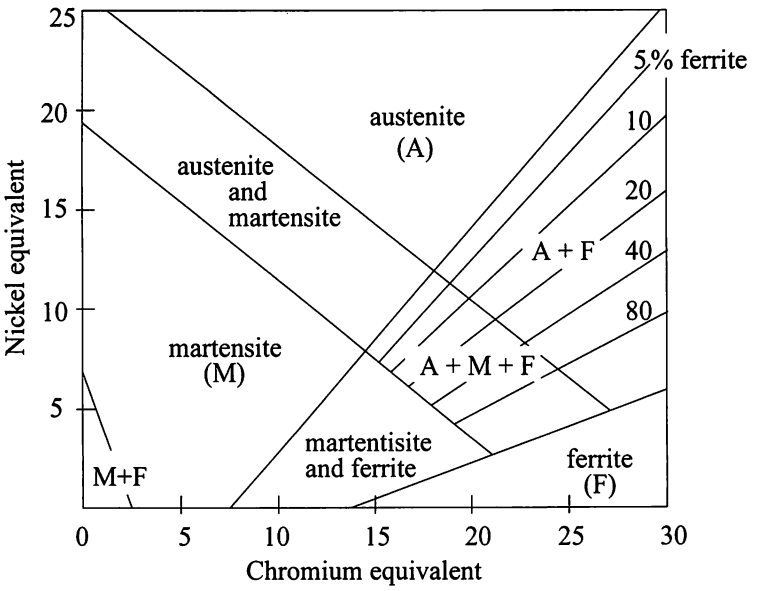

Figure 1.4 Schaeffler diagram for evaluating the effects of alloying additions on the microstructure of steel welds. Cr equivalent = (Cr) + 2(Si) + 1.5(Mo) + 5(V) + 5.5(Al) + 1.75(Nb) + 1.5(Ti) + 0.75(W). Ni equivalent = (Ni) + (Co) + 0.5(Mn) + 0.3(Cu) + 25(N) + 30(C). All concentrations are in wt. %. (modified from Honeycombe & Bhadeshia, 1995).

Transition joints have been used in power plant from as early as the 1930's (Emerson & Hutchinson, 1952). In 1935, a choice of austenitic electrodes was made to weld a carbon steel component for a pressure vessel application by an engineer in the Krupp steel works. This selection of steels for welding was based on the assumption that a PWHT would not be necessary. However, tests of the weld integrity during fabrication showed that this component would fail immediately and the boiler would spring many leaks. Needless to say, the welding was stopped.

Austenitic electrodes can be used in some circumstances, for example welding a $2\frac{1}{4}$Cr1Mo steel to an austenitic type 347 stainless steel turbine pipe (0.07 wt. % C, 17.69 wt. % Cr, 11.12 wt. % Ni, 0.93 wt. % Cb), followed by a PWHT for about 700 °C for 3 h. Problems may occur due to the different thermal expansion coefficients between the austenitic and ferritic steel. However, carbon partitioning is concentrated in the less critical $2\frac{1}{4}$Cr1Mo/austenitic weld metal region ultimately lowering the repair costs (Emerson & Hutchinson, 1952).

Unwanted microstructures formed in a weld metal can be detrimental to its mechanical properties, leaving the weld susceptible to defects and excessive localised corrosion attack. The type of microstructure that can be expected in a dissimilar steel weld deposit can be estimated

using a Schaeffler diagram, Figure 1.4. The Schaeffler diagram plots the compositional limits of the austenite, ferrite and martensite microstructures of the steel at room temperature, on the basis of empirical chromium and nickel equivalents of the weld composition.

1.1.3.2 Dilution and heat treatments

Welded microstructures and the heat-affected zone (HAZ) of the parent steel often have a high hardness associated with them. Preheating the parent steels prior to welding minimises critical temperature gradients during and after welding, modifies the microstructure and reduces the hardness in the weld and HAZ (Lancaster, 1999). To decrease the likelihood of reheat cracking in the coarse grain HAZ of creep-resistant steels, the amount of preheat which leads to grain growth must be controlled (Easterling, 1983).

During welding, mixing of the parent and filler metal during fabrication is called dilution and leads to a mixed composition zone at the weld junction. This is of particular importance in dissimilar steel welds as care must be taken to ensure that the weld metal has the desired composition (Lancaster, 1999). The degree of dilution can be controlled by the correct selection of filler metal for the weld, edge preparation and joint fit-up. Minimising dilution reduces the chance of producing a crack-sensitive weld metal. Excessive dilution in dissimilar steel welds can be controlled by '*buttering*' – a process of depositing weld metal to the edges of the joint before the weld is filled up. The parent metal and the buttered layer can undergo a separate PWHT before the completing the weld. Therefore, the buttered layer and separate PWHT limits carbon partitioning between the parent steel and weld metal.

A final PWHT given to the whole dissimilar steel weld alleviates any internal stresses and improves its ductility without any significant losses in strength. A typical PWHT to relax stresses in welds is in the region of 600 °C for a minimum of 1 h per 25 mm thickness (Lancaster, 1999). Post-weld heat treating the weld also reduces the risk of stress corrosion cracking and in-service hydrogen cracking (Bailey, 1994). The PWHT for low-alloy ferritic welds in power plant are normally performed between the operating temperature and the Ac_1 temperature of the steel to avoid any austenite formation at the weld. As PWHT initiates carbon partitioning across the dissimilar steel junction, it must be managed carefully.

1.1.3.3 The effects of carbon migration

Due to the severe thermal cycle and high restraints imposed during welding, it is sometimes likely that cracks occur. The types of cracking phenomena associated with welding are arranged with respect to their positions within the weld deposit itself, at the fusion line between the weld

and the parent metal, or in the adjacent HAZ of the parent steel (Easterling, 1983; Lancaster, 1999).

WELD DEPOSIT	FUSION ZONE	HAZ
• Hydrogen attack	• Liquation cracking	• Lamellar tearing
• Gas porosity		• Cold cracking
• Solidification cracking		• Reheat cracking

Cracks formed in the dissimilar steel welds have been observed after about 35 000 h service due to rapid disruption of the low structural stability weld (Toft & Yeldham, 1972). The cracks found in the dissimilar steel welds can be; a Type IV cracks found in the intercritically transformed metal at the edge of the HAZ, reheat cracks in the coarse grained HAZ because of poor control of the PWHT and residual stresses, Type IIIa cracks found in the fine grained HAZ next to the weld interface caused by carbon depletion in this region, and creep or fatigue cracks (Brett, 1998; Brett & Smith, 1998). Cracks in susceptible dissimilar steel welds occur in the steel with the weakest structural stability. For example if a ferritic Cr – Mo – V steel was welded with a $2\frac{1}{4}$Cr1Mo steel electrode, serious defects can be formed in the HAZ immediately after welding.

In a ferritic/ferritic type dissimilar steel weld, carbon diffuses out of the lower alloy steel leaving a soft decarburised zone. The decarburised zone contains only a few carbides so the local creep properties deteriorate (Lundin *et al.*, 1989).

At the weld interface on the high-alloy side of the dissimilar steel weld, the steel hardens as the incoming carbon precipitates causing existing carbides to grow or new carbides to precipitate (Lundin 1982; Kim *et al.*, 1992; Buchmayr, 1993). Figure 1.5 shows a carburised zone growing over time, at a PWHT temperature of 620 °C, in an austenitic filler metal, (0.019 wt. % C, 13.01 wt. % Ni, 24.69 wt. % Cr, 1.73 wt. % Mn). The hardness in the carburised region has increased from 321 HV to 549 HV during PWHT between 20 and 200 h.

Any internal stresses that may have formed on cooling a dissimilar steel weld are relaxed as plastic deformation in the low-alloy steel or as newly formed lattice defects. Within the decarburised zone, the dislocations arrange into a cellular structure during reheating. The lower alloy steel then contains a higher defect density and a reduced stability compared to the neighbouring hardened regions in the higher alloy steel. It can therefore undergo recovery and recrystallisation. Columnar grains form in the decarburised zone during further heat treatment, growing normal to the weld fusion line in the direction opposite to the flow of carbon diffusion

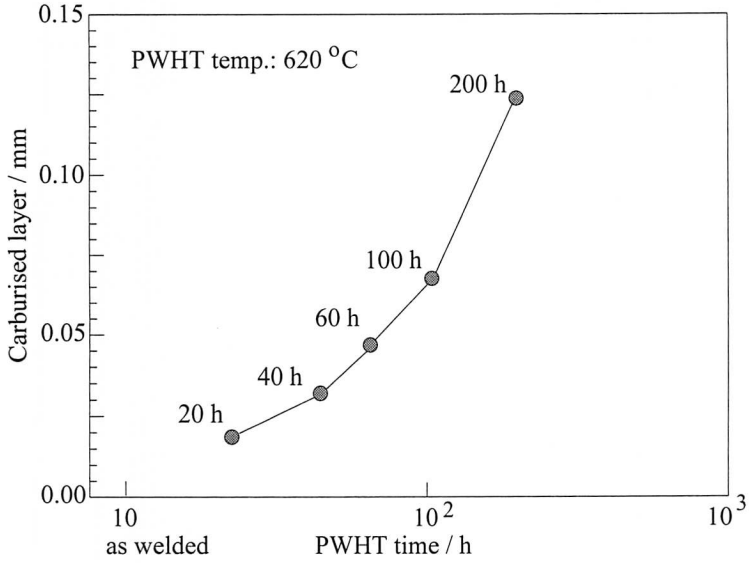

Figure 1.5 Experimental values of the thickness of the carburised layer as a function of the PWHT time (Kim *et al.*, 1992).

opposing the flow of carbon diffusion. This is illustrated on Figure 1.6. This kind of grain coarsening depends on the dissolution of carbides leaving the unpinned grains room to grow.

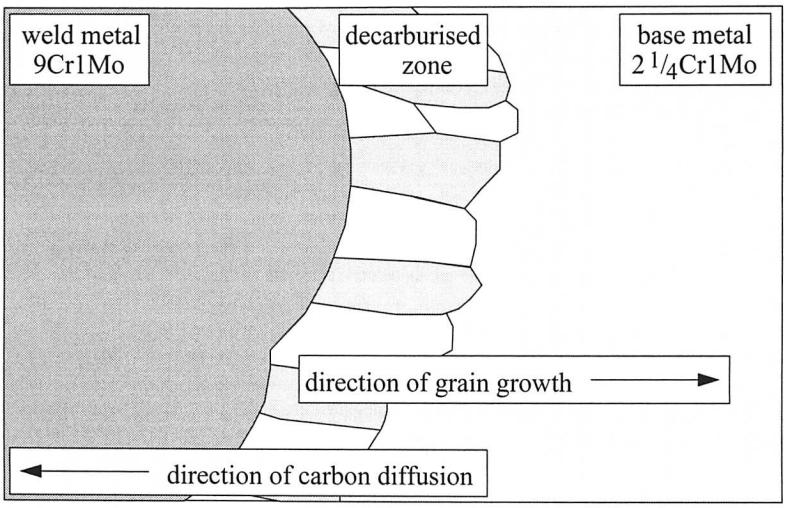

Figure 1.6 An illustration of the directions of grain growth and carbon diffusion during heat treatment of a dissimilar weld.

1.2 Heat treating power plant steels

Creep-resistant $2\frac{1}{4}$Cr1Mo and $\frac{1}{2}$CrMoV steels are widely used in current power plant, thus there are steam pipes operating at 565 °C containing a pressure of 30 MPa. Carbon and low-alloy ferritic steels have been successfully used for many years as part of dissimilar steel welds in service in coal fired power plant (Emerson & Hutchinson 1952; Thielsch, 1952; Tucker & Eberle, 1956; Toft & Yeldham, 1972). Higher alloy ferritic steels are also used for high temperature and higher creep-resistant components (Sikka *et al.*, 1983; Sanderson, 1983).

Many of the vital alloying elements in steel are expensive so they have to be used selectively with a compromise between improved performance and total cost in the context of parts, fabrication, replacement of welds and time that is wasted for repairs in the plant. The roles of non-carbide forming elements in the tempering of ferritic low-alloy steels are either to slow down the softening reaction by retarding the precipitation of cementite, or to control the hardenability since the solutes can be very large in size (Nutting, 1999).

Throughout long-term service, the alloy carbides formed in the steel tend towards an equilibrium state. During tempering, the original fine dispersion of carbides coarsens by Ostwald ripening. In addition, metastable carbides eventually dissolve to be replaced by thermodynamically more stable phases, such as Laves phases. The ferrite grains also tend to coarsen while heat treating. These effects reduce the creep resistance of the steel (Evans & Wilshire, 1993). Steel, or weld metal design should therefore focus on forming a stable dispersion of low solubility carbides.

Cooling low-alloy ferritic steels from the austenite temperature range can form either a bainitic, martensitic or ferrite – pearlite microstructure depending on the cooling rate and the alloy composition. Martensite is formed by the diffusionless transformation of steel from the austenite phase leaving a ferrite phase supersaturated with carbon. The martensitic microstructure can be very hard, but is softened during tempering as excess carbon precipitates.

In comparison to martensite, bainite grows at relatively higher temperatures so some recovery of the microstructure can occur during transformation. In bainite, most of the carbon precipitates as cementite during transformation forming carbides that are generally coarser than those found in martensite. The rate of carbide coarsening during tempering is generally less in bainitic steels than in martensite because of the carbides tempering during bainitic transformation.

When martensite is tempered at $T < 400$ °C, it can soften due to the precipitation of iron

carbides. If the steel contains alloy carbide forming elements, then the hardness may rise again at temperatures in excess of 500 °C due to the formation of precipitates such as V_4C_3 and Mo_2C (Smith & Nutting, 1957). This is called secondary hardening.

A bainitic microstructure formed in a low-alloy steel shows good resistance to creep when subject to low stresses and short-term tests. At high testing temperatures, the properties of the bainitic steel become degraded compared to the creep properties of ferrite – pearlite steels. A ferrite – pearlite steel has better intermediate term, low stress creep resistance. However, as in both microstructures carbides will eventually spherodise, over long-term service the creep strength of both steels are expected to converge (Viswanathan, 1974).

1.2.1 $2\frac{1}{4}$Cr1Mo steel

Steam pipes made from $2\frac{1}{4}$Cr1Mo steels are able to withstand an operating temperature of 565 °C. $2\frac{1}{4}$Cr1Mo steel has good weldability and creep ductility. After slow cooling from the austenitic temperature range, a $2\frac{1}{4}$Cr1Mo steel can have a mixed microstructure of ferrite and bainite with carbon mostly in the form of cementite. Further heat treatment causes the cementite to become richer in chromium and other substitutional solutes. In a fully bainitic microstructure, the cementite enriches more rapidly than when it is in a mixture of bainite and allotromorphic ferrite. This is because the bainite regions then have a larger fraction of cementite due to the partitioning of carbon during the formation of allotromorphic ferrite (Thomson & Bhadeshia, 1994). Eventually the cementite gives way to more stable alloy carbides (Pilling & Ridley, 1982). The alloy carbides contain a high fraction of the substitutional solutes. The general precipitation sequence given for a quenched and tempered low carbon $2\frac{1}{4}$Cr1Mo steel has been determined by Baker & Nutting (1956), M is the substitutional solute in the alloy carbide:

$$\begin{array}{ccccccc} \text{cementite} & \rightarrow & M_2C & \rightarrow & M_{23}C_6 & \rightarrow & M_6C \\ & & + & & & & \\ & & M_7C_3 & & \rightarrow & & M_7C_3 \end{array}$$

The plot in Figure 1.7 shows which carbides are expected during the heat treatment of a $2\frac{1}{4}$Cr1Mo steel that was austenitised at 960 °C and then cooled to room temperature at a rate of 300 °C s^{-1} (Nutting, 1999). At high temperatures, the precipitation of higher order alloy carbides happens faster than at lower temperatures. The kinetics of nucleation and growth, and dissolution of carbides are governed by both interstitial and substitutional diffusion of solutes, that is again temperature dependent.

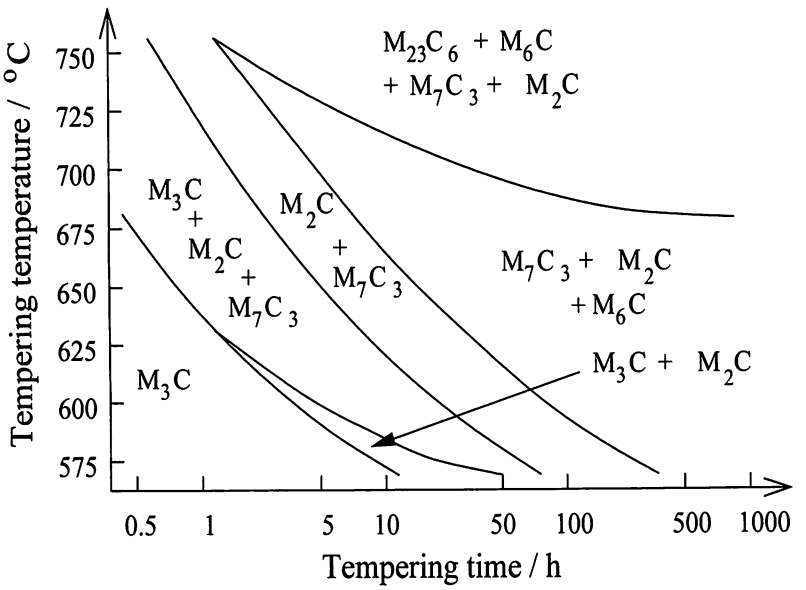

Figure 1.7 Tempering normalised $2\frac{1}{4}$Cr1Mo steel (modified from Nutting, 1999).

$M_{23}C_6$ and M_7C_3 alloy carbides nucleate simultaneously in $2\frac{1}{4}$Cr1Mo steel as the cementite dissolves to release solute. Evidence suggests that $M_{23}C_6$ carbides nucleate at the ferrite grain boundaries and may incorporate molybdenum and vanadium as well as chromium (Nutting, 1999). Heat treating at 700 °C stimulates M_6C carbides to form at the expense of $M_{23}C_6$. M_6C initially has a low molybdenum content and can precipitate on prior austenite grain boundaries (Doig *et al.*, 1982), or according to Nutting (1999), M_6C appears to be nucleated on the ferrite grain boundaries.

When the metastable carbides go back into solution, both carbon and the substitutional solutes are transferred in to the more stable carbides. The coarsening of alloy carbides during heat treatment can lead to gradual ferrite grain growth as grain boundary pinning forces decreases with carbide volume fraction.

Decreasing the carbon content, from 0.09 to 0.018 wt. % C, in a $2\frac{1}{4}$Cr1Mo steel (2.30 wt. % Cr, 0.99 wt. % Mo, 1.00 wt. % Mn, 0.45 wt. % Si) tempered at 700 °C gave similar carbide precipitation sequence as if the carbon content had remained constant but the chromium and molybdenum content of the steel had increased (Pilling & Ridley, 1982).

An increase in the carbon content of a $2\frac{1}{4}$Cr1Mo steel, and for that matter in other creep-resistant steels, allows the reprecipitation of cementite occurs as the stable alloy carbide after a long time (Race, 1992; MTDATA, 1996).

1.2.2 $\frac{1}{2}$CrMoV steel

A low-alloy $\frac{1}{2}$CrMoV steel usually has a ferrite – pearlite microstructure. When used for high pressure parts of the power plant, the steel can suffer severe degradation in its creep properties during service above 565 °C (Du *et al.*, 1992). However, the ability of vanadium creep-resistant steels to maintain a stable carbide dispersion at temperatures up to 565 °C means they have been used extensively in the power plant.

The transformation to ferrite and pearlite, a lamellar mixture of cementite and ferrite, occurs during cooling from austenite. Pearlite nodules nucleate at the austenite grain boundaries and grow into the austenite grain (Honeycombe & Bhadeshia, 1995). Strong carbide forming elements chromium and vanadium added to $\frac{1}{2}$CrMoV steel increase its hardenability and encourage the precipitation of stable alloy carbides to remain insoluble even at very high temperatures (see Aaron & Kotler, 1971). A steel containing as little as 0.1 wt. % vanadium can form very stable vanadium carbides which pin the austenite grain boundaries and hence lead to finer ferrite grains after transformation. Crucially, strong carbide forming elements added to a steel in a dissimilar steel weld can limit the amount of carbon migration by holding onto the carbon in the steel (Gemmill, 1966).

During tempering, the cementite lamellae in pearlite begin to spherodise and coarsen. This happens at a faster rate in grain boundary pearlite compared to pearlite within the grains due to fast diffusion paths along the grain boundaries. Alloy carbides are then formed at the expense of cementite.

A vanadium containing steel can form small plate or rod-like carbides that nucleate periodically at the ferrite/austenite interface during the phase transformation. This is called interphase precipitation and gives a banded appearance to the ferrite grains; the inter-band spacing is determined by the height of the steps of which move along the interface (Honeycombe, 1976).

1.2.3 9 wt. % Cr steel

Modified 9Cr1Mo ferritic steel is designed for more demanding conditions than can be tolerated by the low-alloy steels. It contains 9 wt. % chromium with 1 wt. % molybdenum and was found to have a higher creep strength at all temperatures. A ferritic 9Cr1Mo steel that has been modified with 0.06 – 0.10 wt. % niobium and 0.18 – 0.25 wt. % vanadium (and with an optimised silicon content) shows sufficient creep rupture strength for services in power plant with steam temperatures up to 600 °C (Sikka *et al.*, 1983). Niobium and vanadium form very stable carbides and carbonitrides. The stability of carbides increases in the order of type of

main solute content:

$$\text{chromium} \rightarrow \text{molybdenum} \rightarrow \text{vanadium} \rightarrow \text{niobium}$$

The creep strength of a modified 9Cr1Mo steel alloy is higher than most standard and modified alloys containing between 2 to 12 wt. % chromium.

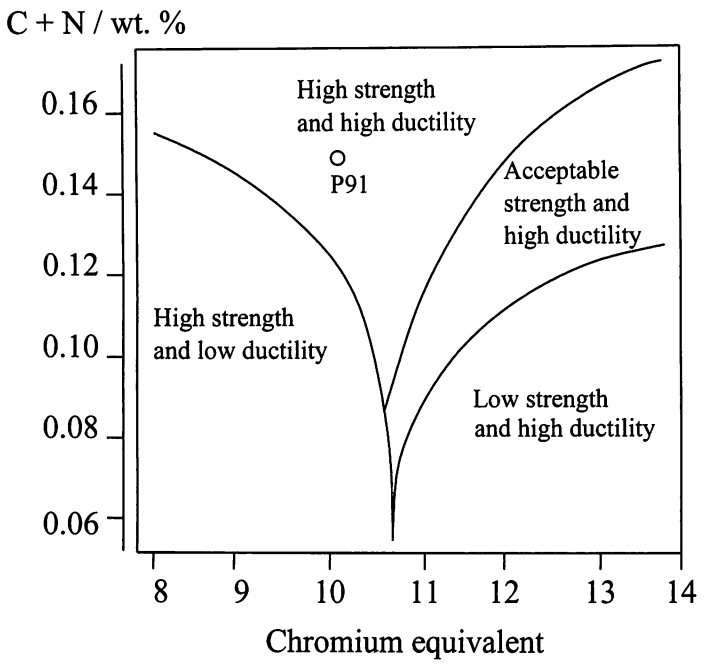

Figure 1.8 Effect of chemical composition on the creep properties of 9 wt. % Cr steel (Brühl *et al.*, 1989).

Figure 1.8 shows that the modified 9Cr1Mo steel lies in an optimum composition regime region which predicts high strength and ductility. The microstructure of the modified 9Cr1Mo steel alloy P91 (0.099 wt. % C, 8.75 wt. % Cr, 0.96 wt. % Mo, 0.204 wt. % V, 0.070 wt. % Nb) in Figure 1.8 is heavily tempered martensite.

It has been reported that modified 9Cr1Mo steel becomes fully martensitic after austenitising and cooling at a rate greater than 100 °C s^{-1} (Prader *et al.*, 1995). A slower cooling rate promotes the nucleation of ferrite without the formation of any bainite; and at cooling rates below 30 °C s^{-1}, no martensite forms at all. The martensite start and martensite finish temperatures have been raised by the precipitation of a secondary phase in the austenite during cooling.

Austenitising modified 9Cr1Mo steel above 1050 °C followed by cooling in air produces a martensitic microstructure peppered with ϵ-carbide plates (Brühl *et al.*, 1989). Some Nb – V

carbonitride particles (MX – where X can be carbon or nitrogen) that form early during tempering also form as fine needle-shaped carbides. Normalising a modified 9Cr1Mo steel followed by tempering at 730 °C dissolves any ϵ-carbide into the matrix and $M_{23}C_6$, a chromium based carbide, precipitates upon martensite lath boundaries. All martensite will transform to ferrite during prolonged tempering with $M_{23}C_6$ carbides form as stringers along prior martensite lath boundaries. There is also a fine dispersion of secondary incoherent MX particles in the microstructure containing up to 80 wt. % vanadium. Laves phases, rich in molybdenum content and M_2X carbonitrides can also be found in tempered modified 9Cr1Mo steel.

A hot-rolled and normalised at 1038 °C modified 9Cr1Mo steel shows a peak in hardness after heat treating at 510 °C. The hardness drops off for heat treatments above 550 °C. The peak in hardness of modified 9Cr1Mo steel was attributed to the MX-type carbides and a fine initial austenite grain size. Modified 9Cr1Mo steel that has been aged at temperatures higher than 760 °C shows a large amount of $M_{23}C_6$ carbides along with MX and possibly a third phase.

1.3 Summary

In this introductory chapter, the operation of the power plant has been briefly discussed along with the use of low-alloy Cr – Mo – V steels and the need for dissimilar steel transition joints in the contemporary power plant. The review of literature has identified the dissimilar steel transition joint as a probable site of premature failure in the power plant, due to carbon partitioning between the low and the high-alloy steels that form the weld leading to the onset of material degradation.

Chapter 2 presents a detailed review of the theory underlying carbon partitioning in transition joints, and this is followed by a critique of literature of published models designed to predict carbon diffusion in these joints in Chapter 3.

Chapter Two

Review of Theoretical Treatments of Carbon Migration

The redistribution of carbon at dissimilar steels joints is not a simple expression of flux in terms of a chemical potential gradient. The migration of carbon in the ferrite, in which its solubility is very small, occurs alongside the dissolution and precipitation of carbides. The purpose here is to review published theoretical treatments of this problem.

2.1 Background

In modern power plant, joining dissimilar steels for mid to high temperature applications in the power plant is inevitable (Pilious & Stránský, 1998). Hence there is the likelihood of considerable carbon redistribution from the low-alloy steel into the high-alloy steel during heat treatment. The redistribution can occur both during heat treatment at the manufacturing stage and during service at elevated temperatures. If one or both of the steels used to form the dissimilar joint is ferritic then the role of the carbides in carbon migration cannot be ignored. The carbides act as sources and sinks for carbon. Carbon diffusion occurs because of concentration gradients of substitutional solutes forming carbon chemical potential gradients indicating these are key aspects of the migration problem. Carbide dissolution in the ferritic steel is usually diffusion-controlled, and it is assumed that the dissolution itself is not the rate limiting step. Hence, the thermodynamics of carbon partitioning is a key aspect of this problem.

2.2 The thermodynamics of phase stability

Throughout the study of carbon redistribution across dissimilar steel welds, the discussion has been concerned with two steels in contact that are together trying to attain a state of lower free energy. The Gibbs free energy of a system G is described by the equation:

$$G = H - TS \tag{2.1}$$

where H is the enthalpy, T is the absolute temperature and S is the entropy of the system. A system is said to be in equilibrium when it tends towards its original state when given an infinitesimal time to do so. It follows that the system must be in a free energy minimum along some reaction coordinate. In Figure 2.1, the configuration of atoms at **A** is at a metastable state where small perturbations encounter a restoring force.

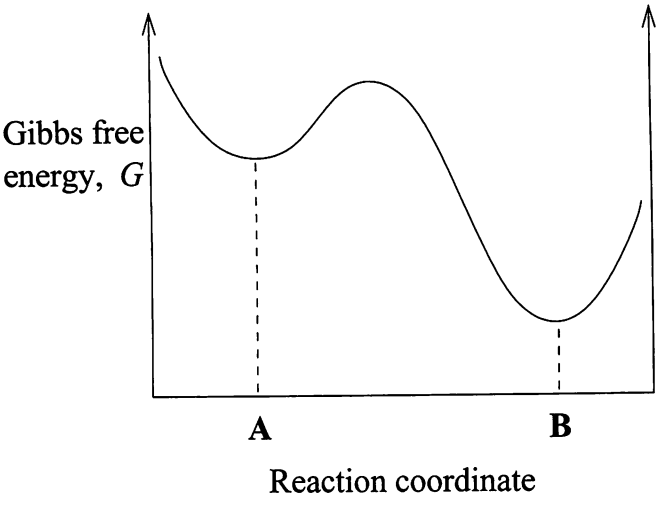

Figure 2.1 A schematic illustration of the Gibbs free energy with the arrangement of atoms (Porter & Easterling, 1992).

Any transformation which results in a decrease in the Gibbs free energy of a system is favoured; therefore, the criterion for a change to be possible is:

$$\Delta G = G_2 - G_1 < 0 \tag{2.2}$$

where G_1 and G_2 are the initial and final free energy states respectively. The change may not necessarily go directly to equilibrium, but is able to pass through a series of intermediate metastable states, for example configuration **B** on Figure 2.1.

In an alloy made up of components A and B, if a small quantity of A, dn_A mol, is added to a large amount of phase at constant temperature and pressure, then the size of the system will increase by dn_A. Also, the free energy of the system will be raised by a small amount dG. If dn_A is small enough, then dG is proportional to the amount of A added. So at constant pressure, temperature and amount of B, n_B, dG can be expressed as:

$$dG = \mu_A dn_A \tag{2.3}$$

The proportionality constant μ_A is also called the partial molar free energy, or the chemical potential of A. The chemical potential of a component is a means of describing the state of this component in a solution. The quantity μ_A depends on the composition of the phase, so dn_A must be so small that the composition is not significantly altered. Therefore the definition of μ_A can be rewritten from equation 2.3 as:

$$\mu_A = \left(\frac{\delta G}{\delta n_A}\right)_{n_B} \tag{2.4}$$

For a binary solution at constant temperature and pressure, the separate contributions from A and B to the change in free energy of the whole system is written as:

$$dG = \mu_A dn_A + \mu_B dn_B \tag{2.5}$$

In general, the molar free energy of a solution containing X_A and X_B mole fractions of A and B respectively is given by:

$$G = \mu_A X_A + \mu_B X_B \quad \text{J mol}^{-1} \tag{2.6}$$

G is a function of X_A and X_B, and μ_A and μ_B are the intercepts on the ordinates representing the pure components. The chemical potentials μ_A and μ_B vary systematically with composition of the phase:

$$\begin{aligned} \mu_A &= G_A^0 + RT \ln a_A \\ \mu_B &= G_B^0 + RT \ln a_B \end{aligned} \tag{2.7}$$

Where G_i^0 is the free energy of the pure component i, and a_i is the activity of i. The chemical potentials of the components shown in equation 2.7 are illustrated in Figure 2.2 in terms of the composition X and temperature T. R is the Universal gas constant.

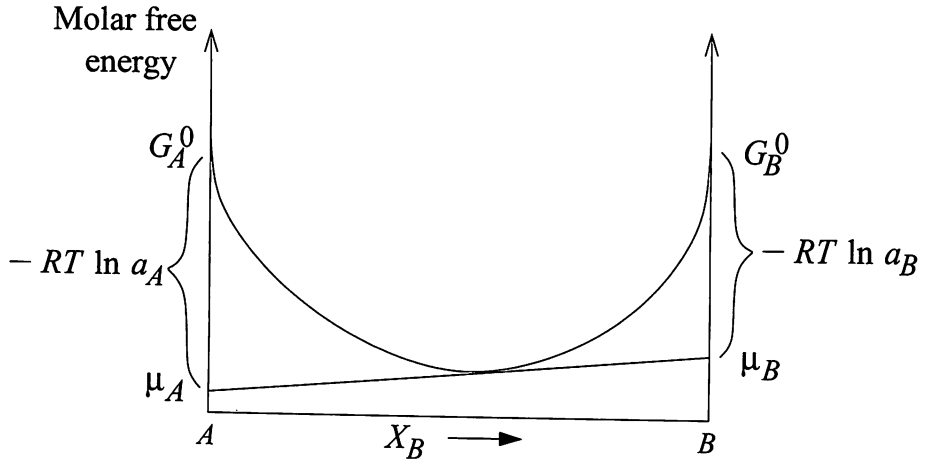

Figure 2.2 The relationship between the free energy curve and chemical potentials, for a general solution (Porter & Easterling, 1992).

2.3 The kinetics of phase transformation

For a phase transformation to proceed, for example from a metastable state to a lower free energy state, an atom will need to overcome an activation energy barrier, Figure 2.3. G_1 and G_2 are the free energies of the initial and final states. The driving force for transformation is the decrease in the free energy so $\Delta G = G_2 - G_1$. Hence the atom must pass through an activated state with a free energy G^* above G_1.

The probability of an atom overcoming this activated state is:

$$\exp\left(-\frac{G^*}{kT}\right) \tag{2.8}$$

where k is the Boltzmann constant. The rate of transformation also depends on the attempt frequency ν of atoms reaching the activated state such that:

$$\text{rate} \propto \nu \exp\left(-\frac{G^*}{kT}\right) \tag{2.9}$$

Using $G^* = H^* - TS^*$, and changing from molar to atomic quantities gives the rate of transformation as:

$$\text{rate} \propto \nu \exp\left(-\frac{H^*}{RT}\right) \tag{2.10}$$

This is an Arrhenius rate equation which can be applied to phase transformations in alloys.

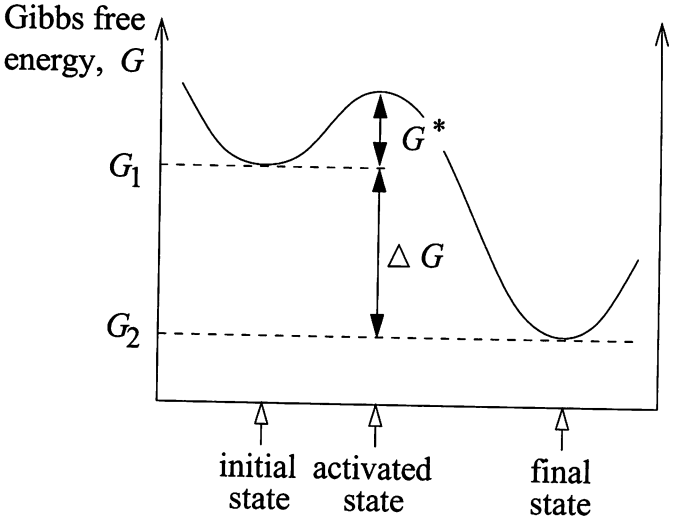

Figure 2.3 Transformations from the initial to the final state through an activated state (Porter & Easterling, 1992).

2.4 Diffusion of matter

Diffusion is the process by which matter is conveyed from one part of the system to another as a result of random molecular motions (Crank, 1975). There are two main methods for atomic diffusion through a solid, depending on the type of site the atom occupies in the crystal lattice. Substitutional atoms replace atoms on the unit cell of the host lattice, and the diffusion of substitutional atoms generally depends on there being a vacant lattice site next to the atom for it to jump into. Interstitial atoms migrate by forcing their way between the larger atoms; this type of diffusion happens at a faster rate than substitutional diffusion.

Pure iron can exist in two crystal forms at atmospheric pressure, body-centred cubic (BCC) iron (ferrite, α-iron) which is stable up to 910 °C, when it transforms to face-centred cubic (FCC) iron (austenite, γ-iron). The addition of carbon to iron forms steel. The atomic size of carbon is so small that it can occupy interstitial sites in both BCC and FCC iron. Carbon resides in the interstities of both structures; the BCC structure is looser than the closely packed FCC and the diffusion coefficient of carbon in BCC is correspondingly larger. The activation energy Q for diffusion is a measure of the probability that an atom will have enough kinetic energy to surmount a potential energy barrier between itself and the vacant site. The frequency at which the atoms will cross this barrier is proportional to the fraction of atoms with kinetic energy in excess of Q. Hence the diffusion coefficient D can be written as:

$$D = D_0 \exp\left(\frac{-Q}{RT}\right) \tag{2.11}$$

where D_0 is a quantity depending on the activation entropy, attempt frequency and details of the crystal structure.

Metallic alloying elements occupy substitutional sites. For substitutional diffusion, the heat of activation Q now includes an activation energy and a heat of formation of vacancies – the total of these is now much larger than for interstitial diffusion.

2.4.1 Interstitial diffusion

When considering the diffusion of a solute, the quantity of diffusing substance that passes per unit time through a unit area of a plane at right angles to the direction of diffusion is known as the flux, J. This flux is assumed to be proportional to the concentration gradient $\delta C/\delta x$ as:

$$J = -D\,\frac{\delta C}{\delta x} \tag{2.12}$$

This is Fick's first law, where the proportionality factor D, with units of $m^2\ s^{-1}$, is known as the diffusivity or diffusion coefficient. Even though the atomic movements can be random,

there are simply more solute atoms moving down a concentration gradient, so this appears as a flux.

Fick's first law only applies if the steady state exists and the concentration at every point is invariant. The dependence of concentration on time is dealt with by Fick's second law. The rate of accumulation of diffusible solute in a given volume element, for cases where the concentration gradient is not constant, is given as the change in concentration in the volume element related to the difference between the inward and outward solute fluxes.

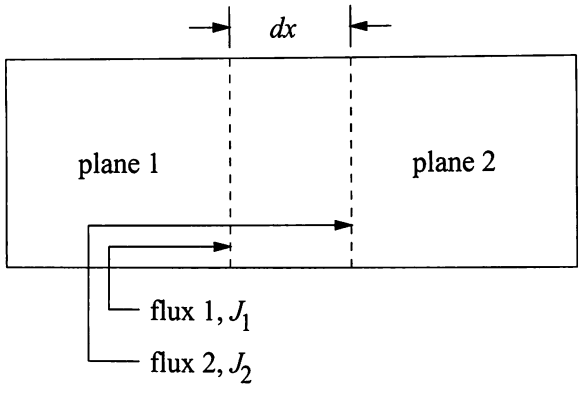

Figure 2.4 Derivation of Fick's second law where the rate of concentration change = $\frac{\delta(J_1-J_2)}{\delta x}$ (Darken & Gurry, 1935).

Consider two parallel unit planes a distance δx apart (Figure 2.4). Using Fick's first law, the flux through the first plane is:

$$J = -D\,\frac{\delta C}{\delta x} \tag{2.13}$$

and the flux out through the second plane is:

$$J + \frac{\delta J}{\delta x}\delta x = -D\,\frac{\delta C}{\delta x} - \frac{\delta}{\delta x}\left(D\,\frac{\delta C}{\delta x}\right) \tag{2.14}$$

By subtraction:

$$\frac{\delta J}{\delta x} = -\frac{\delta}{\delta x}\left(D\,\frac{\delta C}{\delta x}\right) \tag{2.15}$$

But $\delta J/\delta x$, the difference in the flux over distance, equals the negative rate of concentration change, $-\delta C/\delta t$. Thus, the change in concentration over time is written as:

$$\frac{\delta C}{\delta t} = \frac{\delta}{\delta x}\left(D\,\frac{\delta C}{\delta x}\right) \tag{2.16}$$

This is Fick's second law. If D is considered to be independent of concentration, the change in concentration with time $\delta C/\delta t$ becomes:

$$\frac{\delta C}{\delta t} = D\left(\frac{\delta^2 C}{\delta x^2}\right) \tag{2.17}$$

For a steady state condition, $\delta C/\delta t$ equals 0. When the concentration is expected to vary with both position and time, Fick's laws are used as the basis of numerical solutions, together with correct boundary conditions.

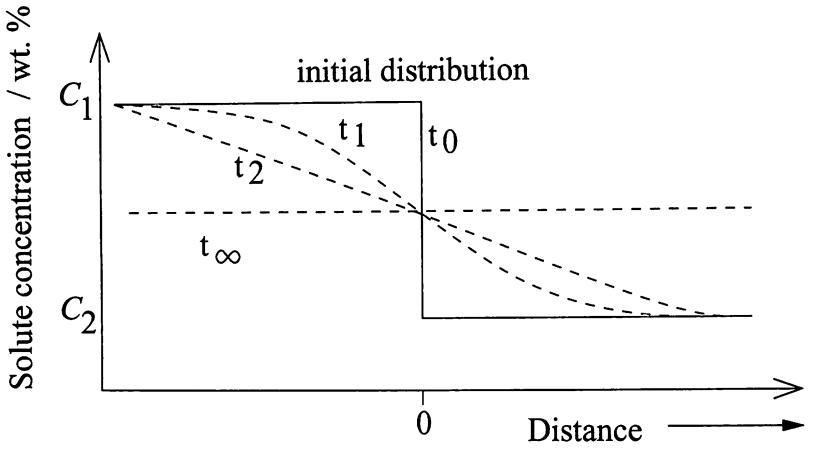

Figure 2.5 Effect of diffusion on solute distribution in an infinite metal alloy, (modified from Smallman & Bishop, 1999).

If there is a sharp interface between two imaginary alloys (Figure 2.5) with an initial distribution of a solute alloying element given by the solid line, solute diffusion produces a progressive change in the solute concentration, which varies as shown by the dashed lines.

The initial and boundary conditions that apply for the infinite diffusion couple in Figure 2.5 are given as (Kirkaldy & Young, 1987):

$$C(x > 0\ ,\ 0) = C_2 \text{ and } C(x < 0\ ,\ 0) = C_1$$

and

$$C(\infty\ ,\ t > 0) = C_2 \text{ and } C(-\infty\ ,\ t < 0) = C_1$$

The application of the above conditions give the solution to Fick's second law as:

$$C = C_2 + \frac{(C_1 - C_2)}{2}\left(1 - \text{erf}\frac{x}{2\sqrt{D\,t}}\right) \tag{18}$$

where

$$\text{erf}\frac{x}{2\sqrt{D\,t}} = \frac{2}{\sqrt{\pi}}\int_0^{x/2\sqrt{(D\,t)}} \exp(-y^2)\,dy$$

The erf (y) is known as the Gauss error function, and as $y \to \infty$, erf $(y) \to 1$. Here, y is a dummy, dimensionless variable.

At the joint interface where $x = 0$, then the concentration of solute is $(C_1 - C_2)/2$. In regions of positive concentration gradient, the solute concentration rises, and in regions of negative concentration gradient, then the concentration falls. When there is no concentration gradient, no solute redistribution occurs.

2.4.2 The thermodynamics of diffusion

Fick's laws are empirical, and assume that the flux of solute is proportional to its concentration gradient (Porter & Easterling, 1992). It is more appropriate to discuss diffusion in terms of free energy gradients. The free energy changes that may take place during diffusion are illustrated in Figure 2.6. Two blocks of $A - B$ solid solution are joined together and held at some temperature so that solute diffusion will occur.

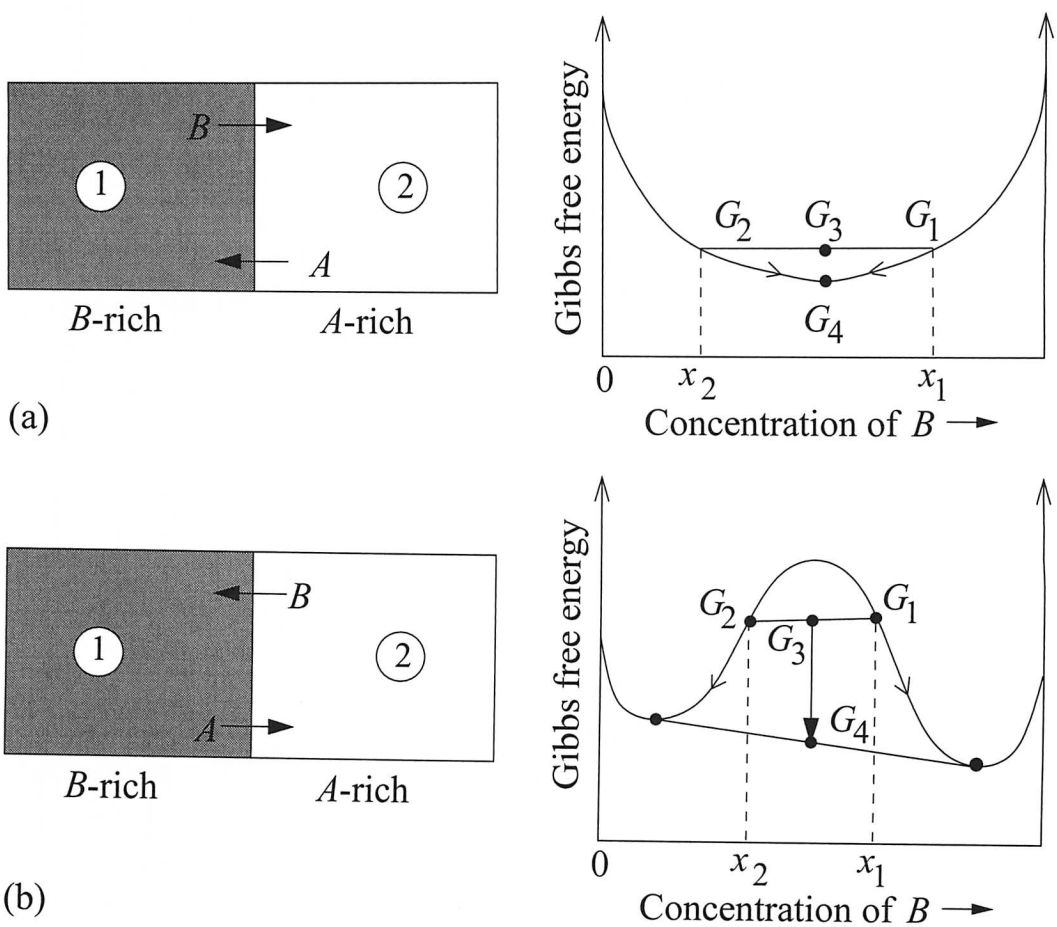

Figure 2.6 Free energy changes during; (a) 'downhill' and (b) 'uphill' diffusion (Porter & Easterling, 1992).

The B-rich side of the joint has a free energy G_1 and the A-rich side has a free energy G_2. The initial free energy of the block as a whole is G_3. After diffusion has occurred G_3 is lowered to G_4. In the case of downhill diffusion, Figure 2.6a, the reduction in the free energy of the system is achieved by solute diffusion down concentration gradients, which also happen to be in the same direction as the chemical potential gradients. Hence the A-rich side is becoming less rich in component A, and vice versa for the B-rich side.

If a homogeneous solution is made up of components A and B, whose free energy diagram is as given on the right hand side of Figure 2.6b, a reduction of free energy is still achieved by the exaggeration of concentration differences. The free energy of the system has now been lowered, this time by an 'uphill' diffusion of solute, *i.e.* up concentration gradients but still down chemical potential gradients.

In real situations, a dissimilar steel weld is made between two steels with different substitutional element contents which is then subject to a high temperature heat treatment. This causes a gradient in the chemical potential of carbon at the joint interface, which drives diffusion. This is an illustration of uphill diffusion, because the carbon chemical potential gradients are in the opposite direction to the carbon concentration gradient.

2.4.3 Diffusion of carbon in austenite with a discontinuity in composition

The Darken experiments (1949) provided the first clear evidence of uphill diffusion of carbon between two steels heated in the austenite phase field. The driving force for isothermal diffusion was recognised as the negative gradient of the chemical potential of carbon.

Darken (1949) studied four weld couple experiments. Pairs of steel that had the same carbon content but a different substitutional solute content were welded together and then heat treated at 1050 °C for about two weeks. Subsequent analysis showed that carbon had partitioned.

The distribution of carbon in each heat treated sample was measured by sectioning the specimens and quantifying the carbon content by a carbon-by-combustion method. Darken observed a discontinuity in carbon concentration at the weld junction, Figure 2.7, which was attributed to an attempt by the system to achieve equilibrium. Darken determined that the rate of diffusion was proportional to the chemical potential gradient multiplied by the mobility and concentration. There was only a minor change in the concentrations of the substitutional solutes during the course of the experiments. Darken reported that within the limits of experimental resolution, the carbon concentration does not change abruptly at the interface even though it changes rapidly in this vicinity.

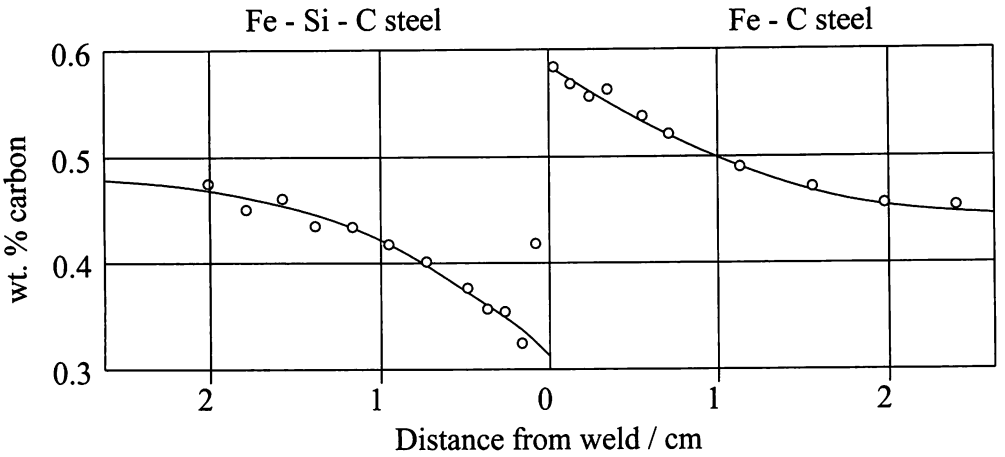

Figure 2.7 Nonuniform distribution of carbon produced from an initially uniform distribution. Carbon migrated from a Fe – Si – C alloy to a Fe – C alloy (modified to SI units from Darken, 1949).

2.4.4 Diffusion along grain boundaries

The grain boundary diffusion coefficient, D_b, is always larger than for diffusion through the lattice (D_l). This reflects the more open structure of grain boundaries, or of defects in general.

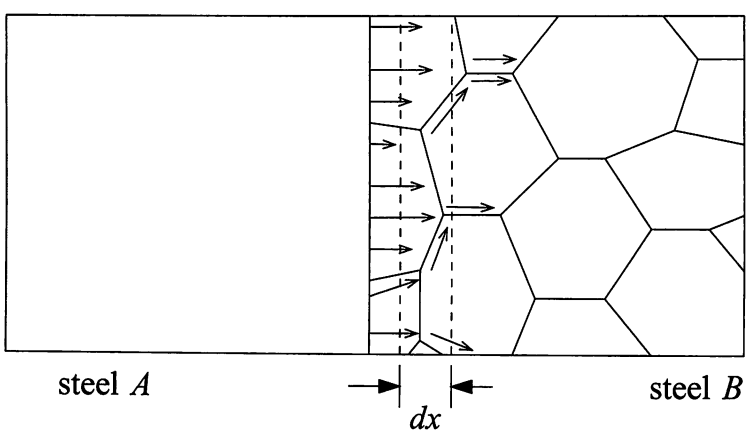

Figure 2.8 The diffusivity paths of atoms diffusing from steel A to steel B (Porter & Easterling, 1992).

Figure 2.8 shows the paths that migrating atoms from steel A into steel B will take during heat treatment. The solute atoms which diffuse along the grain boundaries penetrate faster into steel B than those diffusing through the lattice.

The effectiveness of grain boundary diffusion is described by considering steady-state diffusion

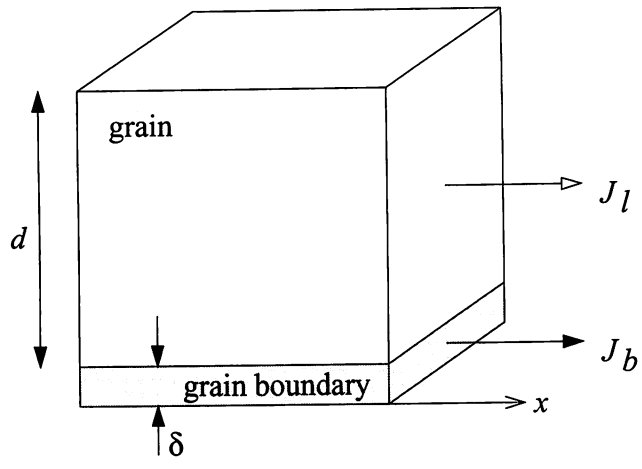

Figure 2.9 Illustration of the combined fluxes from the lattice and the grain boundary during steady state diffusion (Porter & Easterling, 1992).

through a block that contains a single grain boundary parallel to the direction of diffusion, Figure 2.9.

The fluxes of solute through the lattice and along the grain boundary, J_l and J_b respectively, assuming a constant concentration gradient along x, are given by:

$$J_l = -D_l \frac{dC}{dx} \quad \text{and} \quad J_b = -D_b \frac{dC}{dx} \tag{2.19}$$

The contribution to the total flux from grain boundary diffusion depends on the cross section of area through which solute flows from it. If the grain boundary has an effective thickness of δ and the grain size is d, then the total flux is:

$$J = (J_b \delta + J_l d)/d) = -\left(\frac{D_b + D_l}{d}\right)\frac{dC}{dx} \tag{2.20}$$

The apparent diffusion coefficient D_{app} is therefore the sum of the lattice and grain boundary diffusion coefficients in the proportions:

$$D_{\text{app}} = D_l + \frac{D_b \delta}{d} \tag{2.21}$$

Hence the relationship of D_{app} and D_l depends on d and δ.

2.5 The role of carbides in creep resistant steels

Creep is a time dependent process by which thermally activated plastic flow occurs at a stress which is below the yield strength of the material. After the initial strain from the application of load, deformation settles down to a linear steady-rate stage. The final stage of creep coincides with the initiation of micro-cracks at the grain boundaries due to the migration of vacancies here, or by grain boundary sliding (Smallman & Bishop, 1999; Higgins, 1994). A small grain size promotes creep because of an increase in D_{app}. Indeed, the creep rate is found to be proportional to $1/d^2$ where d is the average grain size (Evans & Wilshire, 1993).

The resistance to creep can be improved in many ways. Though the creep rate is small below 0.4 T_m, (where T_m is the melting point of the alloy) it is not always possible to use metal alloys with high melting temperatures. For example tungsten has a melting point of 3380 °C but has poor oxidation resistance and is very expensive. Creep resistance is increased by limiting dislocation movement and making grain boundary sliding difficult. This can be done by:

- The addition of alloying elements which have a low mobility and which contribute to solid solution strengthening.
- The addition of alloying elements that dispersion harden the alloy and hinder grain boundary sliding.
- A reduction in the grain boundary surface per unit volume reduces D_{app}. Grain boundaries can be eliminated by using single crystals; many turbine blades for jet engines are made from single crystals.

The creep resistant steels used in this investigation have most of their carbon content combined as alloy carbides, which also contain a significant portion of metallic solutes. During heat treatment, some of these carbides may dissolve, but the solutes re-precipitate as more stable phases.

Any model for the prediction of carbon migration in the present context must take carbides into account. In the steel with a lower carbon chemical potential (generally with a higher substitutional alloy content), carbide nucleation or growth of the pre-existing carbides occurs because of the incoming carbon from the adjoining steel. More dramatically, a carbon-denuded zone appears in the high carbon chemical potential steel (generally the lower alloyed steel) where the dissolution of carbides also leads to grain growth.

2.5.1 The growth of carbides

Diffusion-controlled growth of a precipitate is illustrated by Figure 2.10, where the one-dimensional growth of carbide B occurs from supersaturated ferrite β on the high-alloy side of a diffusion couple.

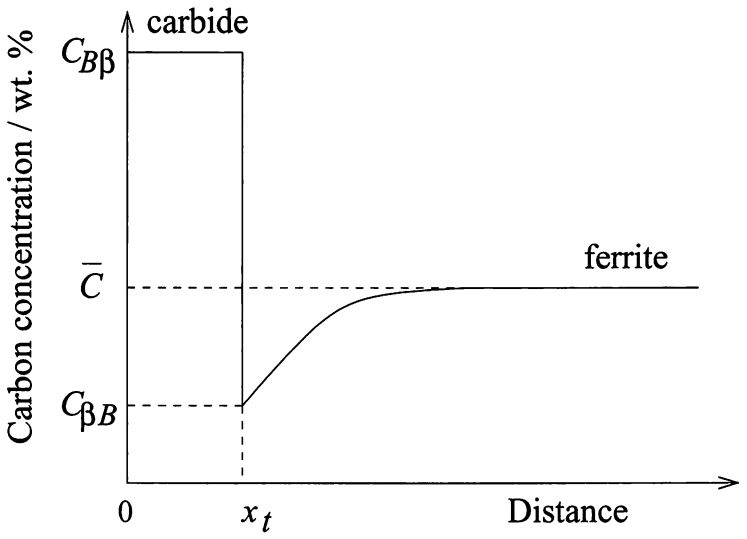

Figure 2.10 A schematic diagram to show the composition variation over distance during the diffusion-controlled growth of a carbide in the carburised zone of a dissimilar steel joint (Reed-Hill & Abbaschian, 1994).

$C_{B\beta}$ is the carbon concentration in the carbide, in equilibrium with ferrite β, and a similar rationale is applied to the concentration $C_{\beta B}$. $\overline{C}$ is the average solute concentration in the steel as a whole.

Over a small time step, dt, a unit area of carbide/matrix interface can proceed forward through the ferrite by a distance dx, Figure 2.11. This converts a volume of equal to $(C_{B\beta} - C_{\beta B})dx$. Therefore, for this to occur, $(C_{B\beta} - C_{\beta B})dx$ carbon atoms must diffuse to the carbide/matrix interface and then cross it. It follows that the gradient of carbon concentration must be evaluated at each position as the interface moves:

$$-Jdt = D_C \frac{dC_{\beta B}}{dx}\bigg|_{x=x_t} dt \tag{2.22}$$

where J is the flux of carbon atoms, D_C is the diffusion coefficient (assumed to be concentration independent) and $dC_{\beta B}/dx$ is the carbon concentration gradient in the matrix at the interface.

The rate at which solute is absorbed by the carbide is given as:

$$(C_{B\beta} - C_{\beta B})\frac{dx}{dt} \tag{2.23}$$

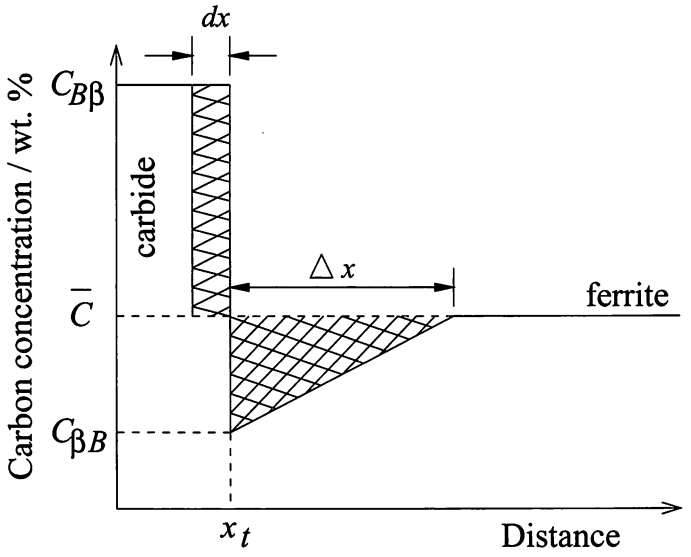

Figure 2.11 A schematic diagram of Zener's approximation for the composition-distance curve.

This is also equal to the flux of solute J that arrives at the interface:

$$J = D_C \frac{\overline{C} - C_{\beta B}}{\Delta x} \tag{2.24}$$

Considering the overall conservation of mass, the following equation can be written:

$$(C_{B\beta} - \overline{C})dx = \frac{1}{2}(\overline{C} - C_{\beta B})\Delta x \tag{2.25}$$

We can now write:

$$(C_{B\beta} - C_{\beta B})dx = D_C \frac{dC_{\beta B}}{dx}\Big|_{x=x_t} dt \tag{2.26}$$

and the interface velocity v can be calculated as:

$$v = \frac{dx}{dt} = \frac{D_C}{(C_{B\beta} - C_{\beta B})} \frac{dC_{\beta B}}{dx} \tag{2.27}$$

The Zener approximate solution to the situation above assumes the concentration-distance profile in the matrix as a straight line. In the carbide, the cross-hatched region represents the amount of carbon that has become combined in the carbide. In the ferrite, the shaded triangle illustrates the distance from which carbon has partitioned to join the carbide.

Equating the two crossed-hatched areas gives:

$$\frac{1}{2}\Delta C_{\beta B}\,\Delta x = (C_{B\beta} - \overline{C})x_t \tag{2.28}$$

where $\Delta C_{\beta B} = \overline{C} - C_{\beta B}$. Rearrangement yields:

$$\Delta x = \frac{2(C_{B\beta} - \overline{C})x_t}{\Delta C_{\beta B}} \tag{2.29}$$

and the concentration gradient is:

$$\frac{\Delta C_{\beta B}}{\Delta x} = \frac{(\Delta C_{\beta B})^2}{2(C_{B\beta} - C_{\beta B})x_t} = \frac{(\overline{C} - C_{\beta B})^2}{2(C_{B\beta} - \overline{C})x_t} \tag{2.30}$$

Substituting this slope into the velocity equation 2.28 yields:

$$v = \frac{dx}{dt} = \frac{D(\overline{C} - C_{\beta B})^2}{(C_{B\beta} - C_{\beta B}) \cdot (C_{B\beta} - \overline{C})x_t} \tag{2.31}$$

Integrating this differential equation gives the relationship for the position of the boundary x_t as a function of time t as:

$$x_t = \alpha_1^* \sqrt{D\,t} \tag{2.32}$$

where the parameter α_1^* is:

$$\alpha_1^* = \frac{(\overline{C} - C_{\beta B})}{\sqrt{(C_{B\beta} - C_{\beta B})} \cdot \sqrt{(C_{B\beta} - C_{\beta B})}} \tag{2.33}$$

The subscript of α_1^* indicates that this is the solution for one-dimensional growth of a carbide. Differentiating $x = \alpha_1^* \sqrt{D\,t}$ gives the growth velocity of the carbide in a greatly simplified form as:

$$v = \frac{dx}{dt} = \frac{\alpha_1^*}{2}\sqrt{D_C/t} \tag{2.34}$$

This shows that for one-dimensional growth, the interface position of a growing carbide varies as $\sqrt{D_C\,t}$ and the velocity as $\sqrt{D_C/t}$. These results have general applications for whenever growth is controlled by diffusion, assuming that the diffusion distance Δx increases with the carbide size.

If the activation energy Q for carbon diffusion in ferritic iron is 82 900 J mol^{-1} then the diffusion coefficient for carbon D_C has been estimated by Reed-Hill & Abbaschian (1994) to be:

$$D_C = D_0 e^{-82\,900/RT} \tag{2.35}$$

So equation 2.34 can be written as:

$$v = \alpha_1^* \left(\frac{D_0}{t}\right)^{\frac{1}{2}} e^{-41\,450/RT} \tag{2.36}$$

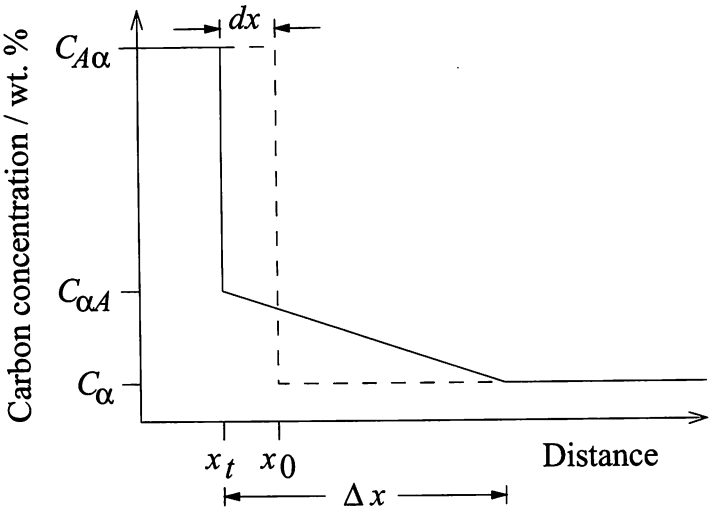

Figure 2.12 The carbon concentration profile around a carbide in equilibrium with its depleted matrix, during dissolution (Aaron, 1968).

For carbon diffusion at low temperatures, below 400 °C, the term $e^{-Q/RT}$ becomes particularly important.

2.5.2 Interference between growing carbides

In diffusion-controlled growth, the interface velocity varies inversely as $\sqrt{t}$. However, this assumes that the far-field concentration remains constant, which will not be the case at the later stages of precipitation when the diffusion-fields of adjacent precipitates begin to overlap. This phenomena is known as "soft impingement" and leads to deviations from the $\sqrt{t}$ dependence. Growth slows down faster than given by equation 2.32, and eventually stops when equilibrium is reached.

2.5.3 Dissolution of a carbide in an infinite matrix

In principle, the dissolution of carbide can be thought of as the reverse of the growth process. However, even though the kinetics are different, a major disparity is that there is no nucleation stage (Reed-Hill & Abbaschian, 1994). The concentration profile expected during dissolution is illustrated on Figure 2.12, again assuming constant concentration gradients.

In the beginning, the matrix has an initial carbon concentration C_α and the equilibrium carbide has a carbon concentration of $C_{A\alpha}$. On raising the temperature, the equilibrium concentration in the ferrite becomes $C_{\alpha A}$ at the carbide/matrix interface, and is maintained as the carbide shrinks (Aaron, 1968; Whelan, 1969; Ågren, 1990). If Zener's simplification is adopted, all the carbon concentration gradients can be assumed to be straight lines, Figure 2.12.

Before dissolution begins, $t = 0$, the carbide width is x_0. Therefore at any time ($t > 0$) the carbide width x_t is defined as:

$$x_t = x_0 - dx \tag{2.37}$$

where dx is the reduction in the carbide width due to carbide dissolution. For one-dimensional dissolution, the conservation of mass requires that during a short time the amount of carbon that is leaving the carbide is equal to the amount entering it, so that this is written as:

$$dx(C_{A\alpha} - C_\alpha) = \frac{1}{2}(C_{\alpha A} - C_\alpha)\Delta x \tag{2.38}$$

where Δx is the distance in the ferrite affected by carbon diffusion out of the carbide.

From Aaron (1968), ∇C_I is the concentration gradient in the matrix, and is given as:

$$\nabla C_I = \frac{C_{\alpha A} - C_\alpha}{\Delta x} \tag{2.39}$$

Substituting equation 2.38 into equation 2.39 gives:

$$\nabla C_I = \frac{(C_{\alpha A} - C_\alpha)^2}{2dx(C_{A\alpha} - C_\alpha)} \tag{2.40}$$

To balance the fluxes from both the carbide and matrix gives the dissolution rate as:

$$\frac{dx}{dt} = \frac{D_C \nabla C_I}{(C_{A\alpha} - C_{\alpha A})} \tag{2.41}$$

At the beginning of dissolution when $dx = 0$ and $t = 0$, then:

$$dx = \left[\frac{(C_{\alpha A} - C_\alpha)}{\sqrt{(C_{A\alpha} - C_\alpha)}\sqrt{(C_{A\alpha} - C_{\alpha A})}}\right]\sqrt{D_C\, t} \tag{2.42}$$

which in turn yields:

$$x_t = x_0 - \left[\frac{(C_{\alpha A} - C_\alpha)}{\sqrt{(C_{A\alpha} - C_\alpha)}\sqrt{(C_{A\alpha} - C_{\alpha A})}}\right]\sqrt{D_C\, t} \tag{2.43}$$

or simply:

$$x_t = x_0 - \Omega\sqrt{D_C\, t} \tag{2.44}$$

with

$$\Omega = \left[\frac{(C_{\alpha A} - C_\alpha)}{\sqrt{(C_{A\alpha} - C_\alpha)}\sqrt{(C_{A\alpha} - C_{\alpha A})}}\right]$$

2.5.4 Carbide dissolution in a binary Fe - C alloy

The simple model by Ågren (1990) describes the dissolution of spherical cementite particles in a binary Fe – C alloy. The model assumes that the carbide shrinkage rate is controlled by

volume diffusion, and that local equilibrium is maintained at the receding phase interface. The effects of surface tension and the composition dependence on the molar volumes of the phases are neglected (Ågren & Vassilev, 1984).

The carbon concentration in the matrix is higher next to the carbide compared to that far away, causing carbide dissolution. The flux of carbon inside the carbide is not considered because it is negligible.

The instantaneous radius of the carbide derived in equation 2.44 is based on a single carbide surrounded by an infinite matrix, without soft impingement.

The time for a cementite particle of radius x_0 to dissolve, t_{diss}, can be found by re-arranging equation 2.44 and setting $x_t = 0$:

$$t_{\text{diss}} = \frac{(x_0)^2}{2\Omega D_C} \tag{2.45}$$

The dissolution time depends strongly on the initial carbide size.

The volume fraction of carbide, V_A, of a uniform carbide size distribution can be found as a function of time:

$$V_A = V_A^0 \left\{ 1 - \frac{2\Omega D_C \, t}{x_0^2} \right\}^{3/2} \tag{2.46}$$

where V_A^0 is the initial volume fraction of carbide. A comparison of different numerical solutions to study the dissolution of a spherical cementite carbide is given in Figure 2.13. The temperature of dissolution was 850 °C and the initial carbide size in the binary Fe – C alloy was 1.5 μm (Ågren, 1990). A relatively good agreement was reported between the simple analytical solutions (Aaron *et al.*, 1970; Whelan, 1969) and the numerical solution by Ågren (1990), however, this is not shown if Figure 2.13.

2.5.5 Carbide dissolution in a low-alloy steel

In the case of low-alloy steels, for example an Fe – j – C steel where j can be an element like chromium or manganese, the situation described in the previous section becomes complicated. Assuming diffusion-controlled dissolution, the study of the kinetics of cementite and $M_{23}C_6$ carbides in alloy steels has been discussed by Hillert *et al.* (1971) and Gullberg (1973). The dissolution of a carbide in a low-alloy steel was considered in stages. The first stage involved the rapid redistribution of carbon from the carbide into the matrix. This happened at the start of carbide dissolution until the concentration of carbon in the matrix had increased. The latter stage of dissolution depended upon the diffusion of the substitutional element j, this becoming the rate limiting part of dissolution.

Carbide dissolution in low-alloy steels tends to be slower than in binary Fe – C steels due to

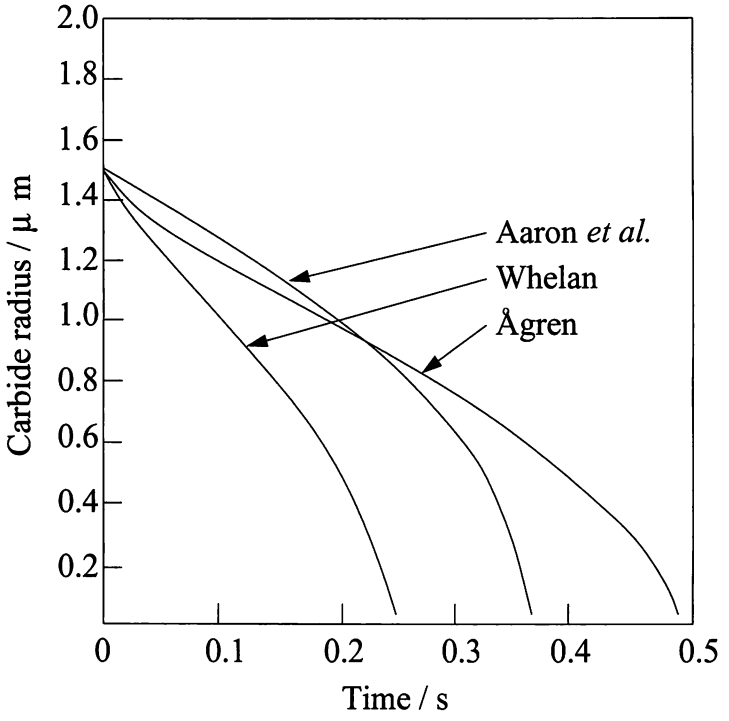

Figure 2.13 Dissolution of a spherical cementite carbide according to different analytical and numerical solutions (modified from Ågren, 1990).

the requirement for substitutional solutes to diffuse to preserve local equilibrium at the moving carbide/matrix interface.

It had also been reported that cementite dissolution in low-alloy steels could be wholly carbon diffusion-controlled if the initial matrix composition lies in a single phase region of a ternary Fe – *j* – C diagram, and at a point corresponding to a lower carbon activity than at the carbide/matrix interface (Ågren, 1990).

Though soft impingement is not taken into account, it is still possible to check if all the carbides can dissolve during a rapid, carbon-controlled reaction. A mass balance for carbon assumes that there is a homogeneous distribution of carbon throughout each phase, so the average carbon content of the alloy, $\overline{C}$, is given as:

$$\overline{C} = V_A \,.\, C_{A\alpha} + (1 - V_A) \,.\, C_{\alpha A} \tag{2.47}$$

Equation 2.48 is valid at the start of dissolution and also when the rapid dissolution reaction is complete, because of a homogeneous carbon content being attained in the matrix.

$$V_A = \frac{\overline{C} - C_{\alpha A}}{C_{A\alpha} - C_{\alpha A}} \tag{2.48}$$

If equation 2.48 yields a negative number, then $\overline{C}$ must be in the carbon poor region of the phase diagram, and this now leads to the total dissolution of all carbides.

For an aluminium-killed low-alloy steel with approximately 0.04 wt% carbon and 0.16 wt% manganese, which was tempered for 2 h at 710 °C then slow cooled, the microstructure before dissolution was one of spheroidal carbides in a ferrite matrix. If this steel is then annealed at between 650 and 550 °C, the cementite became enriched in manganese. It was then found that the dissolution of cementite could be delayed by a factor of 10, proving that alloy elements in the carbide will make their dissolution more sluggish (Ågren, 1990).

2.6 Summary

There are clearly many factors influencing the dissolution and growth of carbides in alloy steels. These ideas, along with the literature about diffusion and grain growth, will be used as a reference for the predictive model that determines the width of the carbon denuded region in the low-alloy side of a dissimilar joint during heat treatment, and also for the practical experiments which study the affects of carbon redistribution. The following chapter discusses the theory used in the models to predict carbon partitioning.

Chapter Three

Carbon Migration Across Ferritic Joints

There have been many attempts at modelling the redistribution of carbon during the heat treatment of dissimilar metal welds; Christoffel & Curran, 1956; Ågren, 1981; Buchmayr *et al.*, 1989; Kim *et al.*, 1992; Race, 1992; Pilious & Stránský, 1998. The heat treatments considered here are with samples in the ferrite-carbide phase field, so it is pertinent to take into account the process of diffusion and the dissolution of alloy carbides which are the sources and sinks for carbon.

3.1 Background

A dissimilar joint is formed by welding or diffusion bonding two different steels together. Carbon partitions from one steel to the other because of differences in their chemical compositions. The steels are not in equilibrium with each other and this causes the migration of carbon as it tends to homogenise its chemical potential over the joint as a whole. The carbon naturally diffuses down a chemical potential gradient across the weld junction.

As a result, a carbon-depleted zone forms on one side of the junction with a corresponding enriched layer on the other side. The process of partitioning is thermally activated and hence can occur during elevated temperature service, or can be induced by tempering. Since the solubility of carbon in ferrite is minute, the redistribution process involves the dissolution of carbides on the side where the chemical potential of carbon is high, and the precipitation of carbides on the other side.

Carbon is far more mobile than any of the substitutional alloying elements and can diffuse in circumstances where the substitutional lattice is, in effect, frozen.

3.2 Modelling the diffusion distance of carbon in the ferrite phase field

Christoffel & Curran (1956) modelled the carbon partitioning in the following steps:

1. Carbon in solution diffuses from the low-alloy steel into the high-alloy steel, driven by the carbon chemical potential differences.
2. In the high-alloy steel, the arrival of carbon is accommodated by the precipitation of carbides; the net effect is that carbon diffuses down a concentration gradient away from the weld junction into the steel.

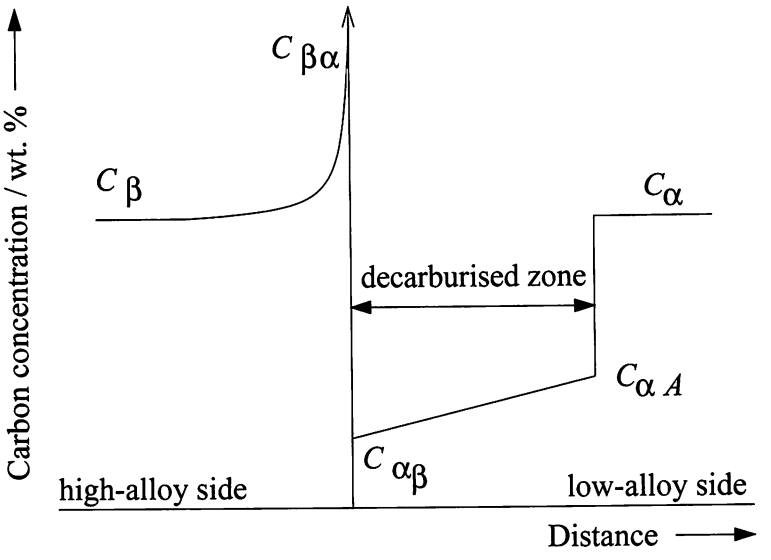

Figure 3.1 A schematic diagram of carbon distribution in a dissimilar weld after some time interval at an elevated temperature (Christoffel & Curran, 1956).

3. In the low-alloy steel, the reduced concentration at the weld junction encourages carbon diffusion towards the junction. When the concentration drops below the solubility limit, carbides dissolve, providing a source for carbon. The dissolution of carbides accounts for the metallographically observed decarburised band which occurs parallel to the fusion surface.

The estimated width of the decarburised zone is shown in Figure 3.1; where $C_{\alpha A}$ is the carbon concentration in the matrix that is in equilibrium with the carbide that is in the low-alloy steel. C_α and C_β are the carbon concentrations in the low-alloy and high-alloy steel, respectively. $C_{\alpha\beta}$ and $C_{\beta\alpha}$ are the carbon concentrations at the dissimilar joint interface in the low-alloy and high-alloy steel, respectively.

The width of the decarburised zone, x_α, was calculated using:

$$x_\alpha = \frac{C_{\alpha A} - C_{\alpha\beta}}{C_\alpha} \sqrt{2D_C t} \tag{3.1}$$

D_C is the diffusion coefficient of carbon in the low-alloy steel, and t is the time.

Equation 3.1 describes the decarburised zone growing proportionally with the square root of time. The relationship between x and $\sqrt{t}$ can be obtained from the solution of the diffusion equation, Fick's second law:

$$\frac{\delta C}{\delta t} = D\frac{\delta^2 C}{\delta x^2} \tag{3.2}$$

Applying a Laplace transform to the diffusion equation, in a semi infinite medium, gives the solution from which the relationship between diffusion distance and time can be determined:

$$C = C_0 \text{ erfc } \frac{x}{2\sqrt{Dt}} \tag{3.3}$$

where C_0 is the initial carbon concentration and erfc(z) = 1 - erf(z). From equation 3.3, the boundary and initial conditions are also satisfied (Crank, 1975):

$$C = C_0,\ x = 0,\ t > 0$$

$$C = 0,\ x > 0,\ t = 0$$

Buchmayr *et al.* (1989) modelled the redistribution of carbon in a transition joint. 1CrMoV steel (0.17 C, 1.08 Cr, 0.92 Mo, 0.23 V wt. %) was welded with a 12Cr filler metal (0.18 C, 11.25 Cr, 0.84 Mo, 0.27 V wt. %). The initial microstructure of the 1CrMoV steel was ferrite with an even distribution of cementite particles. This cementite dissolves to provide carbon that diffuses into the higher chromium steel, which consists of a mixture of ferrite and $M_{23}C_6$ carbides.

The model assumed that chromium does not diffuse during heat treatment, although it affects the chemical potential of carbon. The distribution of cementite was assumed to be controlled by the diffusion of carbon. The width of the decarburised zone was found to vary parabolically with time:

$$x_\alpha = \mathrm{C}\, 2\sqrt{D_C\, t} \tag{3.4}$$

where C = 0.23 and is a constant for the particular combination of steels used. The predicted decarburised zone widths in the 1CrMoV steel are given in Table 3.1.

PWHT	x_α (μm)
680 °C, 2 h	260
680 °C, 10 h	300
730 °C, 2 h	330
730 °C, 10 h	750

Table 3.1 Decarburised zone widths formed in a 12%Cr/1%CrMoV weld during PWHT (Buchmayr *et al.*, 1989).

Though decarburised widths were predicted for 680 and 730 °C, Buchmayr *et al.* found equation 3.4 was actually reliable between 500 – 550 °C only, when chromium carbides began to precipitate. This limits the application of this model to below the PWHT temperature.

3.2.1 Summary

Though the models above (Christoffel & Curran, 1956; Buchmayr *et al.*, 1989) yield similar equations for predicting the diffusion of carbon in the ferritic phase of the steels, the dissolution of carbides is not properly accounted for. The precipitation of alloy carbides in the high-alloy steel absorbs carbon and chromium, hence altering the chemical potential of carbon and changing the driving force for diffusion. The carbides in low-alloy steel are similarly sources of carbon, but the diffusion of carbon through the steel is usually the rate limiting process. The volume fraction, size and type of carbide must be considered when determining the chemical potential gradients of carbon in the steel.

It is assumed in all models that there is equilibrium locally at the joint interface, and the chemical potential of carbon is a function of the instantaneous chemical composition.

3.3 Influence of alloying elements on carbon diffusion

During heat treatment, the width of the decarburised zone may increase by dx_α during a given time increment dt, Figure 3.2 (Kim *et al.*, 1992).

The flux of carbon is given by a product of Fick's first law. On the low-alloy side:

$$J = D_C \, (C_{\alpha A} - C_{\alpha\beta}) \, / \, x_\alpha \tag{3.5}$$

The amount of carbon that crosses the interface over time dt is therefore:

$$Jdt = D_C \, (C_{\alpha A} - C_{\alpha\beta})dt \, / \, x_\alpha \tag{3.6}$$

The amount of carbon that has left the low-alloy steel is the shaded part on the right hand side of Figure 3.2, and can be expressed as $(C_\alpha - C_{\alpha A}/2 - C_{\alpha\beta}/2)dx_\alpha$. This amount of carbon must be equal to the flux of carbon in a given time, Jdt, so:

$$Jdt = D_C \, (C_{\alpha A} - C_{\alpha\beta})dt \, / \, x_\alpha = (C_\alpha - C_{\alpha A}/2 - C_{\alpha\beta}/2)dx_\alpha \tag{3.7}$$

Solving the differential in equation 3.7 predicts the diffusion distance as:

$$x_\alpha^2 = 2D_C . \, t \, (C_{\alpha A} - C_{\alpha\beta}) \, / \, (C_\alpha - C_{\alpha A}/2 - C_{\alpha\beta}/2) + \mathrm{C} \tag{3.8}$$

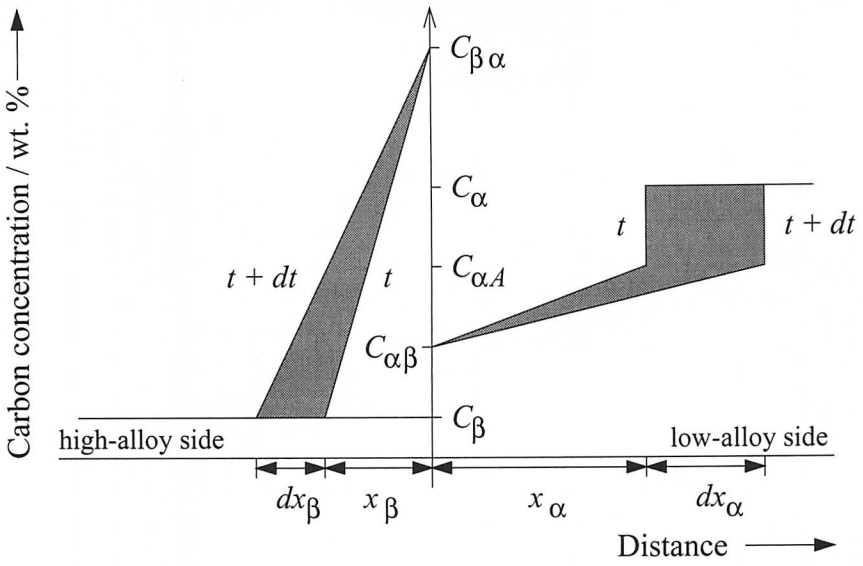

Figure 3.2 An exaggerated diagram to show the carbon concentration, and the decarburised and carburised bands in a dissimilar steel weld (Kim *et al.*, 1992).

x_α can now be termed as the decarburised zone. C is the constant of integration. One of the boundary conditions for equation 3.8 is when the time is zero, the diffusion distance is also zero, hence C = 0 and drops out of the equation.

If the difference between $C_{\alpha A}$ and $C_{\alpha\beta}$ is increased, (for example by selecting a richly alloyed steel), then the decarburised zone will also increase. This is due to the steeper slope between $C_{\alpha A}$ and $C_{\alpha\beta}$ over the decarburised width, which promotes diffusion.

The flux leaving the low-alloy steel enters the carburised zone in the high-alloy steel, β. It follows that:

$$D_C\ (C_{\alpha A} - C_{\alpha\beta})dt\ /\ x_\alpha = \frac{1}{2}(C_{\beta\alpha} - C_\beta)\ dx_\beta \tag{3.9}$$

where x_β is the diffusion distance in β. Re-arranging equation 3.9 gives:

$$x_\alpha\ dx_\beta = 2D_C\ .\ t\ (C_{\alpha A} - C_{\alpha\beta})\ /\ (C_{\beta\alpha} - C_\beta)\ dt \tag{3.10}$$

Similarly, solving the differential in equation 3.10 gives:

$$x_\beta^2 = 2D_C\ .\ t\ (C_{\alpha A} - C_{\alpha\beta})\ /\ x_\alpha(C_{\beta\alpha} - C_\beta) + \mathrm{C} \tag{3.11}$$

C is the constant of integration which, as before, drops out of the equation. Carbide forming elements (chromium, molybdenum, and vanadium) all decrease the chemical potential of

carbon, and the precipitation of carbides in the high-alloy steel alters the solubility limit of carbon in the ferrite and may slow down its diffusivity in the steel.

To predict the decarburised zone width, Pilious & Stránský (1998) discussed the relationship of all the elements present in the steel on the carbon activity.

The decarburised zone width at a given time ($t > 0$) was shown by the relation of carbon activity as:

$$x_\alpha = 2\frac{a_{c\alpha} - a_{c\beta}}{C_\alpha - C_{\alpha\beta}}\sqrt{\frac{D^\alpha t}{\pi}} \tag{3.12}$$

where $a_{c\alpha}$ is the thermodynamic activity of carbon in the low-alloy steel, similarly for $a_{c\beta}$ in the high-alloy steel. The activity of carbon is found by the general expression:

$$a_c = X_c\gamma_c \tag{3.13}$$

where X_c is the atomic fraction of carbon. γ_c is the carbon activity coefficient in the steel, calculated by:

$$\gamma_c = \exp\{\varpi_c^{cr} N_{cr(eq)}\} \tag{3.14}$$

ϖ_c^{cr} is the effective interaction coefficient for chromium on carbon activity and is dependent on temperature and is given by the formula:

$$\varpi_c^{cr} = 10.64 - \frac{36170}{T} \tag{3.15}$$

$N_{cr(eq)}$ in equation 3.14 is the thermodynamic equivalent of chromium in ferrite, in at. %:

$$N_{cr(eq)} = \sum k_{cr(c)}^{(j)} N_j^{(i)} \tag{3.16}$$

$N_j^{(i)}$ is the concentration of element j in steel i and $k_{cr(c)}^{(j)} = \varepsilon_c^j/\varepsilon_c^{cr}$ is the ratio of the interaction coefficient of element j and chromium on carbon where:

$$\varepsilon_c^{cr} = (5.91 \pm 2.77) - \frac{20060 \pm 3270}{T} \tag{3.17}$$

This method of determining carbon activity coefficients is often used for austenitic steels, however it has been applied successfully when finding the activity of carbon in ferrite, to a reasonable first approximation (Pilious & Stránský, 1998).

3.3.1 Summary

The role of substitutional solutes on the diffusion of carbon can be expressed via their influence on the activity of carbon. Some of the substitutional solutes also form carbides which will inevitably influence the partitioning of carbon across a dissimilar metal interface.

3.4 Role of carbides in carbon migration

in ferrite steels, most of the carbon is locked up as carbides, which must be treated as sources and sinks in the partitioning process (Race, 1992).

The '*uphill*' diffusion of carbon across dissimilar ferritic steel joints includes carbide dissolution in the low-alloy steel and reprecipitation in the high-alloy steel. A model that incorporates these phenomena is shown in Figure 3.3.

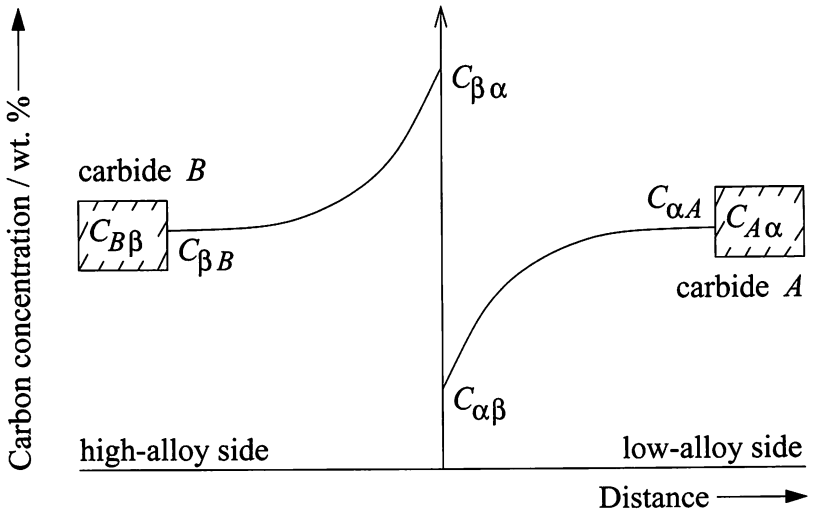

Figure 3.3 Schematic representation of the diffusion model (Race, 1992).

$C_{A\alpha}$ and $C_{B\beta}$ are the concentrations of carbon in the carbides that are in equilibrium with the matrix in the low-alloy and high-alloy steels respectively. The concentration profiles are curved to represent the steeper drop in concentration in the vicinity of the joint interface.

These carbon concentrations were determined using MTDATA (1996) – a computer program that accesses thermodynamic data to determine equilibrium phase diagrams.

The enrichment of the matrix with solute as the carbide dissolves can be balanced against the diffusion flux at the carbide/matrix interface, therefore, the solute concentration at the interface remains fixed. Thus for the ith carbide dissolving, the balance of mass conservation can be written as:

$$\frac{dx_{\alpha i}}{dt}(C_{A\alpha i} - C_{\alpha Ai}) = D_C\left[\frac{dC}{dx}\right]_{x=0} \tag{3.18}$$

$x_{\alpha i}$ is the distance from the joint interface to the ith carbide. Using the Laplace transforms for solution of Fick's second law, and the error function profile assumed from Figure 3.3, the

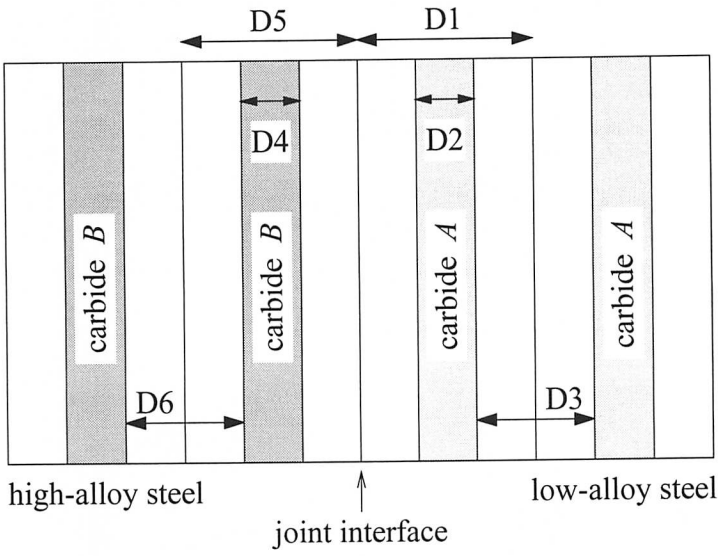

Figure 3.4 Schematic diagram of the computer model (Race, 1992).

diffusion distance from the ith carbide to the dissimilar metal interface, on the low-alloy side, is:

$$x_{\alpha i} = 2\sqrt{\frac{D_C\, t}{\pi}}\,\frac{C_{\alpha Ai} - C_{\alpha\beta i}}{(C_{A\alpha i} - C_{\alpha Ai})} + x^0_\alpha \tag{3.19}$$

where x^0_α is the initial distance from the dissimilar interface to the dissolving carbide. Equation 3.19 gives the decarburised zone width, ξ_α equal to $x_{\alpha i}$.

Similarly, on the high-alloy side, the distance from the dissimilar interface to the closest carbide undergoing growth can be written as:

$$x_{\beta i} = 2\sqrt{\frac{D_C\, t}{\pi}}\,\frac{C_{\alpha\beta i} - C_{\beta\alpha i}}{(C_{B\beta i} - C_{\beta Bi})} + x^0_\beta \tag{3.20}$$

where x^0_β is the distance from the dissimilar interface to the first carbide that grows on the high-alloy side.

This model is illustrated using rectangular slabs as carbides surrounded by ferrite matrix on either side of the dissimilar joint interface in Figure 3.4.

The initial carbide thicknesses, D2 and D4, are assumed constant, their volume fractions are given by MTDATA (1996). Consequently, the other dimensions in the model are determined using Figure 3.4:

$$\mathrm{D1} = \frac{\mathrm{D2}}{V_A} \quad \text{and} \quad \mathrm{D5} = \frac{\mathrm{D4}}{V_B}$$

$$\mathrm{D3} = \mathrm{D1} - \mathrm{D2} \quad \text{and} \quad \mathrm{D6} = \mathrm{D5} - \mathrm{D4}$$

where V_A and V_B are the relevant volume fractions of carbides.

The decarburised zone width at the beginning is set to x_α^0, equal to D3/2. As the carbide D2 begins to dissolve, ξ_α becomes equal to the amount the carbide has dissolved by, plus a small fraction x_α^0 (equation 3.19). When D2 has dissolved completely, ξ_α equals D1 + D3/2, and the dissolution of the second carbide slab begins.

The chemical compositions of the carbides may alter as the carbon concentration changes. Changes in the average carbon concentrations $\overline{C_\alpha}$ and $\overline{C_\beta}$ respectively in the low and the high-alloy steels, are given by:

$$\overline{C_\alpha} = C_{A\alpha} \cdot V_A + C_{\alpha A} (1 - V_A) \tag{3.21}$$

$$\overline{C_\beta} = C_{B\beta} \cdot V_B + C_{\beta B} (1 - V_B) \tag{3.22}$$

This model was tested on dissimilar steel welds for a range of times at the PWHT and ageing temperatures. Experimentally observed deviations from the parabolic laws ($x \propto \sqrt{D_C\, t}$) were predicted by this model.

The model by Race (1992) was found to be reasonably accurate at short times but overpredicted the decarburised zone width after longer heat treatments. This was attributed to changes in the nature of the carbides due to changes in $\overline{C}$.

3.5 Summary

In the published literature, many examples of modelling carbon partitioning in dissimilar steel welds have been found. Initially, models were based only on the composition of the two dissimilar steels, and that effect on the chemical potential gradients either side of the dissimilar joint occurring during tempering. Recent models have included analysis of the role of carbides in carbon partitioning, with the precipitates acting as sources and sinks on the low and high-alloy sides respectively.

The model described in the following chapter will be used to predict decarburised zones in dissimilar steel welds and diffusion bonds, and compared to published literature.

Chapter Four

Modelling Carbon Diffusion Across Dissimilar Steel Welds

The aim of the model introduced here was to predict the width of the carbon depleted zone that forms during heat treatment of a dissimilar steel joint. In this model, two key stages are considered. The first deals with the dissolution of the soluble carbides in the low-alloy steel, close to the dissimilar joint. In the second stage, the carbon diffusion across the dissimilar joint is examined.

4.1 Modelling the overall distribution of carbon

Interstitial carbon diffuses down the chemical potential gradient across a dissimilar steel joint. The diffusion of carbon occurs in a ternary Fe – C – j (j = Cr, Mo, V *etc.*) system where substitutional solutes appear to remain immobile compared to the diffusion of carbon.

The activity coefficient of carbon γ_C in the ferrite in the low-alloy steel may be expressed in terms of the interactions of carbon with the substitutional solutes. Vanadium, chromium, molybdenum and manganese all raise γ_C whereas nickel and silicon lower the activity coefficient of carbon in ferrite.

In section 3.3, equation 3.14 determined the activity coefficient of carbon in a chromium-alloyed steel. From this equation, the thermodynamic equivalent of chromium in ferrite was calculated in terms of the ratio of the interaction of element j on carbon, compared to the effect from chromium, $k^{(j)}_{\mathrm{cr(c)}}$. Table 4.1 shows the progressively weaker attraction between carbon and the elements from vanadium through to silicon.

Element, j	**V**	**Cr, Mo**	**Mn**	**Fe**	**Ni**	**Si**
$k^{(j)}_{cr(c)}$	2.08	1.00	0.386	0	-0.442	-0.673

Table 4.1 Equivalence constants, $k^{(j)}_{cr(c)}$, of elements in steels (Pilious & Stránský, 1998).

The activity coefficient of carbon γ_C, for a ternary Fe – Cr – C alloy, may also be calculated by a numerical expression (Wada *et al.*, 1972b):

$$\log\gamma_C = \frac{2300}{T} - 2.24 + \left(\frac{179}{T}\right) . C_C - \left(\frac{102}{T - 0.033}\right) . C_{Cr} \qquad (4.1)$$

The concentrations of carbon and chromium, C_C and C_{Cr} are expressed in wt. % and T is the absolute temperature. Molybdenum, manganese and chromium are all found to decrease

the activity coefficient in proportion to the carbon content (Wada *et al.*, 1972b). Silicon has the opposite effect on the carbon activity coefficient in ferritic steel (Wada *et al.*, 1972a). This method is, however, restricted to a ternary alloy.

For dilute solutions containing n substitutional elements, another method for calculating the activity coefficient of carbon can be found using (Kirkaldy *et al.*, 1978):

$$\ln\{\gamma_C\} = \sum_{1}^{n} \epsilon_j X_j \tag{4.2}$$

Where ϵ_j is the Wagner interaction parameter between carbon and carbon for j=1, and carbon and substitutional element for $j > 1$. Values of ϵ_j are reported in Table 4.2 for temperatures above the eutectoid temperature, and compositions of steel containing up to 2 wt. % C (Kirkaldy *et al.*, 1978). An assumption is applied that these interaction coefficients in the austenite phase (Table 4.2) are equal to those in ferrite.

Element	ϵ_j
C	8910 / T
Mn	-5070 / T
Si	4.84 - (7370 / T)
Ni	-2.2 -(7600 / T)
Cr	24.4 - (38400 / T)
Mo	3.855 - (17870 / T)
V	-2466 / T

Table 4.2 Wagner interaction coefficients (Kirkaldy *et al.*, 1978).

The three methods of calculating the carbon activity coefficients are compared in Table 4.3 for P91 and $2\frac{1}{4}$Cr1Mo steels (compositions given in Table 4.4).

Author	$\gamma_{C\alpha}$	$\gamma_{C\beta}$	**Elements under consideration**
Pilious & Stránský, 1998	0.442	0.059	Mn, Si, Ni, Cr, Mo, V
Wada *et al.*, 1972b	1.02	0.506	C, Cr
Kirkaldy *et al.*, 1978	0.986	0.267	C, Mn, Si, Ni, Cr, Mo, V

Table 4.3 Comparison of carbon activity coefficient calculations in a $2\frac{1}{4}$Cr1Mo steel ($\gamma_{C\alpha}$) and in a P91 steel ($\gamma_{C\beta}$).

Table 4.3 illustrates the discrepancies in calculating carbon activity coefficient in alloy steels; for carbon redistribution to occur from the low to the high-alloy side of a dissimilar joint, the relationship $\gamma_{C\alpha} > \gamma_{C\beta}$ must be satisfied.

4.1.1 The diffusion coefficient

The diffusion coefficient of carbon in ferrite was determined from a model assuming that in a dilute solid solution, carbon atoms can occupy both the tetrahedral and the octahedral sites in the ferrite BCC lattice (McLellan *et al.*, 1965). This model was fitted with earlier experimental measurements of carbon diffusion in ferrite iron, from authors such as Stanley (1949), who proposed that the carbon diffusion coefficient in ferrite, D_C, is given as:

$$D_C = 7.9 \times 10^{-3} \exp \frac{-18100}{RT}$$

where R is the universal gas constant and T is the temperature at which diffusion is taking place.

The possible jumps a carbon atom can make in the BCC lattice are:

(1) from an octahedral site to another octahedral site, via a tetrahedral site, D^{o-T-o}

(2) from a tetrahedral site to another tetrahedral site, D^{T-T}, also via an octahedral site, D^{T-o-T}

The diffusion coefficient is thus given by:

$$D_C = \phi D^{o-T-o} + (1-\phi) f D^{T-T} + (1-\phi)(1-f) D^{T-o-T} \tag{4.3}$$

Where ϕ is the fraction of interstitial carbon that occupy the octahedral sites and f is the fraction of remaining interstitial carbon atoms that jump via the $T-T$ route. The superscripts of the individual diffusion coefficients indicate the particular jump paths for the carbon atoms.

The following solutions for ϕ and f were obtained:

$$\phi = 1 - (\frac{1}{2}\, e^{\Delta G/kT}\, e^{-\Delta S/k} + 1)^{-1} \tag{4.4}$$

and:

$$f = 0.86$$

In equation 4.4, $\Delta G = G_u^T - G_u^o$, where G_u^T is the change in Gibbs free energy when carbon occupies a tetrahedral site, and G_u^o is the change in Gibbs free energy when carbon occupies an octahedral site. Similarly $\Delta S = S_u^T - S_u^o$ where S_u^T is the vibrational entropy when carbon

is placed in a tetrahedral site, and S_u^o is the vibrational entropy when carbon occupies an octahedral site.

The temperature dependent carbon diffusion coefficient can be modified to account for the influence of the substitutional elements in the steel (Pilious & Stránský, 1998). When considering interstitial carbon diffusion in a dilute ternary Fe – C – j alloy, it is possible to ignore the Onsanger cross-effects of carbon on the diffusion coefficient of, say, chromium because the diffusion coefficient of carbon is several orders of magnitude larger than that of chromium(Kirkaldy & Young, 1987).

4.1.2 Calculating the overall carbon concentration profiles

Assuming direct proportionality between weight fraction and atomic fraction of carbon (used in earlier discussions of γ_C, the chemical composition and the coefficients ε_C^j in the steel are used to calculate the distribution of carbon $C_C^{(x,t)}$, in wt% on each side of the joint interface by the following equation (Pilious & Stránský, 1998):

$$C_C^{(x,t)} = \left\{ \gamma_{C\beta} C_\beta + \frac{1}{2}\left[\gamma_{C\alpha} C_\alpha - \gamma_{C\beta} C_\beta\right] \cdot \left[1 - \operatorname{erf}\left(\frac{x}{2\gamma_C^{(x,t)}\sqrt{D_C\, t}}\right)\right]\right\} / \gamma_C^{(x,t)} \tag{4.5}$$

In equation 4.5, the subscript α applies to the low-alloy side, and similarly the subscript β applies to the high-alloy side of the dissimilar joint. Equation 4.8 is continuous for x in the range $(\infty, -\infty)$ and for all values of $t > 0$, as the carbon diffuses from the α to the β side.

The carbon concentrations at the joint are defined by assuming that the activity of carbon is the same at the interface. For $-x \to 0$, equation 4.5 can be used with the substitution:

$$\lim_{-x \to 0} \gamma_C^{(x,t)} = \gamma_{C\alpha}$$

and equation 4.5 can be simplified by the substitution $\sqrt{D_C^\alpha} = \gamma_{C\alpha}\sqrt{D_C}$ to give the carbon distribution in the low-alloy steel as:

$$C_C^{(x,t)} = \left\{ \frac{\gamma_{C\beta}}{\gamma_{C\alpha}} C_\beta + \frac{1}{2}\left[C_\alpha - \frac{\gamma_{C\beta}}{\gamma_{C\alpha}} C_\beta\right] \cdot \left[1 - \operatorname{erf}\left(\frac{x}{2\sqrt{D_C^\alpha\, t}}\right)\right]\right\} \tag{4.6}$$

Similarly for the high-alloy steel, $x \to 0$, and with the substitutions:

$$\lim_{-x \to 0} \gamma_C^{(x,t)} = \gamma_{C\beta} \quad \text{and} \quad \sqrt{D_C^\beta} = \gamma_{C\beta}\sqrt{D_C}$$

the carbon distribution is:

$$C_C^{(x,t)} = \left\{ C_\beta + \frac{1}{2}\left[\frac{\gamma_{C\alpha}}{\gamma_{C\beta}} C_\alpha - C_\beta\right] \cdot \left[1 - \operatorname{erf}\left(\frac{x}{2\sqrt{D_C^\beta\, t}}\right)\right]\right\} \tag{4.7}$$

	C	Cr	Mo	Mn	Ni	Si	V	$\gamma_{C_{600\,C}}$	$\gamma_{C_{650\,C}}$	$\gamma_{C_{700\,C}}$
$2\frac{1}{4}$Cr1Mo steel	0.12	2.29	0.95	0.54	0.04	0.27	0.005	0.414	0.442	0.468
P91 steel	0.10	8.60	0.92	0.43	0.08	0.33	0.24	0.047	0.059	0.0723

Table 4.4 Chemical compositions (wt. %) and carbon activity coefficients in the steels used.γ_C values are calculated using the method presented by Pilious & Stránský, 1998.

Using equations 4.6 and 4.7, the profiles for carbon distribution after 1 and 10 h in a P91/$2\frac{1}{4}$Cr1Mo diffusion bond aged between 600 and 700 °C are given in Figure 4.1, using the data presented in Table 4.4.

Figure 4.1 illustrates the change in **total** carbon concentration in the steels (C_α and C_β in the low and high-alloy steels respectively). However, this includes no detail of actual carbide or ferrite phases in the steel.

Once established at $t > 0$, the maximum and minimum carbon concentrations in the steels at the dissimilar joint interface are assumed to remain constant during continued heat treatment. As t is increased from 1 to 10 h, the carbon concentration profile on the low-alloy $2\frac{1}{4}$Cr1Mo side widens, extending the decarburised zone. Similarly on the high-alloy P91 side, the build-up of carbon concentration over time steadily thickens the carburised zone. The carburised zone is not as wide as the decarburised zone for any of the given conditions.

After long times, the carbon concentration gradients become less steep. Raising the temperature increases both $\gamma_{C\alpha}$ and $\gamma_{C\beta}$, but the ratio $\gamma_{C\alpha}/\gamma_{C\beta}$ in equation 4.5 decreases, lowering the values of carbon concentration, (Figure 4.1, $x = o$).

4.1.3 Summary

Though these predictions of carbon redistribution in a weld are based correctly on the assumptions of mass conservation and the ratio of $\gamma_{C\alpha}$ and $\gamma_{C\beta}$, these results could not accurately predict the experimentally measured decarburised zones which are reported later in this dissertation. This is because the composition and distribution of the carbides were not accounted for.

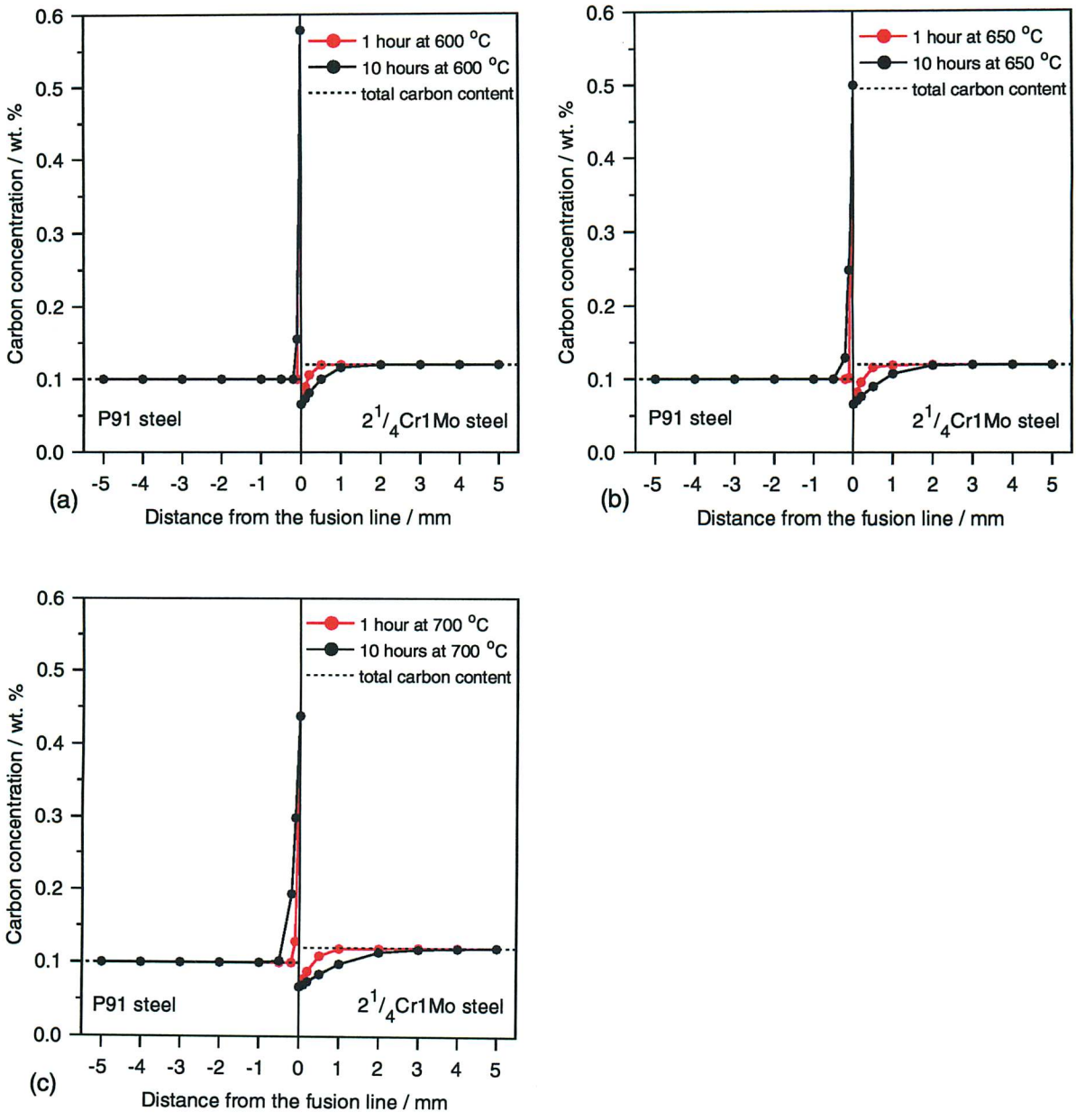

Figure 4.1 Predicted carbon distribution at a P91/2$\frac{1}{4}$Cr1Mo junction after heat treatments for 1 to 10 h at; (a) 600 °C, (b) 650 °C, (c) 700 °C (using the model due to Pilious & Stránský, 1998).

4.2 Predicting the decarburised zone width

Previous attempts to model carbon partitioning in dissimilar joints have assumed a mean field of carbon (Christoffel & Curran 1956; Buchmayr *et al.* 1989; Kim *et al.* 1992; Pilious & Stràнskỳ, 1998), rather than a distribution of discrete sources such as carbides (Race, 1992).

However, the model by Race (1992) assumed that the dissolution of carbides happened at a rate which is consistent with the partitioning of carbon. Furthermore, following the dissolution of carbides, time was not allowed for the homogenization of solute in the matrix. Rather, the decarburised zone width profile was incorrectly adjusted to give a smooth gradient from the extinct carbide to the weld junction.

The numerical model presented here has two parts – carbide dissolution and carbon diffusion. The carbide remains in local equilibrium with the adjacent ferrite, releasing carbon that diffuses normal to the dissimilar steel interface.

The numerical model consists of many discrete blocks, each containing a carbide particle and ferrite (Figure 4.2a). α, β and A represent the ferrite on the low and high alloy steels either side of the dissimilar steel junction, and the carbide in the low-alloy steel, respectively.

During heat treatment, the carbide in the first block begins to dissolve, Figure 4.2b. Solute thus released diffuses down the chemical potential gradient, towards $x = 0$.

After complete dissolution, the block becomes fully ferritic, with the remaining carbon continuing to diffuse toward the weld junction, Figure 4.2c. Following this, the next successive block is considered.

4.2.1 Boundary and initial conditions

These follow previous work on numerical models for second phase dissolution by Tanzilli & Heckel (1968) and Zhou & North (1993). The layout of the blocks in the model is illustrated in Figure 4.3. l is the width of carbide A, and L is the combined width of the carbide and the ferrite matrix, α.

On Figure 4.4, just block 1 is illustrated. At the left-hand side of block 1, $x = 0$, and on the right-hand side $x = L$. No concentration gradients exist at the edges of the block:

$$\left.\frac{dc}{dx}\right|_{x=L} = 0 \tag{4.8}$$

At the moving carbide interface, $x = \xi$:

$$C = C_{\alpha A},\ x = \xi^{-},\ \text{in the matrix} \tag{4.9}$$

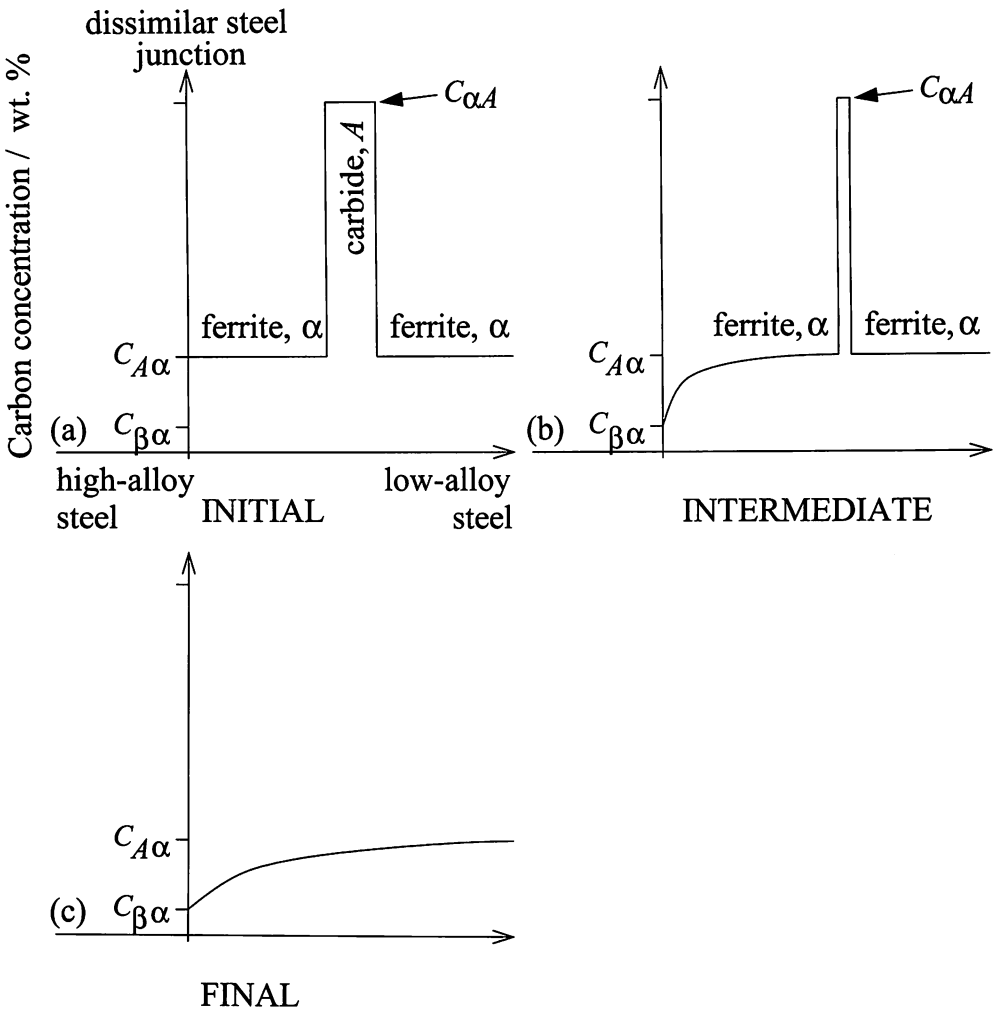

Figure 4.2 Initial, intermediate and final time intervals during carbide dissolution and carbon diffusion next to the dissimilar steel junction.

$$C = C_{A\alpha},\ x = \xi^{+},\ \text{in the carbide} \tag{4.10}$$

The phases are homogeneous to begin with, so that:

$$C = C_{\alpha A},\ t = 0,\ \text{in the matrix} \tag{4.11}$$

$$C = C_{A\alpha},\ t = 0,\ \text{in the carbide} \tag{4.12}$$

Neglecting density differences, the average carbon concentration $\overline{C}$ of the block is:

$$\overline{C} = \frac{(L - l)\,.\,C_{\alpha A} + l\,.\,C_{A\alpha}}{L} \tag{4.13}$$

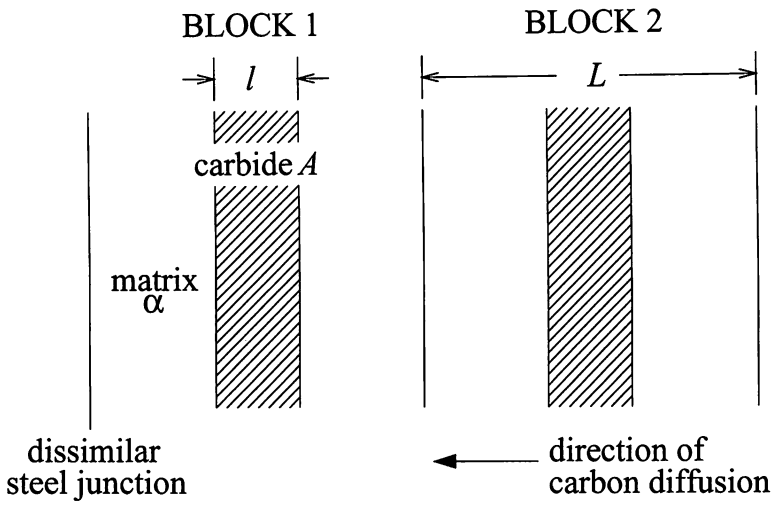

Figure 4.3 Diagram to show the blocks on the low-alloy side of a dissimilar joint.

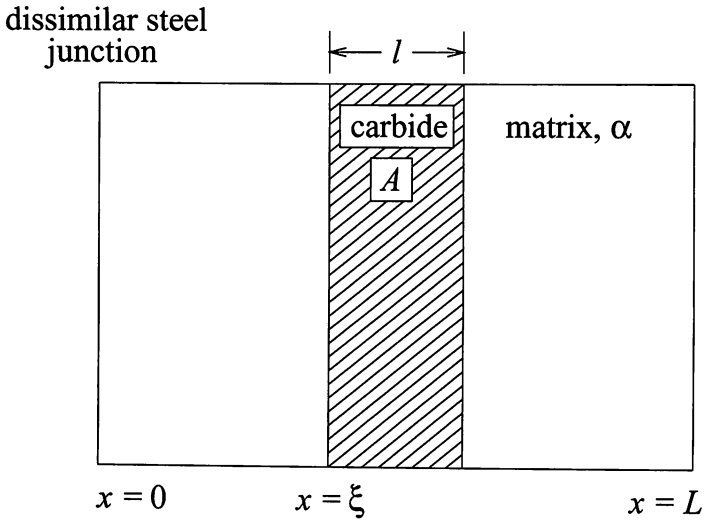

Figure 4.4 A magnified diagram of the block, showing the position of the moving interface, $x = \xi$.

The partition coefficient k_p is described as the ratio of carbon activity coefficients in the two ferrite phases that are adjacent to the dissimilar joint as:

$$k_p = \frac{\gamma_{C\alpha}}{\gamma_{C\beta}} \tag{4.14}$$

A larger k_p enhances carbon redistribution.

4.2.2 The carbon concentrations at the α/β interface

The need to equalise chemical potentials at the α/β interface sets the disparate carbon concentrations $C_{\alpha\beta}$ and $C_{\beta\alpha}$, Figure 4.5. $C_{\beta B}$ is the carbon concentration in the ferrite in equilibrium with the carbide in the high-alloy steel. Since:

$$C_{\alpha\beta} \neq C_{\alpha A} \text{ and } C_{\beta\alpha} \neq C_{\beta B}$$

concentration gradients will arise on both the α and β sides.

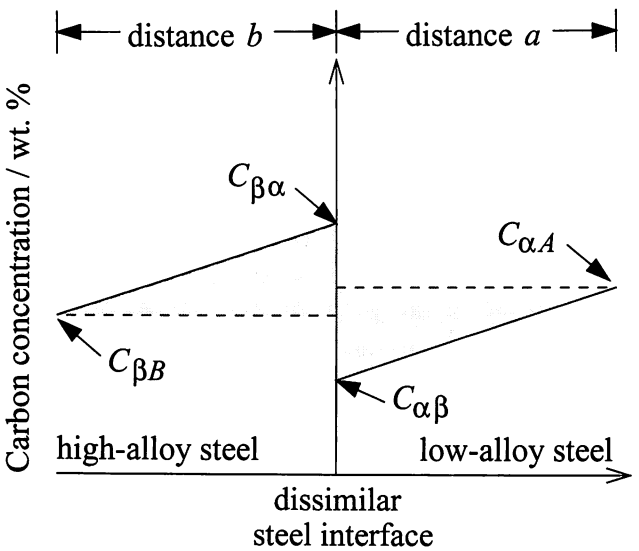

Figure 4.5 A schematic diagram to determine the interface concentrations $C_{\alpha\beta}$ and $C_{\beta\alpha}$. At the interface there is no gradient in carbon chemical potential, however due to the dissimilar steels, $C_{\alpha\beta} \neq C_{\beta\alpha}$.

To maintain mass balance, the flux of carbon leaving α must equal that entering β:

$$\frac{1}{2}a(C_{\alpha A} - C_{\alpha\beta}) = \frac{1}{2}b(C_{\beta\alpha} - C_{\beta B}) \tag{4.15}$$

Rearrangement gives:

$$\frac{(C_{\alpha A} - C_{\alpha\beta})}{(C_{\beta\alpha} - C_{\beta B})} = \frac{b}{a} \tag{4.16}$$

The partition coefficient, k_p can also be quoted as the ratio of the carbon concentration at the dissimilar joint interface:

$$k_p = \frac{C_{\alpha\beta}}{C_{\beta\alpha}} \tag{4.17}$$

So that:

$$C_{\beta\alpha} = \frac{(aC_{\alpha A} + bC_{\beta B})}{(k_p a + b)} \tag{4.18}$$

4.2.3 Dissolution of carbides

The depletion of carbon causes the dissolution of carbides in α. Figure 4.6 illustrates the carbon concentration gradients that exist around the dissolving carbide.

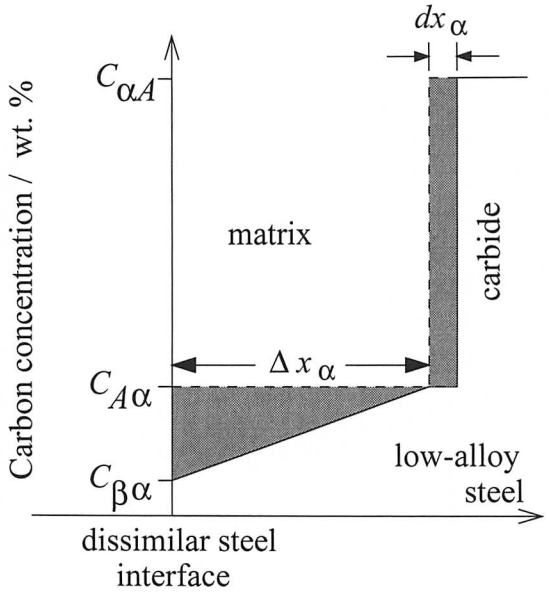

Figure 4.6 A schematic diagram of the first carbide which is dissolving.

Δx_α is the diffusion distance in the ferrite matrix, which is a function of the instantaneous carbide width. The flux towards the α/β interface is:

$$J = D_C^\alpha (C_{\alpha A} - C_{\alpha\beta})/\Delta x_\alpha \tag{4.19}$$

In Figure 4.6, the release of carbon corresponding to the loss of carbide by dx_α must equal the carbon partitioning across the interface:

$$D_C^\alpha (C_{\alpha A} - C_{\alpha\beta})/\Delta x_\alpha = dx_\alpha \,.\, (C_{A\alpha} - C_{\alpha A})/dt \tag{4.20}$$

Eventually, the carbide dissolves completely, followed by diffusion of the excess carbon out of the ferrite matrix.

4.2.4 The decarburised zone width

The width of the decarburised zone is equal to the distance from the dissimilar interface to either the carbide or the edge of the block once the carbide has dissolved. The initial distance

of the A/α interface from the α/β junction is x_α^0, and is set according to the fraction of the carbide:

$$x_\alpha^0 = \frac{(L-l)}{2} \tag{4.21}$$

The diffusion distance, x_α, is found by integrating equation 4.20 across the matrix phase to give:

$$\int_{x_\alpha^0}^{x_\alpha} x_\alpha \Delta x_\alpha = \int_0^t D_C^\alpha \frac{(C_{\alpha A} - C_{\alpha\beta})}{(C_{A\alpha} - C_{\alpha A})} dt \tag{4.22}$$

so that:

$$x_\alpha = \sqrt{\frac{2D_C^\alpha (C_{\alpha A} - C_{\alpha\beta})t}{(C_{A\alpha} - C_{\alpha A})} + x_\alpha^0} \tag{4.23}$$

Now x_α is equal to the decarburised zone width, ξ_α. The programme then steps to the next carbide.

4.3 The finite difference method

To analyse the carbon concentrations at each point in the low-alloy steel, each phase within a block is split into equal sized nodes. Every node falls within the bounds of either the matrix or the carbide. The implicit finite difference method is used to find the concentration at each node.

In the model, the finite difference grid representation is correspondingly split into intervals of distance δx and time δt, Figure 4.7. A point on the grid (x,t) is given the coordinates $(i\delta x, j\delta t)$, where i and j are integers; the concentration of carbon at this point is $C_{i,j}$.

The Crank-Nicholson implicit finite difference method replaces d^2C/dx^2 in Fick's second law by means of its finite difference representation on the jth and $(j+1)$th time rows to give:

$$\frac{C_{i,j+1} - C_{i,j}}{\delta t} = D_C \frac{1}{2}\left\{ \frac{C_{i+1,j} - 2C_{i,j} + C_{i-1,j}}{(\delta x)^2} + \frac{C_{i+1,j+1} - 2C_{i,j+1} + C_{i-1,j+1}}{(\delta x)^2} \right\} \tag{4.24}$$

In equation 4.24, the total error is $O\{(\delta t)^2 + (\delta x)^2\}$. Rearranging equation 4.24 gives the expressions:

$$-rC_{i-1,j+1} + (2+2r)C_{i,j+1} - rC_{i+1,j+1} = rC_{i-1,j} + (2-2r)C_{i,j} + rC_{i+1,j} \tag{4.25}$$

$$r = \frac{\delta t}{(\delta x)^2} D_C \tag{4.26}$$

The left-hand side of equation 4.25 contains three unknowns at the $(j+1)$th time row; and on the right-hand side are three values of known concentration at the current jth time row. If there are N internal grid points in a row, when $j = 0$ and $i = 1, 2, 3, ..., N$, equation 4.25 will

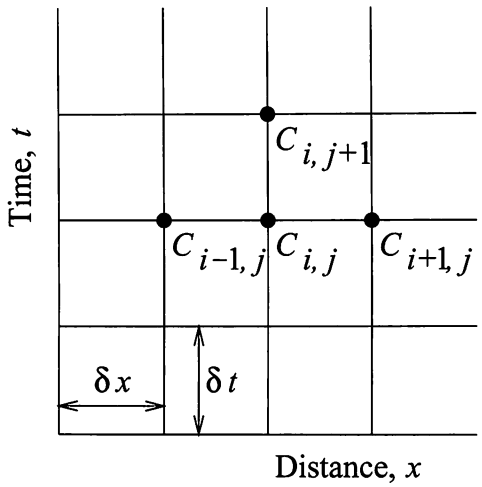

Figure 4.7 The finite difference grid used in the Crank-Nicholson solution (Crank, 1975).

give N simultaneous equations for N unknown values along the first time row. Similarly for $j = 1$, the unknown concentrations expressed along the second time row are found using the concentrations obtained when $j = 0$.

This method, where the solution is a set of simultaneous equations for each time step, is called an *implicit* method. The Crank-Nicholson implicit method has an advantages over other finite difference methods by remaining stable over all values of r (equation 4.26), therefore larger and fewer time steps can be used. This is, however, limited by the accuracy required and having in mind that the high orders of magnitude in the Taylor series have been neglected (see Crank, 1975).

4.3.1 Compatibility and Convergence

When deriving the finite difference set of equations, the higher order terms in the Taylor series were neglected. These constitute a *truncation error.* The truncation error should tend to zero as both δx and δt approach zero, as is the case for the implicit finite difference scheme. If this is not the case, the finite difference method is said to be incompatible and inconsistent with the partial differential equations. The finite difference solution is therefore not likely to approach the sought solution.

Assuming compatibility, the solution of the finite difference equation must converge to the solution of the partial difference equation, as the grid size approaches zero.

4.3.2 Stability

The exact solution of the difference equations can be found by doing calculations to an infinite decimal place, with specified initial and boundary conditions. In practice, each calculation is carried out to a finite number of figures only; therefore rounding-off errors are introduced. Finite difference equations become stable when the rounding-off errors are negligible. The estimations of stability tend to be conservative, and the numerical solutions are more accurate than predicted.

4.4 Summary and flow diagram

Using the procedures from this section, a computer model has been built to predict the decarburised zone width in low-alloy steels. A schematic flow diagram for the model is shown in Figure 4.8. To compute the decarburised zone width growth over time, the Crank-Nicholson implicit finite difference method was used.

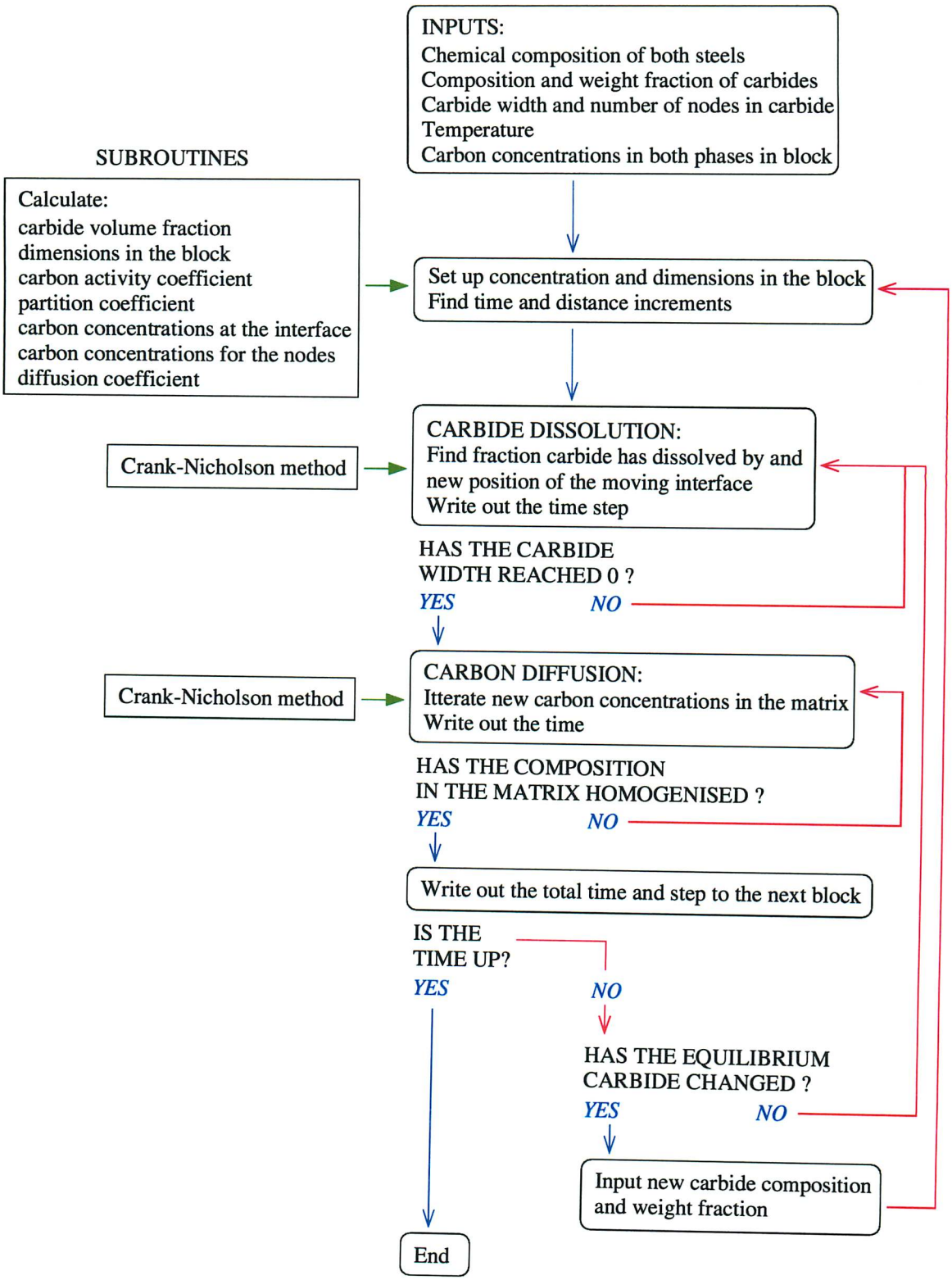

Figure 4.8 A flow chart to illustrate the progression of the computer model to calculate the decarburised zone width.

Chapter Five

Diffusion Bonding Dissimilar Steels

The study of carbon partitioning across the weld junction is made more difficult by two factors: the interface separating the dissimilar metals has a convoluted shape which is not only curved but in some regions, re-entrant. Secondly, the process of fusion causes inevitable dilution effects due to the mixing of the dissimilar metals.

The purpose of the work reported here was to create simple junctions between the dissimilar metals using a diffusion bonding process. This involves the machining of flat faces on the two pieces to be joined, followed by bonding under a compressive load at an elevated temperature, within the austenite phase field. Naturally, some diffusion and plastic flow is expected but the extent of this is, in practice, sufficiently small to create a good model experiment. Thus the macroscopic deformation is limited to less than 5 % when the bonding temperature is 0.5 – 0.8 of the absolute melting temperature of the steel.

5.1 Fabricating the diffusion bond

The surfaces to be bonded must ultimately achieve atomic contact and so must be clean and free from oxides or contaminants. The first stage of bonding is the application of heat and sufficient load to plastically deform any asperities on the mating surfaces. This initial stage of bonding occurs almost instantaneously. The fraction of bonded area then increases according to power-law creep, grain and volume diffusion. It is likely that isolated interfacial voids will be formed during this second stage of bonding; these are eventually eliminated by grain boundary diffusion processes. Each of these stages of bonding are representated in Figure 5.1 (Thornton, 1983; Dunkerton, 1991).

Unlike welding, the advantage of diffusion bonding is that there is no macroscopic disruption at the interface during the bonding process. Diffusion bonding forms low deformation joints using small thermal gradients; thus unwanted microstructures or damage due to residual stresses are avoided, (Derby & Wallach, 1982).

The diffusion bonds in this investigation are made between dissimilar steels using either a modified 9 wt. % Cr steel (P91), a $2\frac{1}{4}$Cr1Mo and a $\frac{1}{2}$CrMoV steel. These steels were chosen to reflect the weld combinations found in contemporary power stations. After fabrication, the bonds were given appropriate heat treatments consistent with the accelerated ageing tests reported in Chapters 6 & 7.

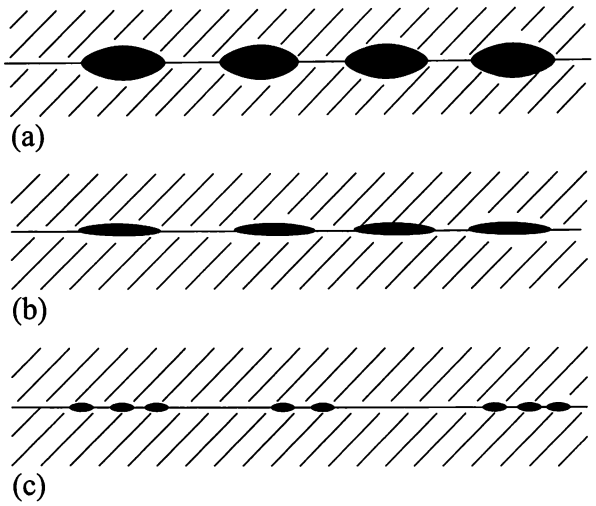

Figure 5.1 Mechanisms of diffusion bonding; (a) initial metal to metal initial contact, (b) point yielding and (c) creep deformation with vacancy diffusion until only a few small voids remain (Dunkerton, 1991).

The amount of carbon partitioned across the bond can be estimated using quantitative image analysis and metallographic examination. Optical and electron microscopes were used to characterise the changes in microstructure, hardness and microhardness.

5.1.1 Preparation of the steels

The bonds are made using two cylinders of steel machined to be 5 mm in height with a 10 mm radius (Figure 5.2). The mating faces on each cylinder were ground using 1200 grit silicon carbide paper prior to joining, in order to achieve uniform surface roughness, Figure 5.2a. This surface roughness comprises of asperities which deform during the initial stages of bonding to give good metal to metal contact.

It has been found that a parallel arrangement of the grinding marks maximises the tensile strength of the bond when compared with a perpendicular arrangement (Elliot *et al.*, 1980). However, the strength of the bonds is not important in this present investigation and it is known that the toughness of the bond is not affected by the orientation of the grinding marks (Thornton, 1983). The relative orientation of the grinding marks was, therefore, not controlled.

The later stages of bonding increase the fraction of bonded area so sample preparation must ensure flatness at the mating surfaces.

The temperature during bonding was monitored using a thermocouple resistance welded to the sample, Figure 5.2b. There are no temperature gradients along the length of the diffusion

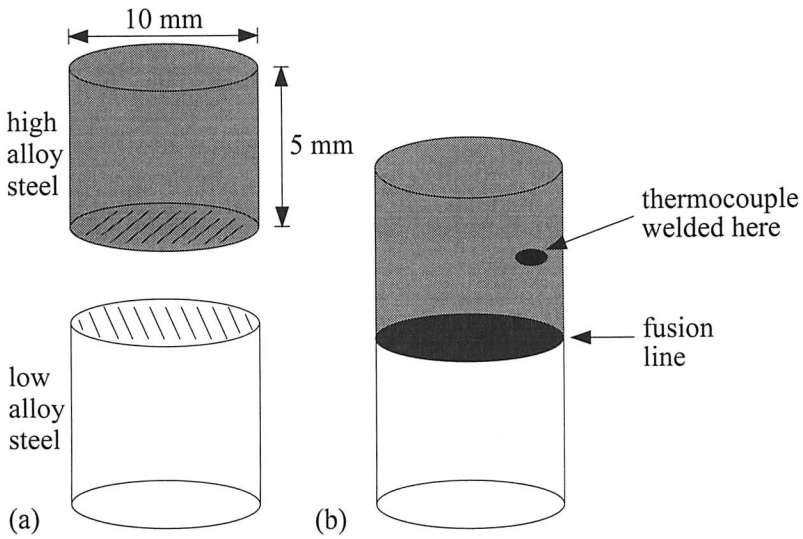

Figure 5.2 The diffusion bond sample; (a) before bonding, (b) showing the position of the thermocouple.

bond during joining (Tylecote, 1968).

The compositions of the steels were measured by 'Quantovac' spectroscopic analysis and are given in Table 5.1.

Steel	C	S	P	Si	Mn	Ni	Cr	Mo	V
$\frac{1}{2}$**CrMoV**	0.10	0.028	0.017	0.16	0.75	0.17	0.39	0.59	0.27
2$\frac{1}{4}$Cr1Mo	0.12	0.022	0.021	0.27	0.54	0.04	2.29	0.95	0.005
P22	0.13	0.014	0.011	0.43	0.52	0.28	2.20	0.99	0.009
P91	0.10	0.002	0.01	0.33	0.43	0.08	8.6	0.92	0.24
new P91	0.11	0.003	0.015	0.26	0.40	0.16	8.3	0.96	0.21

Table 5.1 Composition of the steels used, wt. %.

5.1.2 The bonding conditions

The bonding time and temperature have to be optimised to give the greatest bonded area. The Ac_1 and Ac_3 temperatures measured by dilatation are given in Table 5.2.

Austenite begins to precipitate on the ferrite/carbide boundaries in the steel as the temperature exceeds Ac_1, the sample transforms fully to austenite when the temperature is Ac_3.

Steel	Ac_1	Ac_3
$\frac{1}{2}$CrMoV	801 °C	902 °C
$2\frac{1}{4}$Cr1Mo	831 °C	911 °C
P91	874 °C	925 °C

Table 5.2 The temperatures of the start of transformation to austenite, and when the transformation is complete. The heating rate was 10 °C s^{-1}.

The bonding temperature should ideally be below Ac_1 to avoid austenite formation, but it was found that good bond integrity could not be achieved below the Ac_1 temperature, presumably due to insufficient volume diffusion. The initial stage of bonding was therefore above the Ac_3 temperature where the sample was held for a short time, to be followed by prolonged heat treatment below Ac_1.

Temperature is the major controlling variable of the bonding process because it is important to reduce voids by diffusion in a realistic time, without inducing unwanted microstructures. The grain size of the steels involved could also be considered as a variable of the bonding process, affecting the creep strength of the steels and the diffusion flux (along grain boundaries).

Just before bonding, the two steels were washed in acetone to clean and degrease the mating surfaces. After many trials to achieve a uniform bond with minimum disruption, the best bonding conditions were found to be:

- Heat to 1 000 °C and hold for 10 min;
- cool to 800 °C and hold for a further 10 min;
- furnace cool to room temperature.

The heating and cooling rates were 10 °C s^{-1}, Figure 5.3. A stress of 10 N mm^{-2} was applied to the diffusion bond throughout all stages of the bonding cycle.

The disturbances to the applied load during the heating and cooling cycles of bonding are due to the response of the machine to volume changes caused by phase transformations between ferrite and austenite (Prior, 1994).

The bonding pressure is an important variable since it influences the extent of deformation of surface asperities, but it must be chosen to avoid gross deformation.

A diffusion bond fabricated using a high pressure to compensate for a low bonding temperature was found to be associated with excessive deformation. For example, using 50 N mm^{-2} pressure

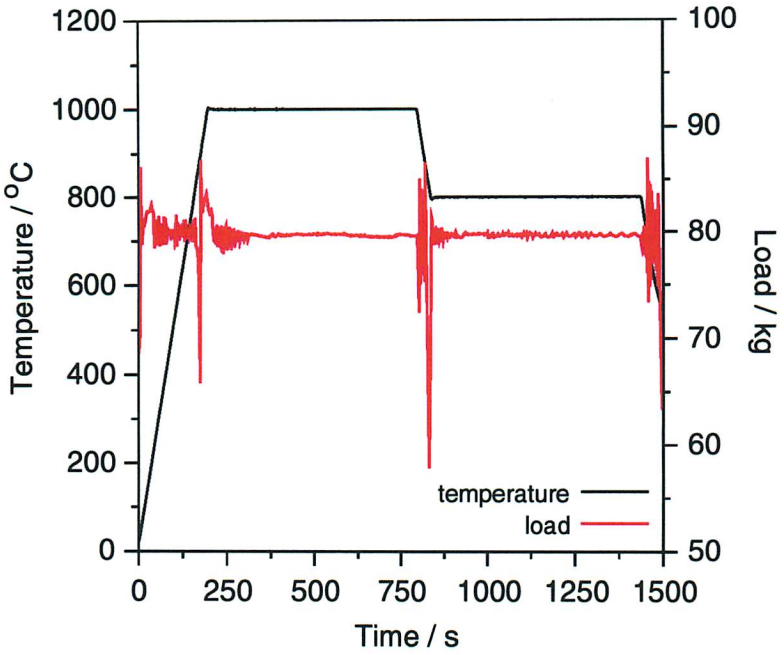

Figure 5.3 A plot to show the applied load and temperature cycle during diffusion bonding.

at 700 °C for 30 min compressed the sample into a barrel shape. Subsequent heat treatment for 64 h at 650 °C recovered the deformed microstructure of the bond together with local recrystallisation in the vicinity of the interface. Carbon redistribution did occur but to a lesser extent than in the bonds made with optimised conditions. This may be due to a lower fraction of easy diffusion paths in the large grained recrystallised microstructure.

5.2 Heat treatment and examination of bonds

After bonding, the samples were cut longitudinally to make sections for heat treatment. These were individually sealed in silica tubes containing an inert argon atmosphere to prevent oxidation or surface decarburisation during heat treatment, Table 5.3. Using the Larson-Miller tempering parameter, P different testing times and temperatures can be extrapolated using:

$$P = T(\log t + C) \times 10^{-3}$$

where T is the absolute temperature, t is the duration of the test in hours and C is a constant taken to be 20 for low-alloy steels (Dieter, 1988).

It is possible that using extrapolation, the long term service of a component at elevated temperatures can be replicated with short-term, higher temperature tests. However, austenite

Diffusion Bond	600 °C	650 °C	700 °C
P91/2$\frac{1}{4}$Cr1Mo	100 h	1, 10, 100, 1 000, 10 000 h	49 and 100 h
P91/P22	-	100 h	-
New P91/2$\frac{1}{4}$Cr1Mo	-	100 h	-
P91/$\frac{1}{2}$CrMoV	-	100 h	-
2$\frac{1}{4}$Cr1Mo/$\frac{1}{2}$CrMoV	-	100 h	-

Table 5.3 Time and temperatures used for ageing the diffusion bonds.

formation sets an upper limit to the maximum temperature to be used in a short-term test. The composition and volume of equilibrium phases in the steel are also dependent on temperature.

After heat treatment, the samples were broken out of the protective silica tubes and quenched in water, to retain the carbide size and distribution that existed during heat treatment. Optical, scanning and transmission electron microscopy, Vickers hardness and microhardness tests were used to characterise the microstructure of the bonds.

The diffusion bond sections were mounted in conductive Bakelite and then ground and polished to a 1 μm finish. The etchants used were Villela's reagent (1 g Picric acid, 5 ml hydrochloric acid and 100 ml methanol) to accentuate the detail of the ferrite/carbide microstructure and Nital (2 % nitric acid in methanol) for the low-alloy steel (Vander Voort, 1984).

The microstructure was studied using a Leitz Laborlux 12 ME S optical microscope and a JEOL 820 SEM on etched samples.

Carbon extraction replicas were made following the method from Smith & Nutting (1957). A thin film of carbon, blue-brown in colour, was evaporated onto the lightly etched surface, under a vacuum of greater than 10^{-4} torr. The film was then scored into small squares and etched in a solution of 5% chloral (5% hydrochloric acid in methanol) at a potential of 3 V, until it began to lift from the surface. The whole sample was then washed in methanol and the replicas floated off in distilled water and caught on copper grids. In order to obtain replicas from selected regions of the sample, the remainder was masked off as shown in Figure 5.4. The replicas were studied using a JEOL 200 TEM.

5.2.1 Identification of precipitates

Electron diffraction was used to identify precipitates. Some carbides have similar lattice parameters making it necessary to know an accurate camera constant in the TEM to identify the

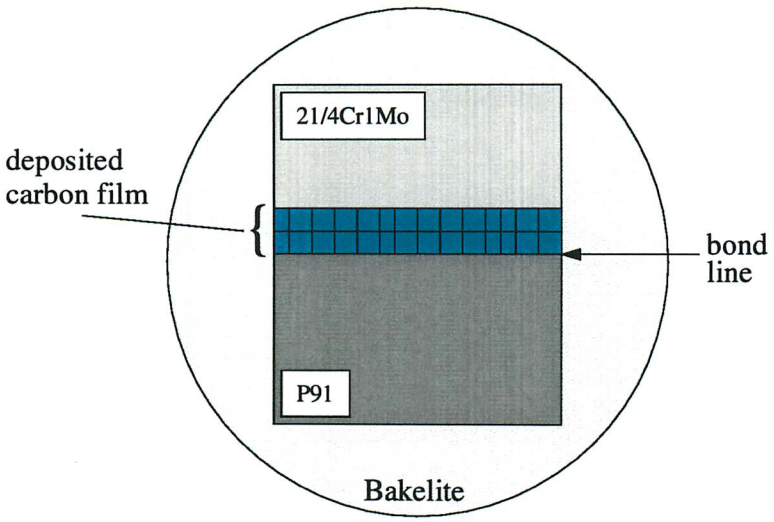

Figure 5.4 An illustration of a diffusion bond mounted in Bakelite. The surface is masked off with *Sellotape* apart from the region of interest; so in this case the carbon film is deposited only in the $2\frac{1}{4}$Cr1Mo steel next to the fusion line.

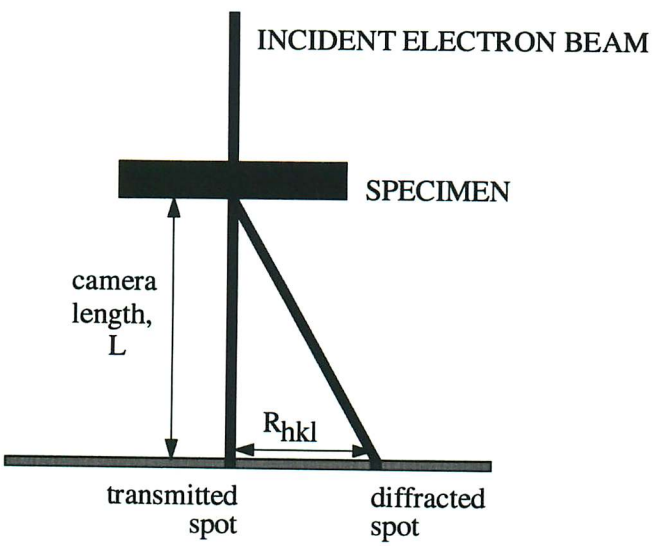

Figure 5.5 Illustration of diffraction in the TEM.

precipitates. The geometry of diffraction is shown in Figure 5.5.

The camera constant used to identify precipitates in the TEM is found by the expression:

$$R_{\mathrm{hkl}} d = \lambda L = \text{camera constant} \tag{5.1}$$

where R_{hkl} is the distance between the transmitted and diffracted beams as measured on the screen

d is the spacing of the {hkl} crystallographic planes

L is the camera length (820 mm on the JEOL 200 CK TEM operated at 200 kV)

λ is the electron wavelength, found by the expression:

$$\lambda = \frac{h}{[2\,m\,e\,V\,(1 + {}^{e\,V}/_{2\,m\,c^2})]^{1/2}} \tag{5.2}$$

h is Planck's constant, m and e are the mass and the charge of the electron respectively, V is the accelerating voltage in the TEM, and c is the speed of light in a vacuum.

To calibrate the camera constant, a film of fine grained gold is deposited on the surface of a copper grid. The lattice parameter of gold is 0.408 Å and the lattice type is cubic – F (Steadman, 1982). As the crystallites are randomly orientated, a ring diffraction pattern is obtained, from which a value for camera constant is found, figure 5.6.

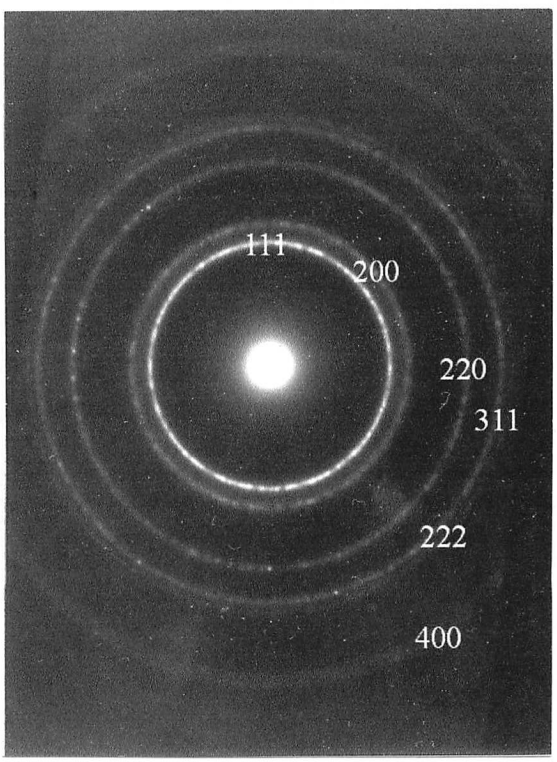

Figure 5.6 Diffraction pattern from a gold film, for calibrating the camera constant.

5.2.2 Testing the diffusion bonds

Vickers hardness tests complied with BS EN ISO 6507-1 using a force of 98.07 N, applied for 10 s (HV 10). The bonds were prepared flat with an even finish and then etched. Before hardness testing, the surfaces were cleaned of any foreign matter (for example oil, scale and oxides).

Indentations were applied onto the surface and placed not less than $2\frac{1}{2}\ d_l$ from the specimen edge and more than 3 d_l apart, where d_l is the mean diagonal length of the indentation, Figure 5.7. This is to avoid distortion of the indentations at the sample edge, or from interference with the deformation fields around neighbouring indentations.

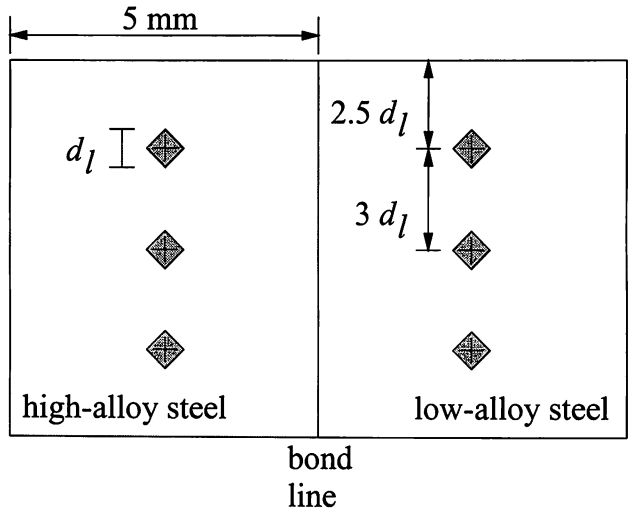

Figure 5.7 The positions of Vickers hardness indents on the low and the high-alloy steel. The distance from the indents to the bond line is approximately 2 - 3 mm.

To illustrate the local maximum and minimum in hardness caused by carbon diffusion, Figure 5.8, microhardness traverses were performed across the bond line and approximately 2 mm into each steel, using a Mitutoyo MVK - H2 hardness testing machine. The load used was 0.9807 N and the dwell time of the indenter was 10 s (HV 0.1).

To test the toughness of the diffusion bonds, a diffusion bond of P91 and $2\frac{1}{4}$Cr1Mo steel that had previously been aged for 100 h at 650 °C was cooled to liquid nitrogen temperature, and hit with a hammer blow to force a crack. Though the toughness of the heat treated bond was not expected to match that of the parent metal samples, (Thornton, 1983), the decarburised zone contained large ferrite grains which are susceptible to failure, Figure 5.9.

The areas affected by carbon diffusion can be measured optically or by changes in hardness.

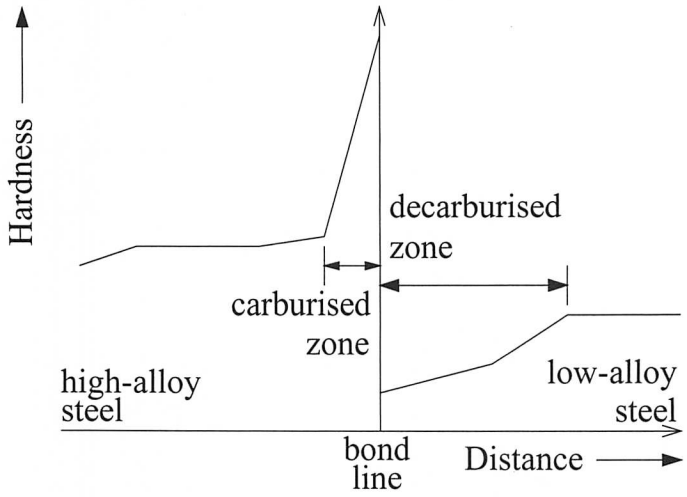

Figure 5.8 An illustration of a profile of hardness from an aged diffusion bond.

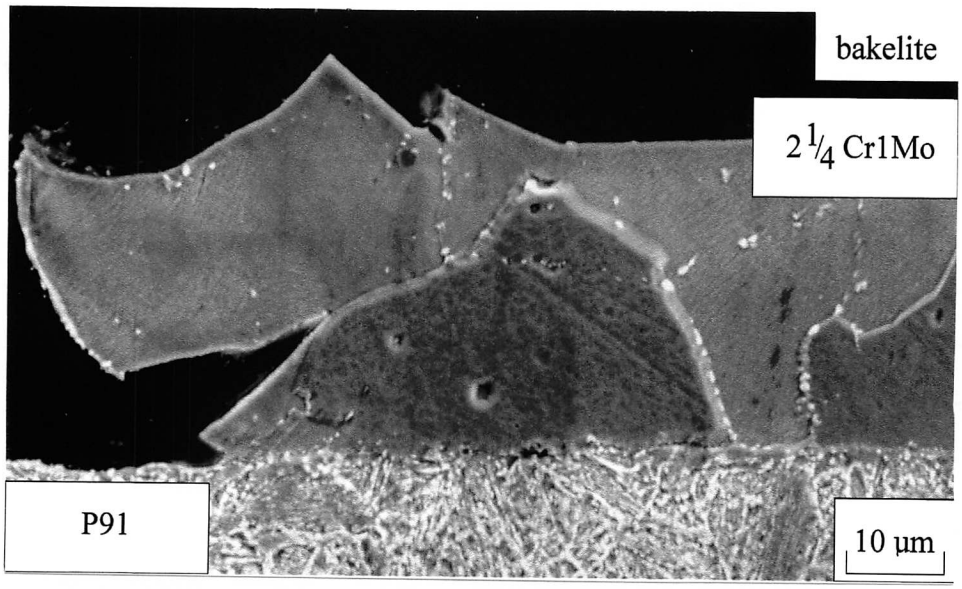

Figure 5.9 A broken P91/$2\frac{1}{4}$Cr1Mo diffusion bond, mounted in Bakelite. Cleavage fracture occurred in the low toughness, carbide-free ferrite grains of the decarburised zone in $2\frac{1}{4}$Cr1Mo steel, 100 h at 650 °C.

Both methods are subject to uncertainty due to the haphazard nature of the grains and distribution of carbides, Figure 5.10.

The carburised zone in the high-alloy steel is like a 'fog' of densely packed carbides at grain

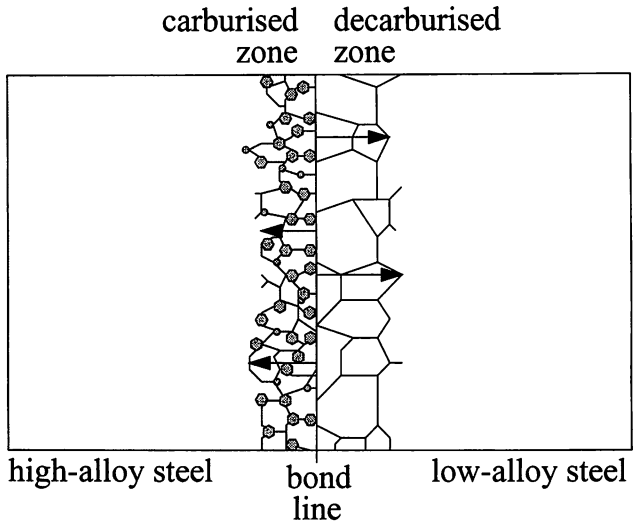

Figure 5.10 A drawing to illustrate the problems of measuring carburised and decarburised zone width in dissimilar steel bonds.

boundaries and within the grains next to the bond line. The carburised zone width is measured from the bond line to where the carbide distribution reverts to the average distribution in the steel.

The width of the decarburised zone is just as hard to measure. The term 'decarburised zone' itself is misleading because some carbides may persist or even re-precipitate during heat treatment. Therefore, what is actually measured is the region of grain growth containing a sparse distribution of carbides. This decarburised zone also exhibits a minimum in hardness. The term decarburised zone will continue to be used for brevity.

5.3 Metallography of P91/2$\frac{1}{4}$Cr1Mo diffusion bonds

The microstructure of the diffusion bonds immediately after joining was tempered martensite in both the P91 and 2$\frac{1}{4}$Cr1Mo steels, the former appearing more refined. TEM investigations revealed that in the 2$\frac{1}{4}$Cr1Mo steel, fine M_7C_3 carbides were sparsely distributed in the ferrite, whereas in the P91 steel, M_7C_3 and vanadium–based carbides were identified immediately after bonding. Subsequent heat treatment of the diffusion bond formed the carburised and decarburised zones as shown in Figure 5.11.

5.3.1 Ageing P91/2$\frac{1}{4}$Cr1Mo diffusion bonds at 650 °C.

After 1 hour at 650 °C (Figure 5.11a) a seam of carbides was precipitated in the P91 steel next to the bond. New carbides may precipitate upon prior austenite grain boundaries and martensite lath boundaries. The small carbide size is apparent on Figure 5.12a. Carbides

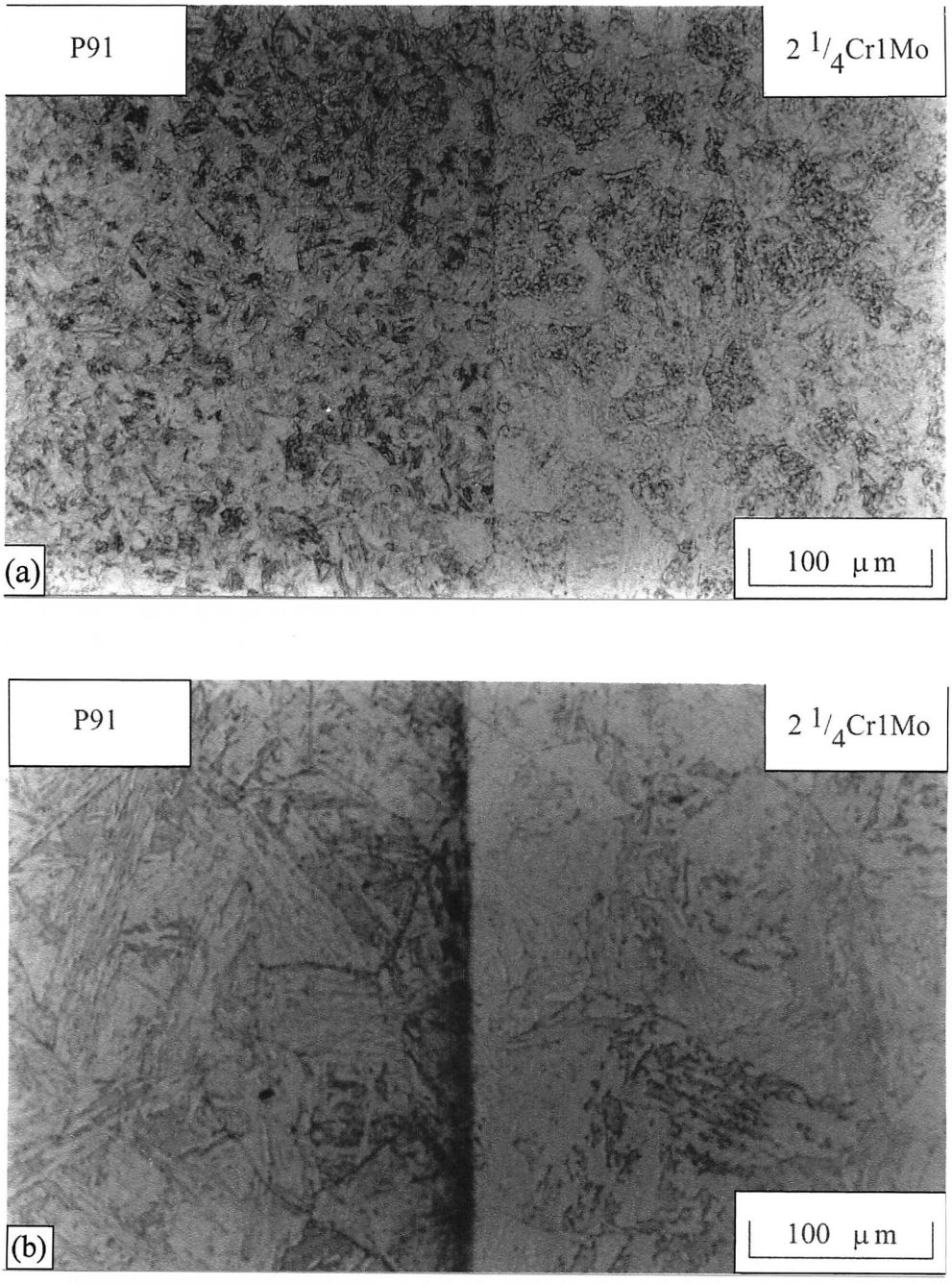

Figure 5.11 A P91/2$\frac{1}{4}$Cr1Mo diffusion bond heat treated at 650 °C; (a) no ageing, (b) 1 h, (c) 10 h, (d) 100 h, (e) 1 000 h, (f) 10 000 h.

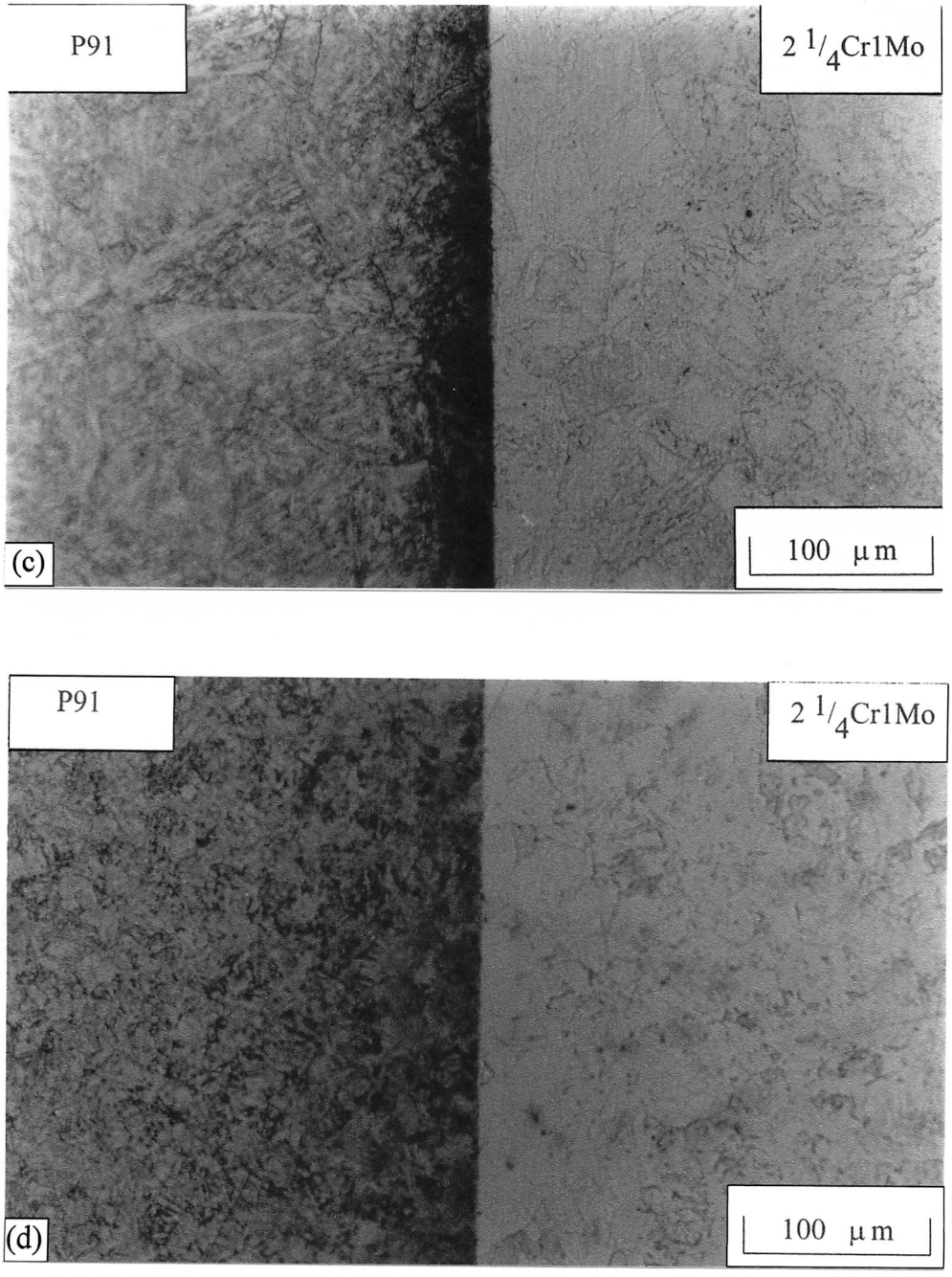

Figure 5.11 A P91/2$\frac{1}{4}$Cr1Mo diffusion bond heat treated at 650 °C; (a) no ageing, (b) 1 h, (c) 10 h, (d) 100 h, (e) 1 000 h, (f) 10 000 h.

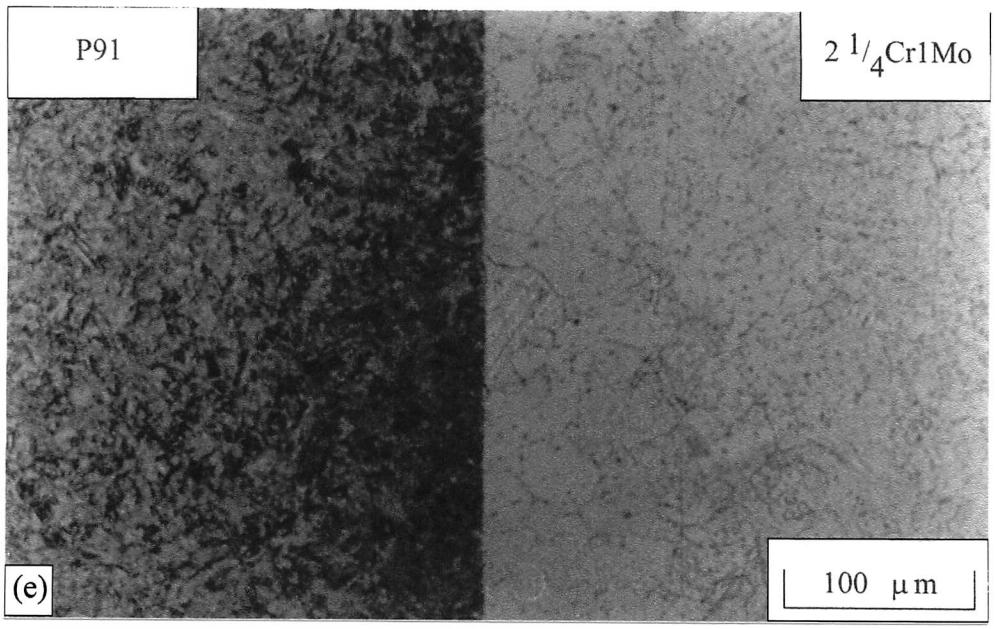

Figure 5.11 A P91/2$\frac{1}{4}$Cr1Mo diffusion bond heat treated at 650 °C; (a) no ageing, (b) 1 h, (c) 10 h, (d) 100 h, (e) 1 000 h, (f) 10 000 h.

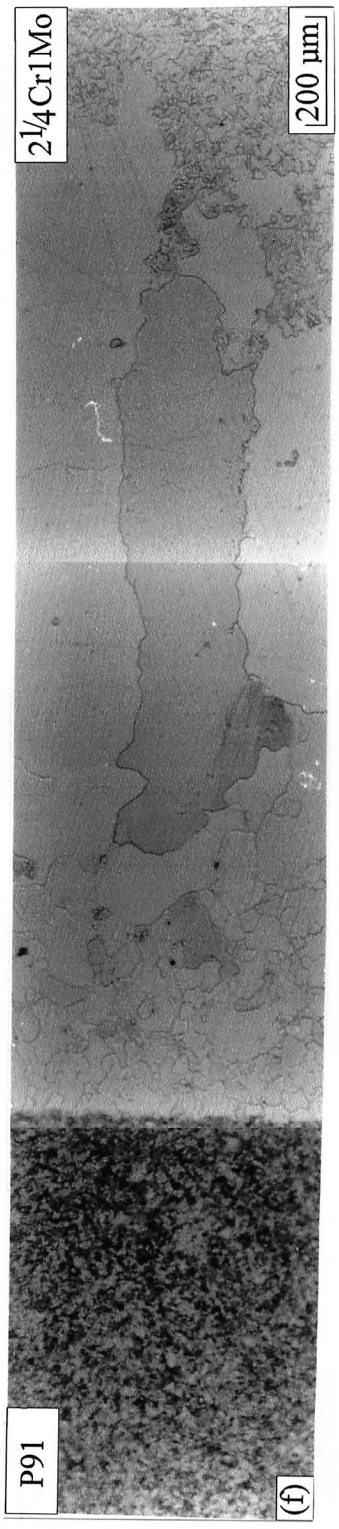

Figure 5.11 A P91/2$\frac{1}{4}$Cr1Mo diffusion bond heat treated at 650 °C; (a) no ageing, (b) 1 h, (c) 10 h, (d) 100 h, (e) 1 000 h, (f) 10 000 h.

could not be resolved next to the bond in $2\frac{1}{4}$Cr1Mo steel, although they were more prevalent on ferrite grain boundaries far from the bond, Figure 5.12b.

A longer duration heat treatment at 650 °C naturally lead to the growth of the zones. After 100 h at 650 °C, a few carbide particles were observed on the recrystallised ferrite grain boundaries in the decarburised zone, Figure 5.13a. There is a large volume fraction of carbides in the carburised zone, Figure 5.13b; coarse M_7C_3 carbides were identified on the ferrite grain boundaries and smaller spherical carbides are distinguished inside the grains.

After heat treating for 1 000 h at 650 °C, larger carbides are found in the decarburised zone, Figure 5.14a; in the $2\frac{1}{4}$Cr1Mo steel, M_6C, Mo_2C and M_7C_3 carbides were identified using the TEM. In the carburised zone, a dense seam of M_7C_3 and VC carbides was found, Figure 5.14b. In the P91 steel, away from the carburised zone, nearly all carbides found were $M_{23}C_6$, Figure 5.15.

After 10 000 h at 650 °C, the decarburised zone grew to almost 2 mm width and was visible by the naked eye (the **total** length of the sample is only 10 mm). The carbides in the carburised zone continued to coarsen, Figure 5.16a, and in the decarburised zone, undissolved carbides in the small equiaxed grains limit further grain growth, Figure 5.16b.

TEM micrographs of the carburised zone of P91 steel aged at 650 °C show extensive carbide precipitation, Figure 5.17. Cementite and M_7C_3 were identified after 1 h, Figure 5.18, which concurs with the notion that the flux of carbon into the Cr-rich steel should lead to the re-precipitation of cementite (Race, 1992).

After 1 000 h, discrete pockets of needle shaped precipitates, thought to be of the MX-type, have precipitated in the carburised zone; unfortunately, no cementite particles were identified after ageing. It was very difficult to obtain informative diffraction patterns in the carburised zone due to the massive precipitation of carbides (cf. Figure 5.17b). The carbide particles tended to cluster, but it was possible to obtain a diffraction from the peripheries of the clusters, Figure 5.19.

During the early stages of tempering at 650 °C, the carburised zone appeared to grow faster than the decarburised zone, Figure 5.20. This is probably due to the relative ease of carbide coarsening and precipitation with the increased carbon content. After 10 000 h, the decarburised zone had grown considerably due to un-restricted grain growth. The elongated grains, which appear to be free of carbides grew anti-parallel to the flux of carbon, perpendicular to the bond line.

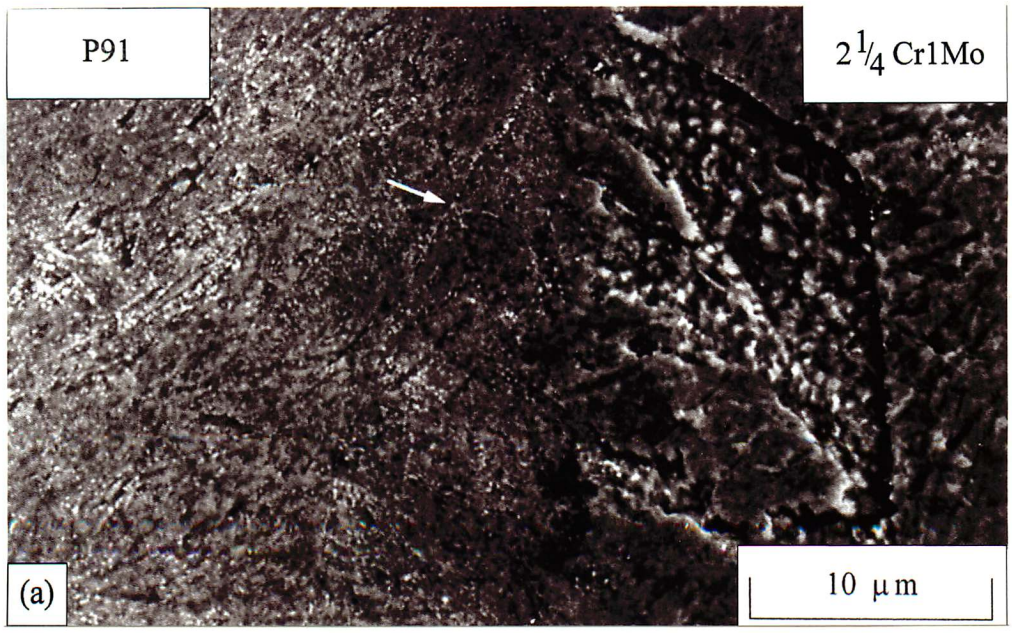

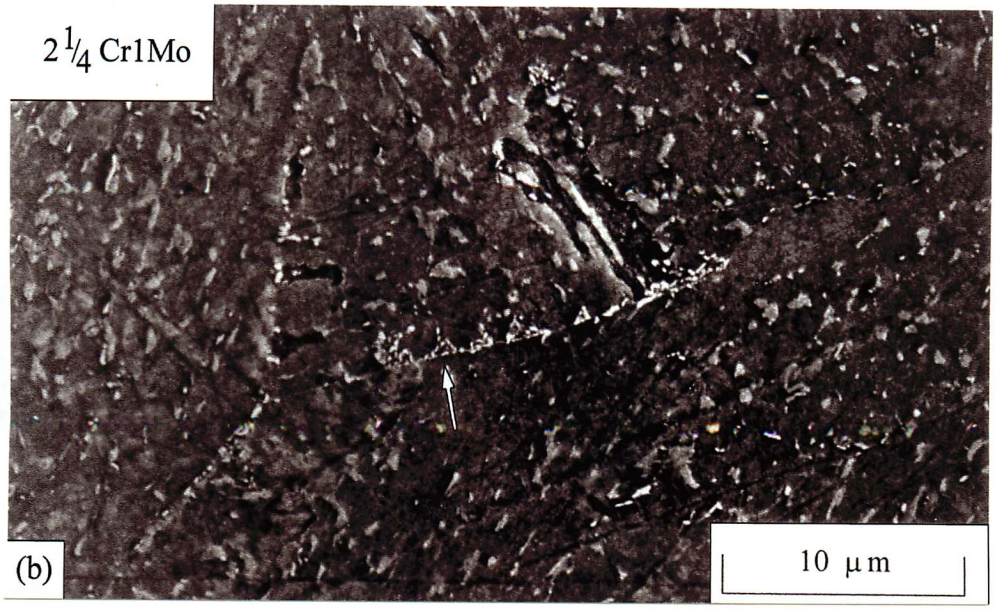

Figure 5.12 SEM micrographs of a P91/2$\frac{1}{4}$Cr1Mo diffusion bond heat treated at 650 °C for 1 h; (a) at the bond line and (b) in the 2$\frac{1}{4}$Cr1Mo steel. Arrows indicate carbides at grain boundaries in the P91 and 2$\frac{1}{4}$Cr1Mo steel, respectively.

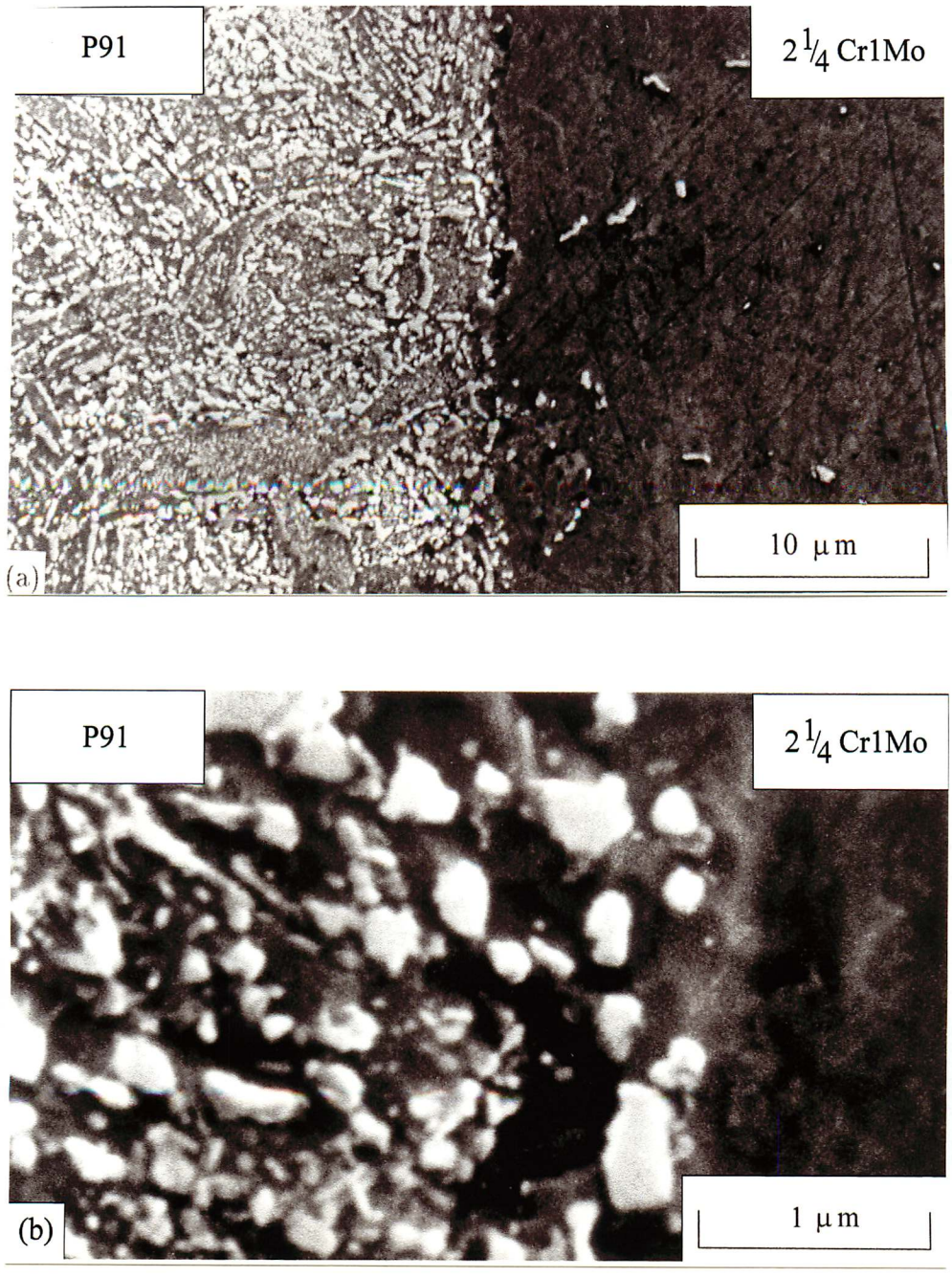

Figure 5.13 SEM micrographs of a P91/2$\frac{1}{4}$Cr1Mo diffusion bond heat treated at 650 °C for 100 h; (a) at the bond line and (b) detail of carbides in the carburised zone.

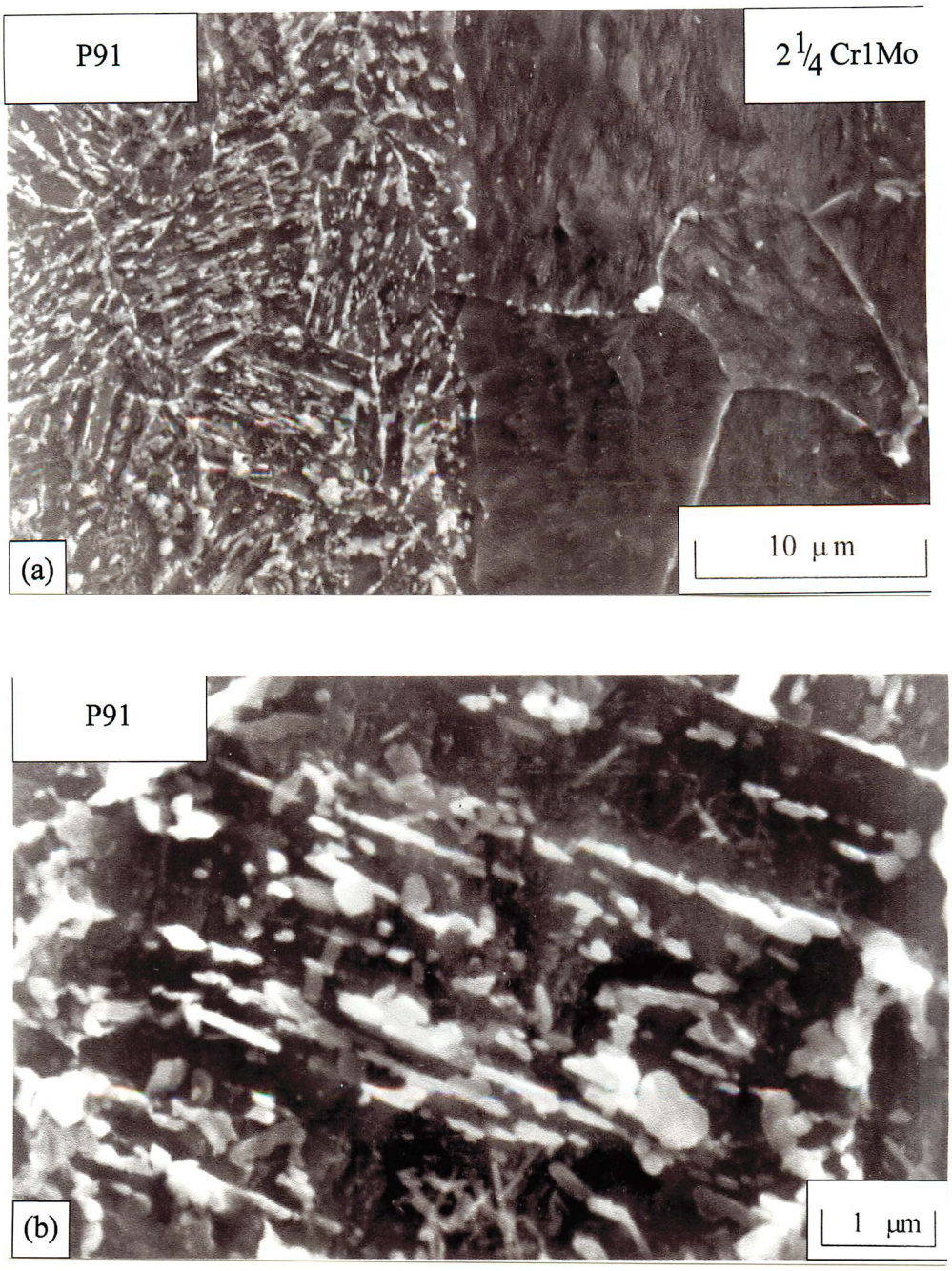

Figure 5.14 SEM micrographs of a P91/2$\frac{1}{4}$Cr1Mo diffusion bond heat treated at 650 °C for 1 000 h; (a) at the bond line and (b) detail of carbides in the carburised zone.

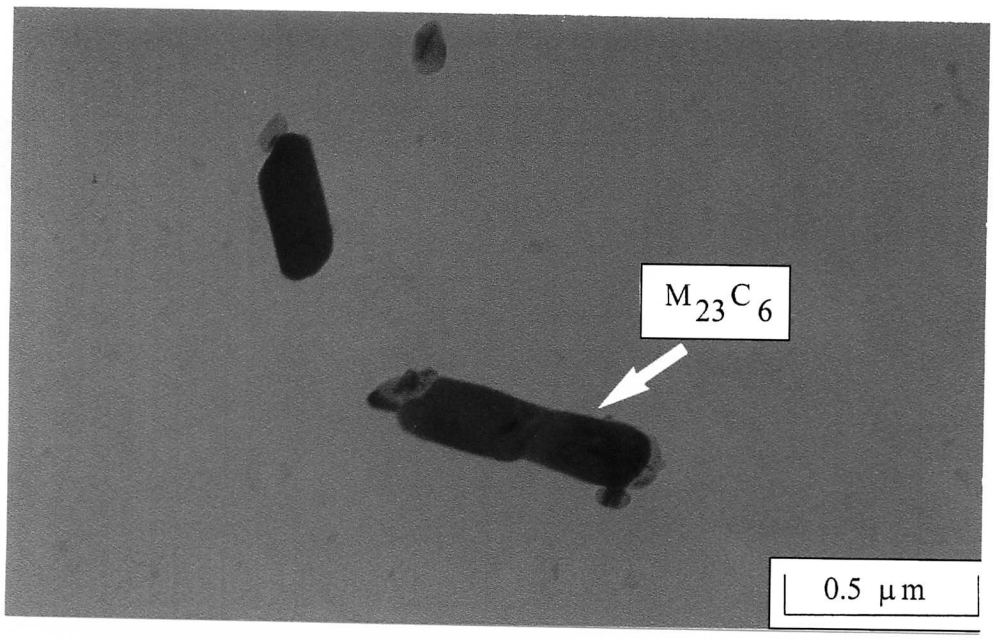

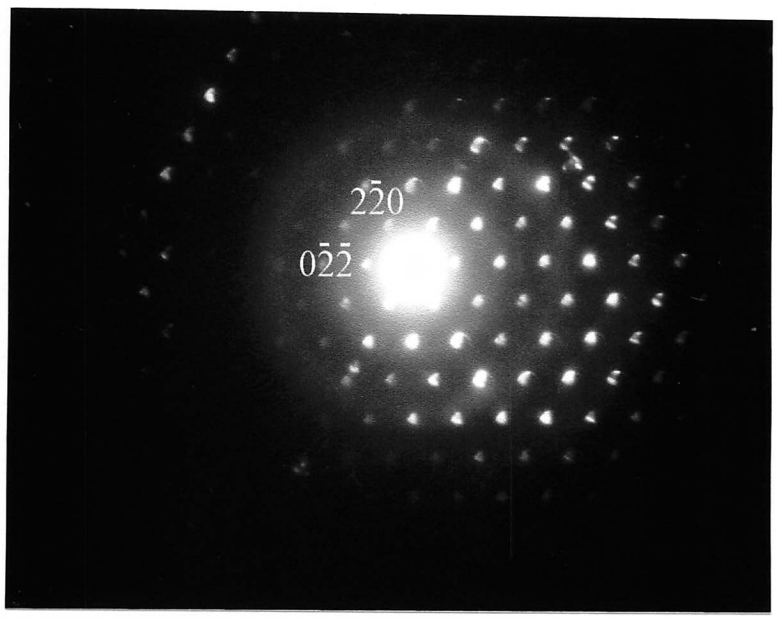

Figure 5.15 TEM micrograph of an $M_{23}C_6$ carbide in the P91 steel of a P91/2$\frac{1}{4}$Cr1Mo diffusion bond heat treated at 650 °C for 1 000 h. The zone axis of this diffraction pattern is $[\bar{1}\ \bar{1}\ 1]$.

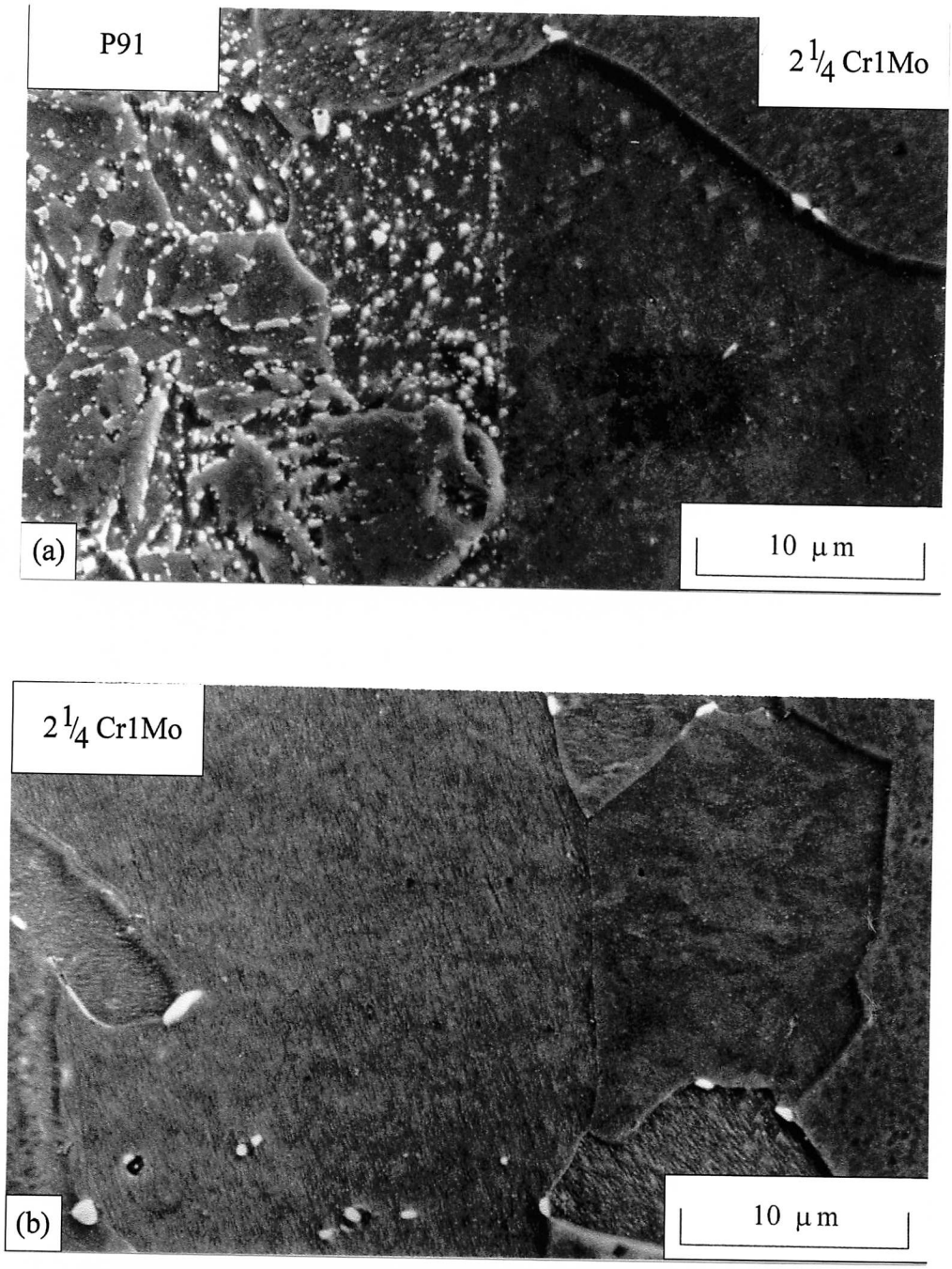

Figure 5.16 SEM micrographs of a P91/2$\frac{1}{4}$Cr1Mo diffusion bond heat treated at 650 °C for 10 000 h; (a) at the bond line and (b) detail of carbides in the decarburised zone.

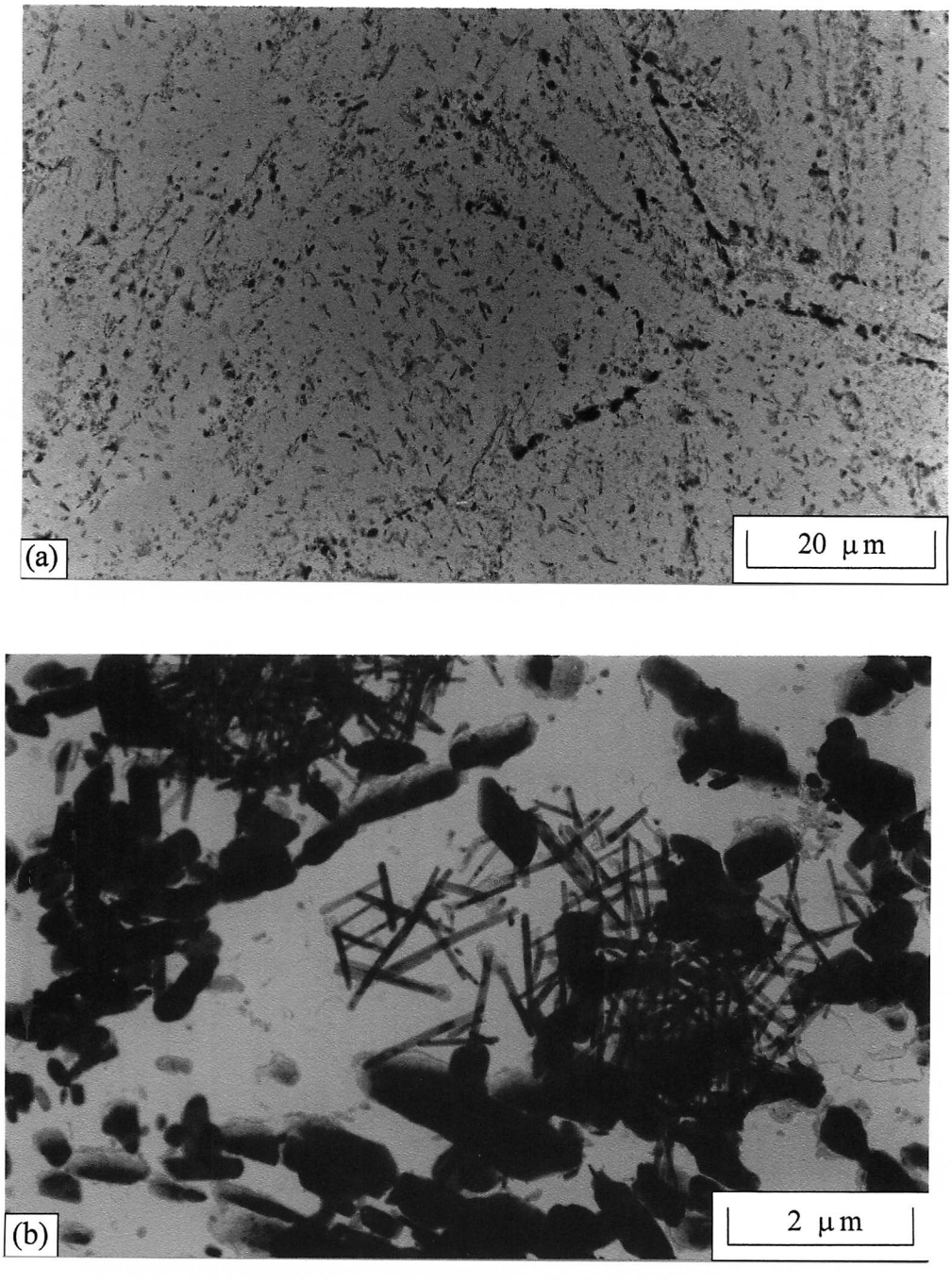

Figure 5.17 Low magnification TEM images of the carburised zone in P91 steel, in a P91/2$\frac{1}{4}$Cr1Mo diffusion bond heat treated at 650 °C for; (a) 1 h, (b) 1 000 h.

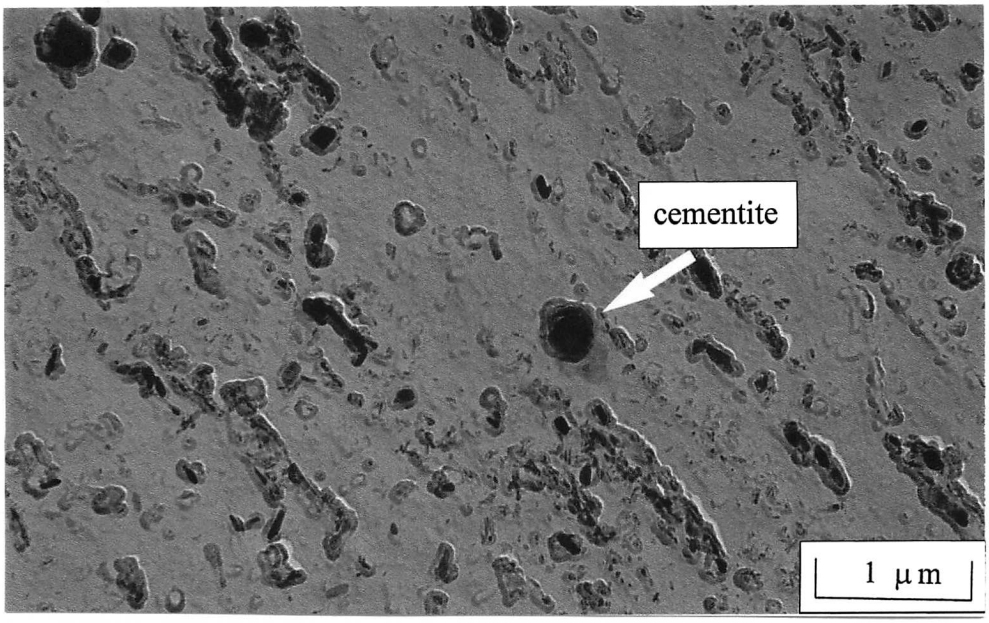

Figure 5.18 TEM micrographs of a cementite in the carburised zone of a P91/2$\frac{1}{4}$Cr1Mo diffusion bond heat treated at 650 °C for 1 h. The zone axis of this diffraction pattern is [9 1 2].

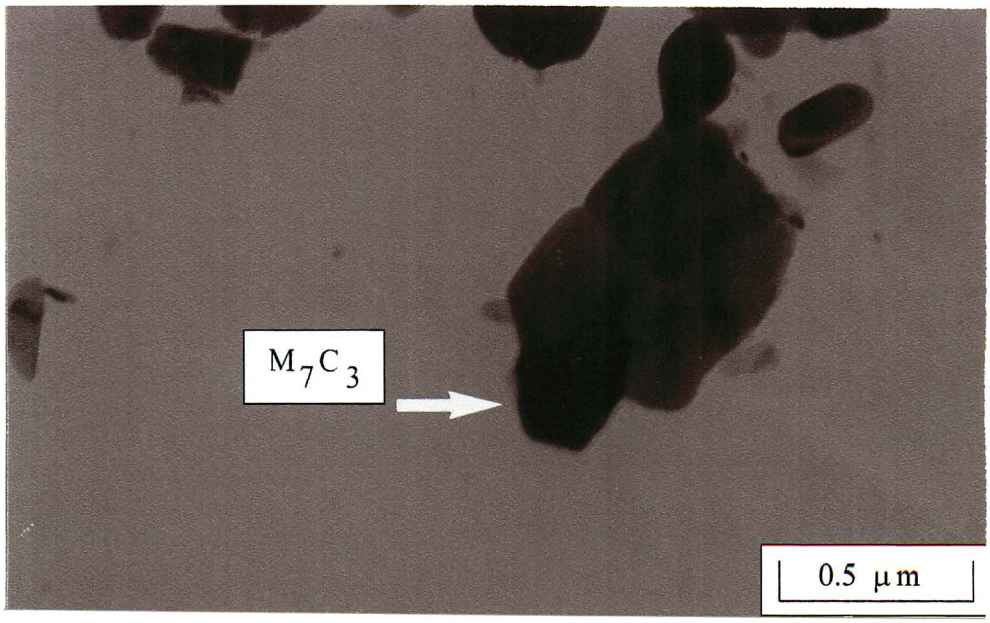

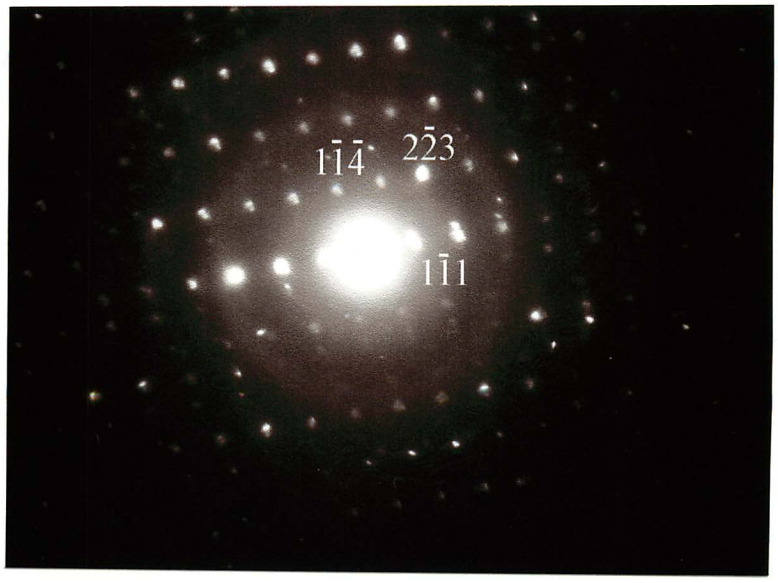

Figure 5.19 TEM micrograph of an M_7C_3 in the carburised zone of a P91/2$\frac{1}{4}$Cr1Mo diffusion bond heat treated at 650 °C for 1 000 h. The zone axis of this diffraction pattern is $[\bar{1}\ \bar{1}\ 0]$.

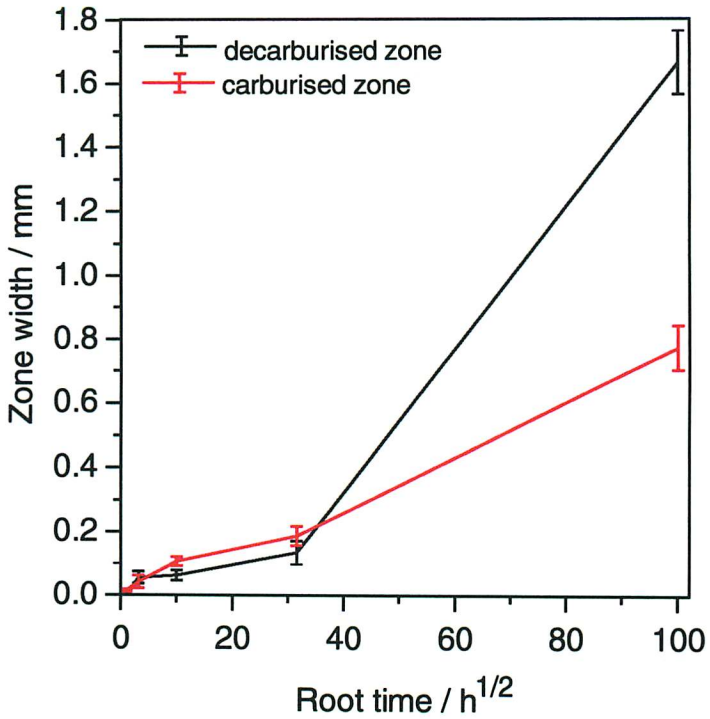

Figure 5.20 The increase of the carburised and decarburised zones during heat treatment at 650 °C.

5.3.2 Heat treatment at other temperatures

The bonds were also heat treated at 600 and 700 °C for 100 h, Figure 5.21. The kinetics of ageing are, as expected, retarded at 600 °C for 100 h, with less intense precipitation in the carburised zone, Figure 5.21a (cf. Figure 5.13). Spherical carbides coarsen on the grain boundaries and a finer precipitation occurs within the grains of P91 steel.

Tempering at 700 °C revealed coarser carbides in the carburised zone, Figure 5.21b. The higher tempering temperature encouraged recrystallisation and accelerated the precipitation process.

Using MTDATA (1996), it is possible to predict the equilibrium phases expected in P91 steel as it carburises. Using the composition of P91 steel given in Table 5.1, and allowing: ferrite, austenite, cementite, M_2C, $M_{23}C_6$, M_7C_3 and vanadium carbide (VC) to be present, it is possible to estimate equilibrium as a function of carbon concentration. For 0.1 wt. % carbon, the equilibrium carbide is predicted to be $M_{23}C_6$ for all of the temperatures studied.

The volume fraction of equilibrium carbide increases with carbon content; however above 0.8 wt.% C, $M_{23}C_6$ is replaced by M_7C_3 as the dominant carbide, Figure 5.22. The precipitation of cementite happens when the carbon content of P91 steel is above 2 wt. % at temperatures between 600 and 700 °C. Naturally, the carbon concentration in ferrite also increases which

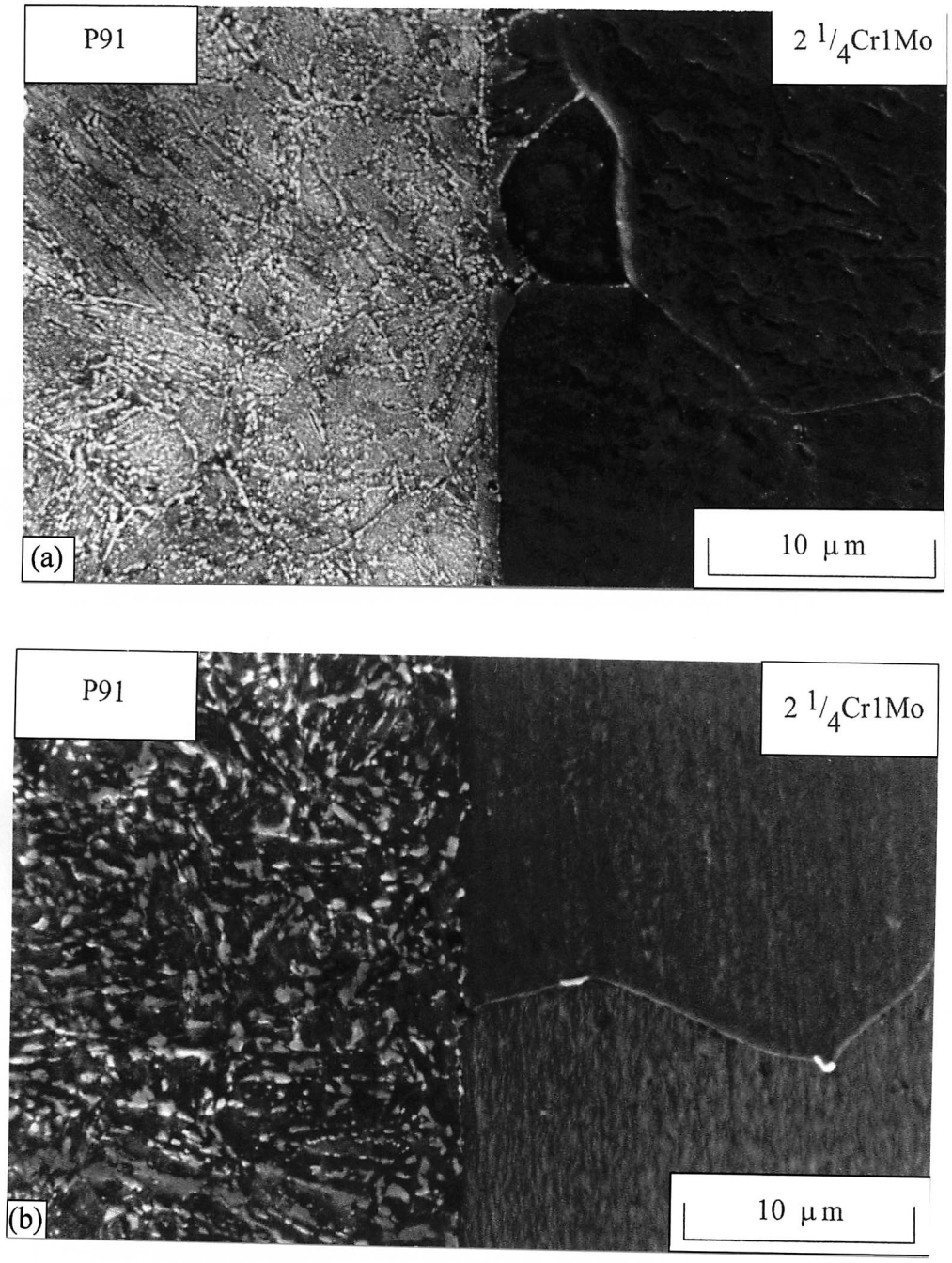

Figure 5.21 SEM micrographs of a P91/2$\frac{1}{4}$Cr1Mo diffusion bond heat treated for 100 h; (a) at 600 °C and (b) 700 °C.

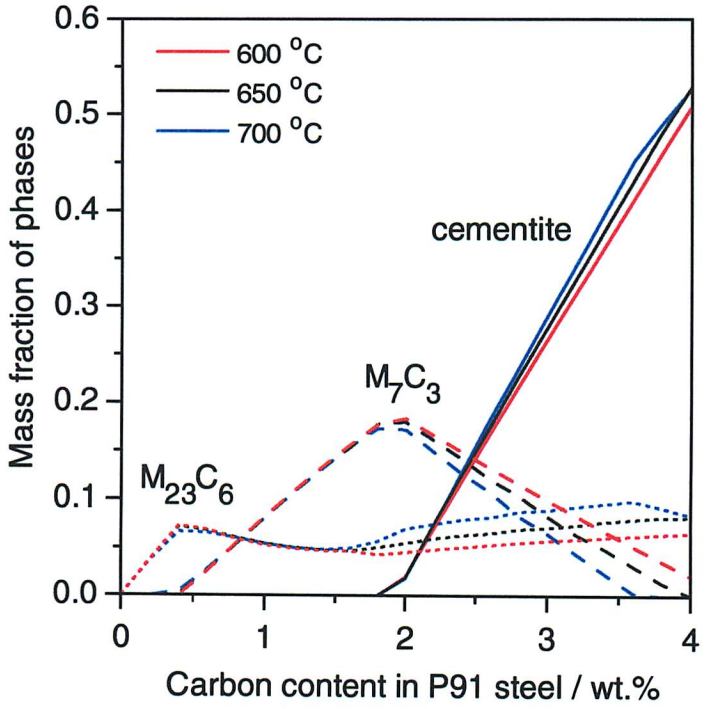

Figure 5.22 The changing mass fractions of carbides as a function of increasing the carbon concentration in a P91 steel.

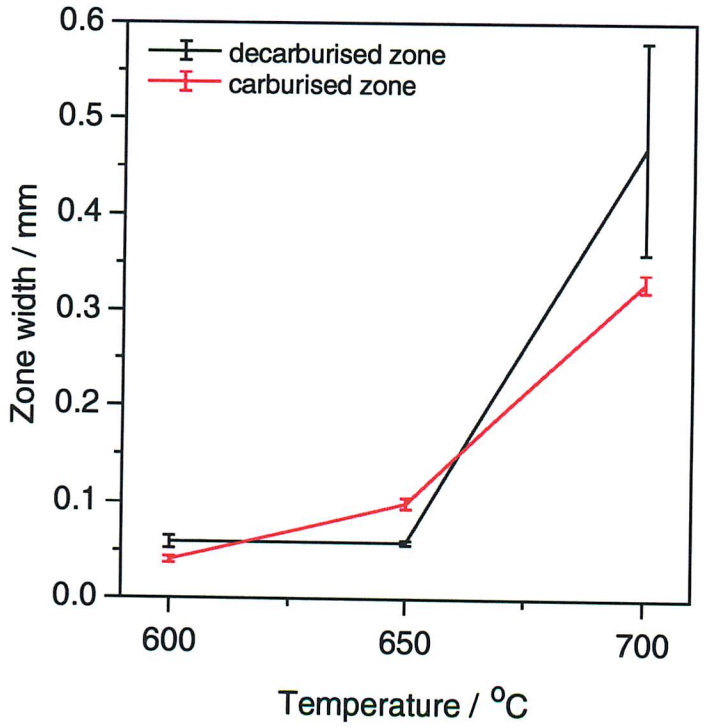

Figure 5.23 A plot to illustrate the increase of the carburised and decarburised zones as the temperature is increased from 600 to 700 °C while heat treating for 100 h.

consequently affects partitioning across the transition joint.

During heat treatment, carbide re-precipitation occurred upon grain boundaries in the carbon-depleted zone as excess substitutional elements tie up some of the carbon in the $2\frac{1}{4}$Cr1Mo steel.

As temperatures is increased from 600 to 650 °C, there was little change in the decarburised zone width, despite growth in the carburised zone, Figure 5.23. However at 700 °C, the measured decarburised zone was larger than the carburised zone as the microstructure had coarsened with temperature.

5.3.3 Minor variations in the composition of the diffusion bond

The composition of the one of the steels in the diffusion bond was changed to see the effect on carbon partitioning. The $2\frac{1}{4}$Cr1Mo steel was replaced with a P22 steel and bonded with the original P91 steel, also a new P91 steel was bonded with the former $2\frac{1}{4}$Cr1Mo steel (see Table 5.1 for compositions).

Figure 5.24 shows micrographs of the new bonds aged for 100 h at 650 °C. Less carbide precipitation was seen in the carburised zone of the new P91 steel and the fraction of carbides remaining in the 2Cr steels was the same in each bond.

The effects of composition variations on the decarburised and carburised zone widths in the 9Cr/2Cr bonds aged for 100 h at 650 °C are shown on Figure 5.25.

Substituting $2\frac{1}{4}$Cr1Mo steel for P22 steel caused negligible changes to the decarburised or carburised zone widths. However, replacing the P91 with the new P91 increased the carburised zone width. This could be due to the higher carbon concentration in the ferrite matrix increasing its chemical potential (MTDATA, 1996). Generally, small variations in substitutional element concentration only mildly affect carbon partitioning.

5.4 Diffusion bonding with $\frac{1}{2}$CrMoV steel

MTDATA was used to illustrate the effects of composition on the ageing characteristics of the bonds. Allowing the phases ferrite, austenite, cementite, M_2C, $M_{23}C_6$, M_7C_3 and VC to be present, the fractions and compositions were calculated, Table 5.4.

The distance from the carbide to the bond line, x_a, can be estimated by finding the length of the block, L, that contains the volume fraction of carbide of width l, Figure 5.26. The fraction of equilibrium carbide V_A (Table 5.4) is used to find L on the low-alloy side as:

$$L = \frac{l}{V_A} \tag{5.3}$$

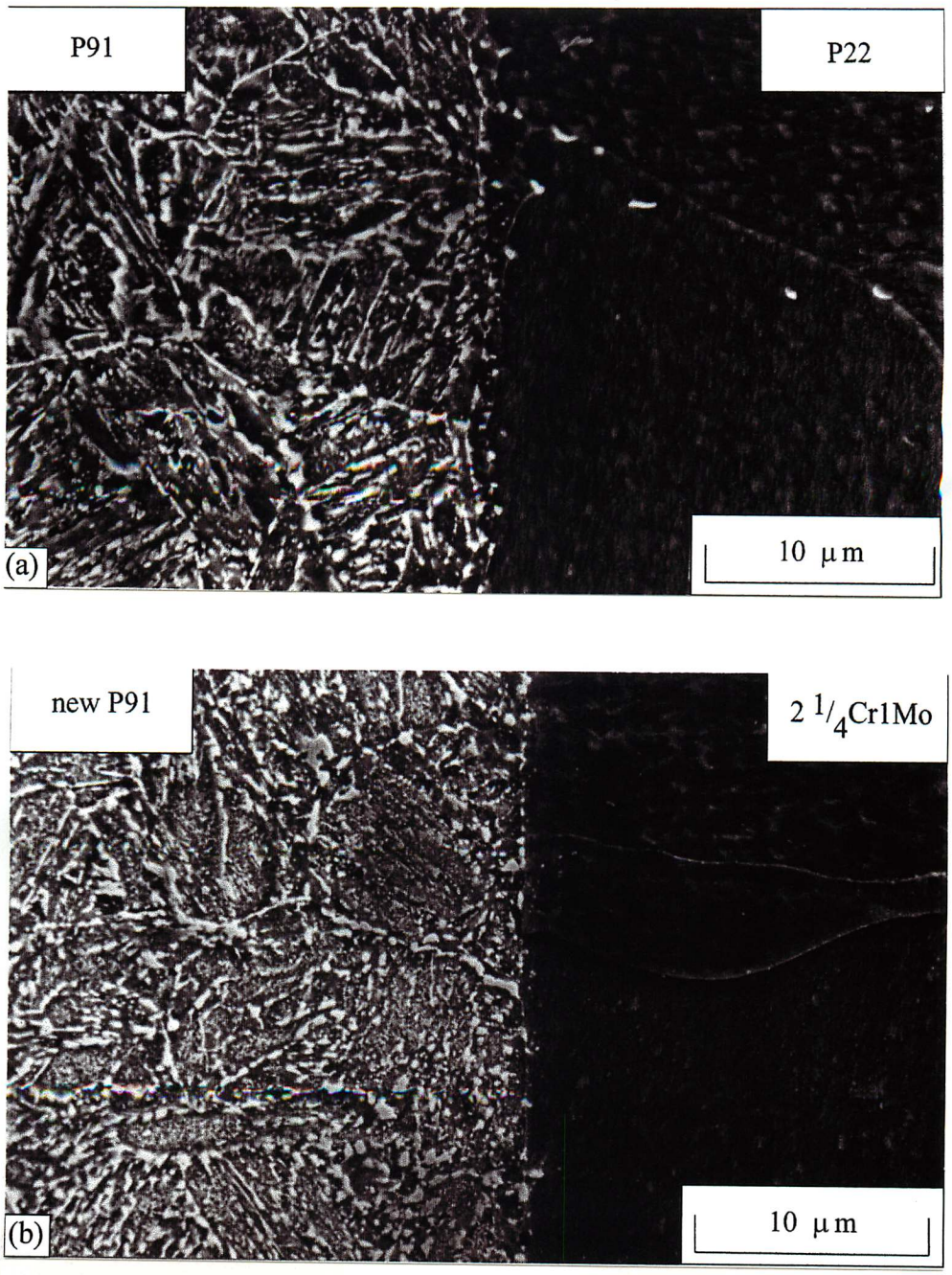

Figure 5.24 SEM micrographs (a) P91/P22 diffusion bond aged for 100 h at 650 °C and (b) new P91/$2\frac{1}{4}$Cr1Mo diffusion bond aged for 100 h at 650 °C.

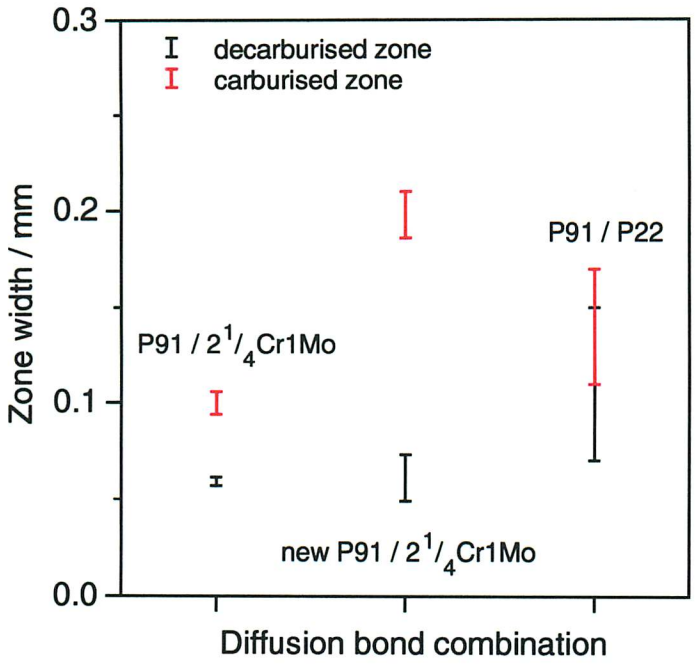

Figure 5.25 A plot to illustrate the change in the carburised and decarburised zones as the composition of the steels in the diffusion bond are altered. The diffusion bonds have been aged for 100 h at 650 °C.

Steel:	$\frac{1}{2}$CrMoV	$2\frac{1}{4}$Cr1Mo	P22	P91	new P91
equilibrium carbide	$M_{23}C_6$	$M_{23}C_6$	$M_{23}C_6$	$M_{23}C_6$	$M_{23}C_6$
wt. % carbon in ferrite	0.00375	0.00053	0.00058	0.00008	0.00008
weight fraction of ferrite	0.99616	0.9664	0.9744	0.9806	0.9787
activity coefficient of carbon	1.273	1.102	1.112	0.674	0.690
volume fraction of carbide	0.0047	0.0287	0.0311	0.0234	0.0257
distance to equilibrium carbide (μm)	105	16.9	15.6	20.9	19

Table 5.4 Variables to calculate carbon concentration gradients in the diffusion bonds. The density of carbide $M_{23}C_6$ is 6.996 g cm^{-3}, and density of ferrite is 8.5 g cm^{-3}. The activity coefficients of carbon is calculated using the method by Wada *et al.* (1972b).

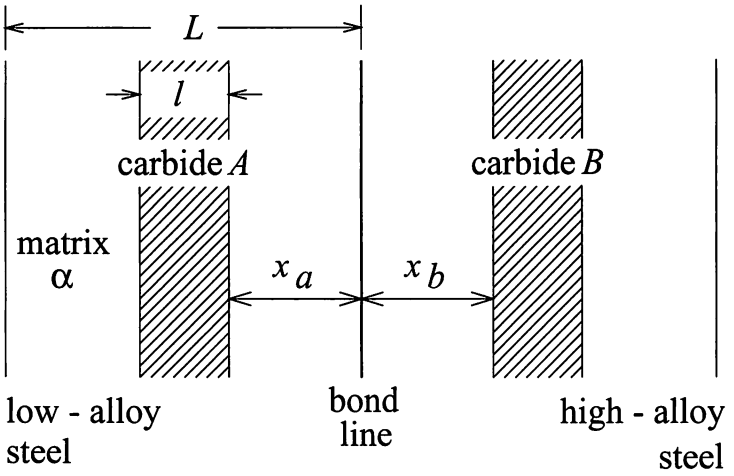

Figure 5.26 Illustration to find the distance from the equilibrium carbide to the bond line. l is assumed to be 1 μm.

Therefore, from Figure 5.26, x_a can be obtained using the equation:

$$x_a = \frac{(L - l)}{2} \tag{5.4}$$

A similar expression may be written for x_b.

Using the data in Table 5.4 and the equations to calculate the interface concentrations, section 4.2.3, the expected carbon concentration gradients adjacent to the bond line, at 650 °C, are plotted in Figure 5.27.

Figure 5.27 shows that minor variations in composition only mildly affect the concentration gradients around the bond line.

In contemporary power plant, common dissimilar welds contain $\frac{1}{2}$CrMoV steel; these can be simulated in diffusion bonds. When a $\frac{1}{2}$CrMoV steel is bonded with a P91 steel, steeper gradients in P91 are brought about by a high interface concentration, $C_{\beta\alpha}$. A larger carbon concentration gradient in the high-alloy steel leads to a more intense precipitation of carbides during ageing, Table 5.5.

It is also noteworthy that when the low-alloy steel is $\frac{1}{2}$CrMoV, $C_{\beta\alpha}$ is higher than $C_{\alpha A}$ for both bond combinations. The shallower concentration gradient between compositions at the interface and the low-alloy steel indicates that carbon is drawn from further distance to maintain equilibrium at the interface.

Immediately after bonding, the microstructure of $\frac{1}{2}$CrMoV steel retained remnants of pearlite on prior austenite grain boundaries (Figure 5.28) and a fine dispersion of vanadium carbides.

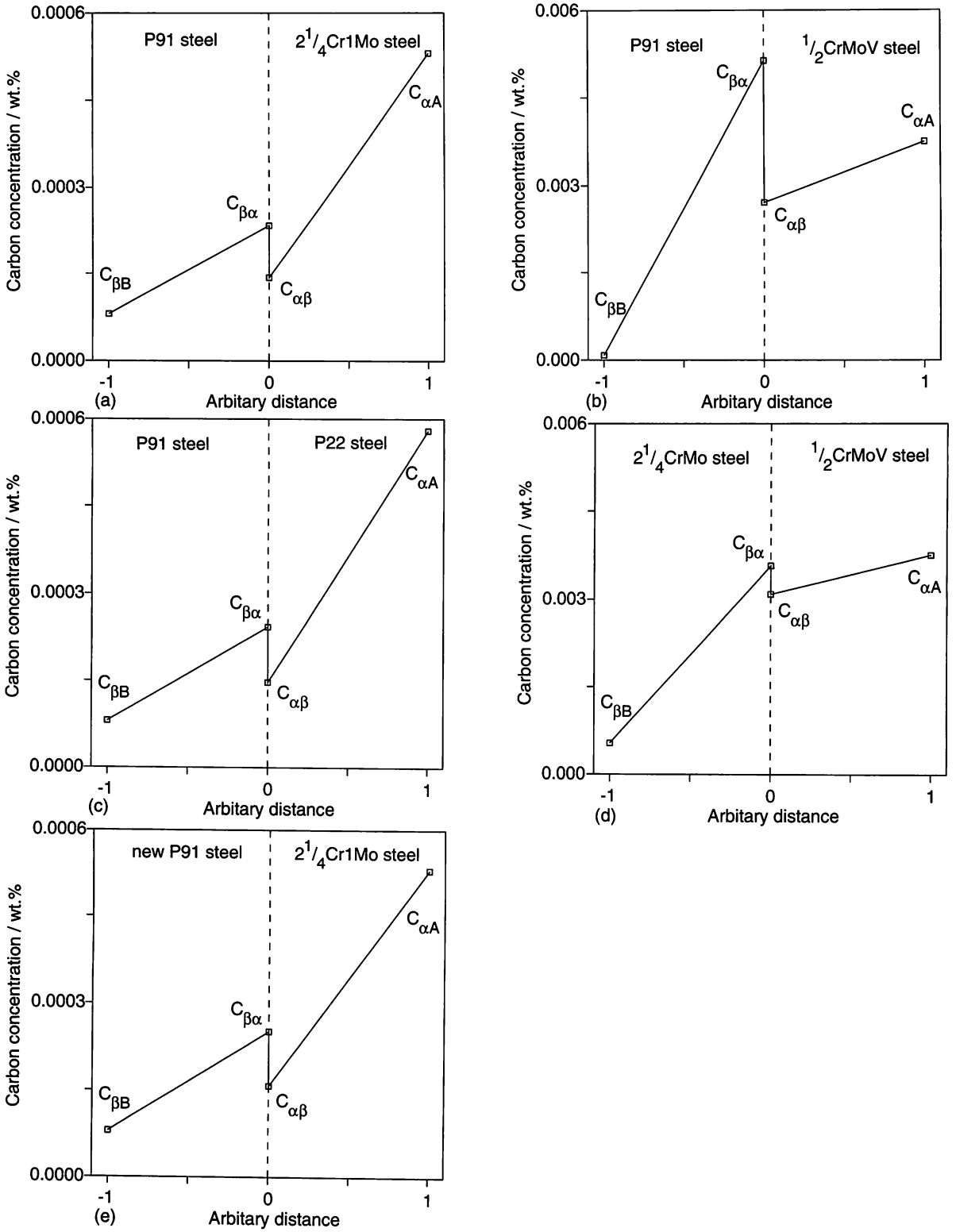

Figure 5.27 Carbon concentration gradients in dissimilar steel diffusion bonds at 650 °C. (a) P91/2$\frac{1}{4}$Cr1Mo bond, (b) P91/$\frac{1}{2}$CrMoV bond, (c) P91/P22 bond, (d) 2$\frac{1}{4}$Cr1Mo/$\frac{1}{2}$CrMoV bond, (e) new P91/2$\frac{1}{4}$Cr1Mo bond.

Diffusion bond	Area percentage of carbides
P91/$2\frac{1}{4}$Cr1Mo	26.6
P91/$\frac{1}{2}$CrMoV	34.4
$2\frac{1}{4}$Cr1Mo/$\frac{1}{2}$CrMoV	32.3

Table 5.5 The observed area percentages of carbides counted in the carburised zone of high-alloy steels in bonds aged for 100 h at 650 °C. All carbides were included in this measurement, the calculated accuracy was ±1 %.

Pearlitic cementite dissolves first during carbon partitioning, followed by the dissolution of more stable carbides.

Figure 5.28 SEM micrograph of remnants of pearlite in the $\frac{1}{2}$CrMoV steel, immediately after bonding with a P91 steel.

There was little indication of ferrite grain growth in the decarburised zone next to the dissimilar steel when the low-alloy steel is a $\frac{1}{2}$CrMoV, Figure 5.29. This was thought to be due to pinning by the persistent carbides.

An obvious carburised zone is seen the high-alloy P91/$\frac{1}{2}$CrMoV diffusion bond, Figure 5.30a. On Figure 5.29b, the carburised zone in $2\frac{1}{4}$Cr1Mo steel appears not to be there, though an SEM micrograph of the bond revealed this was not the case, Figure 5.30b.

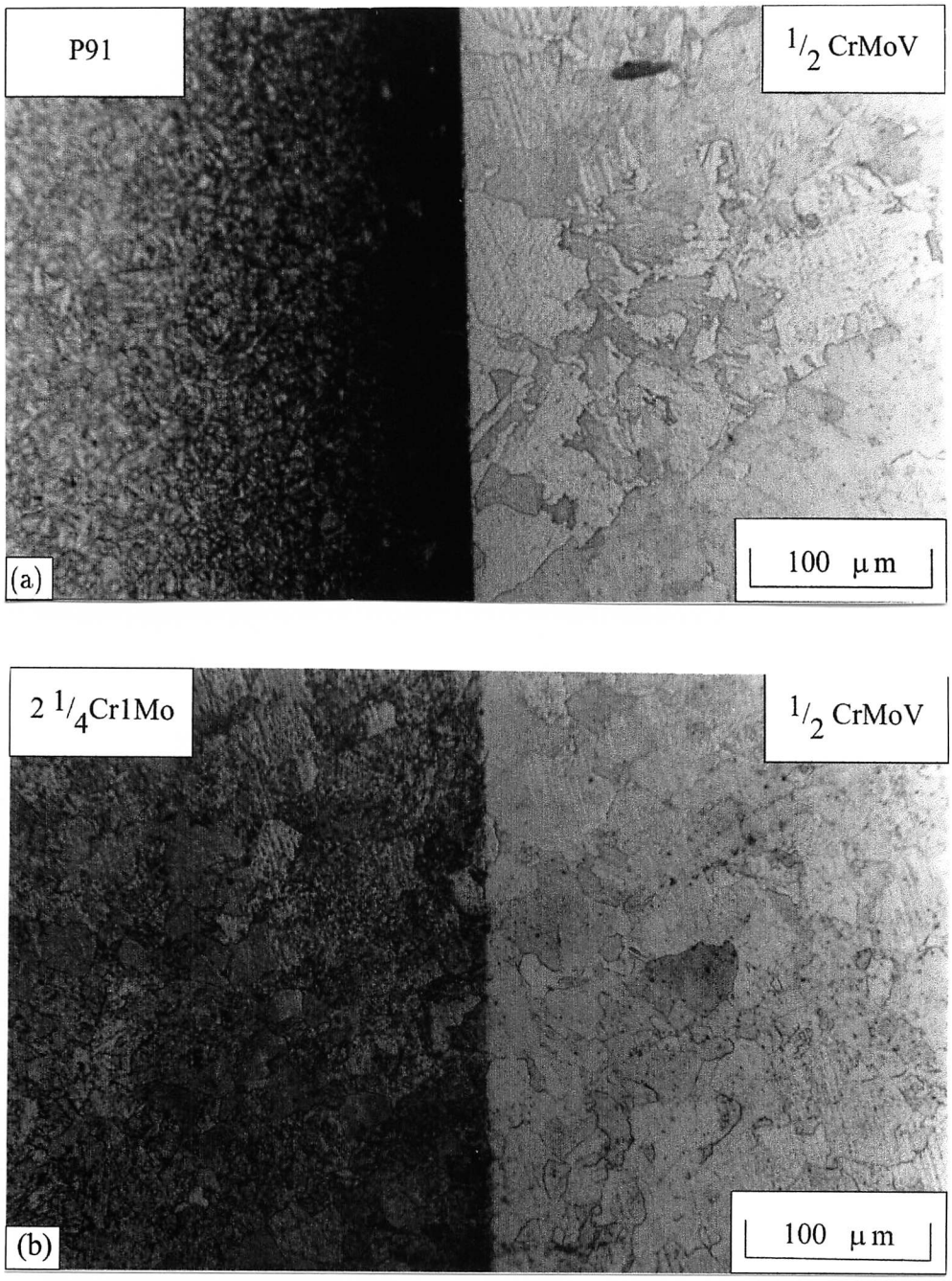

Figure 5.29 Optical micrographs of; (a) P91/$\frac{1}{2}$CrMoV bond and (b) $2\frac{1}{4}$Cr1Mo/$\frac{1}{2}$CrMoV bond. The bonds were aged for 100 h at 650 °C.

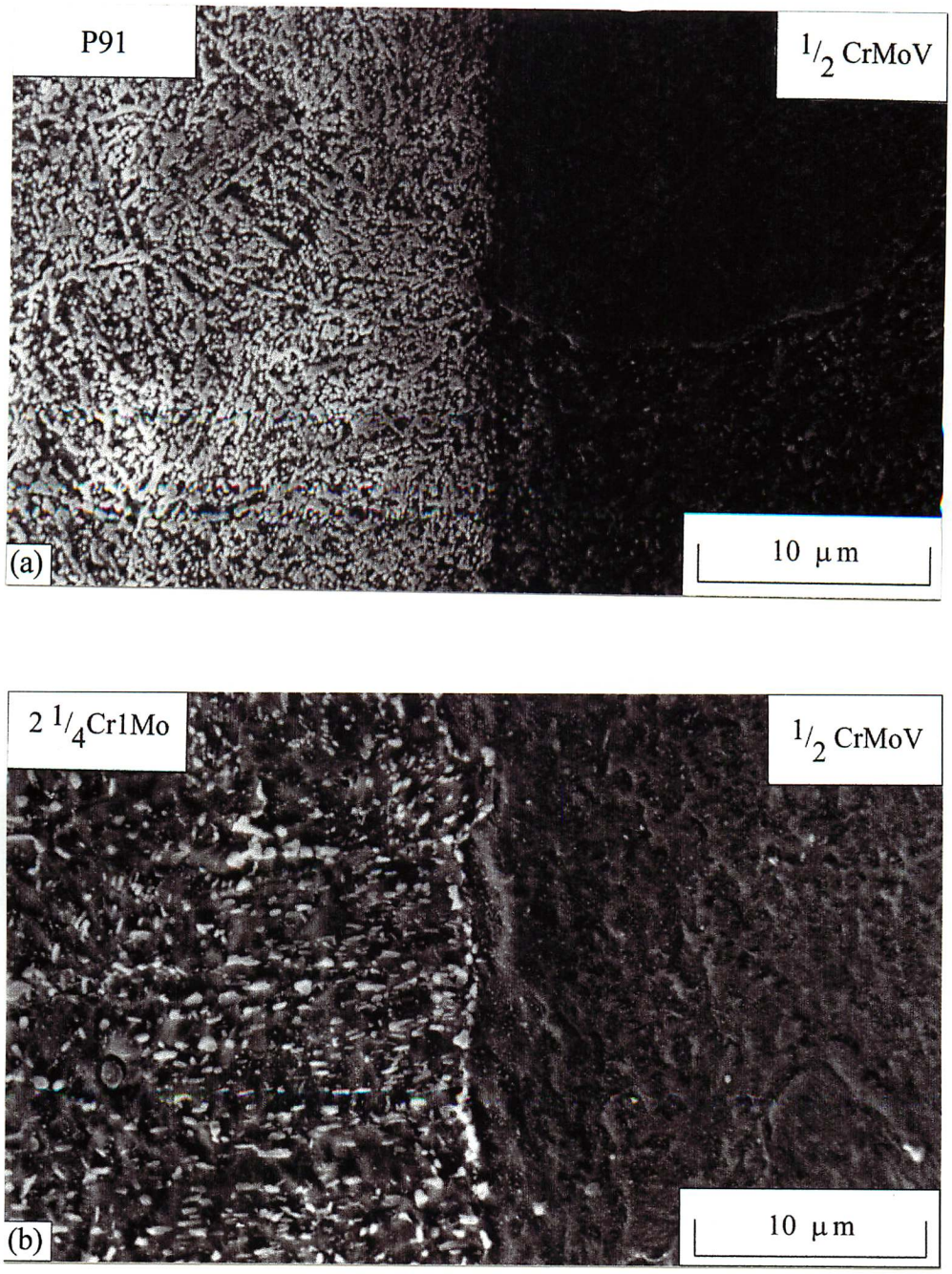

Figure 5.30 SEM micrographs of; (a) P91/$\frac{1}{2}$CrMoV bond and (b) $2\frac{1}{4}$Cr1Mo/$\frac{1}{2}$CrMoV bond. The bonds were aged for 100 h at 650 °C.

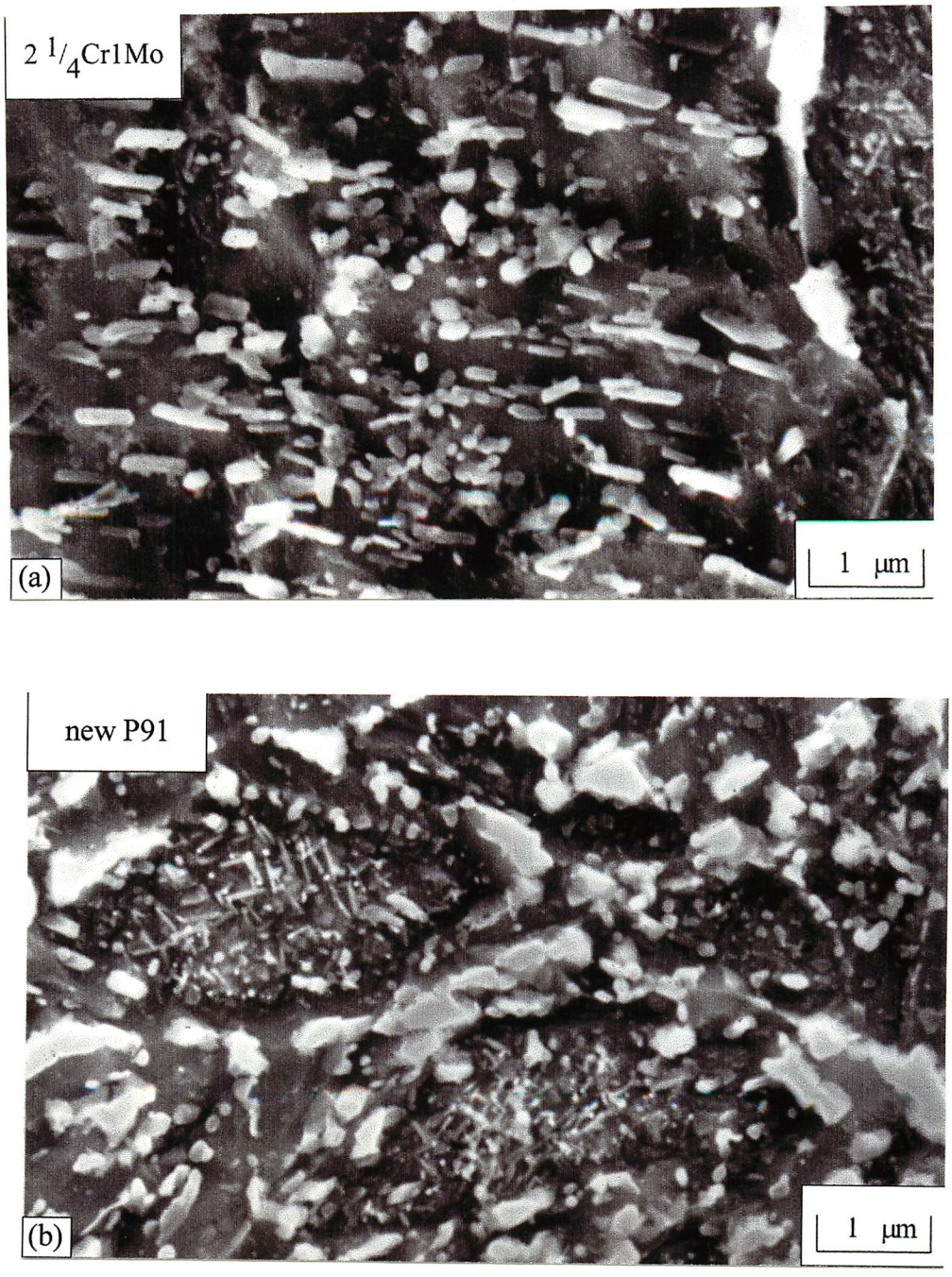

Figure 5.31 SEM micrographs of; (a) carburised zone in $2\frac{1}{4}$Cr1Mo/$\frac{1}{2}$CrMoV bond and (b) carburised zone in new P91/$2\frac{1}{4}$Cr1Mo bond. The bonds were aged for 100 h at 650 °C.

In the $2\frac{1}{4}$Cr1Mo carburised zone, Figure 5.31a, the carbides appear all the same shape and are orientated perpendicular to the dissimilar steel interface, whereas in a P91 carburised zone, coarse carbides are surrounding small pockets of needle carbides, probably of MX-type, Figure 5.31b. The identified precipitates in the carburised zone of $2\frac{1}{4}$Cr1Mo steel were all M_7C_3 carbides, Figure 5.32.

5.5 Vickers hardness

Using the method described in section 5.2.2, the Vickers hardness values of each of the diffusion bonds heat treated are reported in Table 5.6.

The P91, $2\frac{1}{4}$Cr1Mo and $\frac{1}{2}$CrMoV steel harden after the bonding cycle. Subsequent heat treatment softens both the P91 and $2\frac{1}{4}$Cr1Mo steel due to carbide coarsening and grain growth. The softening of these steels happens faster at 700 °C as the kinetics of softening are temperature dependent. When the hardness of P91 and $2\frac{1}{4}$Cr1Mo steel are plotted in order of ascending tempering parameter, P, the P91 steel begins to re-harden at a high P due to the influx of carbon and precipitation hardening, Figure 5.33.

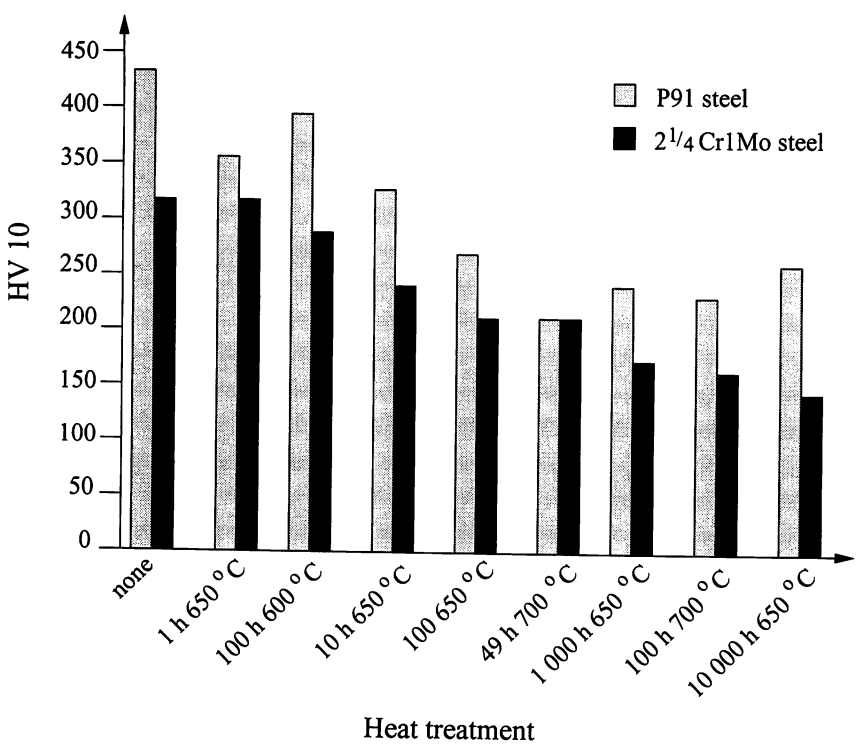

Figure 5.33 The changing hardness of a diffusion bond heat treated under different conditions, in order of ascending P values.

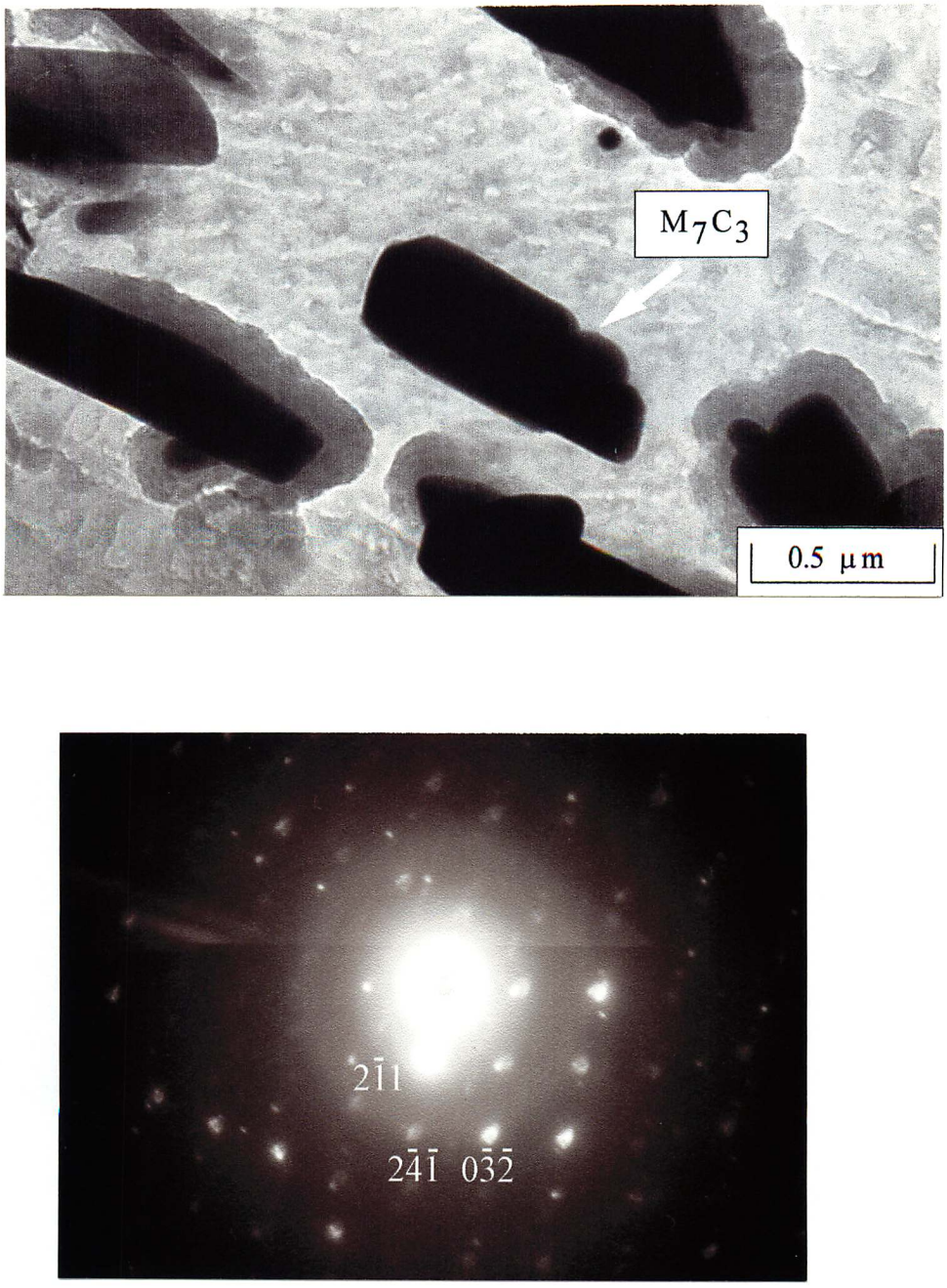

Figure 5.32 TEM micrograph of an M_7C_3 carbide in the carburised zone of a $2\frac{1}{4}$Cr1Mo/$\frac{1}{2}$CrMoV bond heat treated at 650 °C for 1 00 h. The zone axis of this diffraction pattern is $[\bar{5}\ \bar{4}\ 6]$.

Diffusion Bond	Heat Treatment	HV 10	*P*
P91	before bonding	215	-
$2\frac{1}{4}$Cr1Mo	before bonding	147	-
$\frac{1}{2}$CrMoV	before bonding	165	-
P91/$2\frac{1}{4}$Cr1Mo	after bonding, no heat treatment	433 / 317	-
P91/$2\frac{1}{4}$Cr1Mo	100 h, 600 °C	398 / 286	19.2
P91/$2\frac{1}{4}$Cr1Mo	1 h, 650 °C	357 / 318	18.5
P91/$2\frac{1}{4}$Cr1Mo	10 h, 650 °C	324 / 240	19.4
P91/$2\frac{1}{4}$Cr1Mo	100 h, 650 °C	270 / 211	20.3
P91/$2\frac{1}{4}$Cr1Mo	1 000 h, 650 °C	242 / 172	21.2
P91/$2\frac{1}{4}$Cr1Mo	10 000 h, 650 °C	259 / 141	22.1
P91/$2\frac{1}{4}$Cr1Mo	49 h, 700 °C	212 / 210	21.1
P91/$2\frac{1}{4}$Cr1Mo	100 h, 700 °C	228 / 166	21.4
new P91/$2\frac{1}{4}$Cr1Mo	after bonding, no heat treatment	426 / 255	-
new P91/$2\frac{1}{4}$Cr1Mo	100 h, 650 °C	279 / 194	20.3
P91/P22	after bonding, no heat treatment	422 / 335	-
P91/P22	100 h, 650 °C	247 / 198	20.3
P91/$\frac{1}{2}$CrMoV	after bonding, no heat treatment	416 / 224	-
P91/$\frac{1}{2}$CrMoV	100 h, 650 °C	273 / 255	20.3
$2\frac{1}{4}$Cr1Mo/$\frac{1}{2}$CrMoV	after bonding, no heat treatment	243 / 225	-
$2\frac{1}{4}$Cr1Mo/$\frac{1}{2}$CrMoV	100 h, 650 °C	170 / 237	20.3

Table 5.6 Vickers hardness of dissimilar steel bonds after given heat treatment. The position of each hardness indent was between 2 – 3 mm from the bond line.

Low-alloy $\frac{1}{2}$CrMoV steel hardens during heat treatment, and even becomes harder than its $2\frac{1}{4}$Cr1Mo steel neighbour in spite of the $\frac{1}{2}$CrMoV steel decarburising. This may be caused by secondary hardening.

5.6 Microhardness traverses

Microhardness traverses in the locality of the bond line monitor changes in hardness due to carbon partitioning. Though the quantity of affected zones are indicated by changes of hardness, it is difficult to correctly determine their widths by the point where hardness changes

by less than a few HV.

Figure 5.34 shows the changes in hardness across a P91/$2\frac{1}{4}$Cr1Mo bond. Increasing the duration of ageing softens both the P91 and $2\frac{1}{4}$Cr1Mo steel while the carburised and decarburised zones continue to widen. At 700 °C, the hardness of the carburised zones and the minimum in the decarburised zone are lowered, Figure 5.35.

Figure 5.36 show the changes in hardness before and after ageing bonds with a $\frac{1}{2}$CrMoV steel. In the P91/$\frac{1}{2}$CrMoV bond aged for 100 h at 650 °C, there is a minimum and maximum of hardness at the bond line, Figure 5.36b. However, in the $2\frac{1}{4}$Cr1Mo/$\frac{1}{2}$CrMoV bond after ageing, the hardness of the decarburised zone is higher than in the $2\frac{1}{4}$Cr1Mo steel. From the optical micrographs (Figure 5.29), $\frac{1}{2}$CrMoV steel did not show large carbide-free ferrite grains next to the bond line. Therefore, the high hardness in the decarburised zone is attributed to secondary hardening by the vanadium carbides remaining in the $\frac{1}{2}$CrMoV steel.

5.7 Summary

In this chapter, the microscopy and hardness results of many combination of bonds have been collected to illustrate carbon partitioning across the bond during ageing. The decarburised and carburised zones formed grow neatly along the dissimilar steel interface as there is no distortion or compositional mixing involved in the joining processes. Microscopy has revealed that the zones grow easily in bonds during heat treatment, though the decarburised zones were not apparent in $\frac{1}{2}$CrMoV.

These observations will be compared to data from the microscopy and hardness studies in dissimilar welds and eventually, all the results will be analysed with the predictions from computer model.

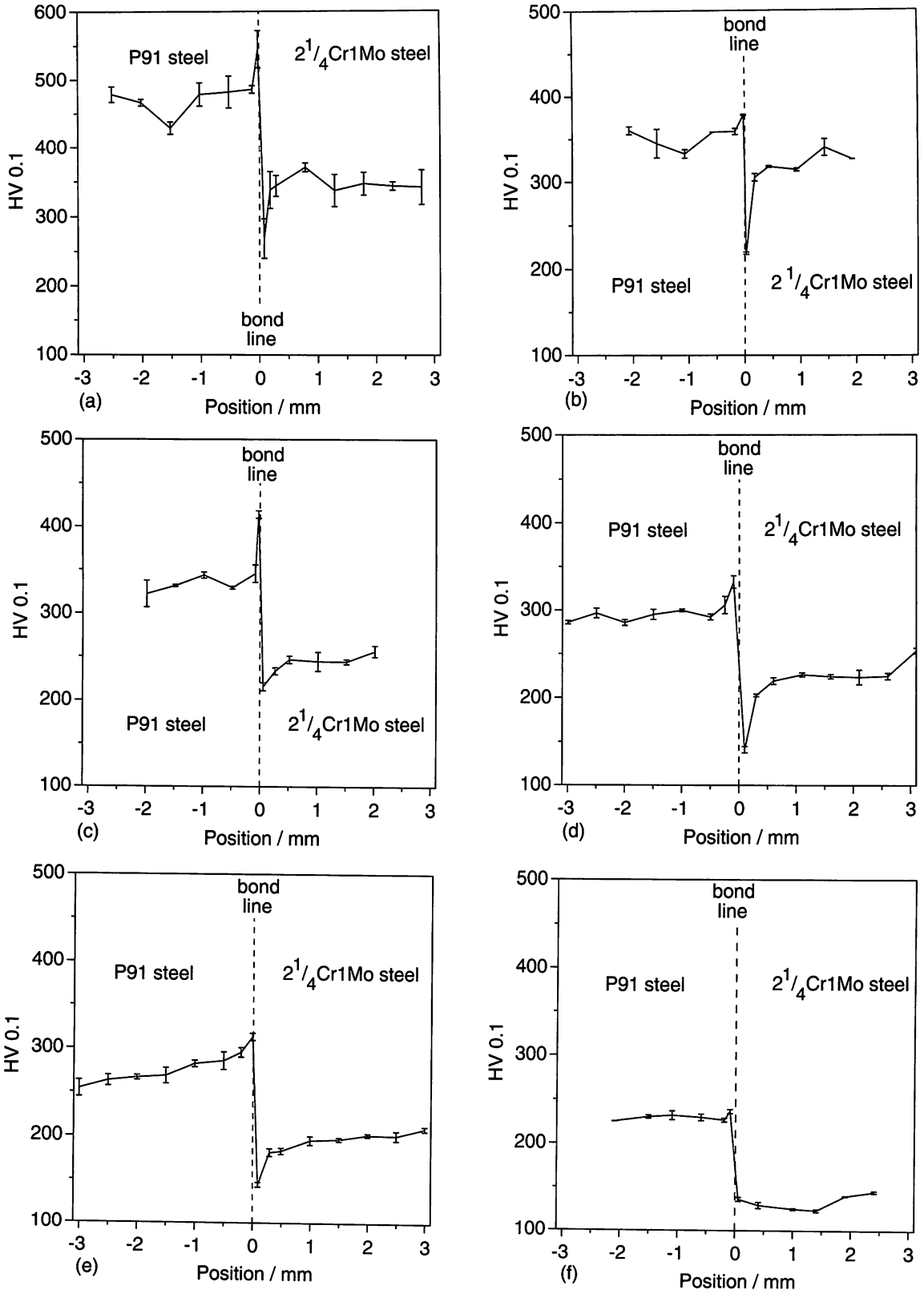

Figure 5.34 Microhardness traverses for P91/2$\frac{1}{4}$Cr1Mo diffusion bonds aged at 650 °C; (a) no ageing, (b) 1 h, (c) 10 h, (d) 100 h, (e) 1 000 h, (f) 10 000 h.

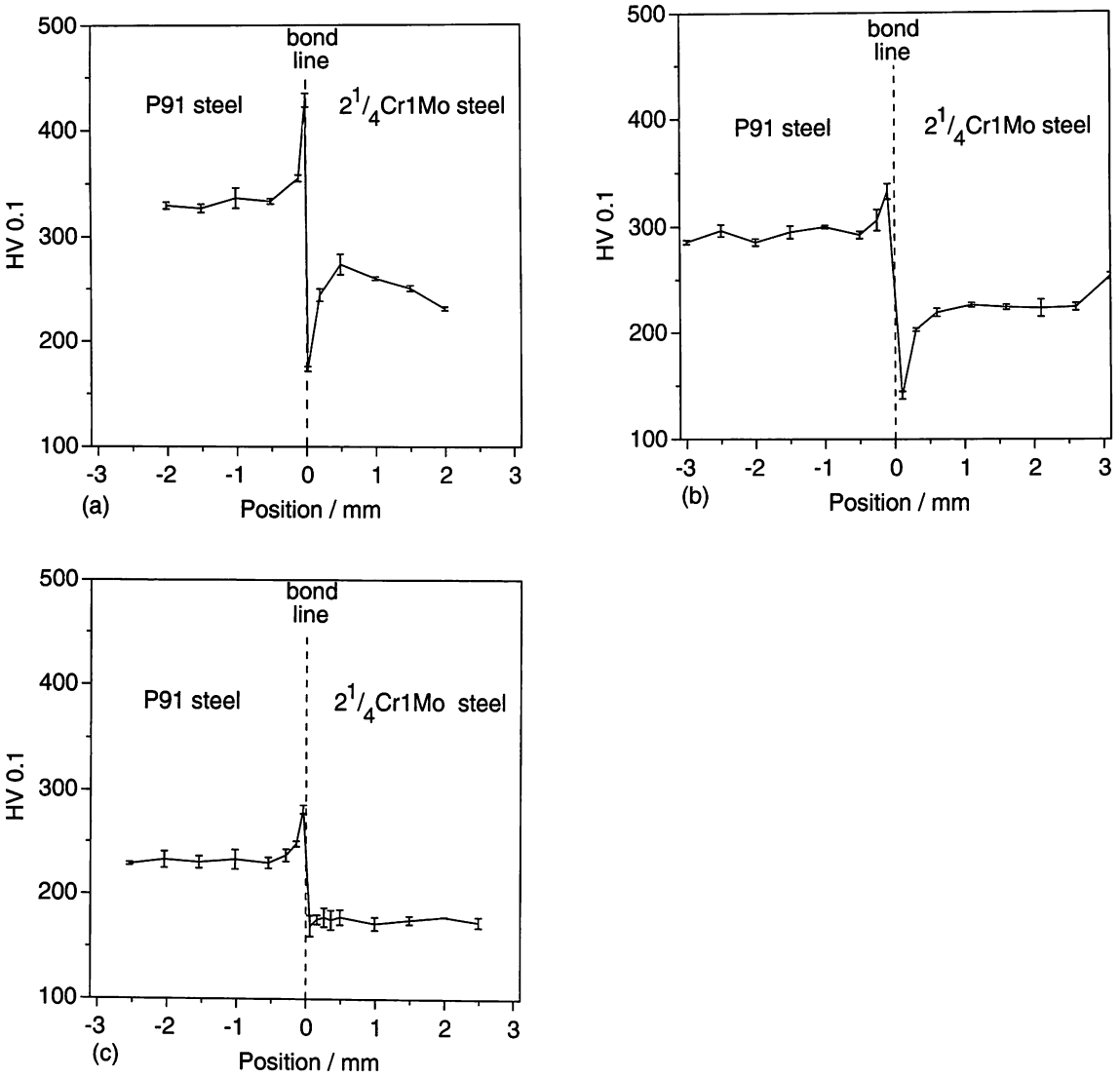

Figure 5.35 Microhardness traverses for P91/2$\frac{1}{4}$Cr1Mo diffusion bonds aged for 100 h at; (a) 600 °C, (b) 650°C, (c) 700°C.

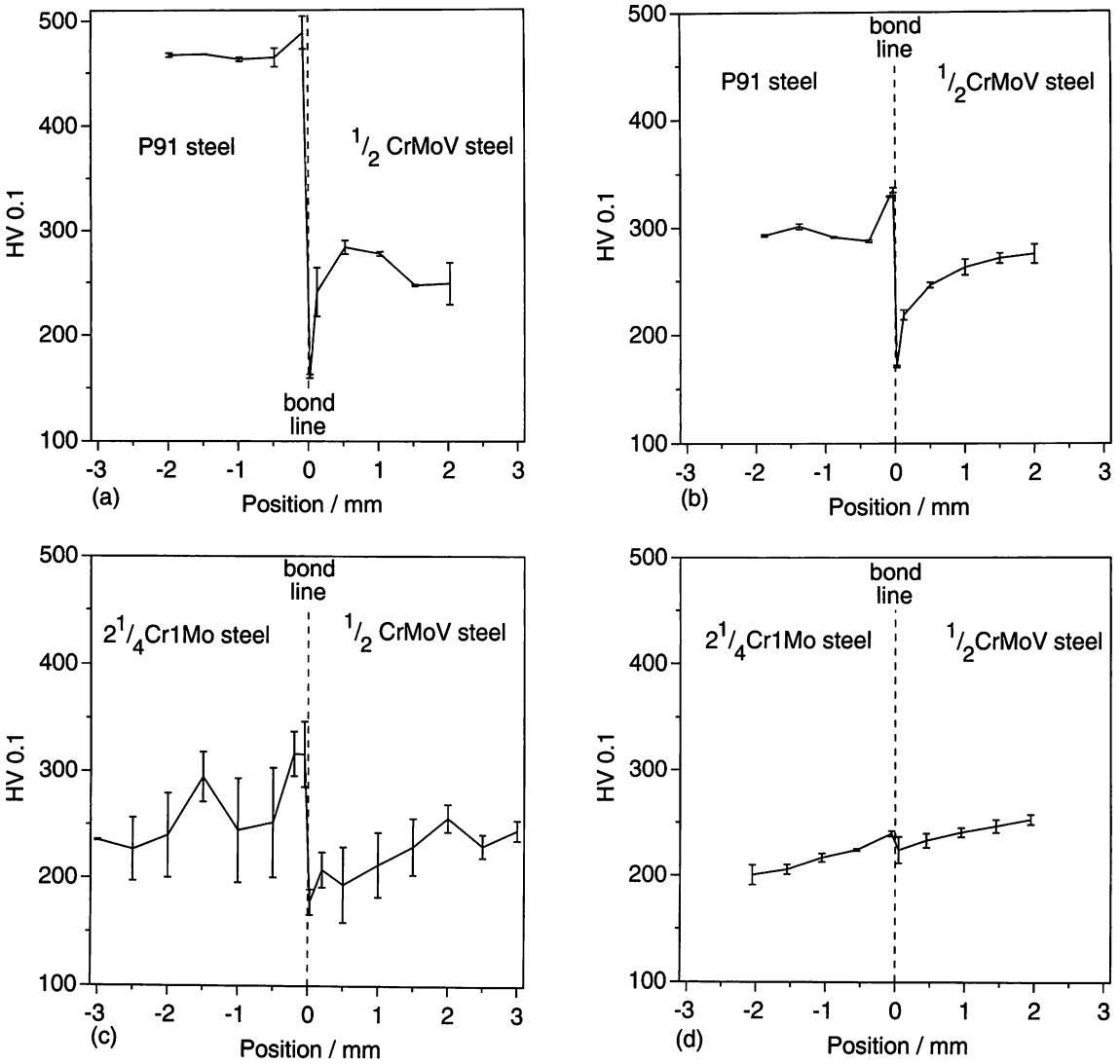

Figure 5.36 Microhardness traverses for diffusion bonds with a $\frac{1}{2}$CrMoV low-alloy steel, at 650 °C; (a) with P91, no ageing, (b) aged 100 h, (c) with a $2\frac{1}{4}$Cr1Mo steel, no ageing, (d) aged 100 h.

Chapter Six

Carbon Partitioning in Vanadium-Free Welds

The partitioning of carbon across a well-defined interface created by diffusion bonding was investigated in Chapter 5. By contrast, the work presented here deals with joints made using fusion welding.

6.1 Introduction to dissimilar steel welds in power plant

Ageing tests performed in the laboratory pose the question as to how welds subject to high temperature-short term conditions will compare with welds which have been in service in power plant. It is important to distinguish any advantages that are gained by decreasing the testing time using a higher temperature from any unwanted microstructural changes, such as grain growth or variations in the volume fractions of carbides or changes in behaviour during destructive testing. In a dissimilar steel weld, the compositions of the filler and parent metals will be different; hence during welding, suitable measures, such as buttering, can help to ensure that the weld has the desired composition. The arrangement and position of the weld passes is also crucial as each deposit of weld metal reheats the previous, with resultant changes in microstructure.

While post-weld heat treatments may induce carbon partitioning across the weld junction. This results in the loss of mechanical and creep strength within the large-grained carbide-free zone of the low-alloy steel, and a loss of toughness in the carburised seam in the high-alloy steel (Buchmayr *et al.*, 1989; Kim *et al.*, 1992; Prader *et al.*, 1995).

6.2 Experimental procedure

The work presented here was performed on samples prepared at the Power Technology Centre. A series of steel butt welds, between a P91 and a $2\frac{1}{4}$Cr1Mo pipe welded with a 9Cr1Mo consumable were provided for study, Table 6.1

The P91 steel was buttered with up to 15 $\pm$ 1 mm of 9Cr1Mo weld metal, using manual metal arc (MMA) welding, Figure 6.1, and given a separate PWHT for 3 h at 765 $\pm$ 15 °C.

The weld was preheated to 200 °C; the root run and tacking of the weld was made using tungsten-inert gas welding plus filler then subsequently filled using numerous passes of MMA welding, Figure 6.2. The whole weld was given a heat treatment for 24 h at the preheat

	C	S	P	Si	Mn	Ni	Cr	Mo	V
$2\frac{1}{4}$Cr1Mo steel	0.12	0.022	0.021	0.27	0.54	0.04	2.29	0.95	0.005
P91 steel	0.1	0.002	0.01	0.33	0.43	0.08	8.6	0.92	0.24
9Cr1Mo weld metal	0.07	0.004	0.013	0.38	0.87	0.32	8.7	1.04	0.01

Table 6.1 Composition (wt. %) of steels in a dissimilar steel weld, determined by optical emission spectroscopy.

temperature to lower the diffusible hydrogen level. The resulting dissimilar steel weld was given a final temper at 720 °C for 3 h.

The weld was then sliced longitudinally to provide samples for diffusion experiments. The sample heat treatment programme was designed to encompass a range of ageing times and temperatures, described in Table 6.2.

The samples were etched for optical metallography and microhardness tests, Figure 6.3 and 6.4.

6.3 Optical metallography

The microstructures of the weld and HAZ immediately after welding are shown in Figure 6.5a. During solidification, the grain growth in the weld occurs epitaxially from those in the HAZ, leaving a columnar austenitic structure in the weld. This solidification microstructure is modified by solid-state transformations during cooling. Further changes occur during PWHT when the microstructure is tempered; some signs of carbon partitioning can be seen in Figure 6.5b.

Some regions of the HAZ become austenitic during multi-pass welding. Therefore, the decarburised zone becomes quite uneven. It was observed that, after short-term heat treatments, the decarburised zone first became apparent in the regions of the HAZ that had been austenitised to the highest temperatures. This was thought to be because the thermal cycles encourage carbon partitioning even during welding.

It is also worth noting that grain growth occurred in the bead overlapping areas of the buttered layer between the 9Cr1Mo and P91 parent steel which had been tempered during deposition, PWHT and ageing, Figure 6.6.

Ageing naturally leads to additional partitioning following the trend which was initialised during PWHT. The effect of temperature on carbon partitioning is illustrated on Figure 6.7

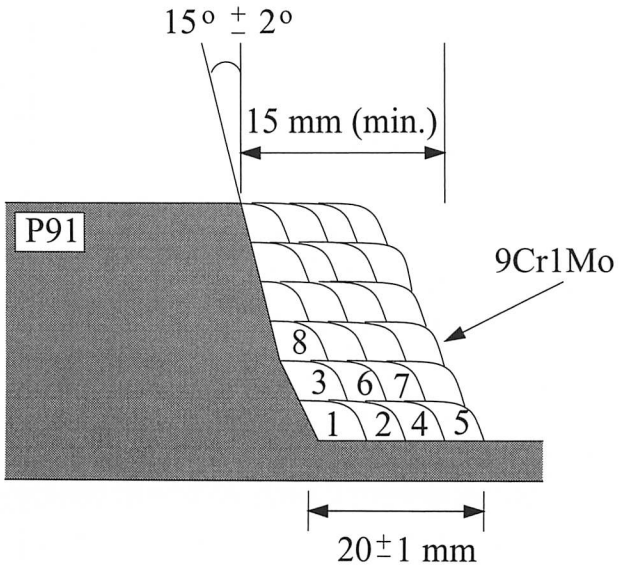

Figure 6.1 Example of buttering P91 with 9Cr1Mo filler, for weld preparation.

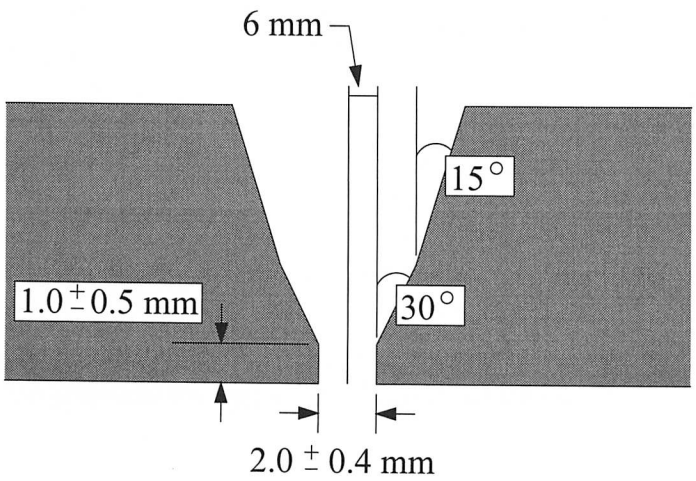

Figure 6.2 Preparation of the joint for filling with weld metal.

PWHT:		**Ageing:**	
Temperature / °C	**Time / h**	**Temperature / °C**	**Time / h**
none	none	none	none
720	3	none	none
720	3	600	10
720	3	600	100
720	3	600	1 000
720	3	650	10
720	3	650	100
720	3	650	1 000
720	3	650	10 000
720	3	730	2
720	3	730	20
720	3	730	77
720	3	730	500

Table 6.2 Details of heat treatments for P91/9Cr1Mo/$2\frac{1}{4}$Cr1Mo steel weld.

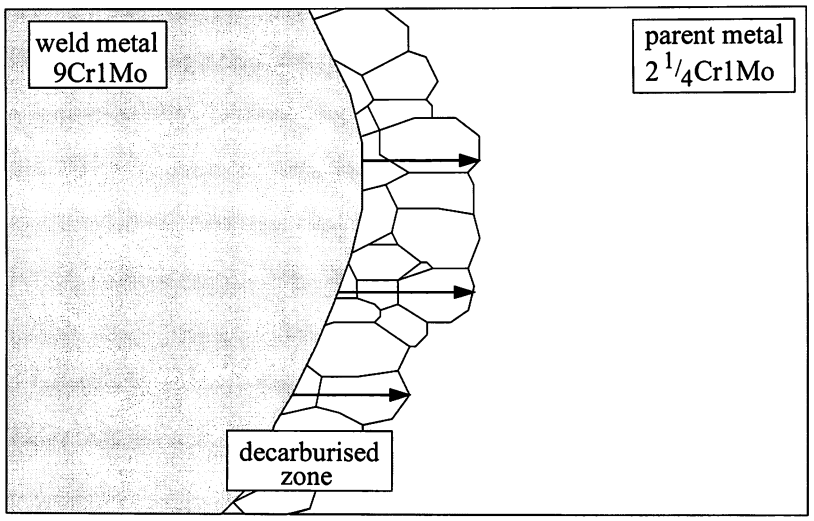

Figure 6.3 A sketch illustrating the size of the decarburised zone defined by the coarse-grained structure, dependent on the location relative to the curved fusion boundary.

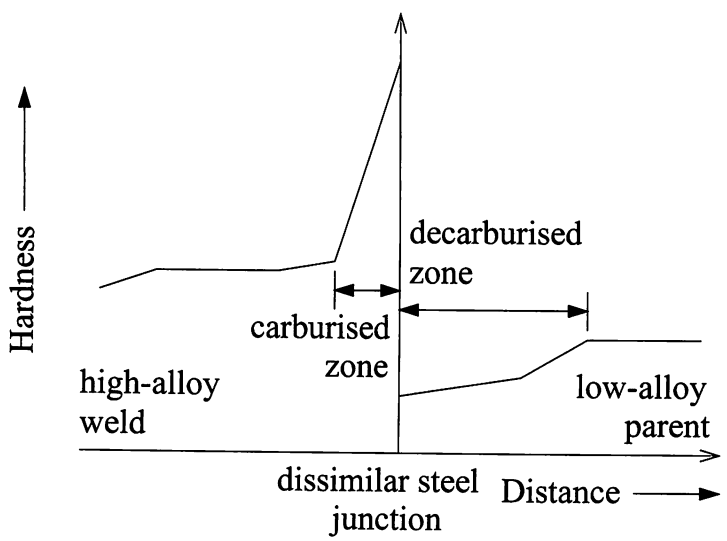

Figure 6.4 An illustration of the hardness profile across the weld junction following heat treatment of the weld.

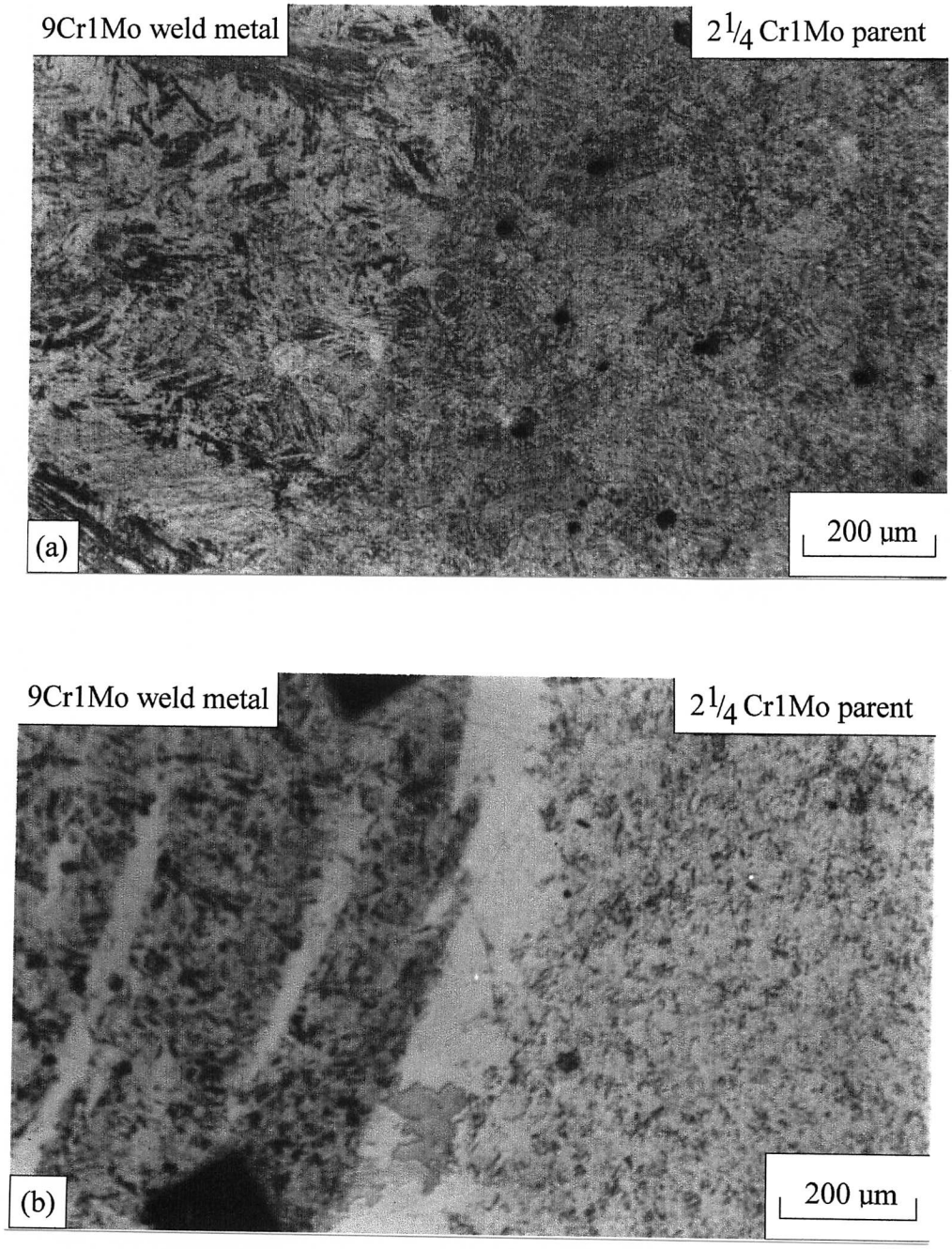

Figure 6.5 The fusion line between a 9Cr1Mo weld and a $2\frac{1}{4}$Cr1Mo parent steel; (a) no ageing and (b) PWHT for 3 h at 720 °C.

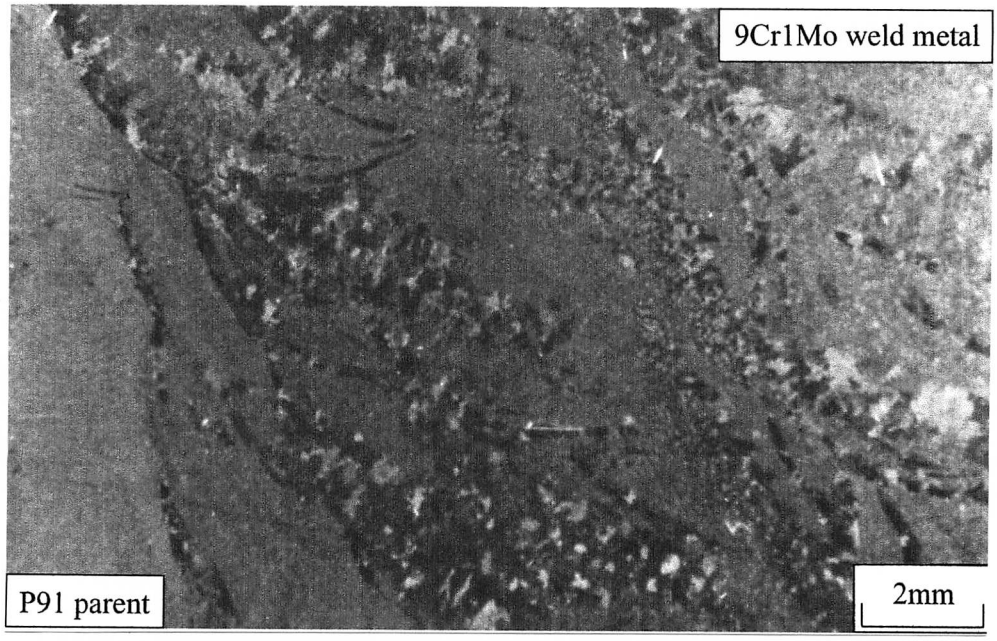

Figure 6.6 A macrograph inside the buttering layer of 9Cr1Mo steel deposited on a P91 parent steel after a PWHT of 3 h at 765 °C followed by 3 h at 720 °C, then aged for 77 h at 730 °C.

where the decarburised zone formed after ageing for 10 h at 650 °C was narrower than that formed after only 2 h at 730 °C.

Decarburised zones continue to grow with prolonged ageing, Figure 6.8. The optically measured decarburised zone widths for a 9Cr1Mo/$2\frac{1}{4}$Cr1Mo dissimilar steel weld are plotted as a function of time and temperature on Figure 6.9. The widths are similar after ageing at 600 and 650 °C but ageing at 730 °C clearly leads to a greater degree of carbon partitioning. The decarburised zones appear to be growing in proportion to $\sqrt{t}$.

The corresponding width of the carburised zone in the 9Cr1Mo weld metal is harder to measure accurately using optical metallography. There are no dramatic changes in microstructure other than the precipitation of fine carbides which cannot be resolved by optical microscopy. Microhardness tests were therefore used to characterise the carburised zones.

6.4 Microhardness measurements across the weld

Microhardness profiles were produced across the fusion line of the 9Cr1Mo/$2\frac{1}{4}$Cr1Mo dissimilar steel welds for all of the heat treatments given in Table 6.2, Figures 6.10 to 6.13. The traverses were taken across the mid-point of a weld bead and the error bars indicate one

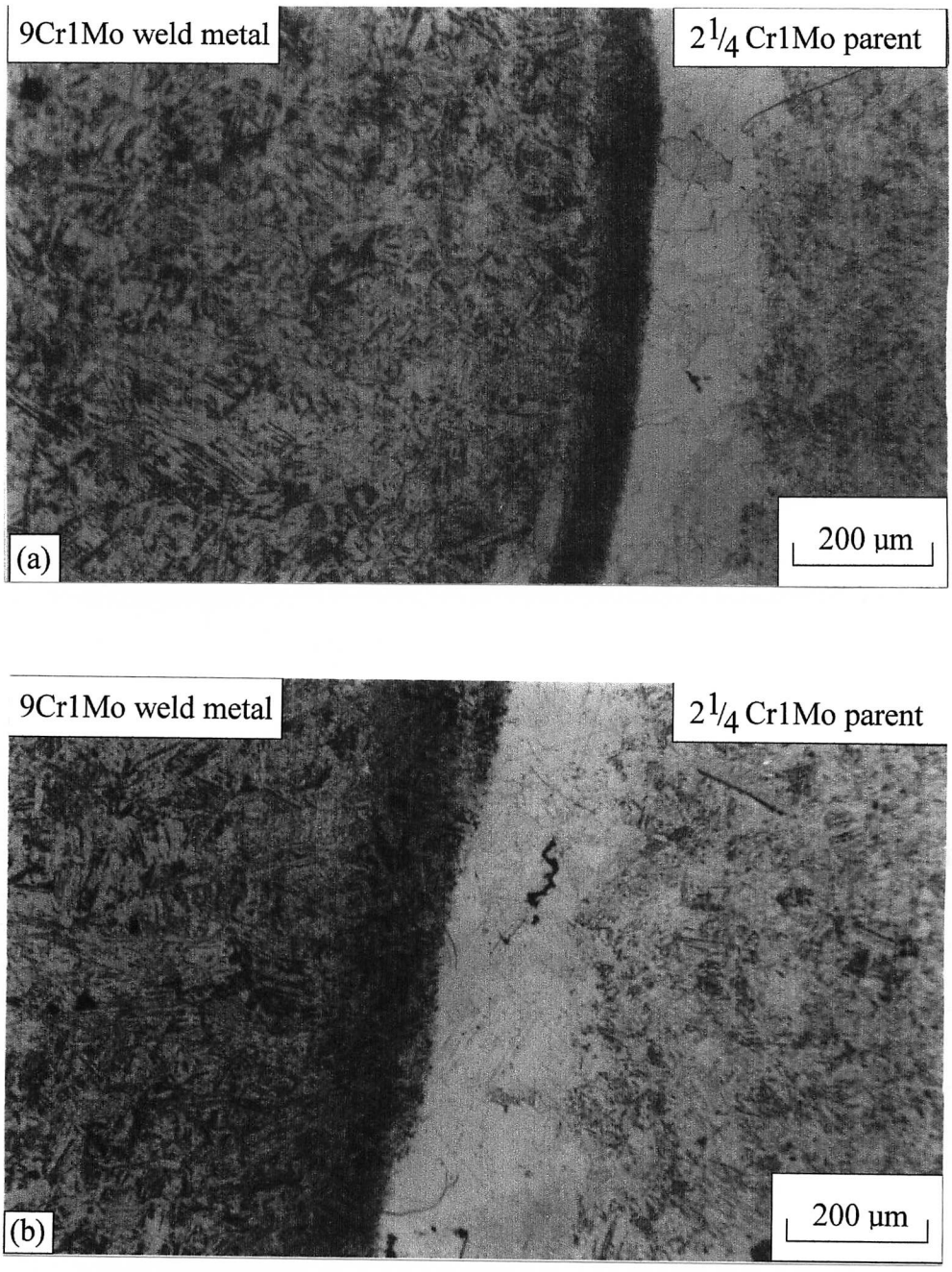

Figure 6.7 The fusion line between a 9Cr1Mo weld and a $2\frac{1}{4}$Cr1Mo parent steel; aged for (a) 10 h at 650 °C and (b) 2 h at 730 °C.

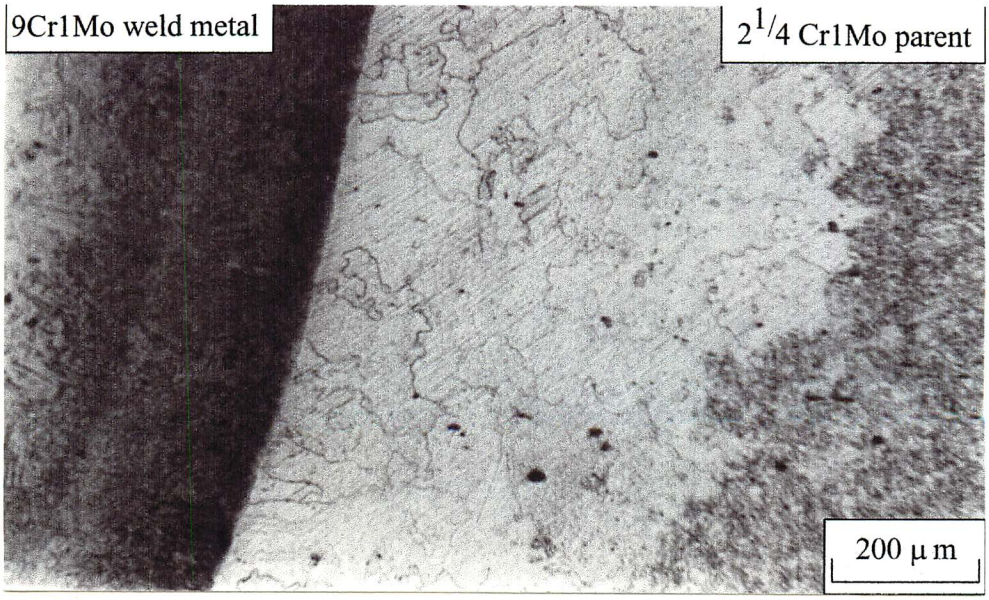

Figure 6.8 The fusion line between a 9Cr1Mo weld and a $2\frac{1}{4}$Cr1Mo parent steel aged for 1 000 h at 650 °C.

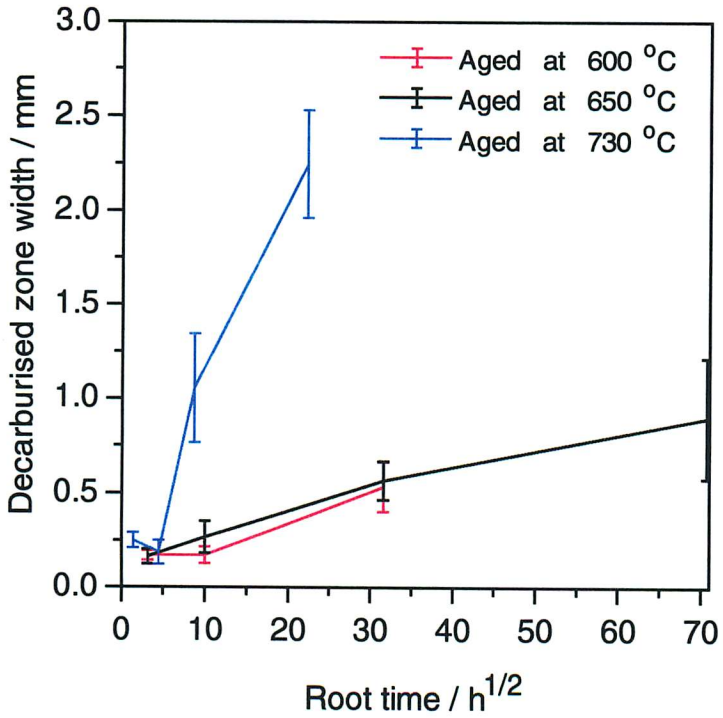

Figure 6.9 A plot to show the variation in decarburised zone widths in 9Cr1Mo/$2\frac{1}{4}$Cr1Mo dissimilar steel welds.

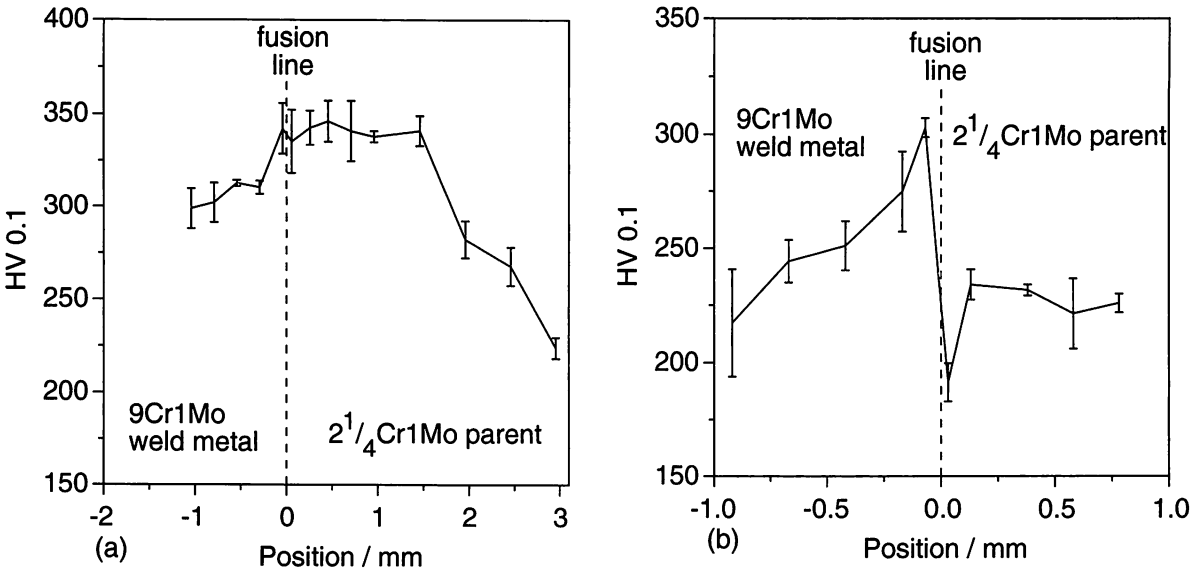

Figure 6.10 A P91/9Cr1Mo/2$\frac{1}{4}$Cr1Mo weld; (a) no post weld heat treatment, (b) post-weld heat treated for 3 h at 720 °C.

standard deviation.

After welding, and before the final PWHT, the hardness in the HAZ decreases away from the weld junction into the 2$\frac{1}{4}$Cr1Mo steel, Figure 6.10a. A PWHT for 3 h at 720 °C causes a minimum in hardness to form in the HAZ adjacent to the fusion line indicating the decarburised zone. There is also a peak in hardness corresponding to the carburised region.

This trend of decreasing hardness toward the fusion line on the low-alloy side, and away from the fusion line on the high-alloy side was reproduced for ageing the weld at 600 and 650 °C (Figures 6.11 and 6.12). Whereas the minimum in hardness in the decarburised zone decreased with time at these temperatures, at 730 °C it did not change, presumably due to the severity of the heat treatment, Figure 6.13. The carbide-free grains became elongated after 500 h at 730 °C, and are similar to those found in diffusion bonds aged for 10 000 h at 650 °C.

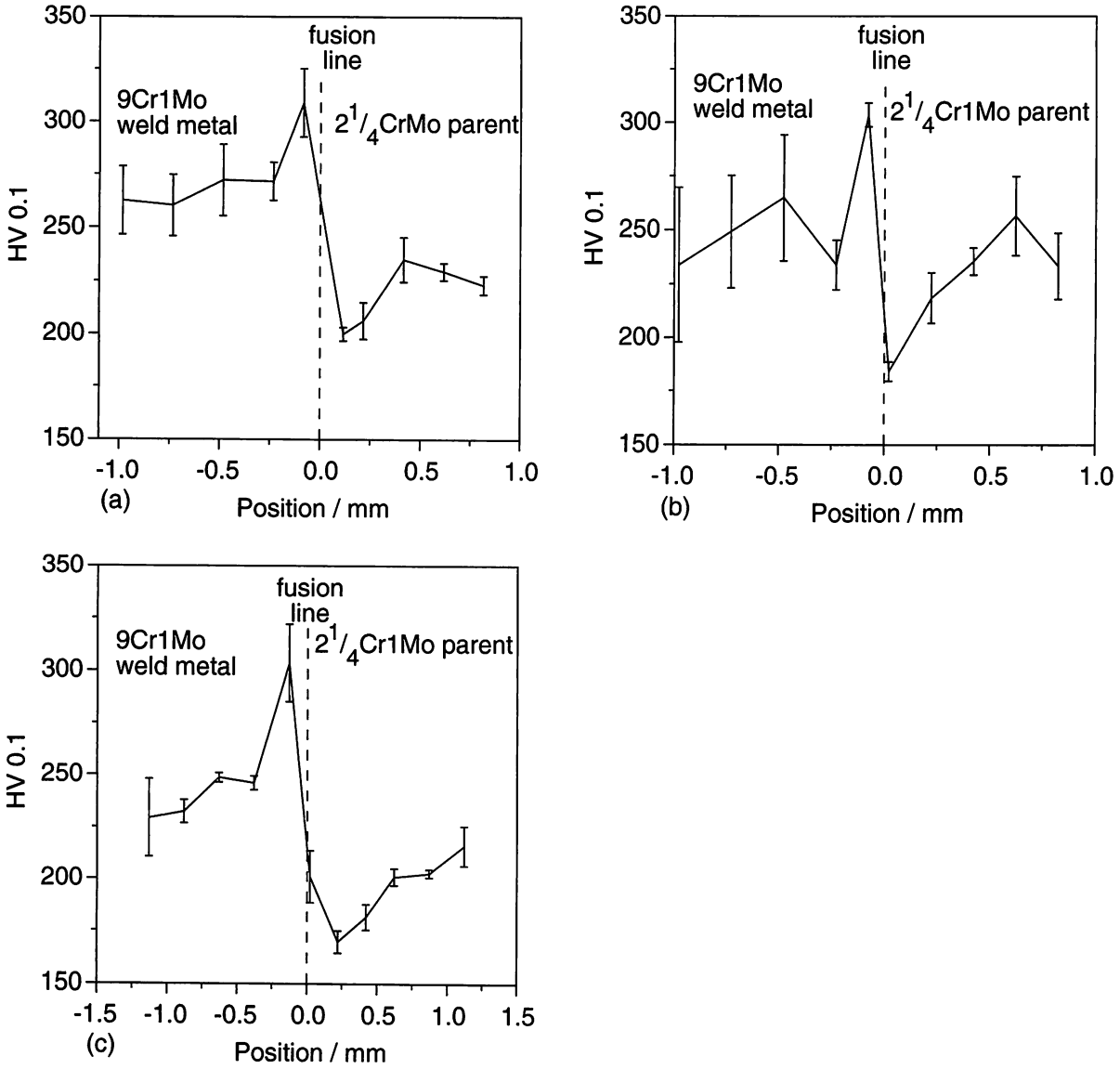

Figure 6.11 A P91/9Cr1Mo/2$\frac{1}{4}$Cr1Mo weld aged at 600 °C for; (a) 10 h, (b) 100 h and (c) 1 000 h.

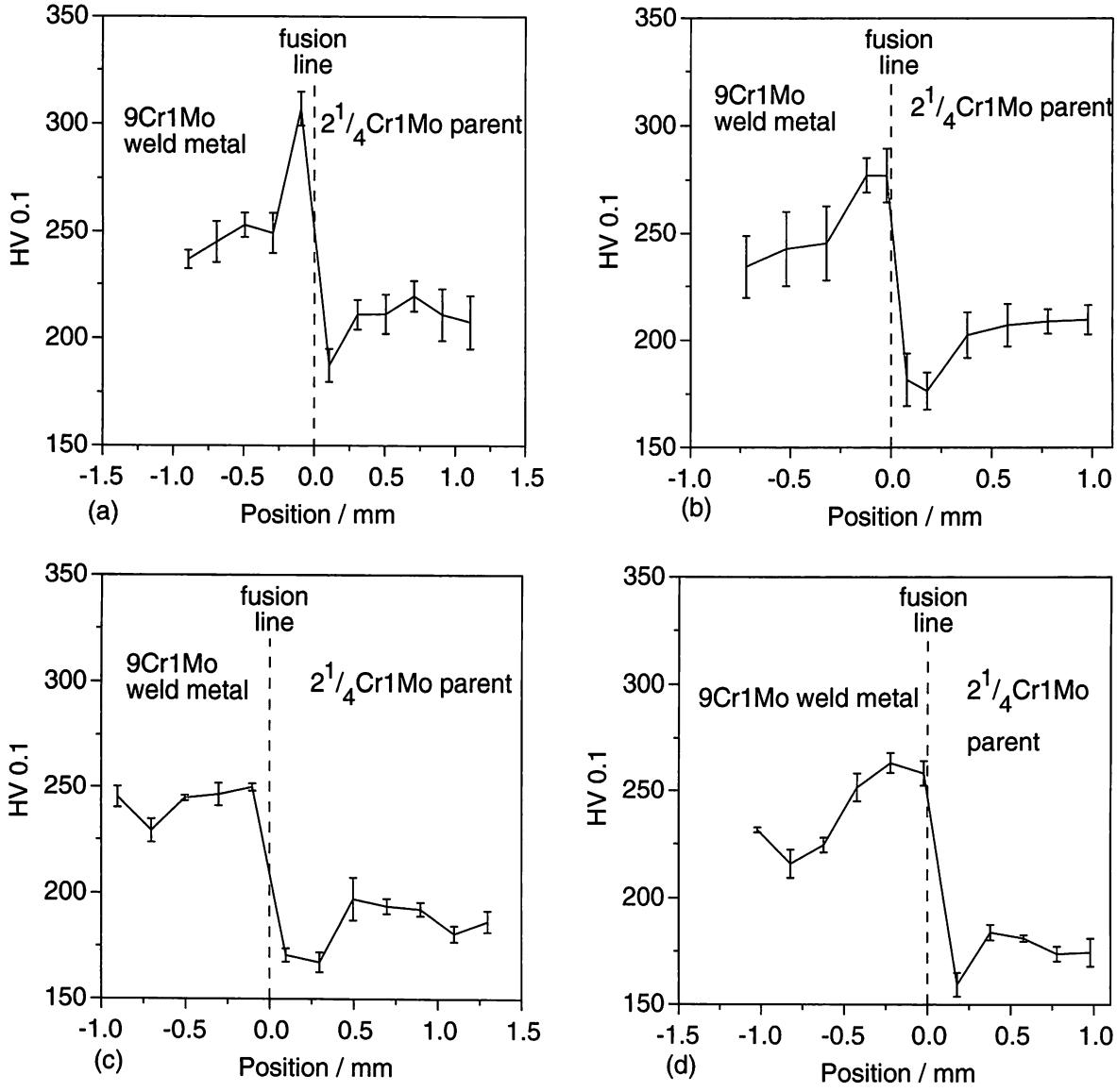

Figure 6.12 A P91/9Cr1Mo/2$\frac{1}{4}$Cr1Mo weld aged at 650 °C for; (a) 10 h, (b) 100 h, (c) 1 000 h and (d) 5 000 h.

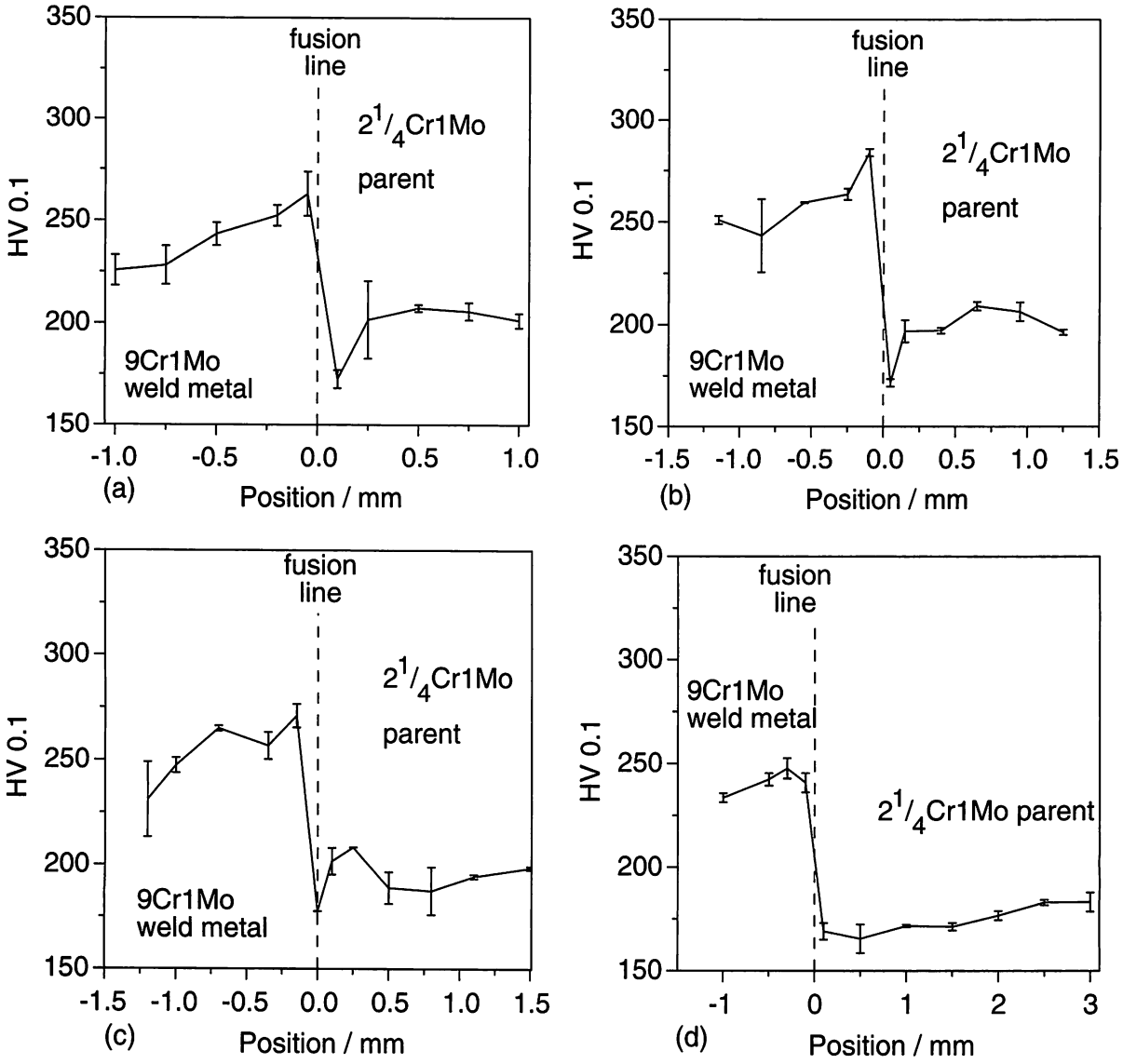

Figure 6.13 A P91/9Cr1Mo/$2\frac{1}{4}$Cr1Mo weld aged at 730 °C for; (a) 2 h, (b) 20 h, (c) 77 h and (d) 500 h.

6.5 Comparison with diffusion bonds

The heat treatments of the welds described in this chapter are similar to the diffusion bonds in Chapter 5.

No significant carbon partitioning could be observed in the as-welded condition, so there were no peaks or troughs in hardness across the fusion line. The final PWHT formed a decarburised zone some 0.17 ± 0.04 mm wide, which continued to grow during subsequent ageing.

In 9Cr1Mo/2$\frac{1}{4}$Cr1Mo dissimilar steel welds, the decarburised zone formed after 100 h at 650 °C was approximately 10 times larger than that in a P91/2$\frac{1}{4}$Cr1Mo bond. This was thought to be because of the PWHT given to the dissimilar steel welds only prior to ageing.

An estimate of the diffusion distance, x, is given by:

$$x \simeq \sqrt{D_C\, t} \tag{6.1}$$

When this was compared to the decarburised zone widths in the bonds and dissimilar steel welds, the diffusion distance was over-predicted by at least a factor of 10 for the shorter heat treatments and was less accurate for very long (10 000 h) or high temperature (above 700 °C) heat treatments. This shows that the crude random-walk estimation of diffusion distance is not representative of the situation in-hand.

At 700 °C and above, the decarburised zone was much wider than at 650 °C, compared with the similar amounts of carbon partitioning from 600 to 650 °C (cf. Figure 5.23 and 6.9 for the bonds and the welds respectively). For each temperature, the decarburised zone appeared to grow approximately linearly with $\sqrt{t}$. The deviation from linearity, reported by Race (1992) did not appear to be happening. However, the heat treatments used here are short-term, higher temperatures tests, and the departure from the square root time predictions may still occur after much longer term heat treatments. It was predicted that the growth of the decarburised zone would slow down at such a time when cementite reprecipitated in the high-alloy steel, causing the interface concentrations to change to such an extent that the respective carbon concentration gradients would level-off (Race, 1992). This effectively halts further diffusion into the steel.

After heat treating diffusion bonds, the carburised zones were almost equal in size to the decarburised zones. This was not seen in the dissimilar steel welds under the same conditions. This is thought to be due to the nature of welding and the dilution of steel in the weld causing composition gradients in the high-alloy weld metal, leading to a high inaccuracy of measurements, as the micrographs illustrate.

6.6 Summary

In this chapter, observations in the decarburised zone of a 9Cr1Mo/$2\frac{1}{4}$Cr1Mo dissimilar steel welds have been reported. The microstructures found were similar to those in diffusion bonds composed of the same steel and, as in the bonds, the decarburised zone width could not be predicted by a simple $x \simeq \sqrt{D_C\, t}$ relationship.

In the following chapter, similar metallographic observations are discussed for welds where the low-alloy steel contained vanadium.

Chapter Seven

Carbon Partitioning in Vanadium-Containing Welds

In Chapter 6, carbon partitioning across a 9Cr1Mo/$2\frac{1}{4}$Cr1Mo dissimilar steel welds was studied. However, in vanadium-containing transition welds taken from service in the power plant or aged in the laboratory, the formation of a decarburised zones during carbon diffusion is, by contrast, less well defined. This chapter deals with the characterisation of microstructures and the amount of carbon partitioning expected whilst ageing vanadium-bearing welds.

7.1 Introduction

Chromium–molybdenum–vanadium based ferritic steels are used extensively in the construction of power plant because of their ability to withstand high service temperatures. This inevitably means that they may form part of a weld with another steel. Carbon partitioning therefore occurs which has been indirectly associated with failures (Emerson & Hutchinson, 1952; Toft & Yeldham, 1972). When failures happen, $\frac{1}{2}$CrMoV steel pipes are sometimes replaced by $2\frac{1}{4}$Cr1Mo steels with transition joints being made using a 2CrMo or a 9Cr1Mo weld metal.

In the heat-affected zone (HAZ) of $\frac{1}{2}$CrMoV steel dissimilar weld, Type IIIa cracks were found after the weld had been in operating at 565 °C for many years in the power plant (Brett & Smith, 1998). It was speculated that Type IIIa cracks were associated with carbon depletion next to the fusion line (Brett, 1998). A further investigation in these welds showed that carbon loss actually occurred over an unexpectedly large area, beyond the HAZ. Another contribution to the initiation of Type IIIa cracks was attributed to the hard carburised zone in the weld metal adjacent to the carbon-free zone.

The microstructure and large amount of carbon diffusion in $\frac{1}{2}$CrMoV steels are different to those found in the decarburised zones of $2\frac{1}{4}$CrMo steel (aged under similar conditions).

7.2 Experimental procedure

The welds used are a $\frac{1}{2}$CrMoV steel pipe with a 2CrMo weld metal (Brett, 1998). The pipe and weld had been in service in a power plant for more than 109 000 h at 565 °C. The weld was deposited using manual metal arc (MMA) welding and the HAZ is about 2 – 3 mm wide.

Some accelerated ageing tests weld were also studied; the weld combinations and heat treatment are listed in the last three rows of Table 7.1.

Steel weld metal combination	Heat treatment
2CrMo/$\frac{1}{2}$CrMoV weld	109 000 h at 565 °C
9Cr1Mo/$\frac{1}{2}$CrMoV weld	504 h at 730 °C
9Cr1Mo/$\frac{1}{2}$CrMoV weld	1 000 h at 654 °C
9Cr1Mo/2$\frac{1}{4}$Cr1Mo weld	1 000 h at 650 °C
9Cr1Mo/2$\frac{1}{4}$Cr1MoV weld	1 000 h at 650 °C

Table 7.1 The combinations of steels used in this investigation, and their heat treatments.

Steel	C	S	P	Si	Mn	Ni	Cr	Mo	V
$\frac{1}{2}$CrMoV steel	0.12	0.031	0.023	0.24	0.56	0.06	0.45	0.51	0.23
2$\frac{1}{4}$Cr1Mo steel	0.11	0.019	0.021	0.27	0.52	0.04	2.22	0.90	0.005
2$\frac{1}{4}$Cr1MoV steel	0.15	0.002	0.007	0.01	0.53	0.16	2.34	0.99	0.27
9Cr1Mo weld	0.07	0.004	0.013	0.38	0.87	0.32	8.7	1.04	0.01

Table 7.2 The chemical compositions of the pipes and the weld metals used, wt. %

In the laboratory aged welds, the 9Cr1Mo weld metal was deposited by MMA welding onto the parent steel. KA82, the $\frac{1}{2}$CrMoV steel was ex-service (175 000 h at 565 °C) whereas the 2$\frac{1}{4}$Cr1Mo and 2$\frac{1}{4}$Cr1MoV steel were virgin steels. All of the aged welds in Table 7.1 were PWHT for 3 h at 720 °C. The compositions of the steels in the laboratory-aged dissimilar steel welds are listed in Table 7.2.

7.2.1 Carbon content analysis

Carbon partitioning studied in 2CrMo/$\frac{1}{2}$CrMoV welds was found to be on such a gross scale that it was possible to take 1 mm slices at approximately 5 mm intervals from the weld junction for chemical analysis (Brett, 1998). The slices are taken parallel to the weld fusion line, taking care to avoid the high carbon zone in the high-alloy weld, Figure 7.1.

The carbon concentration was determined commercially using a Leco CS46 carbon/sulphur apparatus. This involves the ignition of steel in a stream of oxygen in an induction furnace, using a tungsten flux. The resulting carbon dioxide is measured by infra-red absorption. The apparatus was calibrated with each use by means of a certified reference set of standard steels

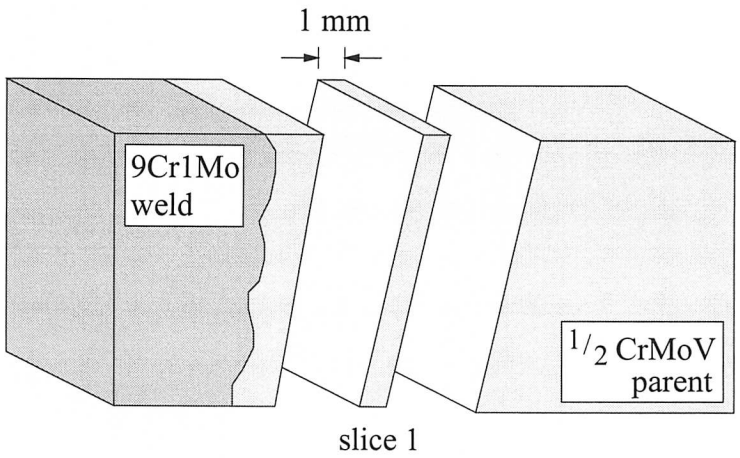

Figure 7.1 A slice of steel taken from a $\frac{1}{2}$CrMoV parent material, average weight of about 1.3 g.

of known carbon content.

All the welds listed in Table 7.1 were similarly analysed.

7.2.2 Microstructural characterisation

Hardness indentations were placed across the fusion boundary in an attempt to correlate the hardness with the carbon content. The corresponding microstructures were studied using optical microscopy, SEM and TEM. For optical and SEM metallography, the samples were ground to a 1200 grit and polished to a 1 μm finish. The 9Cr1Mo weld and $2\frac{1}{4}$CrMo parent were etched with Villela's Reagent to reveal the carbides. The 2CrMo weld metal and $\frac{1}{2}$CrMoV parent were etched using Nital.

TEM carbon extraction replicas were taken from carburised and some decarburised zones of the welds listed in Table 7.1 to identify carbides in the microstructure (see section 5.2.1).

The volume fraction of carbides in the carburised zone were estimated from SEM micrographs. All particles were counted regardless of shape or composition. Optical micrographs taken at known distances from the fusion line were used to measure the fraction of pearlite in the $\frac{1}{2}$CrMoV steel aged for 504 hours at 730 °C.

The pearlite colonies appeared to be randomly distributed in the ferrite microstructure. As these measurements were taken from random samples, it can be assumed that the area fraction is the same as the volume fraction (DeHoff, 1986). The standard error (*s.e.*) associated with

these measurements is:

$$s.e. = \frac{\sigma}{\sqrt{N}}$$

σ is the standard deviation in the distribution of area measurements, and N is the number of measurements.

7.3 Chemical and volume fraction analysis results

The chemically analysed carbon concentrations, as a function of position, are given in Table 7.3 and plotted on Figure 7.2. The discrepancy in the carbon concentrations reported in Tables 7.2 and 7.3 is due to the unreliable measurement of carbon content as part of a commercial compositional analysis, compared with the more accurate LECO method.

Distance from the fusion line / mm	**5**	**10**	**15**	**20**	**25**	**30**	**35**	**40**
2CrMo/$\frac{1}{2}$CrMoV, 109 000 h at 565 °C	0.075	0.088	0.105	0.112	0.11	0.114	0.113	0.113
9Cr1Mo/$\frac{1}{2}$CrMoV, 504 h at 730 °C	0.031	0.048	0.055	0.08	0.12	0.14	0.14	0.14
9Cr1Mo/$\frac{1}{2}$CrMoV, 1 000 h at 654 °C	0.06	0.12	0.12	0.12	0.12	0.12	0.12	
9Cr1Mo/2$\frac{1}{4}$Cr1Mo, 1 000 h at 650 °C	0.1	0.1	0.1	0.1	0.1	-	-	-
9Cr1Mo/2$\frac{1}{4}$Cr1MoV, 1 000 h at 650 °C	0.135	0.151	0.153	0.153	0.151	0.155	-	-

Table 7.3 The carbon concentration (wt. %) in the low-alloy steel away from the fusion line for each dissimilar steel weld combination. The error of the measurements is less than 1 % of the reported carbon content (Personal communication, Bodycote Materials Testing, 1999).

The affect of ageing 9Cr1Mo/$\frac{1}{2}$CrMoV welds at different temperatures is illustrated on Figure 7.2a. The difference in measured carbon concentration between 9Cr1Mo/2$\frac{1}{4}$Cr1Mo and 9Cr1Mo/$\frac{1}{2}$CrMoV welds is plainly illustrated on Figure 7.2b. There is clearly no concentration gradient in 2$\frac{1}{4}$Cr1Mo steel; in this weld a carbide-free zone was observed to be approximately 0.5 $\pm$ 0.1 mm wide.

Figure 7.2c shows that the 9Cr1Mo/$\frac{1}{2}$CrMoV combination is as susceptible to decarburisation as the 2CrMo/$\frac{1}{2}$CrMoV weld. Though the measured carbon concentration next to the weld is lower in the 9Cr1Mo/$\frac{1}{2}$CrMoV weld, ageing the 2CrMo/$\frac{1}{2}$CrMoV weld for 109 000 h at 565 °C caused a larger decarburised zone to form.

The addition of vanadium to 2$\frac{1}{4}$Cr1Mo steel seems to promote the partitioning of carbon (Figure 7.2d), although the effect is not as potent as in $\frac{1}{2}$CrMoV steel.

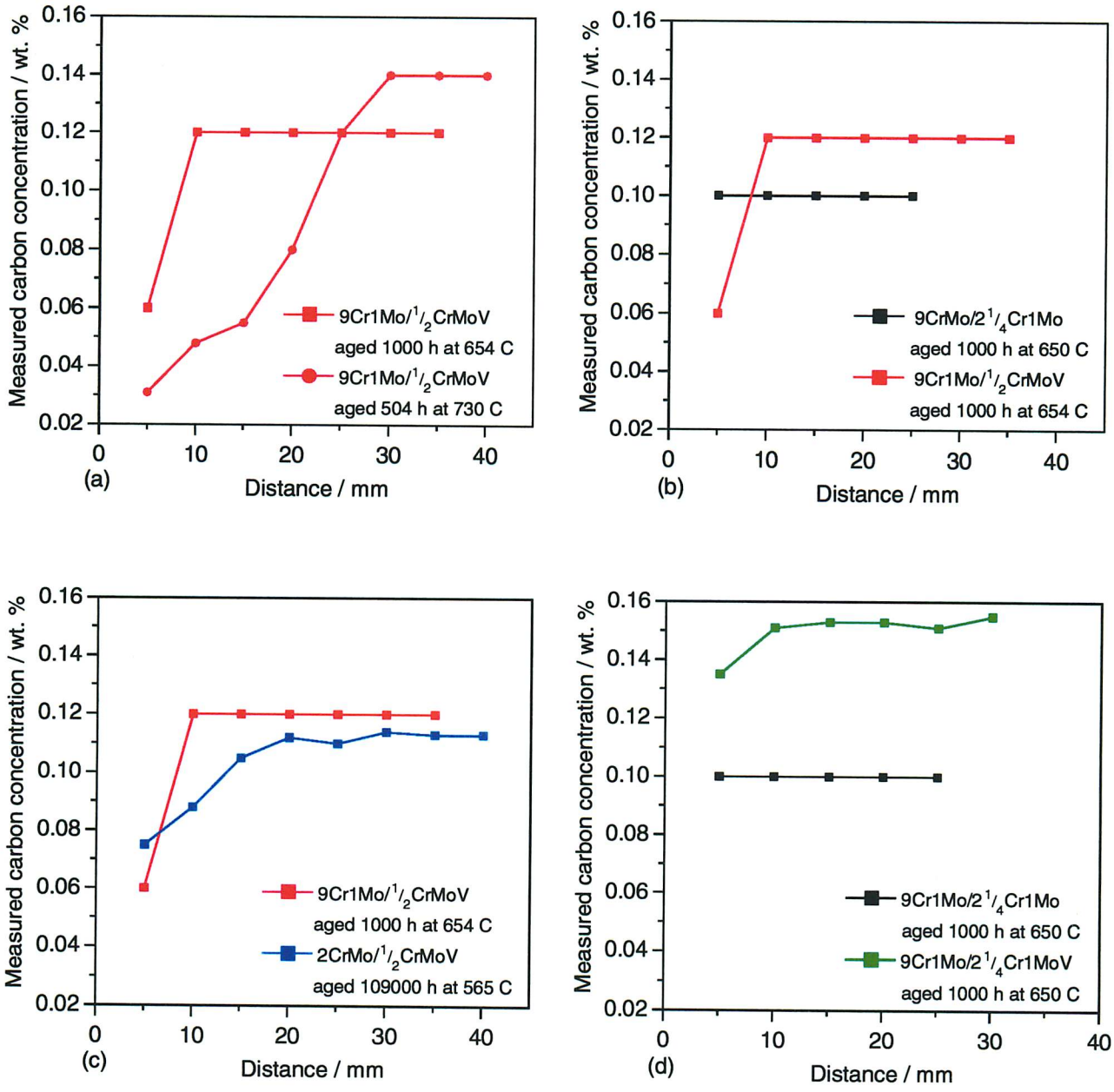

Figure 7.2 Carbon concentration as a function of distance from the weld junction in the low-alloy steel of the dissimilar steel welds given in Table 7.1; (a) 9Cr1Mo/$\frac{1}{2}$CrMoV welds aged at 650 and 730 °C, (b) 9Cr1Mo/2$\frac{1}{4}$Cr1Mo & 9Cr1Mo/$\frac{1}{2}$CrMoV welds aged at 650 °C, (c) 9Cr1Mo/$\frac{1}{2}$CrMoV & 2CrMo/$\frac{1}{2}$CrMoV welds aged at 650 °C, (d) 9Cr1Mo/2$\frac{1}{4}$Cr1Mo & 9Cr1Mo/2$\frac{1}{4}$Cr1MoV welds.

The estimated carbon concentration gradients adjacent to the weld junctions from Table 7.1 are calculated using the method outlined in section 5.2.3 (Figure 7.3). At 730 °C, more carbon diffusion can be expected compared with ageing at 650 °C. In the 9Cr1Mo/$2\frac{1}{4}$Cr1Mo weld, the small difference between the interface and the far field concentrations implies a smaller amount of carbon partitioning, *c.f.* Figure 7.2b. The steeper concentration gradients for the 9Cr1Mo/$\frac{1}{2}$CrMoV weld compared with the 2CrMo/$\frac{1}{2}$CrMoV joint indicate the greater tendency for carbon to partition.

The measured carbon concentration profiles on Figure 7.2 are confirmed by Figure 7.3. Since steep concentration gradients exist in the vanadium-bearing steel, long-range carbon diffusion can be expected. It is interesting to note that none of the vanadium-steels showed large, carbide-free ferrite grains in the decarburised zone, probably due to the occurrence of vanadium carbide in the microstructure.

In the 9Cr1Mo/$\frac{1}{2}$CrMoV dissimilar steel weld aged for 504 h at 730 °C, the microstructure of the low-alloy steel was a mixture of ferrite and pearlite. Using SteCal (1989), a computer program which uses empirical formulae to calculate the properties of low-alloy steels, the Ac_1 temperature of $\frac{1}{2}$CrMoV steel, found using the equation due to Andrews (1965), was 731 °C. Therefore, due to experimental error in temperature measurement whilst ageing 9Cr1Mo/$\frac{1}{2}$CrMoV weld at 730 °C, it is likely that the steel was heated into the austenite range forming ferrite and pearlite on cooling.

The fraction of pearlite as a function of distance from the weld junction is listed on Table 7.4 and plotted on Figure 7.4. Naturally, the pearlite fraction decreases as the weld junction is approached.

Figure 7.5 shows some pearlite colonies located 15 mm from the 9Cr1Mo/$\frac{1}{2}$CrMoV junction. As a result of welding and heat treatment, the pearlite had started to spherodise before dissolving to release carbon.

Alloy carbides present in the microstructure of $\frac{1}{2}$CrMoV are more stable than cementite. Cementite appears to be the carbide most energetically favourable for dissolution, and releases carbon for diffusion. Therefore, during carbon partitioning, carbon is sought from undissolved cementite further away from the dissimilar steel interface. This long-range diffusion of carbon was not seen in low-alloy steels without vanadium. Chromium carbides in the high-alloy steel dissolve fully to form a carbide-free zone.

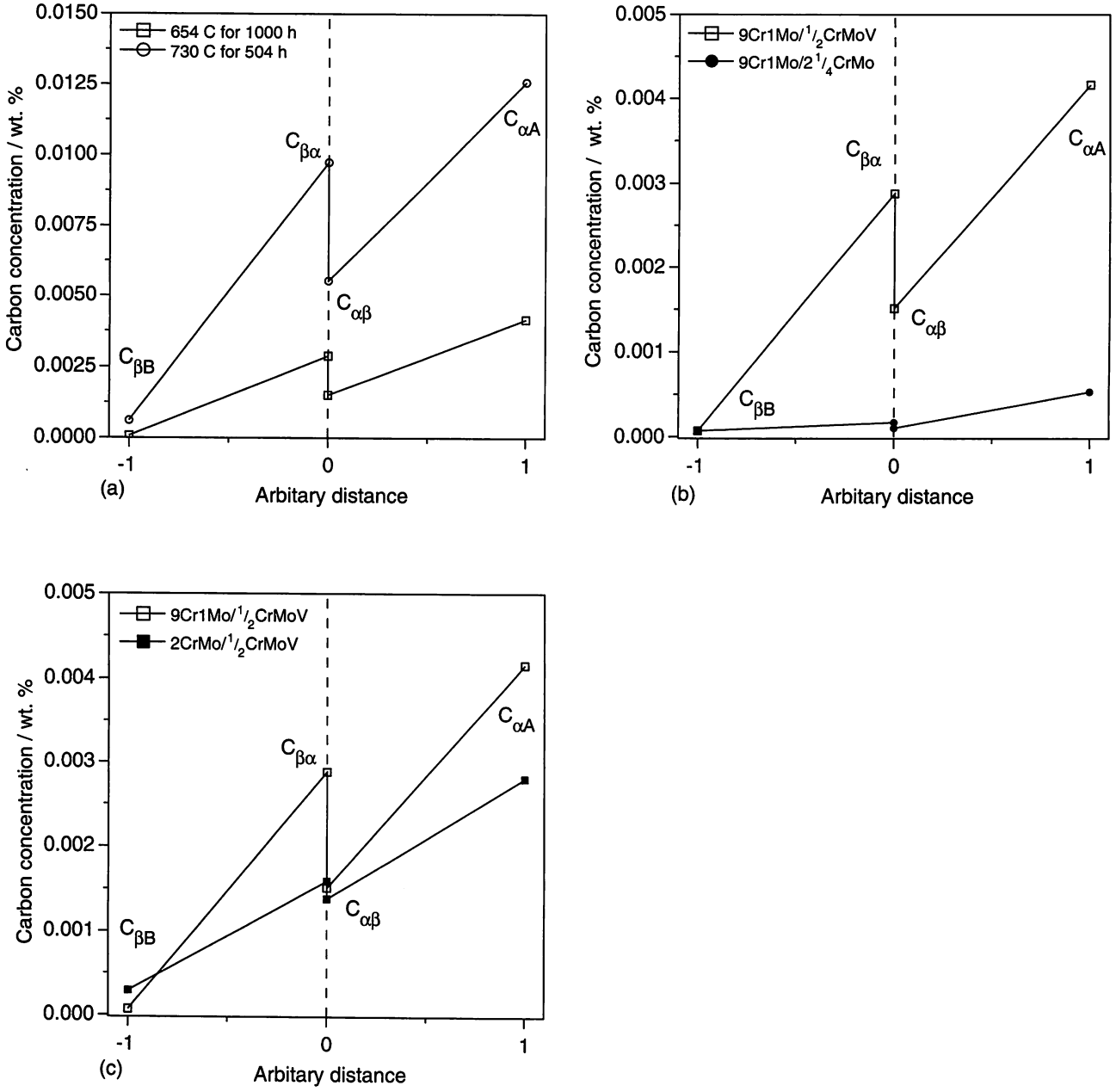

Figure 7.3 Carbon concentration gradients in dissimilar steel welds; (a) comparison between 9Cr1Mo/$\frac{1}{2}$CrMoV welds aged at 650 and 730 °C, (b) comparison between a 9Cr1Mo/$\frac{1}{2}$CrMoV and 9Cr1Mo/2$\frac{1}{4}$CrMo weld, aged at 650 °C, (c) comparison between a 9Cr1Mo/$\frac{1}{2}$CrMoV and 2CrMo/$\frac{1}{2}$CrMoV weld, aged at 650 and 565 °C respectively.

Distance from the fusion line / mm	Volume fraction
5 - 10	0
10 - 15	0.08 $\pm$ 0.01
15 - 20	0.12 $\pm$ 0.03
20 - 25	0.14 $\pm$ 0.02
25 - 30	0.16 $\pm$ 0.02
30 - 35	0.17 $\pm$ 0.01
35 - 40	0.19 $\pm$ 0.01

Table 7.4 The measured volume fraction of pearlite colonies found in a $\frac{1}{2}$CrMoV steel with a 9Cr1Mo weld metal, aged for 504 h at 730 °C.

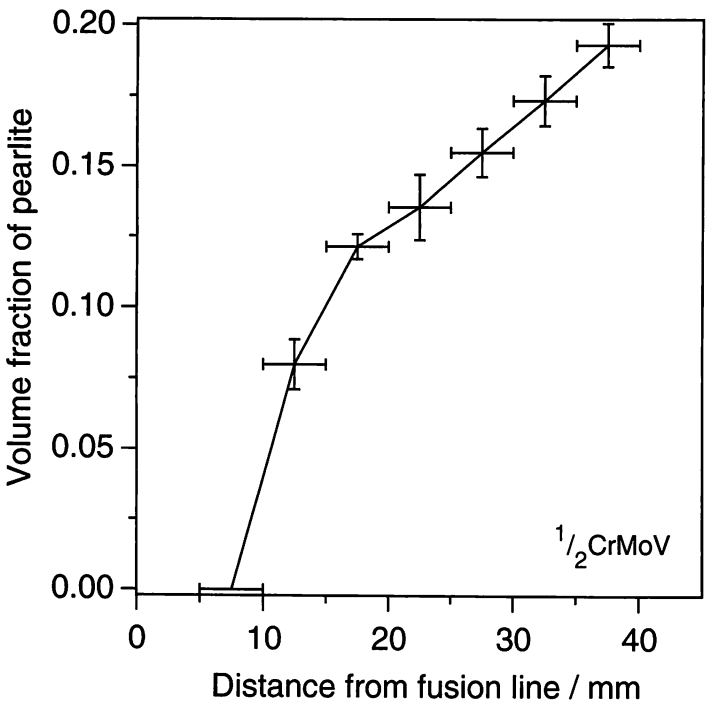

Figure 7.4 Volume fraction of pearlite colonies in a 9Cr1Mo/$\frac{1}{2}$CrMoV dissimilar steel weld aged for 504 h at 730 °C. The horizontal bars represent the width of the sample (5 mm) from which the measurements were taken, the vertical error bars are one standard deviation of the average measured value.

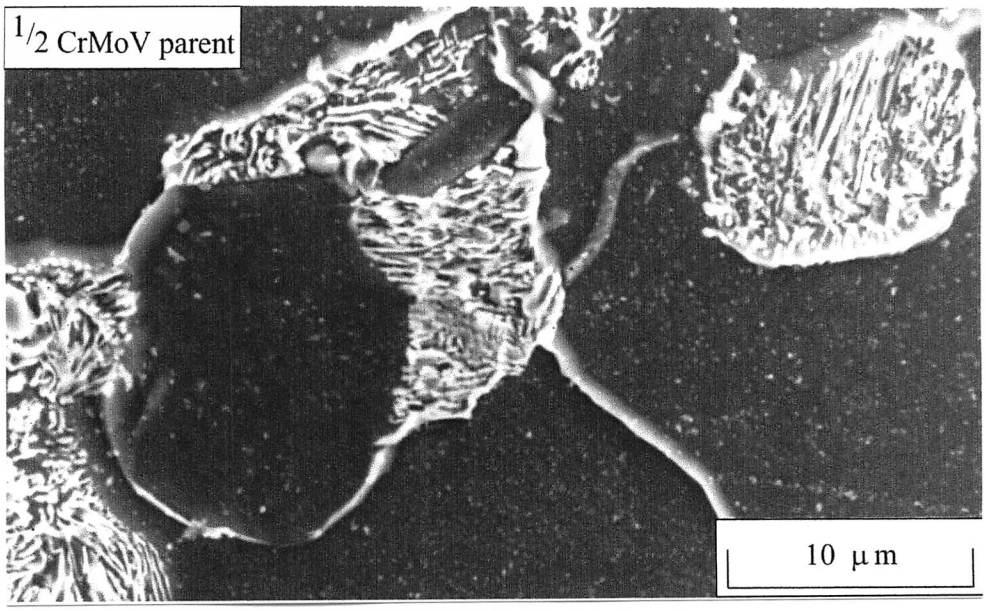

Figure 7.5 A SEM micrograph of pearlite colonies found in $\frac{1}{2}$CrMoV steel 15 mm from the 9Cr1Mo weld junction, aged for 1 000 h at 654 °C.

Distance from weld junction	**9Cr1Mo/$\frac{1}{2}$CrMoV 504 h 730 °C**	**9Cr1Mo/$\frac{1}{2}$CrMoV 1 000 h 654 °C**	**2CrMo/$\frac{1}{2}$CrMoV 109 000h 565 °C**
(mm)	(HV10)	(HV10)	(HV10)
5	124	142	161
10	119	138	159
15	130	132	160
20	128	136	162
25	128	142	-
30	128	138	-
35	128	136	-
40	128	134	-

Table 7.5 The measured macro-hardness in the $\frac{1}{2}$CrMoV steel of the dissimilar steel welds.

7.4 Hardness traverses

The experimental data listed in Table 7.5 show there is little variation in hardness within the $\frac{1}{2}$CrMoV steel where long-range decarburisation has occurred. Microhardness (HV0.1) traverses across the weld junction revealed hardness peaks in the 9Cr1Mo weld. However, a minimum in hardness was only seen in the $2\frac{1}{4}$Cr1Mo steel, Figure 7.6.

Unfortunately, the welds were not protected against surface decarburisation during ageing and this was found to affect the hardness of the steel, the measured volume fraction of pearlite and carbon concentration. Therefore measurements taken too near the edges can be unreliable.

7.5 Optical metallography

Welds containing $\frac{1}{2}$CrMoV steel (or to a lesser extent $2\frac{1}{4}$CrMoV steel) can show long-range decarburisation anything up to 30 mm from the weld junction. It was, however, impossible to optically measure the decarburised zones since there were no regions of total carbide dissolution or coarse grains.

A carburised layer can be observed in the high-alloy welds, implying carbon diffusion; however, this was difficult to measure. Higher resolution microscopy must be used to quantify the effects of carbon partitioning on a finer scale.

7.6 SEM

Scanning electron microscopy at the fusion line of dissimilar steel welds illustrated the carbide distribution in the carburised zone and also the carbides which persist in the decarburised zone. Figure 7.7 shows micrographs at the weld junctions of the dissimilar steel welds listed in Table 7.1. It clearly is difficult to determine the exact position of the weld fusion line, unlike in the bonds describe in Chapter 5.

Three types of carbide-free grains can be seen in the HAZ of the 9Cr1Mo/$\frac{1}{2}$CrMoV weld, Figure 7.8. Just below the weld metal, there is a layer of parallel sided grains, perpendicular to the fusion line, shown at a higher magnification on Figure 7.9. During welding, solidification occurs epitaxially on a partially melted substrate (Fasching *et al.*, 1995; Kou, 1989). These partially-melted '*edge*' grains are thought to be the first decarburised grains in the HAZ after heat treatment. The size of the regions containing either small or extremely large equiaxed grains in the HAZ depend on their relation to the multi-pass weld where the final grain size is a function of the peak temperature to which it has been exposed and the rate of heating and cooling.

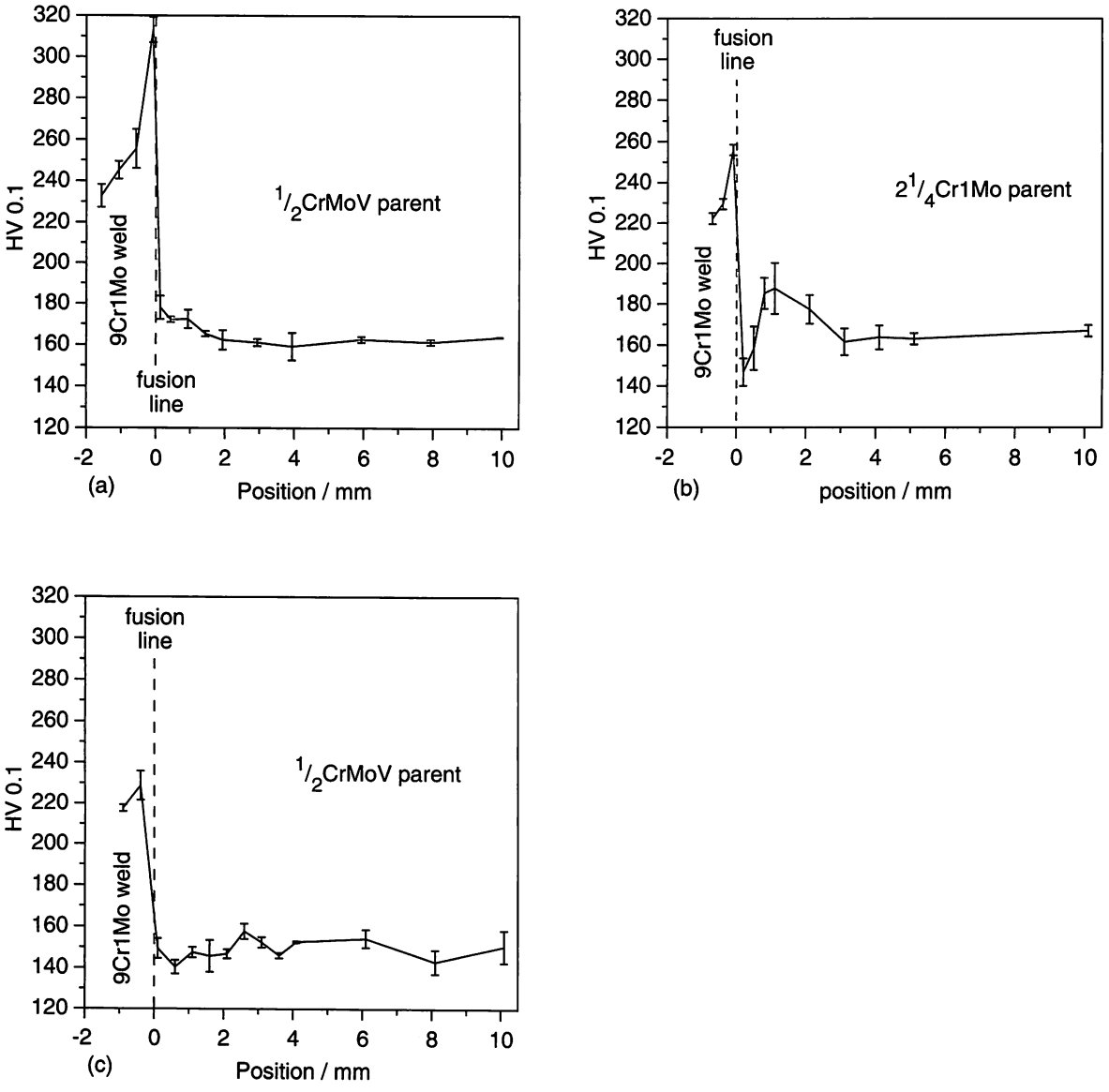

Figure 7.6 Microhardness HV0.1 traverse across an (a) 9Cr1Mo/$\frac{1}{2}$CrMoV and (b) 9Cr1Mo/$2\frac{1}{4}$Cr1Mo welds aged for 1 000 h at 650 °C, and (c) 9Cr1Mo/$\frac{1}{2}$CrMoV weld aged for 504 h at 730 °C.

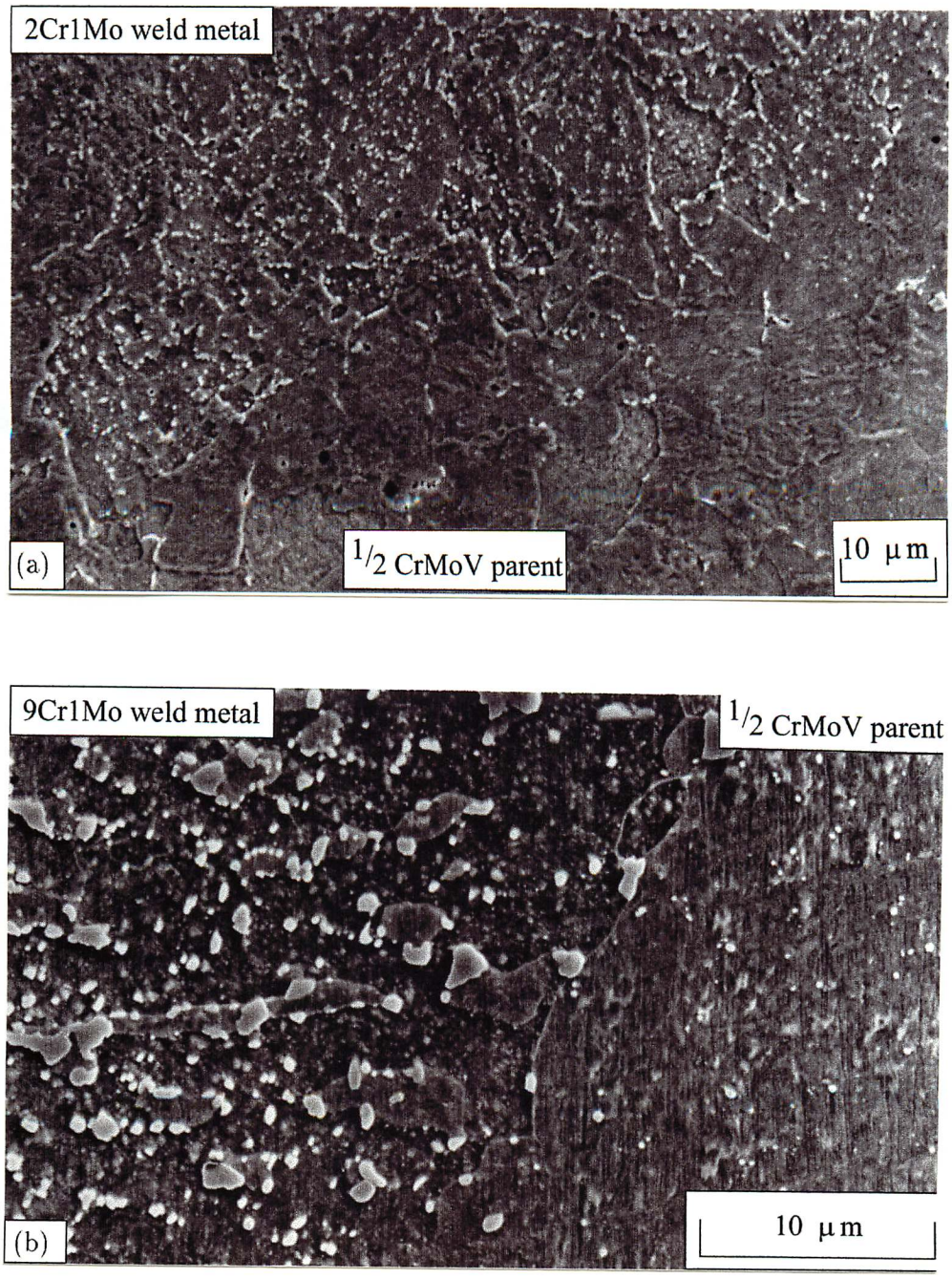

Figure 7.7 SEM micrographs at the fusion line of a; (a) 2CrMo/$\frac{1}{2}$CrMoV weld, 109 000 h at 565 °C; (b) 9Cr1Mo/$\frac{1}{2}$CrMoV weld, 504 h at 730 °C; (c) 9Cr1Mo/2$\frac{1}{4}$Cr1Mo weld and (d) 9Cr1Mo/2$\frac{1}{4}$Cr1MoV weld, 1 000 h at 650 °C.

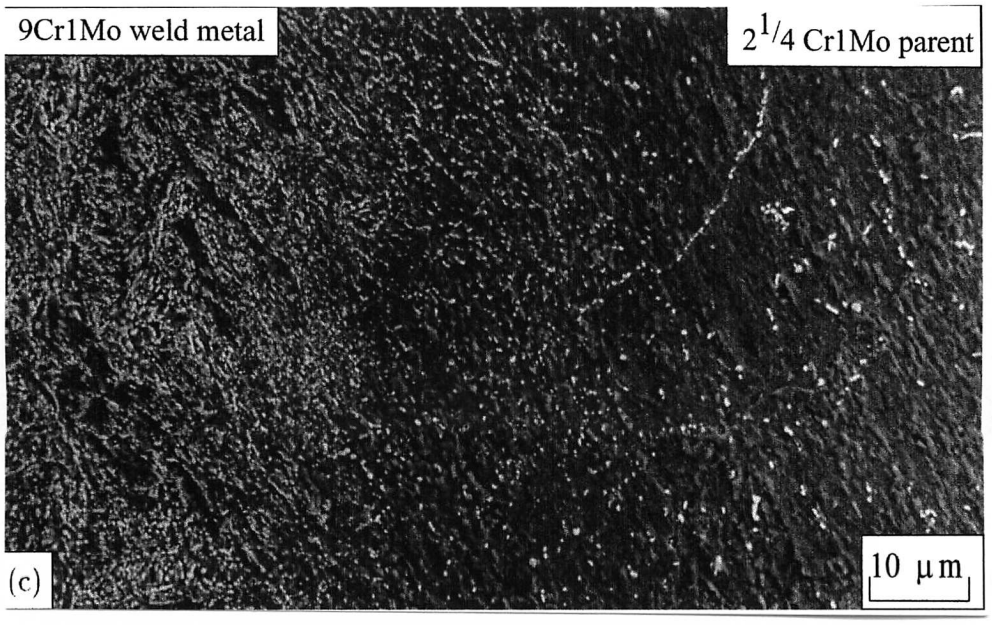

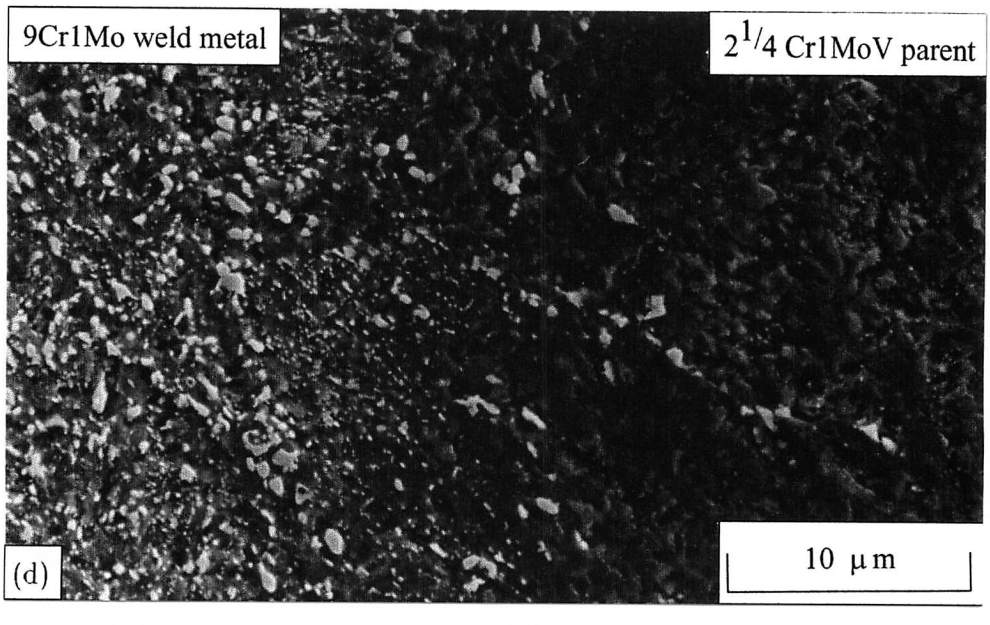

Figure 7.7 SEM micrographs at the fusion line of a; (a) 2CrMo/$\frac{1}{2}$CrMoV weld, 109 000 h at 565 °C; (b) 9Cr1Mo/$\frac{1}{2}$CrMoV weld, 504 h at 730 °C; (c) 9Cr1Mo/$2\frac{1}{4}$Cr1Mo weld and (d) 9Cr1Mo/$2\frac{1}{4}$Cr1MoV weld, 1 000 h at 650 °C.

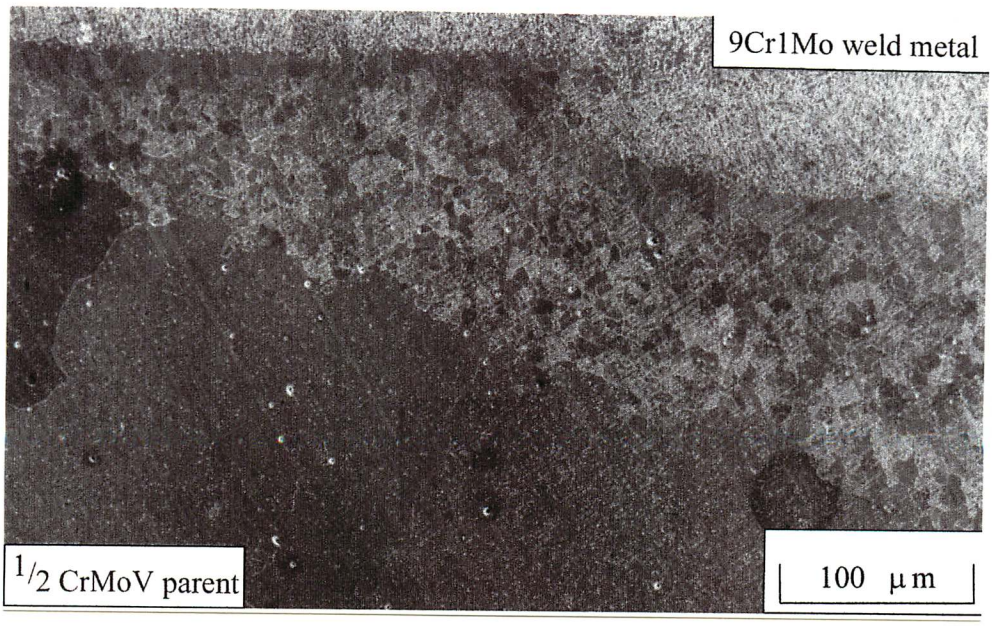

Figure 7.8 Low magnification SEM micrograph at the fusion line of a 9Cr1Mo/$\frac{1}{2}$CrMoV dissimilar steel weld aged for 504 h at 730 °C.

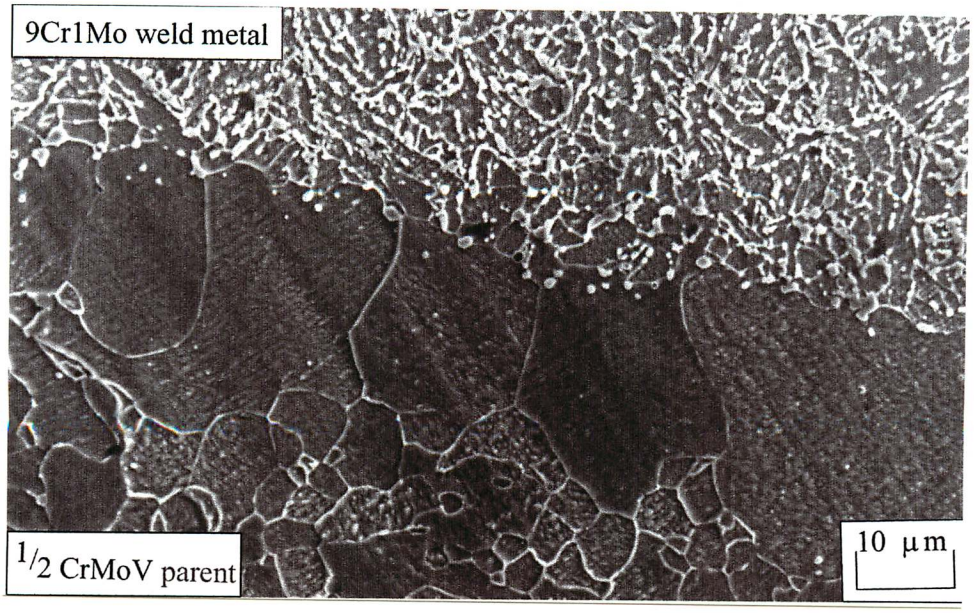

Figure 7.9 Detail of '*edge*' grains next to the weld metal in a 9Cr1Mo/$\frac{1}{2}$CrMoV dissimilar steel weld aged for 504 h at 730 °C.

Figure 7.10 shows high magnification SEM micrographs in the carburised layer of a 9Cr1Mo weld metal. The carbides found in the carburised zone adjacent to a $\frac{1}{2}$CrMoV low-alloy parent steel are generally coarse consistent with the extent of carbon partitioning.

Within the carburised zone in the high-alloy weld metal, the volume fraction of carbide particles was found to be a function of the weld metal composition, and to a lesser extent the low-alloy steel composition, amount of carbon partitioning or temperature, Table 7.6.

The carbide volume fractions in the carburised zones of high-alloy welds are less than those found in similar diffusion bonds, Table 5.6. This may be due to dilution during welding.

7.7 TEM

Low magnification TEM micrographs were taken in the carburised zones of the dissimilar steel welds to illustrate the carbide distribution, Figure 7.11. The carbides in the 9Cr1Mo carburised zone are smaller than those found in the 2CrMo weld. This was not surprising because the latter has had a much longer term ageing during service. Most of the carbides were found to lie along ferrite grain boundaries, and in the higher alloy steel, many carbides also appear to precipitate intergranulary.

Figure 7.12 is a low magnification TEM micrograph in decarburised zone of 9Cr1Mo/$\frac{1}{2}$CrMoV weld aged for 504 h at 730 °C. Here, only a few carbides remain on the ferrite grain boundaries in the decarburised steel.

The carbides in the carburised and decarburised zones which were identified using diffraction are presented in Table 7.7.

Cementite particles were found in the carburised zones of 2CrMo/$\frac{1}{2}$CrMoV and 9Cr1Mo/$\frac{1}{2}$CrMoV welds, Figure 7.13 and 7.14. Using MTDATA (and allowing: ferrite, austenite, cementite, M_2C, $M_{23}C_6$, M_7C_3 and vanadium carbide to be present), Figure 7.15 shows that it is thermodynamically possible to re-precipitate cementite in the weld metals if the carbon content of the steel is raised above 0.06 wt. % in the 2CrMo weld at 565 °C or above 2 wt. % in the 9Cr1Mo weld. Comparing Figure 7.15 with Table 7.6 shows that the measured carbide fractions in the carburised zones show good agreement with the quantitative data predicted by MTDATA as the carbon content of the steel is increased.

In the carburised zones of 9Cr1Mo weld metal, M_7C_3 and M_2C carbides are commonly found adjacent to a $2\frac{1}{4}$Cr1Mo or $2\frac{1}{4}$Cr1MoV steel, Figures 7.16 and 7.17.

In the 9Cr1Mo/$\frac{1}{2}$CrMoV and 9Cr1Mo/$2\frac{1}{4}$Cr1Mo aged welds, TEM replicas were also taken

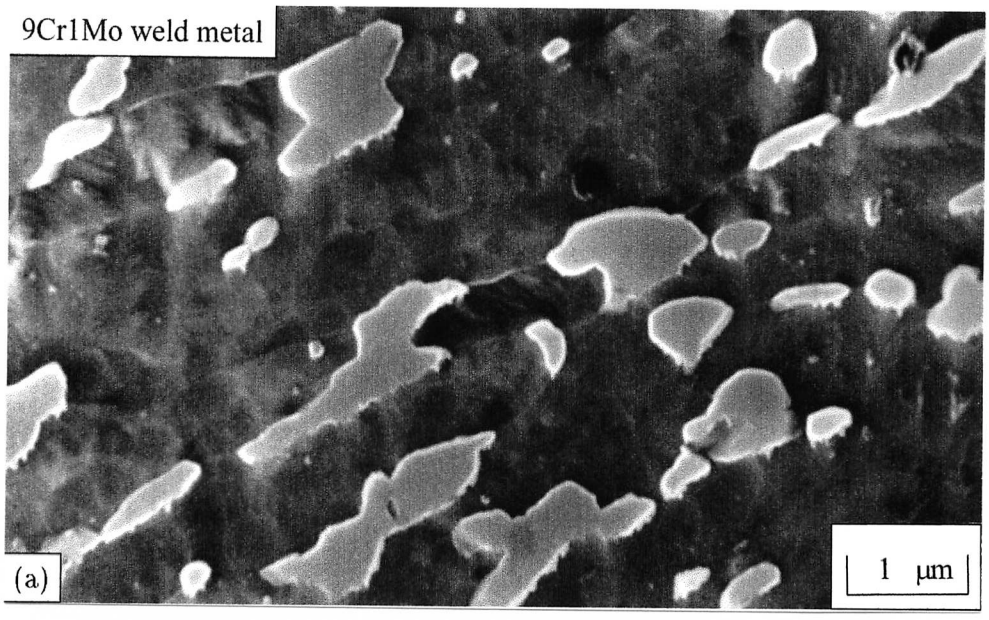

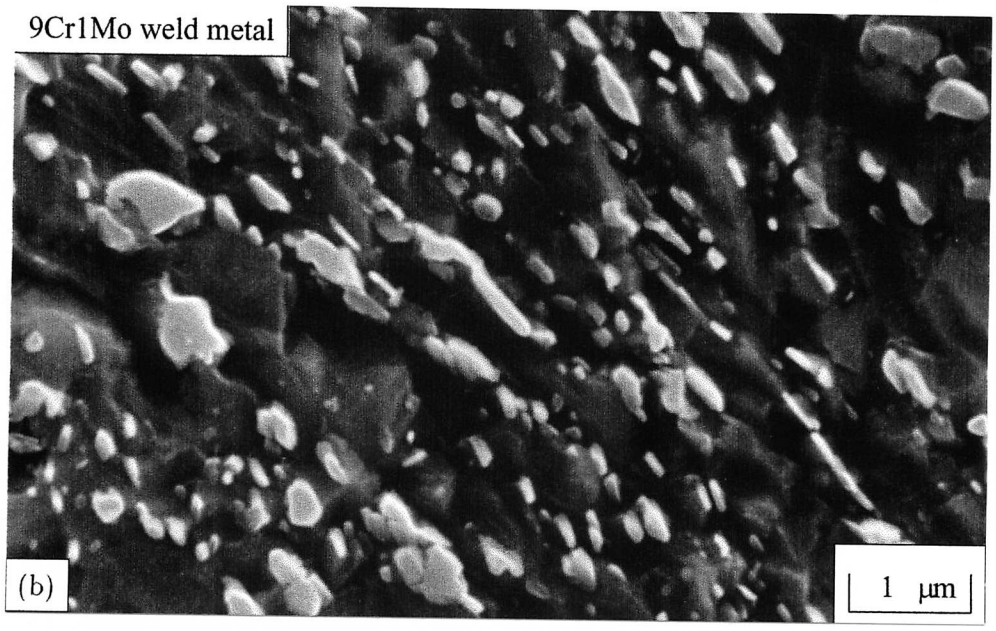

Figure 7.10 SEM micrographs in the carburised zone of a; (a) 9CrMo/$\frac{1}{2}$CrMoV weld, 504 h at 730 °C; (b) 9Cr1Mo/2$\frac{1}{4}$Cr1Mo weld and (c) 9Cr1Mo/2$\frac{1}{4}$Cr1MoV weld, 1 000 h 650 °C.

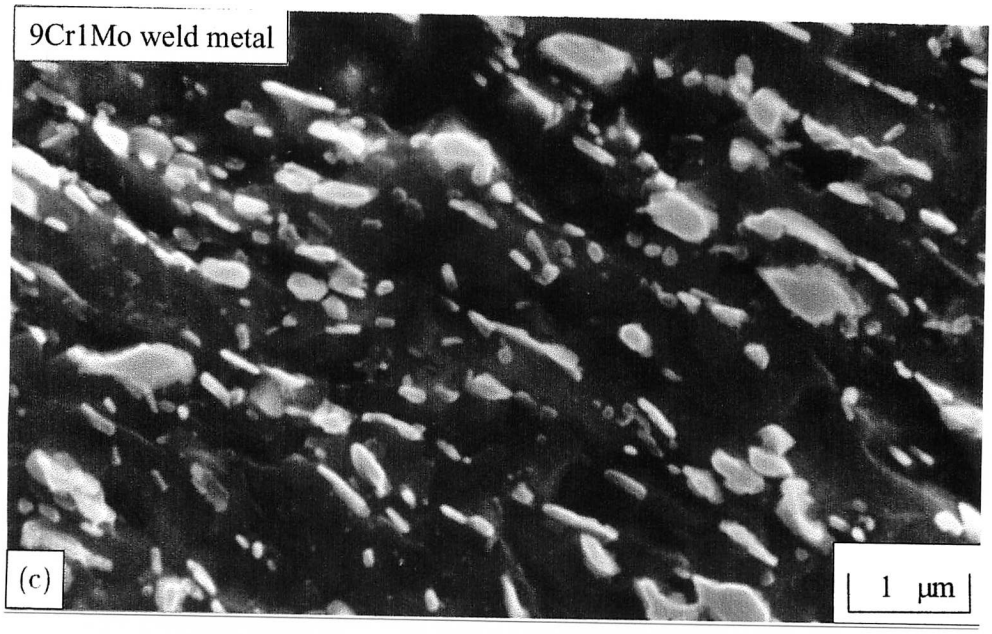

Figure 7.10 SEM micrographs in the carburised zone of a; (a) 9CrMo/$\frac{1}{2}$CrMoV weld, 504 h at 730 °C; (b) 9Cr1Mo/2$\frac{1}{4}$Cr1Mo weld and (c) 9Cr1Mo/2$\frac{1}{4}$Cr1MoV weld, 1 000 h 650 °C.

Dissimilar steel weld	**Heat treatment**	**Volume fraction of carbides**
2CrMo/$\frac{1}{2}$CrMoV weld	109 000 h at 565 °C	0.097 $\pm$ 0.018
9Cr1Mo/$\frac{1}{2}$CrMoV weld	504 h at 730 °C	0.18 $\pm$ 0.008
9Cr1Mo/2$\frac{1}{4}$Cr1Mo weld	1 000 h at 650 °C	0.18 $\pm$ 0.013
9Cr1Mo/2$\frac{1}{4}$Cr1MoV weld	1 000 h at 650 °C	0.18 $\pm$ 0.0026

Table 7.6 The SEM measured volume fraction of carbides in the carburised zone in the high-alloy weld metal, taken close to the weld junction.

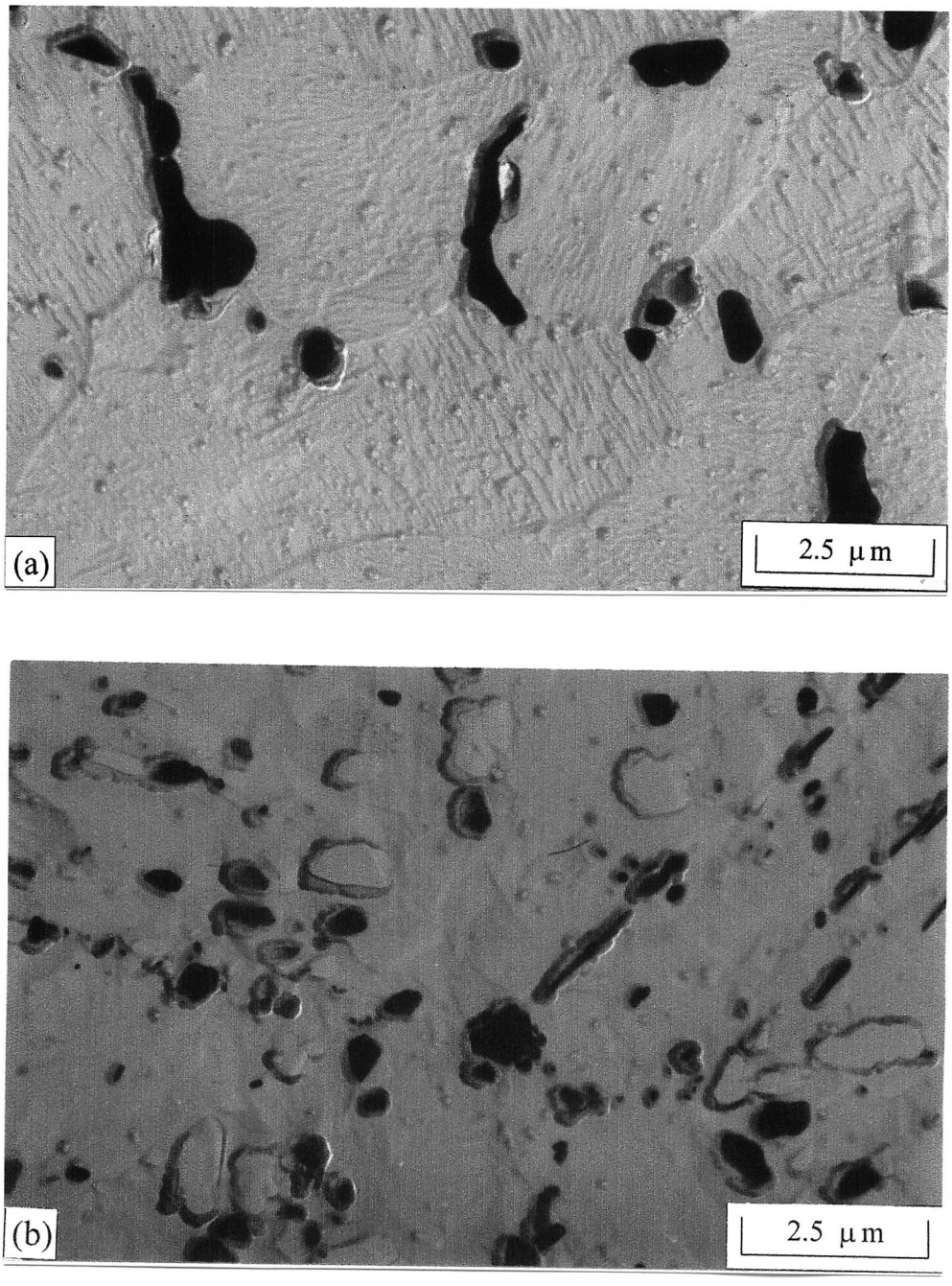

Figure 7.11 TEM micrographs in the carburised zone of; (a) 2CrMo/$\frac{1}{2}$CrMoV weld, 109 000 h at 565 °C; (b) 9Cr1Mo/$\frac{1}{2}$CrMoV weld, 504 h at 730 °C; (c) 9Cr1Mo/2$\frac{1}{4}$Cr1Mo weld, 1 000 h at 650 °C.

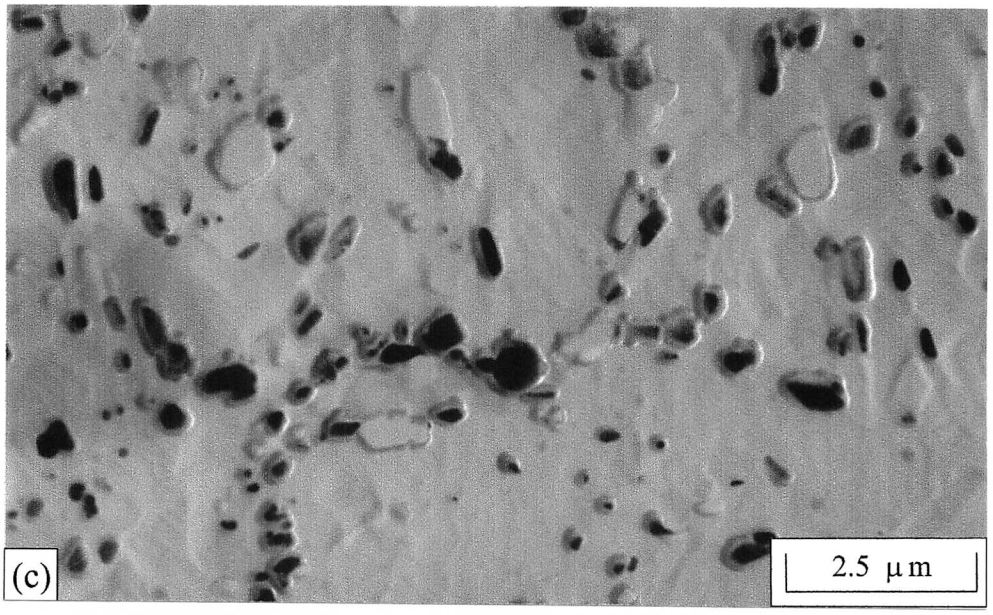

Figure 7.11 TEM micrographs in the carburised zone of; (a) 2CrMo/$\frac{1}{2}$CrMoV weld, 109 000 h at 565 °C; (b) 9Cr1Mo/$\frac{1}{2}$CrMoV weld, 504 h at 730 °C; (c) 9Cr1Mo/2$\frac{1}{4}$Cr1Mo weld, 1 000 h at 650 °C.

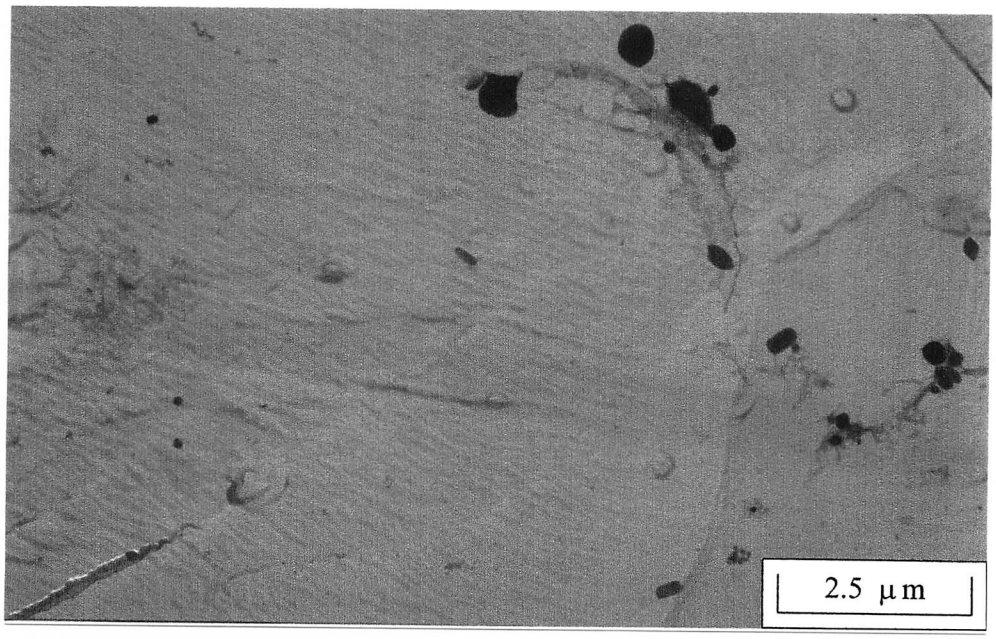

Figure 7.12 TEM micrograph in the decarburised zone of a 9Cr1Mo/$\frac{1}{2}$CrMoV dissimilar steel weld aged for 504 h at 730 °C.

Steel	Dissimilar steel weld	Carbides Identified
2CrMo	2CrMo/$\frac{1}{2}$CrMoV weld, 109 000 at 565 °C	M_7C_3, cementite
9Cr1Mo	9Cr1Mo/$\frac{1}{2}$CrMoV weld, 504 h at 730 °C	M_7C_3, M_2C, cementite
9Cr1Mo	9CrMo/$2\frac{1}{4}$Cr1Mo weld, 1 000 h at 650 °C	M_7C_3
9Cr1Mo	9Cr1Mo/$2\frac{1}{4}$Cr1MoV weld, 1 000 h at 650 °C	M_7C_3, M_2C
$\frac{1}{2}$CrMoV	9Cr1Mo/$\frac{1}{2}$CrMoV weld, 504 h at 730 °C	M_7C_3, M_2C, cementite V_4C_3, M_6C
$2\frac{1}{4}$Cr1Mo	9CrMo/$2\frac{1}{4}$Cr1Mo weld, 1 000 h at 650 °C	M_7C_3, M_2C

Table 7.7 Carbides identified using the TEM, which are found in the carburised and decarburised zones of aged and ex-service dissimilar steel welds.

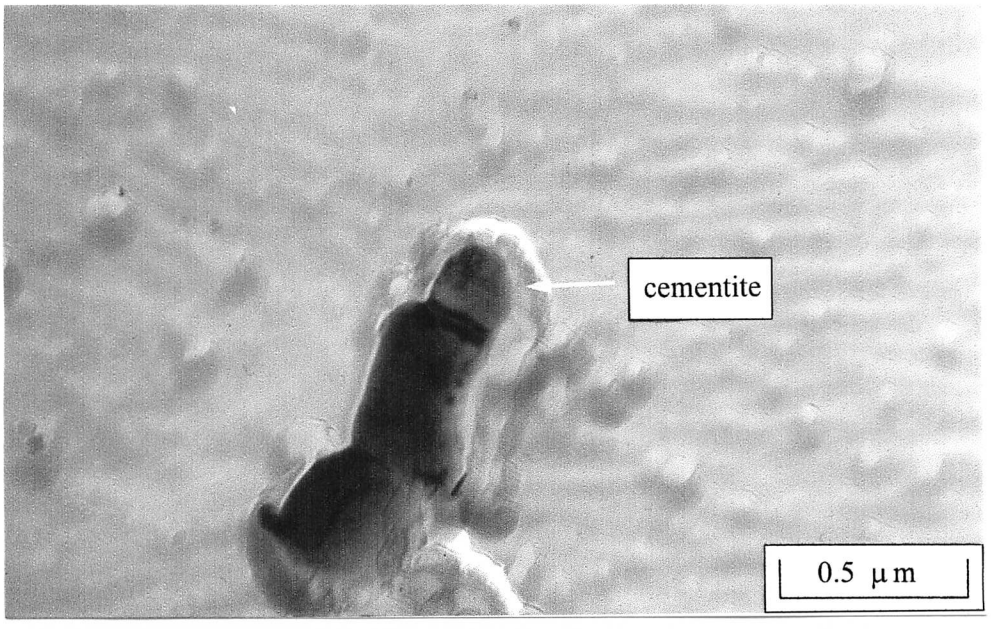

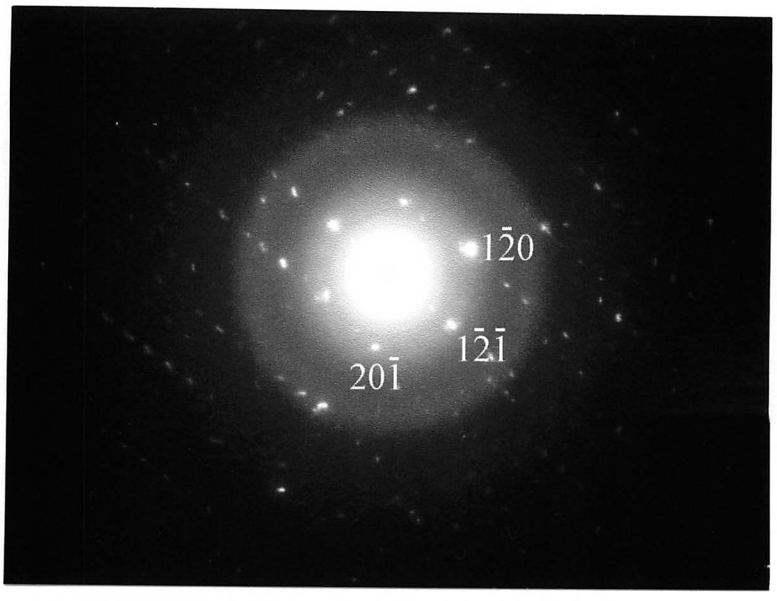

Figure 7.13 TEM micrograph of a cementite carbide in the carburised zone of a 2CrMo/$\frac{1}{2}$CrMoV dissimilar steel weld taken from service in the power plant. The zone axis of this diffraction pattern is [2 $\bar{1}$ 4].

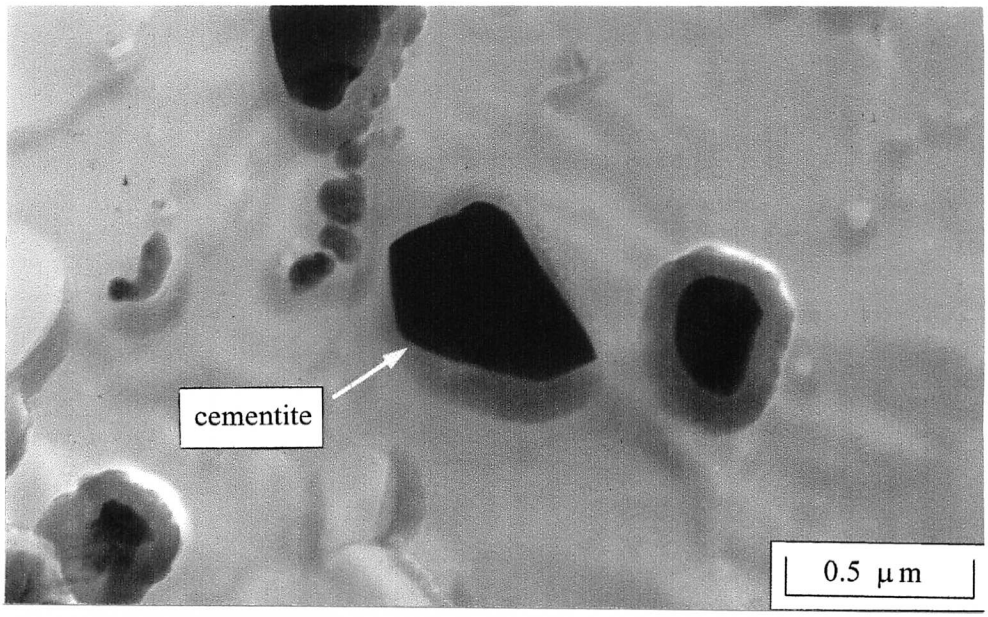

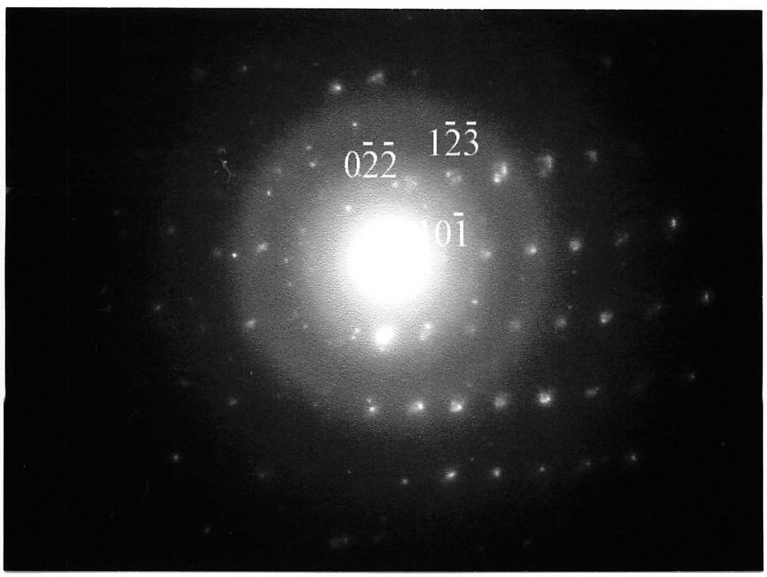

Figure 7.14 TEM micrograph of a cementite carbide in the carburised zone of a 9Cr1Mo/$\frac{1}{2}$CrMoV dissimilar steel weld heat treated at 730 °C for 504 h. The zone axis of this diffraction pattern is [1 $\bar{1}$ 1].

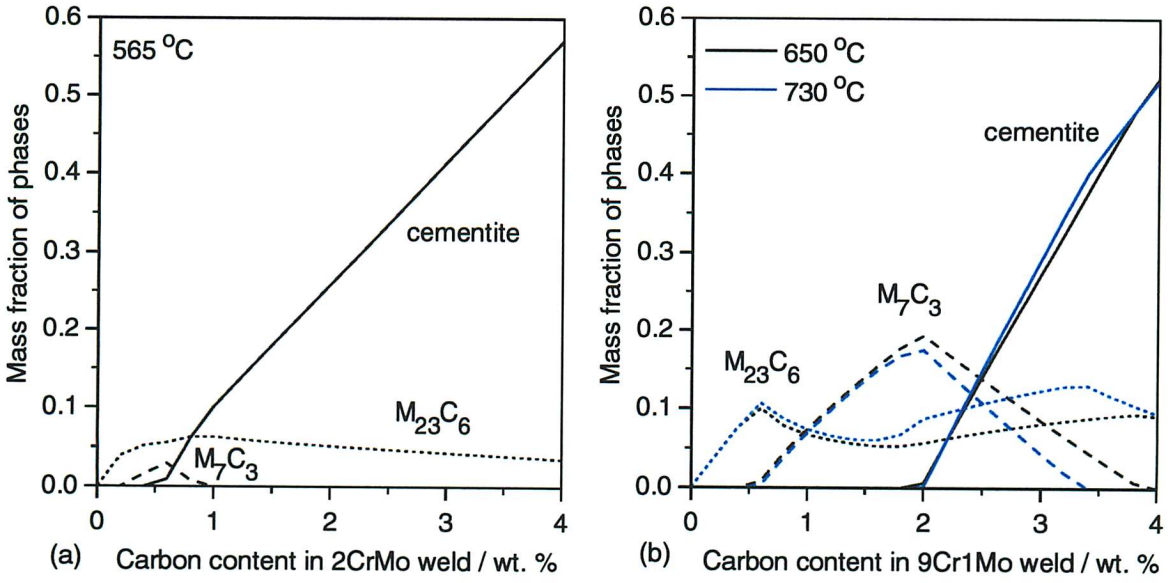

Figure 7.15 The calculated fraction of equilibrium phases for carburising welds, (a) 2CrMo/$\frac{1}{2}$CrMoV and (b) 9Cr1Mo/$\frac{1}{2}$CrMoV dissimilar steel weld.

from within the decarburised zones. It was very difficult to identify which part of the decarburised zones that the replicas were taken from. This becomes important in the 9Cr1Mo/$\frac{1}{2}$CrMoV weld where optical and SEM examination revealed different microstructural regions in the decarburised zone. In both decarburised zones, longer-term ageing M_7C_3 and M_2C carbides were found; in the $\frac{1}{2}$CrMoV steel, M_6C carbides were also identified, Figure 7.18. The carbides found in the decarburised zones of $\frac{1}{2}$CrMoV steels were plainly on the ferrite grain boundaries. These stable alloy-carbides were generally coarser and restricted grain growth. In the case of dissimilar steel welds with a vanadium-containing low-alloy steel, vanadium carbides are able to maintain a fine dispersion throughout the low-alloy steel and restrict grain growth (Honeycombe, 1976; Aaron & Kotler, 1971). It was unfortunate that no vanadium carbides were identified in the decarburised zone of the aged $\frac{1}{2}$CrMoV steel as expected.

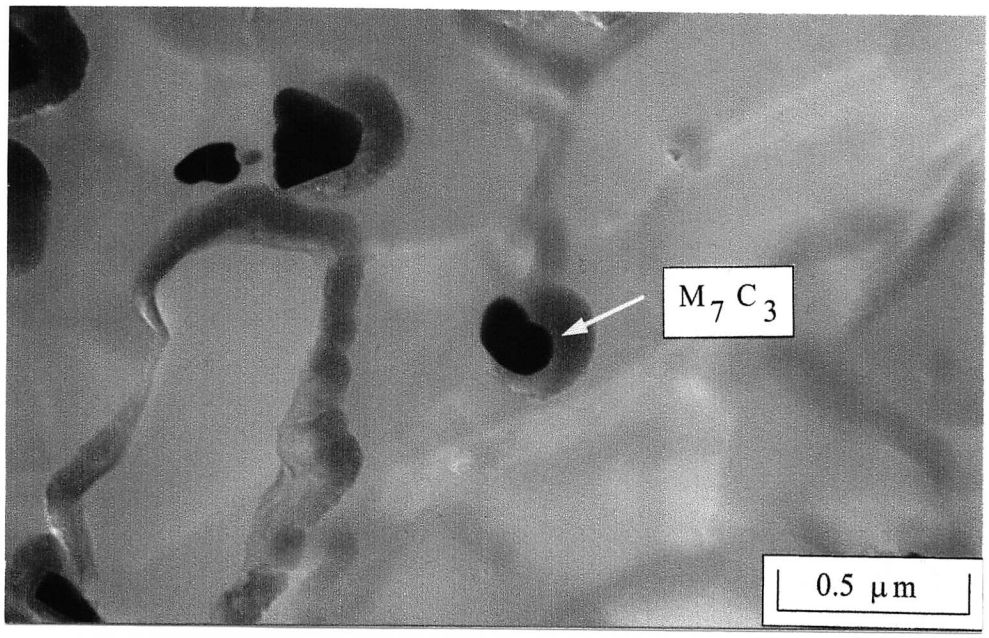

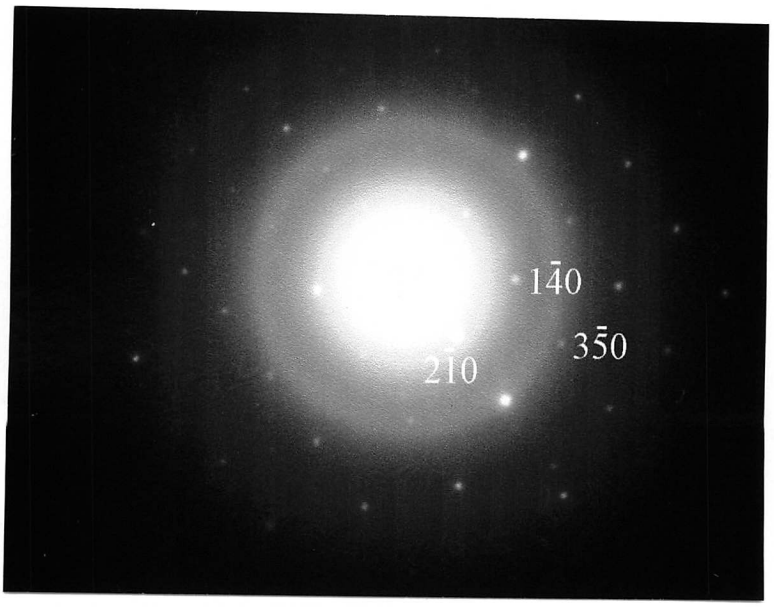

Figure 7.16 TEM micrograph of a M_7C_3 carbide in the carburised zone of a 9Cr1Mo/$2\frac{1}{4}$Cr1Mo dissimilar steel weld heat treated at 650 °C for 1 000 h. The zone axis of this diffraction pattern is [0 0 1].

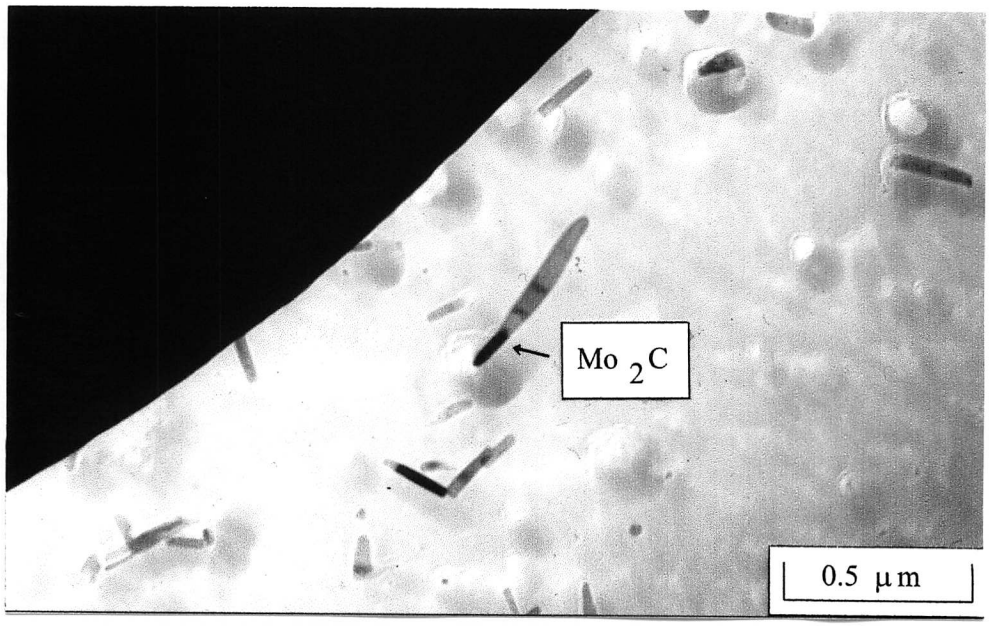

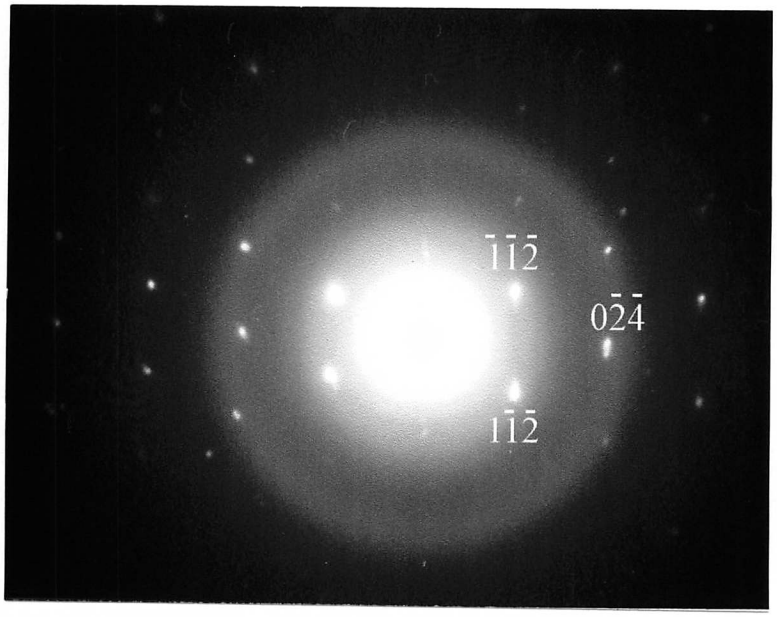

Figure 7.17 TEM micrograph of a Mo_2C carbide in the carburised zone of a 9Cr1Mo/2$\frac{1}{4}$Cr1MoV dissimilar steel weld heat treated at 650 °C for 1 000 h. The zone axis of this diffraction pattern is [0 2 $\bar{1}$].

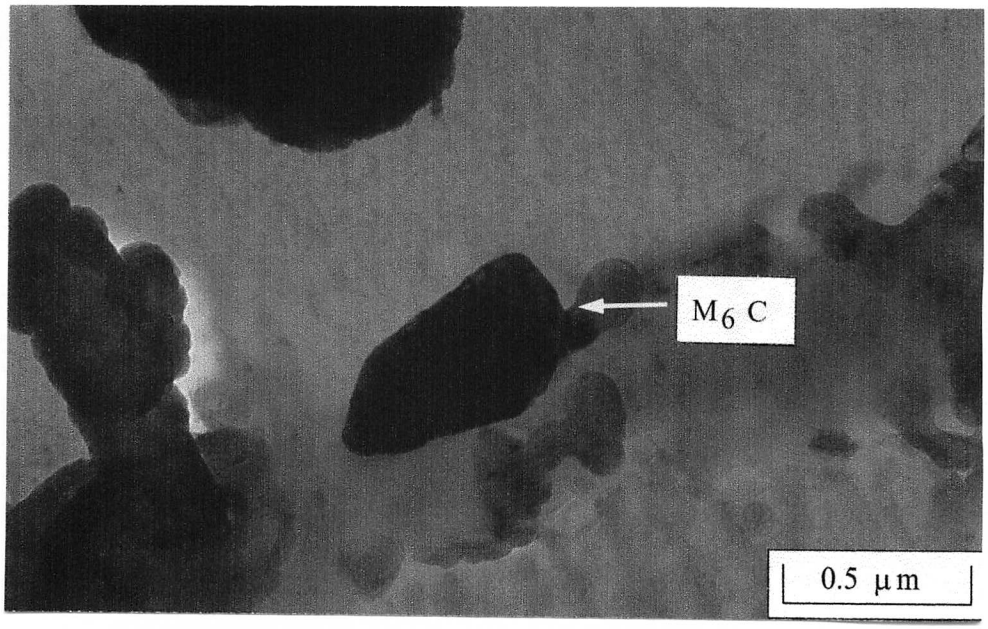

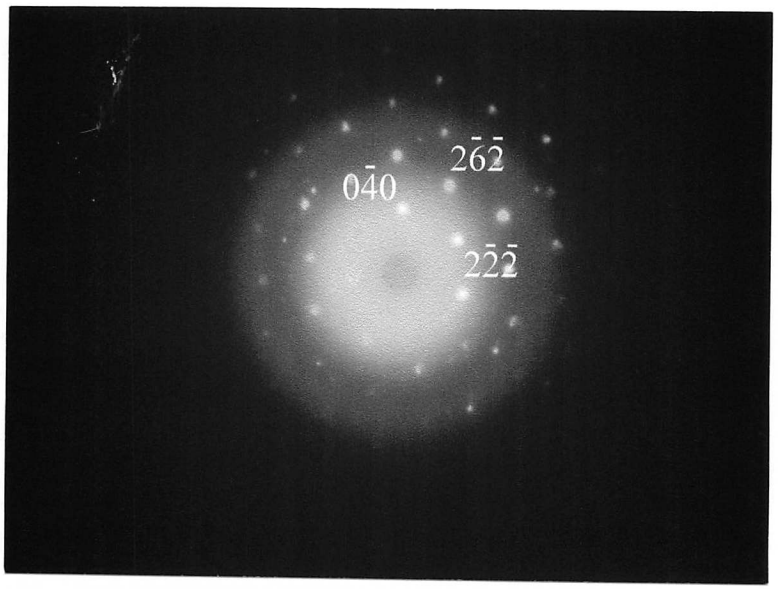

Figure 7.18 TEM micrograph of a M_6C carbide in the decarburised zone of a 9Cr1Mo/$\frac{1}{2}$CrMoV dissimilar steel weld heat treated at 730 °C for 504 h. The zone axis of this diffraction pattern is [1 0 1].

7.8 Summary

In all dissimilar steel welds, a dense seam of carbides can be found in the high-alloy welds after carbon partitioning. When steels contain mainly chromium and molybdenum, the decarburised zones appear smaller and are characterised by a low carbide fraction and a coarse grain size. In vanadium steels, a wider decarburised zone can be identified but stable carbides throughout the steel restrict grain coarsening.

In the following chapter, the validity of the computer model predicting carbide dissolution and carbon diffusion which form the decarburised zone is discussed with respect to measurements made on the diffusion bonds and dissimilar steel welds.

Chapter Eight

Validation of Computer Model

The work presented in the previous chapters has demonstrated that it is possible to observe the effects of carbon migration from a low chromium to high chromium steel during heat treatment. Many of the metallurgical features due to carbon partitioning across a diffusion bond or a dissimilar steel weld were the same, though the extent of partitioning differed. The purpose of the work described in this chapter was to analyse these data, and data from published literature, using the computer model described in Chapter 4.

8.1 The model

The model proposed in Chapter 4 was simple in its construction, involving only the dissolution of a precipitate via a diffusion flux through the matrix, a process repeated as a function of distance from the weld junction.

Initially the carbide and matrix phases are in equilibrium which becomes disturbed by the application of heat and solute partitioning down a chemical gradient across the dissimilar steel junction.

The dissolution of an unstable planar or spherical particle, with no soft impingement due to overlapping diffusion fields, has been analysed carefully over many years (Chapter 2).

The time for a carbide to dissolve is found to be given by (Ågren, 1990):

$$t_{\text{diss}} = \frac{x_0^2}{2\Omega D}$$

where Ω is the supersaturation parameter, dependent on temperature and the carbon concentrations of each phase, D is the diffusion coefficient of solute in the matrix and x_0 is the initial carbide size.

Before dissolution, the average carbon concentration $\overline{C_\alpha}$ (equation 4.17) lies between the interface concentrations $C_{A\alpha}$ and $C_{\alpha A}$ (cf. Figure 2.12) in the carbide and matrix respectively. While the carbide is dissolving, $\overline{C_\alpha}$ decreases until it lies between $C_{\alpha A}$ and $C_{\alpha\beta}$ in the single phase matrix, Figure 8.1. At higher temperatures, the equilibrium carbon concentrations in each phase increase, hence more time is needed for $\overline{C_\alpha}$ to drop below a limit which effectuates the dissolution of the following carbide.

Further from the dissimilar steel junction, the influence of the carbon concentration $C_{\alpha\beta}$ on carbide dissolution and diffusion flux is decreased. As the time is recorded after carbide

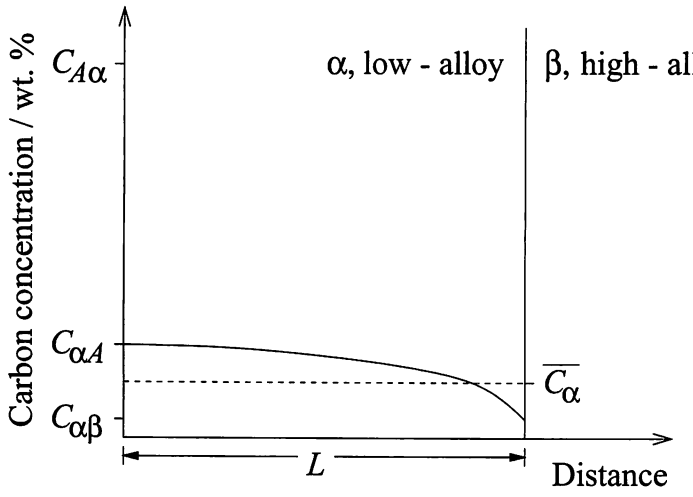

Figure 8.1 The distribution of carbon after carbide dissolution next to the dissimilar steel junction.

dissolution and diffusion of carbon through the matrix, the decarburised zone takes on a stepwise appearance when plotted.

8.2 Rapid carbide dissolution adjacent to the dissimilar interface

The time step used in the model was based on the diffusion coefficient of carbon, modified to take into account interactions of carbon with other solutes in the steel:

$$\Delta t = \frac{r \,.\, \Delta x^2}{D_C} \leq 1 \tag{8.1}$$

Equation 8.1 is a re-arrangement of equation 4.31 where r can be equal to 1. As the diffusion coefficient of carbon, D_C, rises exponentially with temperature, the time step decreases and so does t_{diss}. The concentrations of the equilibrium phases in the steel were estimated using MTDATA (1996), allowing ferrite, austenite, cementite, $M_{23}C_6$, M_7C_3, M_6C, vanadium carbide as the phases and carbon, silicon, manganese, chromium, molybdenum, nickel, vanadium as the components. This was done for the diffusion bond whose composition is described in Table 8.1.

Steel	C	S	P	Si	Mn	Ni	Cr	Mo	V
$2\frac{1}{4}$Cr1Mo	0.12	0.022	0.021	0.27	0.54	0.04	2.29	0.95	0.005
P91	0.10	0.002	0.01	0.33	0.43	0.08	8.6	0.92	0.24

Table 8.1 Composition of the steels used in the diffusion bond, wt. %.

Figure 8.2 plots the calculated dissolution of a 1 μm size $M_{23}C_6$ carbide in the low-alloy steel of a P91/2$\frac{1}{4}$Cr1Mo bond, heat treated at 600, 650 or 700 °C.

Experimental and theoretical analyses of cementite dissolution in a Fe – Cr – C steel have identified that for uniform carbide shrinkage, dissolution is dependent on maintaining local equilibrium at the moving interface and volume diffusion (Hillert *et al.*, 1971; Gullberg, 1973; Ågren & Vassiliev, 1984; Liu & Ågren, 1991). In this work, the dissolution of a chromium-based carbide will be slower than un-alloyed cementite in the same Fe – Cr – C steel because the diffusion of chromium must also be accounted for.

Figure 8.3 shows that the carbide dissolution process is insensitive to small changes in the composition of 2$\frac{1}{4}$Cr1Mo steel when it is joined to P91. On the other hand, changing the type of steel used in the bond has a large effect on dissolution, as illustrated on Figure 8.4. This is because the gradients in the carbon chemical potential across the dissimilar steel junction are affected by composition (section 5.3.3). Carbide dissolution is therefore much faster in the P91/$\frac{1}{2}$CrMoV bond than for 2$\frac{1}{4}$Cr1Mo/$\frac{1}{2}$CrMoV bond.

In Figure 8.5, the size of the carbide particle, normalised with respect to its initial size, is plotted as a function of time at temperature. Naturally a coarser carbide takes longer to dissolve as expected from the parabolic dependence of diffusion distances over time (*i.e.* $x_0 \propto \sqrt{t_{\text{diss}}}$).

The carbon concentrations in ferrite next to the equilibrium carbide ($C_{\alpha A}$ and $C_{\beta B}$) were estimated using MTDATA for the P91/2$\frac{1}{4}$Cr1Mo bond, Table 8.2.

As the carbide dissolves, releasing solute which diffuses out of the low-alloy steel, the average carbon concentration in the steel decreases as a function of time, Figure 8.6.

As the chemical potential of carbon is a function of temperature, raising the temperature increases the diffusivity of carbon and chromium and the concentration gradient over distance, thereby speeding-up dissolution. $C_{\alpha A}$, and hence $\overline{C_\alpha}$, diffusion coefficient and initial carbide size can all modify homogenisation time (Tanzilli & Heckel, 1968).

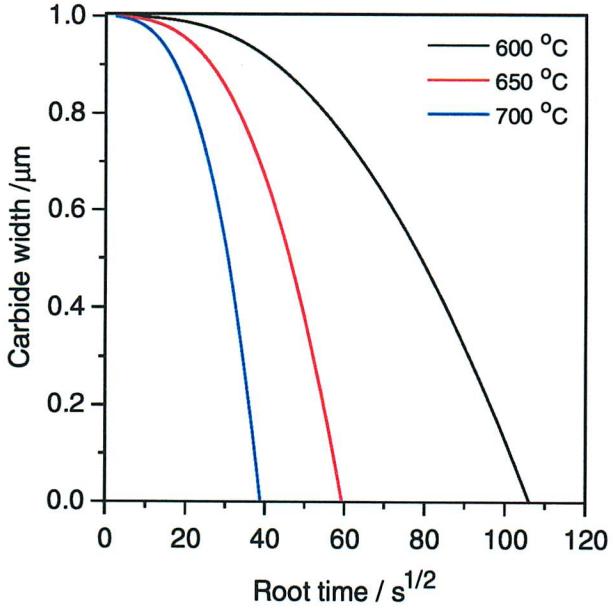

Figure 8.2 The dissolution of a 1 μm size $M_{23}C_6$ carbide in the $2\frac{1}{4}$Cr1Mo steel, adjacent to the dissimilar steel junction of a P91/$2\frac{1}{4}$Cr1Mo diffusion bond heat treated between 600 and 700 °C.

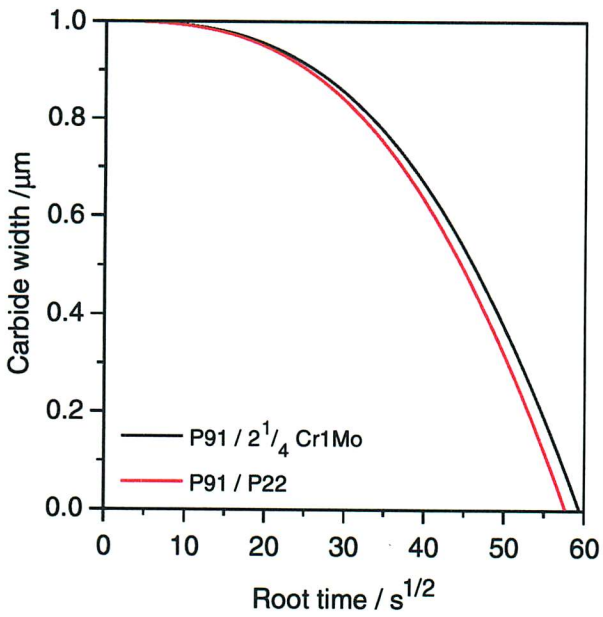

Figure 8.3 The dissolution of a 1 μm size $M_{23}C_6$ carbide in the low-alloy steel, adjacent to the dissimilar steel junction of a new P91/$2\frac{1}{4}$Cr1Mo and a P91/P22 diffusion bond, at 650 °C.

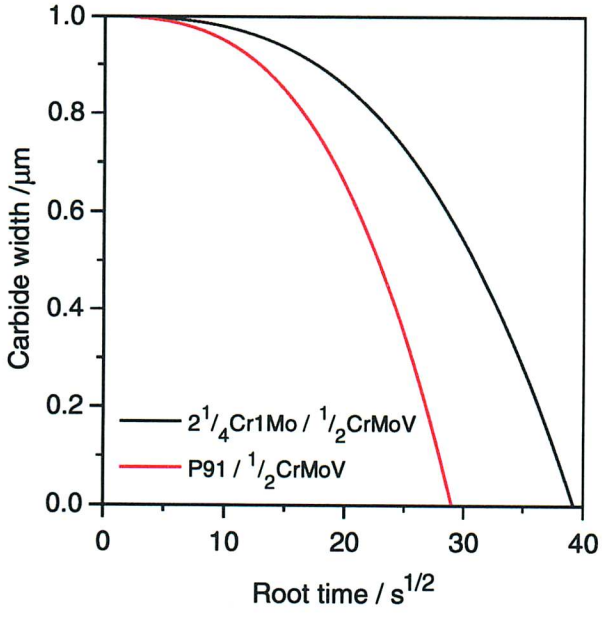

Figure 8.4 The dissolution of a 1 μm size $M_{23}C_6$ carbide in the $\frac{1}{2}$CrMoV steel, adjacent to the dissimilar steel junction of a P91/$\frac{1}{2}$CrMoV and a $2\frac{1}{4}$Cr1Mo/$\frac{1}{2}$CrMoV diffusion bond, at 650 °C.

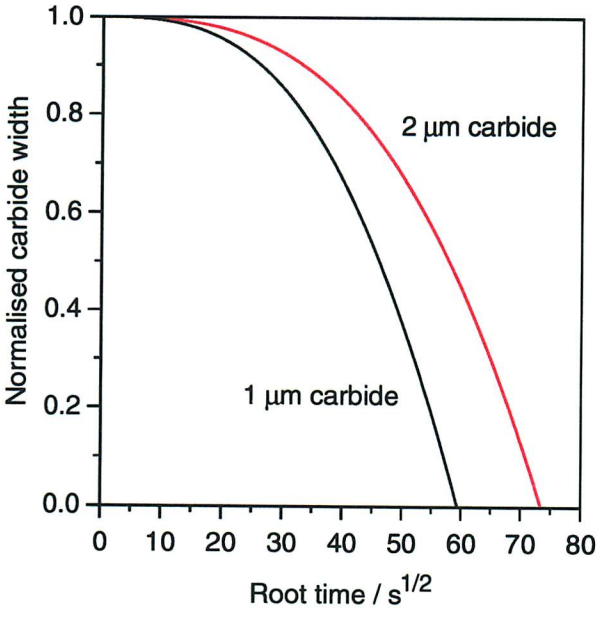

Figure 8.5 The dissolution of a 1 and 2 μm size $M_{23}C_6$ carbides in the $2\frac{1}{4}$Cr1Mo steel, adjacent to the dissimilar steel junction of a P91/$2\frac{1}{4}$Cr1Mo diffusion bond, at 650 °C.

$2\frac{1}{4}$Cr1Mo	Volume fraction of carbide	$C_{A\alpha}$	$C_{\alpha A}$	$C_{\alpha\beta}$
600 °C	0.028	5.06	0.00013	0.000017
650 °C	0.028	5.07	0.00053	0.000070
700 °C	0.028	5.08	0.00177	0.000270
P91	Volume fraction of carbide	$C_{B\beta}$	$C_{\beta B}$	$C_{\beta\alpha}$
600 °C	0.022	5.14	0.00003	0.00015
650 °C	0.021	5.15	0.00007	0.00053
700 °C	0.021	5.17	0.00031	0.00180

Table 8.2 Carbon concentrations and volume fractions of carbide in a P91/$2\frac{1}{4}$Cr1Mo diffusion bond. All concentrations are in wt. % and the equilibrium carbide was $M_{23}C_6$ at all temperatures. The notation in this table is explained in Chapter 4.

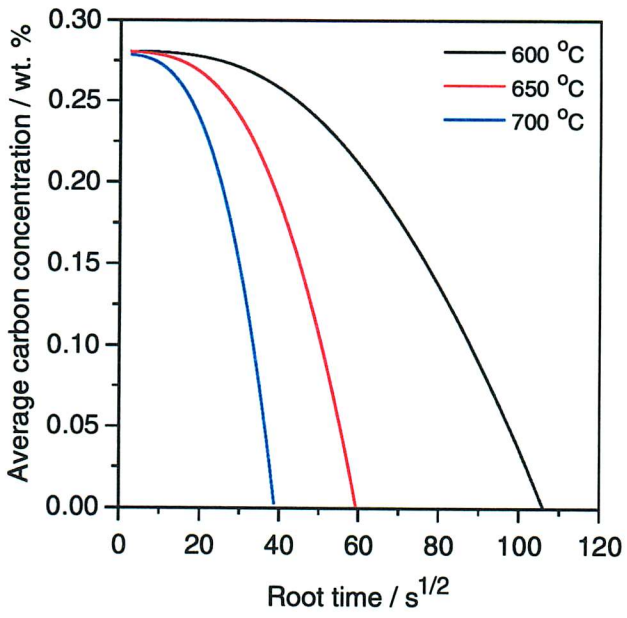

Figure 8.6 The change in average carbon concentration in $2\frac{1}{4}$Cr1Mo steel, close to the dissimilar steel junction of a P91/$2\frac{1}{4}$Cr1Mo diffusion bond, at 650 °C.

8.2.1 Summary

The important constituents of the model are therefore:

- composition of the both the steels used in making the dissimilar joint
- temperature and carbon diffusion coefficient
- initial carbide size
- the average carbon concentration in the low-alloy steel

8.3 Calculation of the decarburised zone width

Using the P91/2$\frac{1}{4}$Cr1Mo bond described in Chapter 5, together with equilibrium data obtained using MTDATA and a carbide size of 1 μm, predictions were made for decarburised zone widths for annealing at 600, 650 and 700 °C, Figure 8.7.

The calculations for annealing at 600 and 650 °C tend to overestimate the observed widths of the decarburised zones. Tempering between 600 and 700 °C causes the carbides in 2$\frac{1}{4}$Cr1Mo steel to coarsen and become fewer in number leaving the steel softer and more susceptible to creep (Smith & Nutting, 1957, Baker & Nutting, 1959; Abdel-Latif *et al.*, 1982, Evans & Wilshire, 1993). This is illustrated in Figure 8.8 and it was found that increasing the carbide size to 2 μm gives a more accurate prediction of decarburised zone at 700 °C, Figure 8.9.

The same computer model was applied to predicting the decarburised zones for the dissimilar steel welds, reported in Chapter 6. Again, MTDATA calculations and estimations of carbide sizes were based on the composition and ageing conditions in the welds. The predictions of decarburised zone widths in a 9Cr1Mo/2$\frac{1}{4}$Cr1Mo dissimilar steel weld are given on Figure 8.10.

For heat treating at 600 and 650 °C, the calculations under-predicted the decarburised zones, but nevertheless correctly revealed the trend of the experimentally measured profiles. Annealing at 730 °C caused rapid decarburisation. Race (1992) also noted that when modelling decarburised zones in welds at 720 °C, the predictions from the model were 'slightly low', but could not explain the discrepancy, Figure 8.11.

8.3.1 Modelling Christoffel & Curran's results

The model was applied to published data on carbon migration. The compositions of the steels used in an investigation by Christoffel & Curran (1956) are presented in Table 8.3.

The dissimilar steel welds were 14Cr1$\frac{1}{2}$Mo/2$\frac{1}{4}$Cr1Mo and 14Cr1$\frac{1}{2}$Mo/5Cr$\frac{1}{2}$Mo combination, and were aged at 600, 650 and 700 °C.

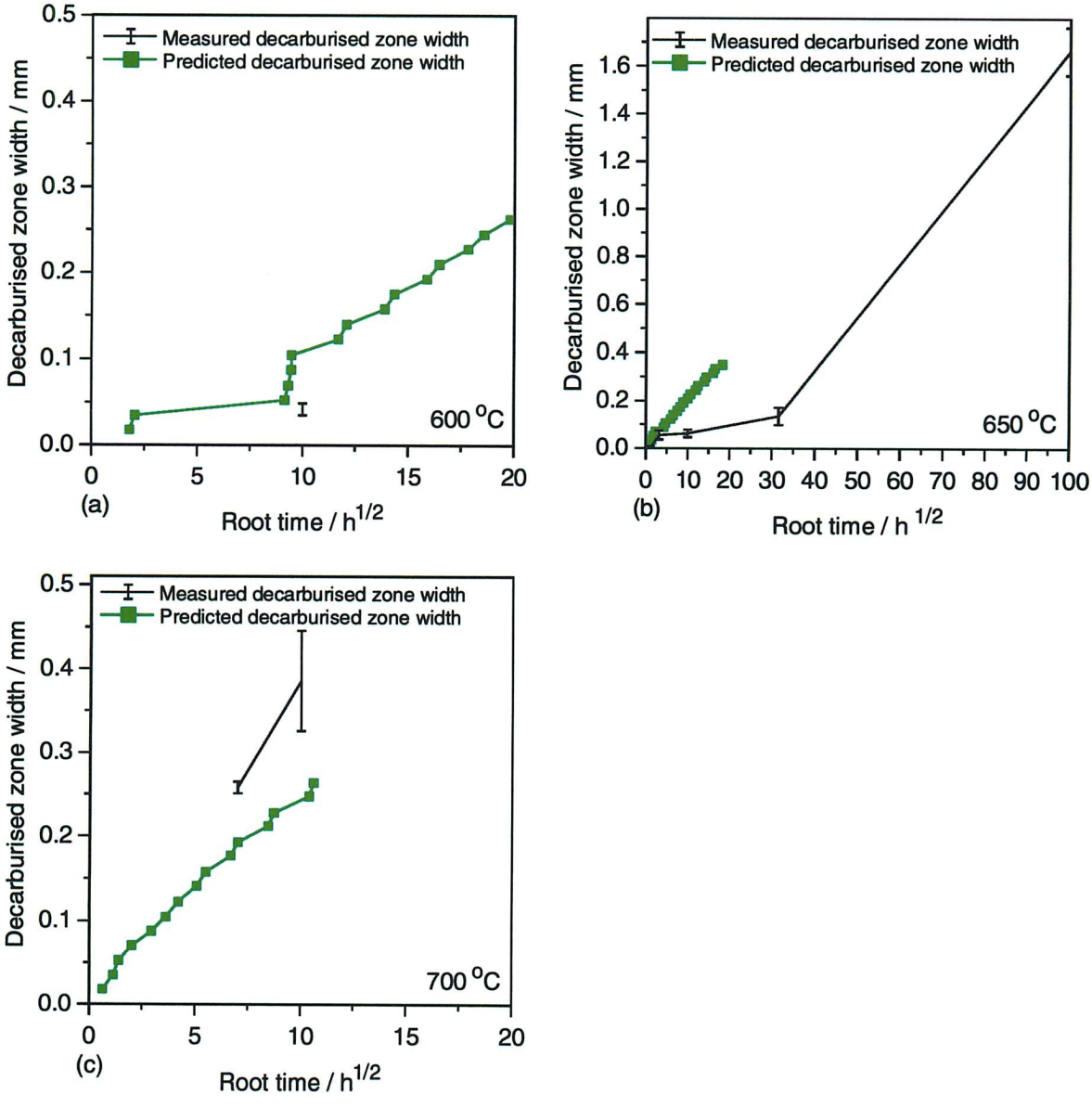

Figure 8.7 Measured and calculated decarburised zones in a P91/2$\frac{1}{4}$Cr1Mo bond aged at 600, 650 700 °C. The dissolving carbide was set to be $M_{23}C_6$ with a width of 1 μm.

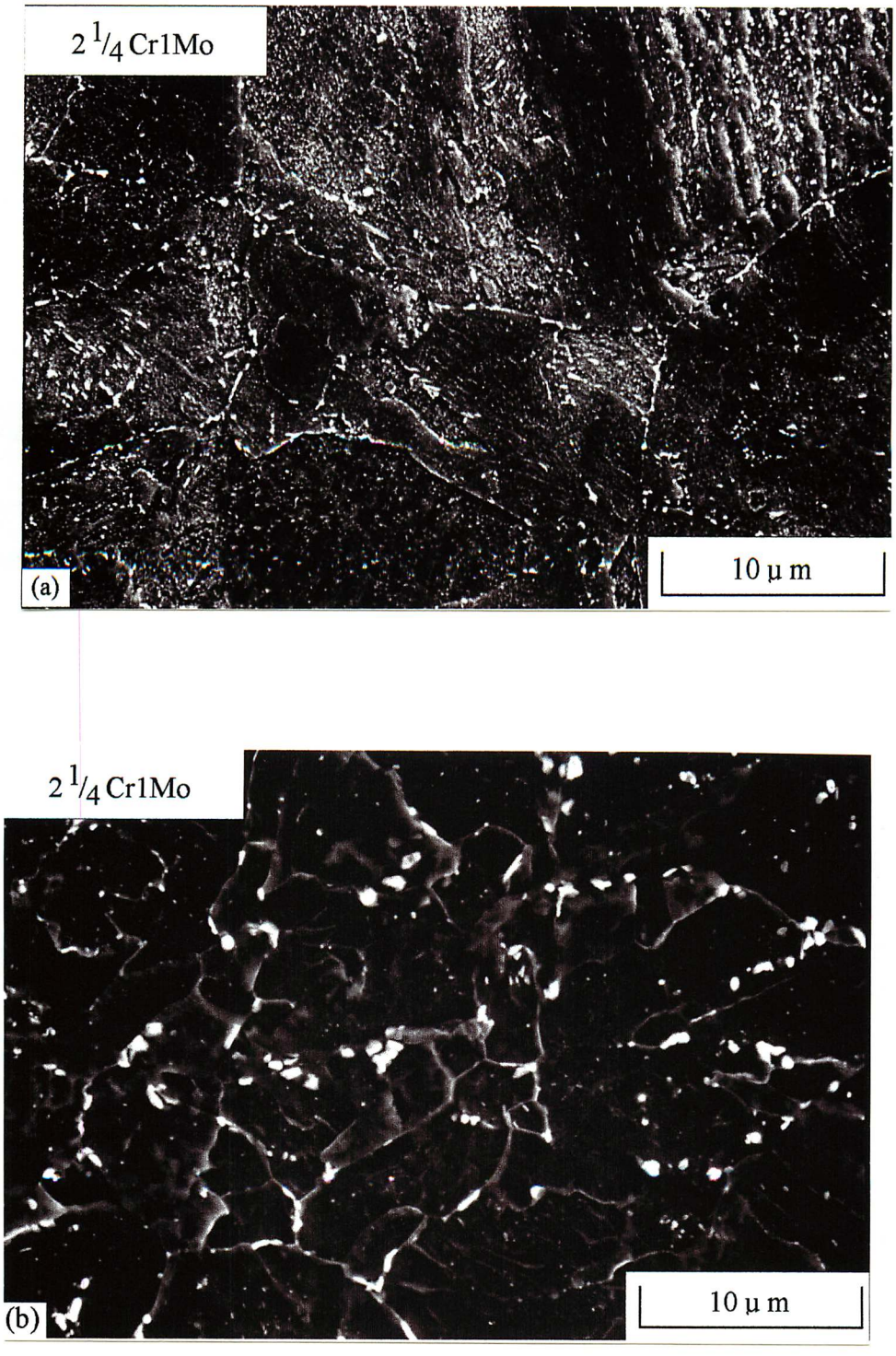

Figure 8.8 $2\frac{1}{4}$Cr1Mo steel aged at (a) 600 °C for 100 h and (b) 700 °C for 49 h, in a P91/$2\frac{1}{4}$Cr1Mo bond.

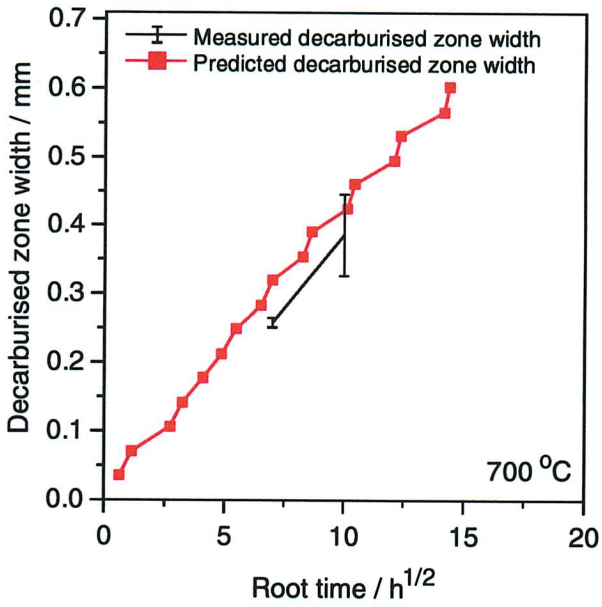

Figure 8.9 Measured and calculated decarburised zones in a P91/2$\frac{1}{4}$Cr1Mo bond aged at 700 °C. The dissolving carbide was set to be $M_{23}C_6$ with a width of 2 μm.

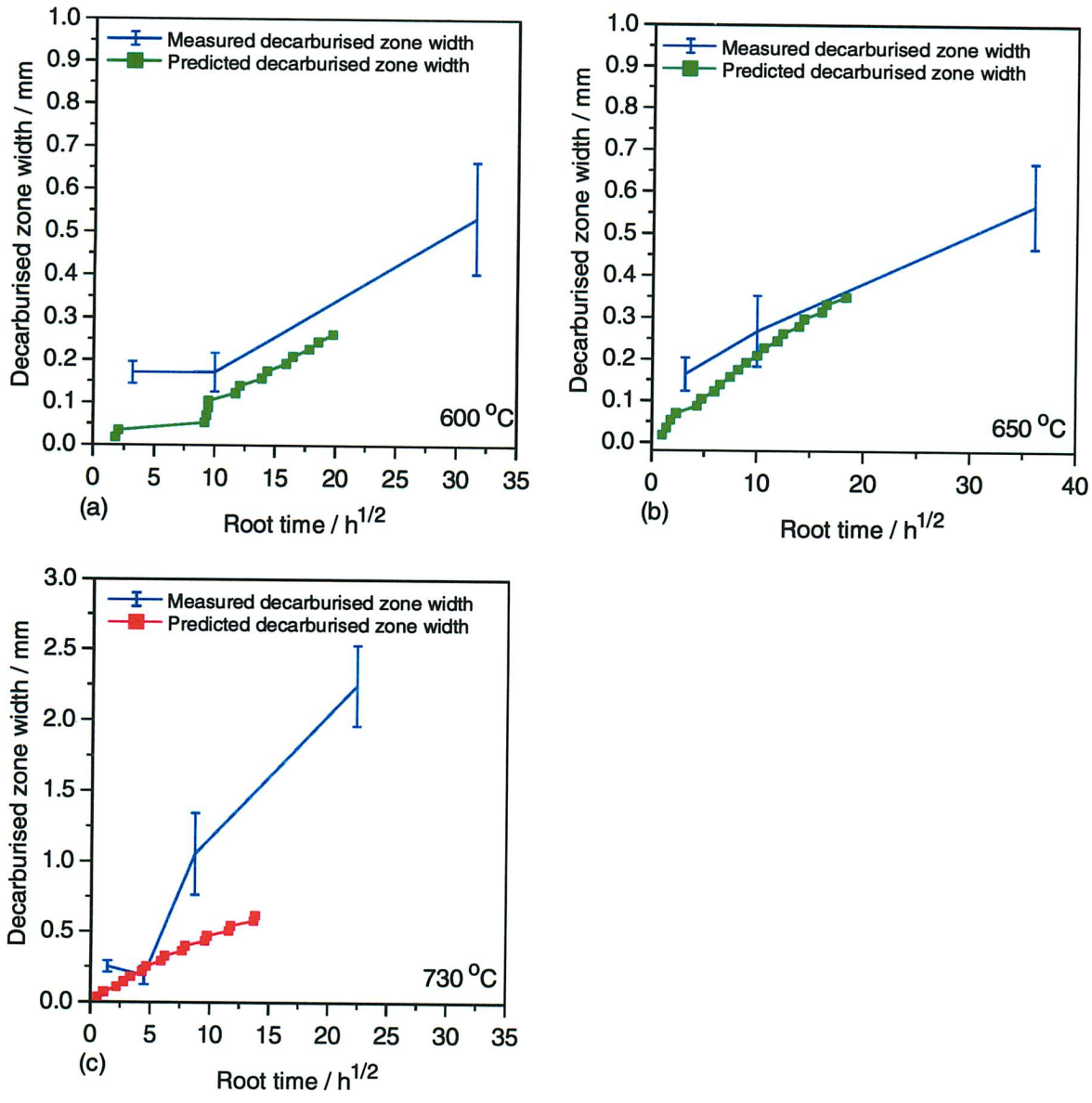

Figure 8.10 Measured and calculated decarburised zones in a P91/2$\frac{1}{4}$Cr1Mo dissimilar steel weld aged at 600, 650 and 730 °C. The dissolving carbide was set to be $M_{23}C_6$ with a width of 1 μm at the lower temperatures and 2 μm at 730 °C.

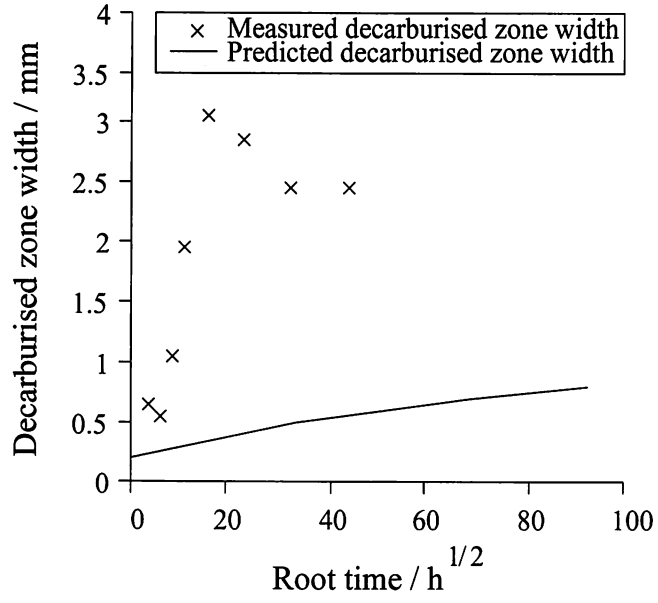

Figure 8.11 Measured and calculated decarburised zones in a P91/2$\frac{1}{4}$Cr1Mo dissimilar weld aged at 720 °C. The dissolving carbide was set to be 5 μm wide (Race, 1992).

	C	Cr	Mo
2$\frac{1}{4}$Cr1Mo steel	0.12	2.4	1.05
5Cr$\frac{1}{2}$Mo steel	0.04	4.77	0.47
14Cr1$\frac{1}{2}$Mo steel	0.09	14.93	1.50

Table 8.3 Composition of steels used, wt. % (Christoffel & Curran, 1956).

Figures 8.12 and 8.13 plot Christoffel & Curran's experimental results for these welds alongside the model results. For the 14Cr1$\frac{1}{2}$Mo/2$\frac{1}{4}$Cr1Mo weld, the precipitation of an M_7C_3 carbide from an $M_{23}C_6$ in 2$\frac{1}{4}$Cr1Mo was accounted for. Though no error was reported in the experimental results, most of the predicted values agree well with the published data.

The equation proposed by Christoffel and Curran (1956) for predicting the diffusion distance x_α, or decarburised zone width, is given by:

$$x_\alpha^2 = \frac{C_{\alpha A} - C_{\alpha\beta}}{C_{A\alpha}} 2D_C\, t \tag{8.2}$$

Table 8.4 reports the calculated decarburised zone widths using equation 8.2 and the experimentally observed widths for a 14Cr1$\frac{1}{2}$Mo/2$\frac{1}{4}$Cr1Mo weld at 650 °C and of course the predicted results by the current work.

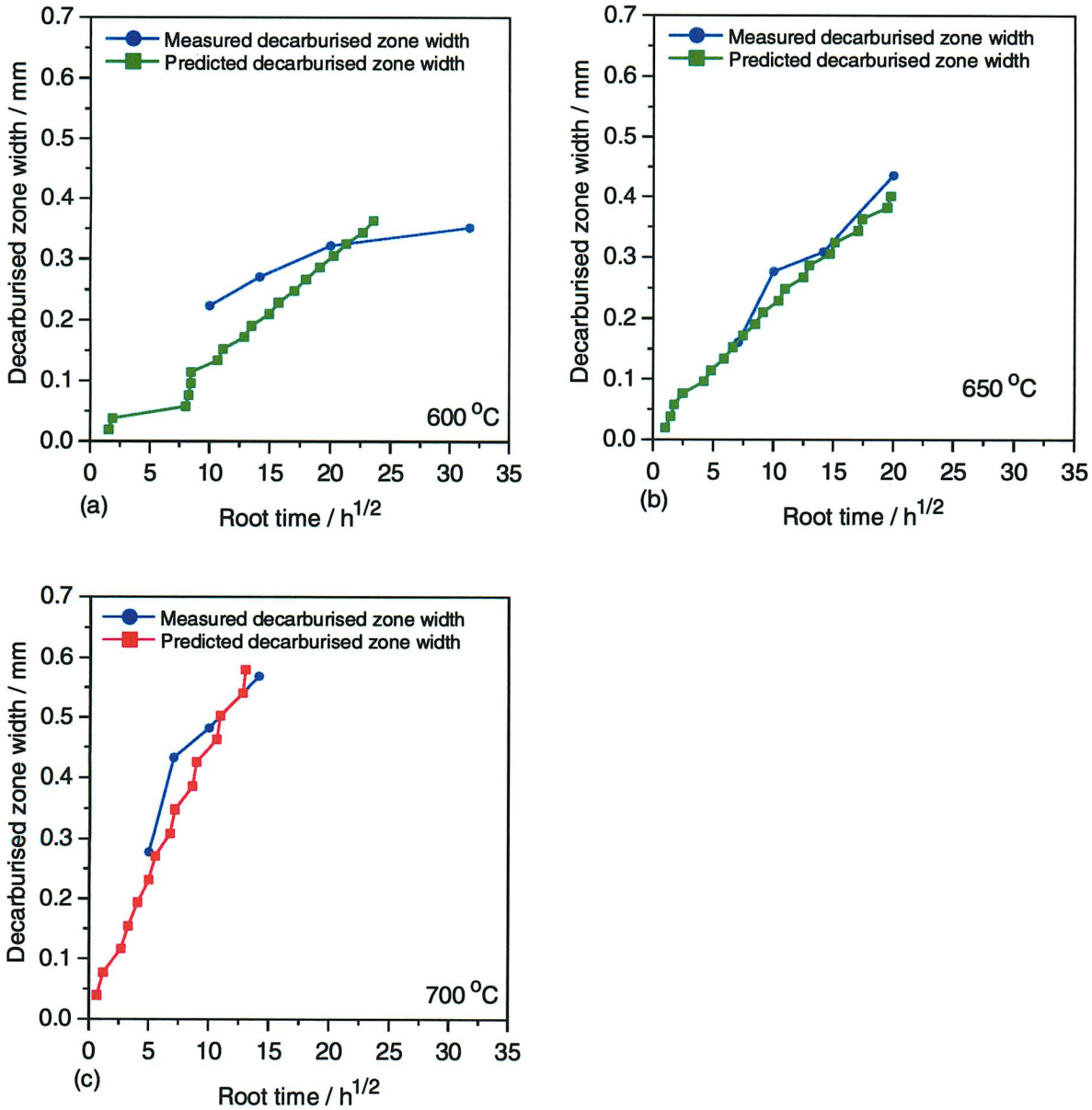

Figure 8.12 Measured and calculated decarburised zones in a 14Cr1$\frac{1}{2}$Mo / 2$\frac{1}{4}$Cr1Mo weld aged at (a) 600 °C, (b) 650 °C, (c) 700 °C. The dissolving carbide was set to be $M_{23}C_6$ and the width was 1 μm at 600 and 650 °C, and 2 μm at 700 °C.

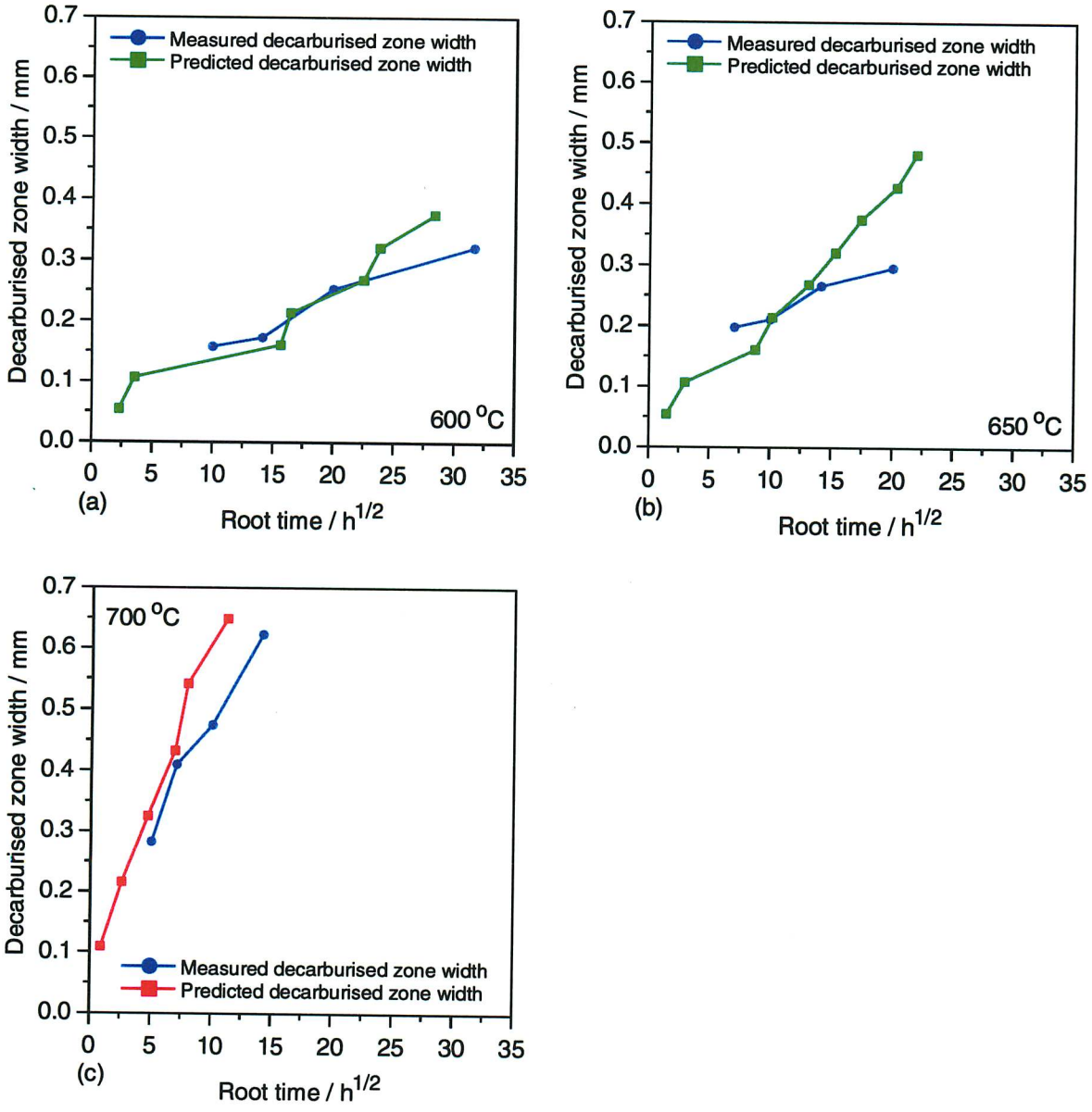

Figure 8.13 Measured and calculated decarburised zones in a 14Cr1$\frac{1}{2}$Mo / 5Cr$\frac{1}{2}$Mo weld aged at (a) 600 °C, (b) 650 °C, (c) 700 °C. The dissolving carbide was set to be $M_{23}C_6$ and the width was 1 μm at 600 and 650 °C, and 2 μm at 700 °C.

Time	Measured width / mm	Calculated width / mm (Christoffel & Curran)	Calculated width / mm (present work)
50 h	0.161	0.038	0.172
100 h	0.277	0.053	0.229
200 h	0.306	0.075	0.306
400 h	0.436	0.106	0.402

Table 8.4 Measured and calculated decarburised zone widths in a 14Cr1$\frac{1}{2}$Mo/2$\frac{1}{4}$Cr1Mo weld aged at 650 °C using the equation proposed by Christoffel & Curran (1956) and the present model. MTDATA was used to calculate the relevant concentrations.

		C	Cr	Mo	V	Fe	Volume fraction
$\frac{1}{2}$**CrMoV**	$M_{23}C_6$	5.03	15.6	15.4	0	bal.	0.014
	V_4C_3	17.2	0	0	82.8	0	0.0039
9Cr1Mo	$M_{23}C_6$	5.14	62.8	18.7	0	bal.	0.016

Table 8.5 Composition and volume fraction of carbides in 9Cr1Mo/$\frac{1}{2}$CrMoV dissimilar steel weld, heat treated at 650 °C. All concentrations are in wt. %.

As can be seen from Table 8.4, there is little agreement between the measured and calculated results using the equation due to Christoffel & Curran. On the other hand, the model from the present work shows excellent agreement with the data, albeit with an assumed particle size of 2μm.

8.4 Decarburised zone in steel containing vanadium

It is difficult to compare decarburised zone widths in low-alloy steels containing vanadium as it was not possible to measure the zone as a function of time. A long, drawn-out procedure of chemical analysis must be used to measure the quantity of diffusion, but this was not practical in bonds made from $\frac{1}{2}$CrMoV steel because they were too small. However, the computer model can be used to check the rate of dissolution of different carbides next to the weld junction.

The compositions of the steels in 9Cr1Mo/$\frac{1}{2}$CrMoV dissimilar steel weld were reported in Table 7.2. The concentrations and fractions of the equilibrium carbides predicted using MTDATA (using the phases listed earlier in section 8.1.1) are listed in Table 8.5.

The carbon concentration in V_4C_3 is significantly higher than in $M_{23}C_6$, and it is known that

V_4C_3 is more stable than the chromium-based carbides at the heat treatment temperatures (Ashby & Easterling, 1982). The carbon concentration in the ferrite of $\frac{1}{2}$CrMoV steel $C_{\alpha A}$ was the same adjacent to either V_4C_3 or $M_{23}C_6$ carbide because it is possible for both vanadium and chromium carbides to co-exist in three-phase equilibrium this steel (Shaw & Quarrell, 1957).

Figure 8.14 shows the dissolution of an $M_{23}C_6$ carbide in $\frac{1}{2}$CrMoV steel adjacent to a 9Cr1Mo weld metal at 650 °C. In Figure 8.15, the dissolution of a V_4C_3 carbide in the same steel is plotted. It can be seen that the vanadium-based carbide took over two times longer to dissolve and so the $M_{23}C_6$ carbide would dissolve preferentially and quicker too.

8.5 Summary

The simple computer model used here was found to be appropriate for predicting the decarburised zone widths in low-alloy ferritic steel, as part of a dissimilar joint alongside a high-alloy steel. Excellent agreement was found between the experimental and calculated results for the dissimilar steel joints investigated in the present work and previously published data. It was unfortunate that decarburised zones in vanadium-containing low-alloy steels were difficult to validate. Therefore, the model should be used with caution for such steels.

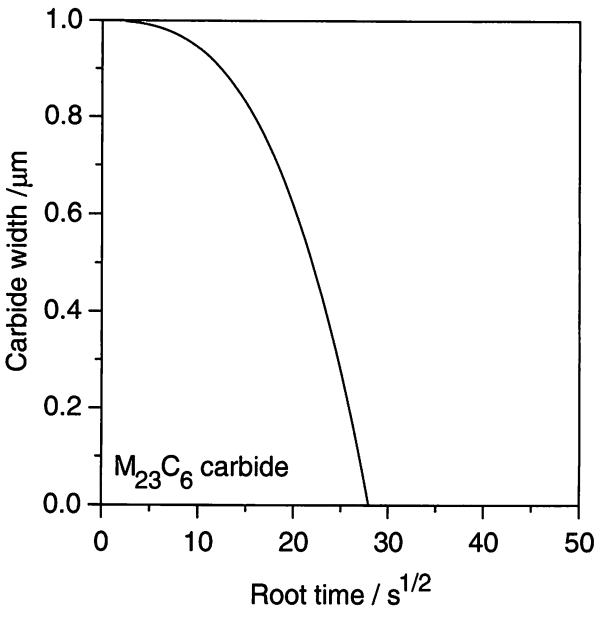

Figure 8.14 The dissolution of a 1 μm size $M_{23}C_6$ carbide next to the dissimilar steel junction in a 9Cr1Mo/$\frac{1}{2}$CrMoV dissimilar steel weld, aged at 650 °C.

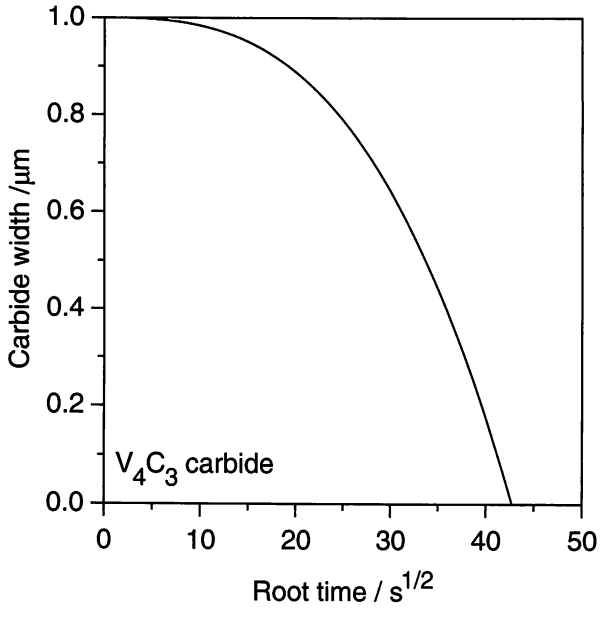

Figure 8.15 The dissolution of a 1 μm size V_4C_3 carbide next to the dissimilar steel junction in a 9Cr1Mo/$\frac{1}{2}$CrMoV dissimilar steel weld, aged at 650 °C.

Chapter Nine

Summary and Further Work

9.1 Summary

The aim of this work was to enable the estimation of carbon partitioning across dissimilar metal welds of the kind used in the construction of power plant. Metallographic analysis demonstrated the stages in the evolution of the decarburised zone as a function of time, generally characterised by a low carbide volume fraction and ferrite grain growth, together with intense precipitation within the corresponding carburised zones. These effects cause anything between 100 and 150 HV difference in hardness within a distance of 1 mm on either side of the weld junction.

Diffusion bonding ferritic steels at high temperature assured a flat interface with a sharp discontinuity in composition across the junction. Carbon partitioning began immediately after the sample was heated to a sufficiently high temperature, with accompanying precipitate dissolution on one side of the joint. As there was no mixing of the steels at the junction and no unwanted microstructures, the decarburised zone and the zone with intense carbide precipitation appeared uniformly along the interface. The decarburised zone can be up to 2 mm wide after aging for 10 000 h at 650 °C – which is about 20 % of the actual sample length.

Though diffusion bonding simplified the study of carbon diffusion, the development of microstructure can be different in a dissimilar steel weld. Welding causes the disruption of steels at the fusion boundary and significant intermixing of the component steels. The situation is further complicated in multi-pass welding where the decarburised zone width is dependent on the position relative to the weld and where microstructural variations due to welding can become exaggerated. Decarburised zones were found to occur first in re-austenitised regions with a large grain size, then eventually along the whole length of the weld junction. The decarburised and carburised zones in the multi-pass welds were less uniform and hence harder to measure accurately.

Vanadium containing welds showed a different behaviour. During carbon partitioning, carbide dissolution did not occur in the close proximity of the weld junction. It appears that only some of the carbides dissolve, leaving the more stable carbides in $\frac{1}{2}$CrMoV steel which keep the grain size small. The diffusion of carbon in $\frac{1}{2}$CrMoV steel was found to happen over a very long range. Consequently, the decarburised zone was difficult to estimate until a carbon

content analysis was used to quantify the carbon concentration as a function of distance from the weld junction.

This was also seen, to a lesser extent, in $2\frac{1}{4}$Cr1MoV steel. As both vanadium and chromium carbides co-exist in these steels, a higher volume fraction of chromium carbides are in $2\frac{1}{4}$Cr1MoV steel which leads to a greater extent of carbide dissolution next to the weld and accordingly diffusion is confined nearer to the fusion boundary.

A computer model was constructed to predict the extent of diffusion expected in a ferritic dissimilar steel weld, based on experimental observations of carbide dissolution and carbon diffusion. Firstly, the dissolution occurs next to the weld junction due to a chemical potential discontinuity at the weld junction. Subsequently, carbon released from the carbide diffuses away to maintain the chemical equilibrium at the weld interface. Important factors that must be considered when modelling the formation of decarburised zones were found to be:

- temperature
- time
- composition of both steels
- initial carbide size and distribution

It was disappointing that the computer model could not be applied to modelling decarburised zones forming in the low-alloy steel that contains vanadium. Decarburised zones were not easily visible in the vanadium steel and it was felt the model could not be applied to studying carbon partitioning in these welds. Further work must be undertaken to analyse the early stages of carbon partitioning in vanadium-bearing welds to identify key differences between these and other welds.

9.2 Further work on observations of carbon partitioning

The characterisation of decarburised zones based on the composition of the alloy and the ageing conditions has been thoroughly investigated. Future investigations might now focus on the properties of the carburised zones in welds. The strength of a weld is weakened by the hard carburised zone, therefore, the size of this zone and further understanding of the microstructures and mechanical properties here are extremely important (Kral & Stránský,1975; Pilious & Stránský,1987).

The large amount of carbon that enters the high-alloy steel is thought to tie-up almost all the excess carbide forming elements, forming a region containing a high volume fraction of stable

carbides. It would be pertinent to investigate the changing microstructures within and beyond the perimeter of the dark etching band. An investigation beyond the expected decarburised zone led to the discovery of long-range carbon diffusion in vanadium low-alloy steels, therefore it is possible that carbon diffusion may continue into the high-alloy steel without forming carbides. This may then have to be taken into consideration when repair-welding the transition joints.

It is also relevant to continue studying ways of restricting carbon diffusion in dissimilar welds. Methods of introducing barriers and grading composition of steels in welds have been attempted with varying degrees of success (Kral *et al.*, 1983). These techniques have not been applied successfully to ferritic welds and have not been modelled using numerical methods. Strong carbide formers (vanadium or maybe niobium) in low-alloy welds do not form narrow carbide-free zones, so the mismatch in microstructural and mechanical properties at the weld junction is limited; use of these elements calls for an additional study into the occurrence of Type IIIa cracking. Optimising the post-weld heat treatments of transition joints may also limit the amount of carbon diffusion.

9.3 Further work on computer modelling

The model proposed in this dissertation is capable of estimating the decarburised zone widths. The method is based on the Crank-Nicholson finite difference representation of the solution of Fick's second law, and therefore has a great deal of flexibility for application to other situations:

- The kinetics of precipitation of carbides in the carburised zone, taking into account the conservation of mass of carbon leaving the low-alloy steel. The diffusion controlled growth of a second phase could in principle be incorporated into the model as it is based on the rate of growth being proportional to the square root of time (Zener, 1949, cited by Reed-Hill & Abbaschian, 1994). The relationship between time and the carburised zone width is expected to be similar to the decarburised zone width.
- The computer model may also be extended for use on austenitic steels by removing the dissolution of discrete carbon sources and assuming a constant supply of carbon from all of the matrix.

References

AARON, H. B., (1968). Met. Sci. Journal, **2**, 192-193.

AARON, H. B., FAINSTEIN, D. & KOTLER, G. R., (1970). Journal of Applied Physics, **Vol. 41**, 4404.

AARON, H. B. & KOTLER, G. R., (1971). Met. Trans., **Vol. 2**, Feb., 393-408.

ABDEL-LATIF, A. M., CORBETT, J. M. & TAPLIN, D. M. R., (1982). Met. Sci. **Vol. 16**, 90-96.

ÅGREN, J., (1990). Scandinavian Journal of Metall., **Vol. 19**, 2-8.

ÅGREN, J., (1981). Scandinavian Journal of Metall., **Vol. 10**, 134-140.

ÅGREN, J. & VASSILEV, G. P. V., (1984). Mat. Sci. and Eng., **Vol. 64**, 95-103.

ANDREWS, K. W. (1965). J.I.S.I., **Vol. 203**, 721-727.

ASHBY, M. F. & EASTERLING, K. E., (1982). Acta Metall., **Vol. 30**, 1969-1978.

ASM Speciality Handbook, (1996) *"Carbon and Low Alloy Steels."* Edited by J. R. Davis.

BAILEY, N., (1994). *"Weldability of Ferritic Steels."* Published by Abington Publishing.

BAKER, R. G. & NUTTING, J., (1959). J.I.S.I., **Vol. 192**, 257-268.

BEECH, J. & WARRINGTON, D. H., (1966). J.I.S.I., **Vol. 204**, 460-468.

BRETT, S. J. & SMITH, P. A., (1998). Baltica IV: International Conference on Plant Maintenance for Managing Life and Performance, Helsinki - Stockholm - Helsinki, September 7-9.

BRETT, S. J., (1998). IMechE Conference: Integrity of High Temperature Welds, Forte Posthouse, Nottingham, November 3-4.

BRÜHL, F., HAARMANN, K., KALWA, G., WEBER, H. & ZSCHAU, M., (1989a). VGB Kraftwerkstechnik, **Vol. 12**, 1-12.

BRÜHL, F., CERJAK, H., MÜSCH, H., NIEDERHOFF, K. & ZSCHAU M., (1989b). VGB Kraftwerkstechnik, **Vol. 12**, 12-19.

BUCHMAYR, B., (1993). *"Mathematical Modelling of Weld Phenomena."* **Vol. 1**, 277-240.

BUCHMAYR, B., CERJAK, H., WITWER, M. & KIRKALDY, J. S., (1989). ASMI Second International Conference on Trends in Welding, May 14^{th} – 18^{th}, 237-242.

CHRISTOFFEL, R. J. & CURRAN, R. M., (1956). Welding Research Supplement, 457s-468s.

CRANK J., (1975). *"The Mathematics of Diffusion."* Published by Clarendon Press, Second Edition.

DARKEN, L. S., (1949). Trans. A.I.M.E., **Vol. 180**, 430-438.

DARKEN, L. S. & GURRY, R. W., (1935). *"Physical Chemistry of Steels."* Published by M^{c}Graw-Hill Book Company Inc.

DEHOFF, R. T., (1986). *"Applied Metallography."* Edited by G. F. Vander Voort, Van Nostrand Reinhold Company.

DERBY, B. & WALLACH, E. R., (1982). Met. Sci., **Vol. 16**, 49-56.

DIETER, G. E., (1988). *"Mechanical Metallurgy."* Published my McGraw-Hill Book Company.

DOIG, P., LONSDALE, D. & FLEWITT, P. E. J., (1982). Met. Sci., **Vol. 16**, 335-344.

DOOLEY, R. B., STEPHENSON, G. G., TINKLER, M. J., MOLES, M. D. C. & WESTWOOD H. J., (1982). Welding Research Supplement, 45s-49s.

DU, X., WHITEMAN, J. A., THOMSON, R. C. & BHADESHIA, H. K. D. H., (1992). Mat. Sci. and Eng., **Vol. A155**, 197-205.

DUNKERTON, S. B., (1991). *"Diffusion Bonding 2."* Edited by D. J. Stephenson, Elsevier Science Publishers Ltd, 1-11.

EASTERLING, K., (1983). *"Introduction to the Physical Metallurgy of Welding."* Published by Butterworths.

ELLIOT, S., BUCKLOW, I. A. & WALLACH, E. R., (1980). Journal of Mat. Sci., **Vol. 15**, 2823-2833.

EMERSON, R. W. & HUTCHINSON, W. R., (1952). Welding Research Supplement, 126s-141s.

EVANS, R. W. & WILSHIRE, B., (1993). *"Introduction to Creep."* Published by The Institute of Materials.

FASCHING, A. A., EDWARDS, G.R. & DAVID, S. A., (1995). Trends in Welding Research, Proceedings of the Fourth International Conference, June 5^{th} – 8^{th}, ASM International, 147-152.

GEMMILL, G. M., (1966). *"The Technology and Properties of Ferrous Alloys for High Temperature Use."* Published by Newnes Ltd.

GRAHAM, M. R., (1975). *"Turbine Generator Materials."* Materials in the Power Plant, The Institution of Metallurgists.

GULLBERG, R., (1973). J.I.S.I., **Vol. 211**, 59-65.

HIGGINS, R. A., (1994). *"The Properties of Engineering Materials."* Published by Edward Arnold.

HILLERT, M., NILSSON, K. & TÖRNDHAL, L. E., (1971). J.I.S.I., **Vol. 209**, 49-66.

HONEYCOMBE, R. W. K., (1976). Metall. Trans., **Vol. 7A**, 915-936.

HONEYCOMBE, R. W. K. & BHADESHIA, H. K. D. H., (1995). *"Steels, Microstructure and Properties."* Second Edition, published by Edward Arnold.

IRVINE, K. J., (1975). *"Steel for the Power Industry."* Materials in the Power Plant, The Institution of Metallurgists.

KIM, B-C, ANN, H-S & SONG, J-T, (1992). Trends in Welding Research, Proceedings of the Third International Conference, June 1st – 5th, ASM International, 307-313.

KIRKALDY, J. S., THOMSON, B. A. & BAGANIS, E. A., (1978). *"Hardenability Concepts with Application to Steel."* Edited by D. V. Doane and J. S. Kirkaldy, A.I.M.E., 82-125.

KIRKALDY, J. S. & YOUNG, D. J., (1987). *"Diffusion in the Condensed State."* Published by Institute of Metals.

KOU, S., (1989) Trends in Welding Research, Proceedings of the Second International Conference, May 14th – 18th, ASM International, 137-146.

LANCASTER, J. F., (1999). *"Metallurgy of Welding, Sixth Edition."* Published by Abington Publishing.

LIU, Z. & ÅGREN, J., (1991). Metall. Trans., **Vol. 22A**, 1753-1759.

LUNDIN, C. D., (1982). Welding Research Supplement, 58s-63s.

LUNDIN, C. D., KHAN, K. K. & YANG, D., (1989). ASMI Second International Conference on Trends in Welding, May 14th – 18th, 291-296.

MCLELLAN, R. B., RUDEE, M. L. & ISHIBACHI, T., (1965). Trans. Met. Soc. A.I.M.E., **Vol. 233**, 1938-1943.

MTDATA *Metallurgical and Thermodynamical Databank* (1996). **Version 4.60**, National Physics Laboratory, Teddington, Middlesex, UK.

NUTTING, J., (1999). *"Advanced Heat Resistant Steel for Power Generation."* Edited by J. Viswanathan and J. Nutting. Published by The Institute of Materials.

PILIOUS, V. & STRÁNSKÝ, K., (1987). Kovove Materialy, **Vol. 25**, No. 2, 121-130.

PILLING, J. & RIDLEY, N., (1982). Metall. Trans., **Vol. 13A**, 557-563.

PORTER, D. A. & EASTERLING, K. E., (1992). *"Phase Transformations in Metals and Alloys."* Published by Chapman & Hall.

PRADER, P., CERJAK, H. & DAVID, S. A., (1995). Trends in Welding Research, Proceedings of the Fourth International Conference, June 5th – 8th, ASM International, 247-252.

PRIOR, G. K., (1994). Materials Forum, **Vol. 18**, 265-276.

RACE, J. M., (1992). *"Carbon Migration Across Dissimilar Metal Welds."* PhD Thesis, University of Cambridge.

RACE, J. M. & BHADESHIA, H. K. D. H., (1992). Mat. Sci. and Tech., **Vol. 8**, 875-882.

REED-HILL, R. E. & ABBASCHIAN, R., (1994). *"Physical Metallurgy Principles."* PWS publishing Company.

RICHARDSON, F. D., (1953). J.I.S.I., **Vol. 175**, 33-51.

SANDERSON, S. J., (1983). American Society for Metals, 85-91.

SCHUSTER, F. A. & CERJAK, H., (1995). ASME Cogen-Turbo Power Conference, August 23^{th} – 25^{th}.

SIKKA, V. K., WARD, C. T. & THOMAS, K. C., (1983). American Society for Metals, 65-84.

SHAW, S. W. K. & QUARRELL, A. G., (1957). J.I.S.I., **Vol. 185**, 10-22.

SMALLMAN, R. E. & BISHOP, R. J., (1999). *"Modern Physical Metallurgy and Materials Engineering."* Published by Butterworth - Heinemann.

SMITH, E. & NUTTING, J., (1957). J.I.S.I., **Vol. 187**, 314-329.

STANLEY, J. K., (1949). Metals. Trans., **Vol. 185**, 752-761.

STEADMAN, R., (1982). *"Crystallography."* Published by Van Nostrand Reinhold Company.

STECAL (1989) ASM International

TAKEDA, Y. & MASUYAMA, F., (1991). First International Conference on Heat Resisting Materials, Wisconsin, USA.

TANZILLI, R. A. & HECKEL, R. W., (1968). Trans. of the Metall. Soc. of A.I.M.E., **Vol. 242**, 2313-2321.

THIELSH, H., (1952). Welding Research Supplement, 37s-63s.

THOMSON, R. C. & BHADESHIA, H. K. D. H., (1994). Journal of Mat. Sci., **Vol. 18**, (7), 205-208.

THORNTON, C. E, (1983). *"The Structure and Mechanical Properties of Diffusion Bonds in Steels."* PhD Thesis, University of Cambridge.

TOFT, L. H. & YELDHAM, D. E., (1972). Welding Research Related to Power Plant, CEGB, 5-19.

TUCKER, J. T. & EBERLE, F., (1956). Welding Research Supplement, 529s-540s.

TYLECOTE, R. F., (1968). *"The Solid Phase Welding of Metals."* Edward Arnold (Publishers) Ltd.

VANDER VOORT, G. F., (1984) *"Metallography, Principles and Practice."* McGraw - Hill Publishers.

VISWANATHAN, R., (1974). Metals Tech., 284-294.

WADA, T., WADA, H., ELLIOT, J. F. & CHIPMAN, J., (1972a). Metall. Trans., **Vol. 3**, 1657-1662.

WADA, T., WADA, H., ELLIOT, J. F. & CHIPMAN, J., (1972b). Metall. Trans., **Vol. 3**, 2865-2872.

WHELAN, M. J., (1969). Met. Sci. Journal, **3**, 95-97.

ZHOU, Y. & NORTH, T. H., (1993). Modelling Simul. Mat. Sci Eng., **Vol. 1**, 505-516.

APPENDIX

The target of this modelling is to produce a semi-quantitative understanding of the process mechanics for carbon partitioning in low-alloy steels. This program predicts the decarburised zone width as a function of composition and heat treatment by the dissolution of a carbide and the diffusion of carbon from the low-alloy to high-alloy steel in a ferritic dissimilar steel weld. The program code is written in Fortran 77. In some parts, calculations from MTDATA (1996) must be used.

```
C  AK is the partition coefficient
C  AREA is the difference between the old and new areas under the curves
C  AVALL is the average carbon concentration on the low-alloy side
C  CALA is the carbon concentration in the matrix, on low-alloy side (wt.  %)
C  CAAL is the carbon concentration in the carbide, on low-alloy side (wt.  %)
C  CALBE is the carbon concentration at the joint interface, on
C  low-alloy side (wt.  %)
C  CBEB is the carbon concentration in the matrix, on high-alloy side (wt.  %)
C  CBBE is the carbon concentration in the carbide, on high-alloy
C  side (wt.  %)
C  CBEAL is the carbon concentration at the joint interface, on high-alloy
C  side (wt.  %)
C  CC1 is the carbon content in the low-alloy steel (wt.  %)
C  CC2 is the carbon content in the high-alloy steel (wt.  %)
C  CCR1 is the chromium content in the low-alloy steel (wt.  %)
C  CCR2 is the chromium content in the high-alloy steel (wt.  %)
C  DMU is the diffusion coefficient (μm^2 s^-1)
C  D10 is the width of the block containing carbide and matrix,
C  low-alloy side (μm)
C  D20 is the width of the carbide, low-alloy side (μm)
C  D30 is the distance from carbide to joint interface, low-alloy side (μm)
C  D40 is the width of the carbide, high-alloy side (μm)
C  D50 is the width of the block containing carbide and matrix,
C  high-alloy side (μm)
C  D60 is the distance from carbide to joint interface, high-alloy side (μm)
C  DIFF is the difference between a real and an integer value
C  DIFXI is the fraction of width the carbide has shrunk by
C  DT is the time step (s)
C  DXA and DXALPHA are distance increments in carbide and matrix,
C  respectively (μm)
C  TEMP temperature (K)
C  M is the closest node to the left-hand side of the moving interface
C  MLATER is used to find the total number of nodes in the block
C  N is the number of nodes lying in the carbide and the adjoining matrix
C  on the right-hand side
C  NA is the number of nodes in the carbide
C  NC is the newly calculated value at a node
C  NHCA is the number of nodes on the low-alloy side
C  OC is the old value at the node
C  P is the fraction of DXA between M and the moving interface (μm)
C  SQDIST is the change in carbide width (μm)
```

```
C  SQHEIGHT is the numerical difference between CAAL and CALA, low-alloy side
C  THOUR is the time (h)
C  TIMEEND is the time to completion of the model (s)
C  TOTTIME is the summed time as the program runs (s)
C  TOTDIS is the total width of the symmetry element (μm)
C  VFA is the volume fraction of carbide on the low-alloy side
C  VFB is the volume fraction of carbide on the high-alloy side
C  WX is the weight fraction of element X
C  XINODE is the distance to the node on the left-hand side of the
C  moving interface (μm)

C  ************************************************************

      IMPLICIT DOUBLE PRECISION (A-H,O-Z)
      DOUBLE PRECISION TEMP,NA,DXA,D3
      DOUBLE PRECISION VFA0,VFB,D20,NHCA,U(50000),CALA,CBEB,CAAL
      DOUBLE PRECISION DM,DMU,NDT,MLATER,N,L,NDXA,NDT
      DOUBLE PRECISION AINTER-F-L-COMP,AINTER-F-R-COMP,TEMP
      DOUBLE PRECISION AK,AVALL,AREANEW,AREAOLD,CALBE,MM,TOTTIME,THOUR
      DOUBLE PRECISION OC(50000),NC(50000),NOC(50001),NNC(50001)

C  This file collects the results during dissolution.
      OPEN(1,FILE='DATA-OUTPUT.OUT')
C  This file contains the results for tracing the moving interface and average
C  carbon content in the block for each time step during dissolution.
      OPEN(2,FILE='RESULTS')
C  This file contains the concentrations at each node once the block has
C  homogenised.
      OPEN(3,FILE='DATADIF')
C  This file prints out the decarburised zone width, along with the square
C  root of time.
      OPEN(4,FILE='DECARBZONE')
C  This file contains all the data from each block which has been analysed.
      OPEN(5,FILE='DATABLOCK')

C  Firstly, the inputs are read into the program.  Then, the volume fraction
C  of carbide on the low-alloy side is calculated using the VOLFRAC subroutine
C  with data from MTDATA (1996).  This, along with a known carbide width, D20,
C  is used to find the width of the matrix in the block.  Then, knowing the
C  number of nodes in the carbide, NA, the distance
C  increments DX are calculated.
```

```
      TIMEEND=3600000
      CALL READ(DCARBIDEA,WFA,DCARBIDEB,WFB,D20,NA,TEMP,
     & WC1,WSI1,WMN1,WCR1,WMO1,WV1,WC2,WSI2,WMN2,WCR2,WMO2,WV2,
     & CAAL,CALA,CBEB)
      CALL VOLFRAC (DCARBIDEA,WFA,DCARBIDEB,WFB,VFA0,VFB)
      CALL DIMEN(D20,VFA0,VFB,D3,D60,DXA,TOTDIS,NA,NDXA,N,NHCA,NEWNHCA)
      D2=D20
      D30=D3
      WRITE (*,*) 'Distance from carbide to interface, low-alloy side', D3
      WRITE (*,*) 'Distance from interface to carbide, high-alloy side', D60
      WRITE (*,*) 'Total width is ', TOTDIS

C  Next, the carbon activity coefficients are calculated
C  (Pilious & Stránský, 1998) and then used to find the carbon
C  concentrations at the joint interface CALBE and CBEAL. The nodes in the
C  block are assigned values with respect to whether they lie in the
C  carbide or matrix.

      CALL CONVERT(GAMMAC,WC1,WSI1,WMN1,WCR1,WMO1,WNI1,WV1,TEMP)
      GAMMAC1=GAMMAC
      CALL CONVERT(GAMMAC,WC2,WSI2,WMN2,WCR2,WMO2,WNI2,WV2,TEMP)
      GAMMAC2=GAMMAC
      AK=GAMMAC2/GAMMAC1
      WRITE(*,*) 'The partition coefficient is; ',AK
      CALL CALCIF (D3,CALA,D60,CBEB,AK,CALBE,CBEAL)
      WRITE(*,*) 'Carbon concentration at the interface, low-alloy side',CALBE
      WRITE(*,*) 'Carbon concentration at interface, high-alloy side',CBEAL
      M=NA
      MM=M
      CALL ASSIGN-NODES(MM,CAAL,N,CALA,CALBE,OC)
      TOTTIME=0
      T=0
      MLATER=MM
      P=D20-(M*DXA)
      M=MM
      NEND=NHCA-MLATER

C  SQHEIGHT is the difference between the carbon concentrations lying at the
C  carbide/matrix interface and is used for finding the amount of solute
C  subtracted from the carbide during dissolution.  The carbon diffusion
C  coefficient, calculated in CLACDIFFCOEFF subroutine is multiplied by the
```

```
C  carbon activity coefficient in the low-alloy steel to account for the
C  interactions of substitutional solutes on carbon.

      SQHEIGHT=CAAL-CALA
      CALL CLACDIFFCOEFF(TEMP,DM)
      DMU=DM*1D+12
      DMU=DMU*(GAMMAC1*GAMMAC1)
      R=0.5
      NDT=R*(NDXA*NDXA)
      DT=(NDT*TOTDIS*TOTDIS)/DMU
      WRITE(*,*) 'Real DT; ', DT
      J=0
      AINTER-F-L-COMP=CALA
      AINTER-F-R-COMP=CALBE
          DO 101 I=1,N
          NC(I)=OC(I)
101       CONTINUE
      L=0

C  Inside the following loop in the program, carbide dissolution is analysed.
C  The new values (NC) calculated from the previous time step become the old
C  values (OC) for the current time.

999   CONTINUE
          IF (L .GT. 0) THEN
          N=NEWNHCA
          WRITE(*,*) 'Carbide number; ',L+1
          DO 102 I=1,M
          OC(I)=CAAL
102       CONTINUE
          DO 103 I=M+1, N-1
          OC(I)=CALA
103       CONTINUE
          AINTER-F-L-COMP=CALA
          OC(N)=OCRIGHT
          AINTER-F-R-COMP=OCRIGHT
          AREAOLD=0
          AREANEW=0
          AREAA=0
          AREA=0
          AVALL=0
```

```
          ENDIF
        JJ=0

990     CONTINUE
        CLOSE(1)
        OC(M+1)=CALA
        P=D20-(DXA*M)
        WRITE(*,*) 'The new width of the carbide; ', D20
          IF (M .LT. MLATER) THEN
          P=D20-(DXA*M)
          XINODE=DXA*M
          ENDIF
        NN=0

110     CONTINUE
        J=J+1
        II=0
        NN=0
          DO 115 I=M+1,N-1
          NN=NN+1
          II=II+1
          NOC(II)=OC(I)
          NNC(II)=0
115       CONTINUE
          IF (M .LT. MLATER) THEN
          AINTER-F-L-COMP=CALA
          NOC(M+1)=CALA
          ENDIF

    C  This CRANK-NICH subroutine (Crank, 1975) iterates new carbon concentrations
    C  for each node lying within the matrix phase.

        CALL CRANK-NICH(NOC,NNC,AINTER-F-L-COMP,AINTER-F-R-COMP,NN,M)
          DO 120 I=1,M
          NC(I)=CAAL
120       CONTINUE
        II=0
          DO 121 I=M+1,N-1
          II=II+1
          NC(I)=NNC(II)
121       CONTINUE
```

```
          IF (M .LT. MLATER) THEN
          NC(M+1)=CALA
          ENDIF
        NC(N)=OC(N)

C  The TOTAL-AREA subroutine uses the new concentration values to calculate
C  the area under the curve, indicating solute depletion next to the
C  dissimilar steel interface.

        AREAOLD=AREANEW
        CALL TOTAL-AREA (NN,NNC,DXA,CALA,CALBE,AREAOLD,AREANEW)
        AREA=AREAA+AREANEW
           IF (AREA .LT. 0.000000000000) THEN
           WRITE(*,*) 'ERROR, the area is negative.'
           ENDIF
        TOTTIME=TOTTIME+DT
        SQDIST=AREANEW/SQHEIGHT
        PCHANGE=P-SQDIST
        P=P-PCHANGE
        D20=D20-P
        AREAA=AREA
        XINODE=DXA*M
           DO 122 I=1,N
           OC(I)=NC(I)
122        CONTINUE

C  After carbide dissolution, the volume fraction of carbide and the average
C  carbon concentration in the low-alloy steel are re-calculated.

           IF (M .GE. 0) THEN
           DIFXI=(D2)-D20
              IF (DIFXI .EQ. 0.00000) THEN
              GOTO 130
              ELSE
              GOTO 131
              ENDIF
131        PERCENT=DIFXI/D2
              VFAP=VFA0*PERCENT
              VFA=VFA0-VFAP
130        CONTINUE
              IF(VFA .LE. 0.000000) THEN
```

```
            GOTO 132
            ELSE
            AVTOT=0
            DO 134 I=1,N
            AVTOT=AVTOT+OC(I)
134       CONTINUE
            AVALL=AVTOT/N
            ENDIF
132       CONTINUE
            ENDIF
          IF(L. EQ. 0) THEN
          CALL CALCIF (D3,AVALL,D60,CBEB,AK,CALBE,CBEAL)
          NC(N)=CALBE
          ELSE
          NC(N)=OCRIGHT
        ENDIF
        OC(N)=NC(N)
        AINTER-F-L-COMP=CALA
        IF(L .EQ. 0) THEN
        AINTER-F-R-COMP=CALBE
        ELSE
        AINTER-F-R-COMP=OCRIGHT
        ENDIF
            IF (JJ .EQ. 5) THEN
            WRITE(2,135) SQRT(TOTTIME-TIMEBLOCK), D20, AVALL
135         FORMAT (F11.6,F11.6,F11.6,F11.6,F11.6)
            JJ=0
            ENDIF
        JJ=JJ+1
            IF (M .LE. -1.00000000) GOTO 111
            IF (D20 .LE. XINODE) GOTO 136
        GOTO 110
136     WRITE(*,*) 'Have reached node number; ', M
        THOUR=TOTTIME/3600
        WRITE(*,*) 'The total time in seconds and hours; ', TOTTIME, THOUR
        OPEN(1,FILE='DATA-OUTPUT.OUT')

    C  When a node lying in the carbide has been passed by the moving
    C  carbide/matrix interface, the carbon concentrations are written
    C  to file (1).
```

```
          DO 140 II=1,M
          WRITE(1,107) II, CAAL
140       CONTINUE
          DO 141 II=M+1,N-1
          WRITE(1,107) II, OC(II)
107       FORMAT (I7, F11.6)
141       CONTINUE
       II=N
       WRITE(1,107) II, OC(N)

   C  File (1) is closed and then re-opened so it's contents can be read.

       CLOSE(1)
       OPEN(1,FILE='DATA-OUTPUT.OUT')
          DO 142 II=1,N
          READ(1,*) II, OC(II)
142       CONTINUE

   C  The node on the left-hand side of the moving carbide/matrix interface is
   C  found in CALCM subroutine.

       CALL CALCM (D20,DXA,MM)
       M=MM
          IF (M .LE. -1.0) THEN
          GOTO 111
          ENDIF
       GOTO 990
111    WRITE (*,*) 'This has now reached the last node'
          IF (TOTTIME .GE. TIMEEND) THEN
          WRITE(*,*) 'We have come to the end', THOUR
          STOP
          ELSE
          GOTO 150
          ENDIF
150       CONTINUE
       WRITE(*,*) 'Time to dissolve the carbide; ', THOUR
       WRITE(4,*) SQRT(THOUR),(((N+NNN)*DXA)/1000)
       NN=0
       CLOSE(1)
       OPEN(1,FILE='DATA-OUTPUT.OUT')
          DO 159 II=1,N
```

```
          NN=NN+1
          READ (1,107) II,NNC(II)
          NOC(II)=NNC(II)
159       CONTINUE
       CLOSE(1)

   C  The dissolving carbide is analysed between the carbide and the dissimilar
   C  steel interface only, therefore after dissolution all the nodes in the
   C  block are now considered during the homogenisation of carbon.  Nodes
   C  falling on the left-hand side of the carbide are set initially to CALA.
   C  From the second block onwards, data from previous blocks are included
   C  in the analysis.

       OPEN(4,FILE='DATA-OUTPUT.OUT')
       OPEN(9,FILE='DATADIF')
          DO 160 II=1,NN-MLATER
          NNC(II)=CALA
160       CONTINUE
          DO 161 II=1,NN
          READ(1,*) II, NOC(II)
          NNC(II+NEND)=NOC(II)
161       CONTINUE
          IF(L .GT. 0) THEN
             DO 162 II=1,NNN
             READ(3,*) II, NOC(II)
             NNC(II+NN+NEND)=NOC(II)
162       CONTINUE
          NNN=(L+1)*NNOLD
          NNEND=INT(NNN/2)
          WRITE(*,*) NNN,NNEND
          ELSE
          NNOLD=NEND+NEWNHCA
          NNN=NNOLD
          NNEND=NEND
          ENDIF
       AVTOT=0
          DO 164 I=1,NNN
          AVTOT=AVTOT+NNC(I)
164       CONTINUE
       AVALL=AVTOT/NNN
       CLOSE(1)
```

```
      CLOSE(3)
      WRITE(*,*) 'NNN',NNN
         DO 165 II=1,NNN
         NOC(II)=NNC(II)
165      CONTINUE
      D3=NNN*DXA
      CALL CALCIF (D3,CALA,D60,CBEB,AK,CALBE,CBEAL)
      AINTER-F-L-COMP=CALA
      AINTER-F-R-COMP=CALBE
      WRITE(*,*) AINTER-F-L-COMP,AINTER-F-R-COMP,AVALL
      OPEN(3,FILE='DATADIF')
      J=0
170   CONTINUE
      CALL CRANK-NICH(NOC,NNC,AINTER-F-L-COMP,AINTER-F-R-COMP,NNN,M)
      TOTTIME=TOTTIME+DT
         DO 171 II=1,NNN
         NOC(II)=NNC(II)
171      CONTINUE
      THOUR=TOTTIME/3600

   C  When the central node falls below the average composition in the block, it
   C  is said to have 'finished' and the program moves onto the next block.

         IF (NOC(NNEND) .LT. AVALL) THEN
         WRITE(*,*) 'The block ', L+1, ' has finished in ', THOUR,' hours.'
         WRITE(*,*) 'The distance of block ', L+1,' is; ', NNN*DXA
         WRITE(*,*) 'And the average composition is; ', AVALL
         WRITE(4,*) SQRT(TOTTIME/3600),((NNN*DXA)/1000)
         TIMEBLOCK=TOTTIME
         GOTO 172
         ELSE
         GOTO 170
         ENDIF
172      CONTINUE
         DO 173 II=1,NNN
         WRITE(3,*) II, NOC(II)
173      CONTINUE
      OCRIGHT=NOC(1)
         IF (TOTTIME .GE. TIMEEND) THEN
         WRITE(*,*) 'We have come to the end', THOUR
         STOP
```

```
          ELSE
       GOTO 175
          ENDIF
175       CONTINUE
       CLOSE(3)
       NEWNHCA=NEWNHCA
       D20=D2
       TOTDIST=(NNN*DXA)+D30+D20
       WRITE(*,*) 'Distance from LHS of carbide to block interface; ',TOTDIST
       NHCA=NEWNHCA+NNN
       N=NHCA
       D3=TOTDIST-D20
       CALL CALCIF (D3,CALA,D60,CBEB,AK,CALBE,CBEAL)
       D20=D2
       MM=MLATER
          IF(JI .EQ. 1) THEN
          GOTO 180
          ELSE
          JI=0
          ENDIF

C  Whilst ageing 2¼Cr1Mo steel, the equilibrium carbide re-precipitates
C  as a more stable carbide (Baker & Nutting, 1956).  The following lines call
C  for a change in carbide type after a given time and temperature
C  of heat treatment.

          IF (TEMP .LE. 873 .AND. TOTTIME .GE. 18000) THEN
          CALL CARBIDE-CHANGE(TEMP,DCARBIDEB,WFB,VFA0,VFB,
     &       D20,D3,D60,DXA,L,NA,NDXA,N,NHCA,NEWNHCA,TOTDIS,CALA,
     &       CBEB,AK,CALBE,CBEAL,MM,CAAL,OC)
          JI=1
          TOTDIST=(NNN*DXA)+D3+D20
          ENDIF
          IF (TEMP .EQ. 923 .AND. TOTTIME .GE. 3600) THEN
          CALL CARBIDE-CHANGE(TEMP,DCARBIDEB,WFB,VFA0,VFB,
     &       D20,D3,D60,DXA,L,NA,NDXA,N,NHCA,NEWNHCA,TOTDIS,CALA,
     &       CBEB,AK,CALBE,CBEAL,MM,CAAL,OC)
          JI=1
          TOTDIST=(NNN*DXA)+D3+D20
          ENDIF
          IF (TEMP .GE. 973 .AND. TOTTIME .GE. 1800) THEN
```

```
          CALL CARBIDE-CHANGE(TEMP,DCARBIDEB,WFB,VFA0,VFB,
     &       D20,D3,D60,DXA,L,NA,NDXA,N,NHCA,NEWNHCA,TOTDIS,CALA,
     &       CBEB,AK,CALBE,CBEAL,MM,CAAL,OC)
          JI=1
          TOTDIST=(NNN*DXA)+D3+D20
          ENDIF
180     CONTINUE
        WRITE(*,*) 'JI', JI
        TOTDIS=TOTDIST
        WRITE(*,*) TOTDIS, TOTDIST

    C  The carbon concentrations for each node are written into file (5) to be
    C  used in the next block.

        OPEN(5,FILE='DATABLOCK')
           DO 181 IA=1,MM
           U(IA)=CAAL
           OC(IA)=CAAL
           WRITE(5,*) (IA), OC(IA)
181        CONTINUE
           DO 182 IALPHA=MM+1,NEWNHCA
           U(IALPHA)=CALA
           OC(IALPHA)=CALA
           WRITE(5,*) (IALPHA), OC(IALPHA)
182        CONTINUE
        OPEN(3,FILE='DATADIF')
           DO 138 II=1,NNN-1
           READ(3,*) II, OC(II)
           WRITE(5,*) (II+NEWNHCA), OC(II)
183        CONTINUE
        U(IALBE)=CALBE
        OC(IALBE)=CALBE
        OC(NNN+NEWNHCA)=CALBE
        II=NNN+NEWNHCA
        WRITE(5,*) (II), OC(NNN+NEWNHCA)
        M=MM
        CLOSE(3)
        CLOSE(5)
        L=L+1
           IF (TOTTIME .LE. TIMEEND) THEN
           GOTO 999
```

```
      ELSE
      WRITE(*,*) 'We have come to the end', TOTTIME
      ENDIF
   STOP
   END

C  ********************************************************
C  This subroutine asks for the appropriate data to run the model.

   SUBROUTINE READ(DCARBIDEA,WFA,DCARBIDEB,WFB,D20,NA,TEMP,
  &    WC1,WSI1,WMN1,WCR1,WMO1,WV1,WC2,WSI2,WMN2,WCR2,WMO2,WV2,
  &    CAAL,CALA,CBEB)
   REAL DCARBIDEA,DCARBIDEB
   DOUBLE PRECISION WFA,WFB,D20,NA,TEMP
   DOUBLE PRECISION WC1,WSI1,WMN1,WCR1,WMO1,WV1
   DOUBLE PRECISION WC2,WSI2,WMN2,WCR2,WMO2,WV2,CAAL,CALA,CBEB

   WRITE(*,*) 'Choose the type of carbide in low - alloy side; '
   WRITE(*,*) '1 = M-23C-6'
   WRITE(*,*) '2 = Fe-3C'
   WRITE(*,*) '3 = M-7C-3'
   WRITE(*,*) '4 = V-4C-3'
   WRITE (*,*) DCARBIDEA
   WRITE(*,*) 'and the weight fraction of the carbide; '
   WRITE (*,*) WFA
   WRITE(*,*) 'Choose the type of carbide in high - alloy side; '
   WRITE(*,*) '1 = M-23C-6'
   WRITE(*,*) '2 = Fe-3C'
   WRITE(*,*) '3 = M-7C-3'
   WRITE (*,*) DCARBIDEB
   WRITE(*,*) 'and the weight fraction of the carbide; '
   WRITE (*,*) WFB
   WRITE (*,*) 'What is the width of carbide, (um)?  '
   WRITE(*,*) D20
   WRITE(*,*) 'How many nodes in the carbide, low-alloy side?'
   WRITE(*,*) NA
   WRITE(*,*) 'Enter the temperature:  '
   WRITE(*,*) TEMP
   WRITE(*,*) 'For the low-alloy side;'
   WRITE(*,*) 'enter wt.  % of carbon:'
   WRITE(*,*) WC1
```

```
      WRITE(*,*) 'enter wt.  % of silicon:'
      WRITE(*,*) WSI1
      WRITE(*,*) 'enter wt.  % of manganese:'
      WRITE(*,*) WMN1
      WRITE(*,*) 'enter wt.  % of chromium:'
      WRITE(*,*) WCR1
      WRITE(*,*) 'enter wt.  % of molybdenum:'
      WRITE(*,*) WMO1
      WRITE(*,*) 'enter wt.  % of nickel:'
      WRITE(*,*) WNI1
      WRITE(*,*) 'enter wt.  % of vanadium:'
      WRITE(*,*) WV1
      WRITE(*,*) 'For the high-alloy side;'
      WRITE(*,*) 'enter wt.  % of carbon:'
      WRITE(*,*) WC2
      WRITE(*,*) 'enter wt.  % of silicon:'
      WRITE(*,*) WSI2
      WRITE(*,*) 'enter wt.  % of manganese:'
      WRITE(*,*) WMN2
      WRITE(*,*) 'enter wt.  % of chromium:'
      WRITE(*,*) WCR2
      WRITE(*,*) 'enter wt.  % of molybdenum:'
      WRITE(*,*) WMO2
      WRITE(*,*) 'enter wt.  % of nickel:'
      WRITE(*,*) WNI2
      WRITE(*,*) 'enter wt.  % of vanadium:'
      WRITE(*,*) WV2
      WRITE(*,*) 'Enter carbon concentration in carbide, low-alloy side'
      WRITE(*,*) CAAL
      WRITE(*,*) 'Enter carbon concentration in matrix, low-alloy side:'
      WRITE(*,*) CALA
      WRITE(*,*) 'Enter carbon concentration in matrix, high-alloy side:'
      WRITE(*,*) CBEB
      RETURN
      END

C     ************************************************************
C     This subroutine calculates the volume fraction of carbides on either sides
C     of the dissimilar steel junction.
C     WFA is the weight fraction of carbide on the low-alloy side.
C     DCA is the density of carbide on the low-alloy side.
```

```
C  VCA is the volume of carbide on the low-alloy side.
C  WFFA is the weight fraction of ferrite on the low-alloy side.
C  DF is the density of ferrite
C  VFFA is the volume of ferrite on the low-alloy side
C  TOTVOLA is the total volume of phases on the low-alloy side.
C  VOLFRACA is the volume fraction of carbide present on the low-alloy side.
C  Variables ending in 'B' are for the high-alloy side.

      SUBROUTINE VOLFRAC(DCARBIDEA,WFA,DCARBIDEB,WFB,VOLFRACA,VOLFRACB)
      IMPLICIT DOUBLE PRECISION (A-H,O-Z)
      REAL DCARBIDEA,DCARBIDEB
      DOUBLE PRECISION WFA,WFB,DCA,DCB,VCA,VCB
      DOUBLE PRECISION WFFA,WFFB,DF,VFFA,VFFB,TOTVOLA,TOTVOLB
      DOUBLE PRECISION VOLFRACA,VOLFRACB

      DCARBIDEA=DCARBIDEA
          IF (DCARBIDEA.EQ.1) THEN
          DCA=6.996
          ENDIF
          IF (DCARBIDEA.EQ.2) THEN
          DCA=7.704
          ENDIF
          IF (DCARBIDEA.EQ.3) THEN
          DCA=6.965
          ENDIF
          IF (DCARBIDEA.EQ.4) THEN
          DCA=5.533
          ENDIF
      WFA=WFA
      VCA=WFA/DCA
      DCARBIDEB=DCARBIDEB
          IF (DCARBIDEB.EQ.1) THEN
          DCB=6.996
          ENDIF
          IF (DCARBIDEB.EQ.2) THEN
          DCB=7.704
          ENDIF
          IF (DCARBIDEB.EQ.3) THEN
          DCB=6.965
          ENDIF
      WFB=WFB
```

```
      VCB=WFB/DCB
      WFFA=1-WFA
      WFFB=1-WFB
      DF=8.5
      VFFA=WFFA/DF
      VFFB=WFFB/DF
      TOTVOLA=VCA+VFFA
      TOTVOLB=VCB+VFFB
      VOLFRACA=VCA/TOTVOLA
      VOLFRACB=VCB/TOTVOLB
      WRITE(*,200) 'Volume fraction of carbide on low-alloy side:',VOLFRACA
200   FORMAT(A40,F11.7)
      WRITE(*,200) 'Volume fraction of carbide on high-alloy side:',VOLFRACB
      RETURN
      END

C  *******************************************************
C  This subroutine calculates the dimensions of the block in which the carbide
C  is dissolving.

      SUBROUTINE DIMEN(D20,VFA0,VFB,D3,D60,DXA,TOTDIS,NA,NDXA,N,
     &    NHCA,NEWNHCA)
      DOUBLE PRECISION VFA0,VFB,D40,D20,D10,D50,D3,D60,TOTDIS
      DOUBLE PRECISION ND20,DXA,NA,NDXA,ND3,NDXALPHA,NHCA,N
      D40=D20
      D10=D20/VFA0
      D50=D40/VFB
      D3=(D10-D20)/2
      D60=(D50-D40)/2
      TOTDIS=D20+D3
      DXA=D20/NA
      WRITE(*,*) 'distance between nodes; ',DXA
      NALPHA=DINT(D3/DXA)
      DXALPHA=(D3/NALPHA)
      ND20=D20/TOTDIS
      ND3=D3/TOTDIS
      NDXA=ND20/NA
      NDXALPHA=ND3/NALPHA
      N=NA+NALPHA
      NHCA=N
      NEWNHCA=NHCA
```

```
      RETURN
      END

C  ******************************************************
C  This subroutine converts from weight percent to atomic faction for each
C  element in the steel.
C  ICOMP is the number of elements in the steel.

      SUBROUTINE CONVERT(GAMMAC,WC,WSI,WMN,WCR,WMO,WNI,WV,TEMP)
      IMPLICIT DOUBLE PRECISION (A-H,K-Z),INTEGER(I,J)
      DOUBLE PRECISION EFFINTCOEF,GAMMAC
      REAL ATMFC,ATMFSI,ATMFMN,ATMFCR,ATMFMO,ATMFNI,ATMFV,ATMFFE

      TOTMOL=0
      ICOMP=8
      RAMC=12.011
      ATMFC = WC/RAMC
      RAMSI=28.086
      ATMFSI=WSI/RAMSI
      RAMMN=54.938
      ATMFMN=WMN/RAMMN
      RAMCR=51.996
      ATMFCR=WCR/RAMCR
      RAMMO=95.94
      ATMFMO=WMO/RAMMO
      RAMNI=58.71
      ATMFNI=WNI/RAMNI
      RAMV=50.942
      ATMFV=WV/RAMV
      WFE=100-WC-WSI-WMN-WCR-WMO-WNI-WV
      RAMFE=55.847
      ATMFFE=WFE/RAMFE
      TOTMOL = ATMFC+ATMFSI+ATMFMN+ATMFCR+ATMFMO+ATMFNI+ATMFV+ATMFFE
      ATMFC=ATMFC/TOTMOL
      WRITE(*,*) 'The atomic fraction of carbon,', ATMFC
      ATMFSI=ATMFSI/TOTMOL
      ATMFMN=ATMFMN/TOTMOL
      ATMFCR=ATMFCR/TOTMOL
      WRITE(*,*) 'The atomic fraction of chromium,', ATMFCR
      ATMFMO=ATMFMO/TOTMOL
      ATMFNI=ATMFNI/TOTMOL
```

```
      ATMFV=ATMFV/TOTMOL
      ATMFFE=ATMFFE/TOTMOL
      EFFINTCOEF=10.64-(36170/TEMP)
      CALL ACTCOF (ATMFSI,ATMFMN,ATMFCR,ATMFMO,ATMFNI,ATMFV,
     &    EFFINTCOEF,GAMMAC)
      RETURN
      END

C  ************************************************************
C  This subroutine calculates carbon activity coefficient, for both the low
C  and high-alloy steels.

      SUBROUTINE ACTCOF (ATMFSI,ATMFMN,ATMFCR,ATMFMO,ATMFNI,ATMFV,
     &  EFFINTCOEF,GAMMAC)
      IMPLICIT DOUBLE PRECISION (A-H,O-Z)
      DOUBLE PRECISION EFFINTCOEF,GAMMAC
      REAL ATMFSI,ATMFMN,ATMFCR,ATMFMO,ATMFNI,ATMFV
      REAL NCJSI,NCJMN,NCJCR,NCJMO,NCJNI,NCJV

      NCJSI=ATMFSI*-0.673
      NCJMN=ATMFMN*0.386
      NCJCR=ATMFCR*1
      NCJMO=ATMFMO*1
      NCJNI=ATMFNI*-0.442
      NCJV=ATMFV*2.08
      SUM=NCJSI+NCJMN+NCJCR+NCJMO+NCJNI+NCJV
      GAMMAC=DEXP(EFFINTCOEF*SUM)
      RETURN
      END

C  ************************************************************
C  This subroutine calculates the carbon concentrations at the dissimilar
C  steel junction using the partition coefficient AK.

      SUBROUTINE CALCIF(D3,CALA,D60,CBEB,AK,CALBE,CBEAL)
      IMPLICIT DOUBLE PRECISION (A-H,O-Z)
      DOUBLE PRECISION D3,CALA,D60,CBEB,AK,CALBE,CBEAL
      CBEAL=((D3*CALA)+(D60*CBEB))/((AK*D60)+D3)
      CALBE=AK*CBEAL
      RETURN
      END
```

```
C  ************************************************************
C  This subroutine assigns values to each node lying in the carbide and on the
C  right-hand side of the block.

      SUBROUTINE ASSIGN-NODES(MM,CAAL,N,CALA,CALBE,OC)
      IMPLICIT DOUBLE PRECISION (A-H,O-Z)
      DOUBLE PRECISION U(5000),OC(5000),MM,CAAL,N,CALA,CALBE

         DO 301 IA=1,MM
         U(IA)=CAAL
         OC(IA)=CAAL
301      CONTINUE
         DO 302 IALPHA=MM+1,N-1
         U(IALPHA)=CALA
         OC(IALPHA)=CALA
302      CONTINUE
      U(IALBE)=CALBE
      OC(IALBE)=CALBE
      OC(N)=CALBE
      RETURN
      END

C  ************************************************************
C  This subroutine calculates the diffusion coefficient of carbon in ferritic
C  low-alloy steel.
C  R is the universal gas constant, J/K/mole.
C  TEMP is the temperature in Kelvin.
C  PHI is the phi in McLellan et al., dimensionless.
C  DOTO is the contribution from Octahedral-Tetrahedral-Octahedral
C  diffusion.
C  DTT is the contribution from tetrahedral-tetrahedral diffusion.
C  D is the net diffusion coefficient in units of m**2/s.
C  F is the f in McLellan et al.

      SUBROUTINE CLACDIFFCOEFF(TEMP,D)
      IMPLICIT DOUBLE PRECISION (A-H,O-Z)
      DOUBLE PRECISION R,TEMP,PHI,DOTO,DTT,F,D
      R=8.3143d+00
      F=0.86d+00
      PHI=1.0D0-1.0/(0.5D0*DEXP(7.2D03*4.184/(R*TEMP))
     &    *DEXP(4.4D0)+1.0D0)
```

```
      DOTO=3.3D-07*DEXP(-19.3D03*4.184D0/(R*TEMP))
      DTT=3.0D-4*DEXP(-14.7D03*4.184D0/(R*TEMP))
      D= PHI*DOTO+(1.0D0-PHI)*F*DTT+(1.0D0-PHI)
     &    *(1.0D0-F)*DOTO
      WRITE(*,*) 'the diffusion coefficient at',TEMP, 'is', D
      RETURN
      END

C  ************************************************************
C  This subroutine uses the Crank-Nicholson implicit finite difference method
C  (Crank, 1975) to find new carbon concentrations in the matrix
C  after each time step.
C  ADIFF is the absolute difference.
C  AINTER-F-L-COMP is the concentration of C at the LHS.
C  AINTER-F-R-COMP is the concentration of C at the RHS.
C  R is the stability of the implicit finite difference method.
C  TOL is the tolerance.

      SUBROUTINE CRANK-NICH(NOC,NNC,AINTER-F-L-COMP,AINTER-F-R-COMP,N,M)
      IMPLICIT DOUBLE PRECISION (A-H,O-Z)
      DOUBLE PRECISION NOC(50000),NNC(50000),AINTER-F-L-COMP,AINTER-F-R-COMP

      R=0.5
         DO 400 I=1,N
         NNC(I) =0.0
400      CONTINUE
      TOL=0.0000001
      DIFF=0.0
         DO 410 K=1,5000
         ADIFF=0.0
            DO 420 I=1,N
            IT1=I-1
               IF (IT1 .LE. 0) THEN
               T1=R*AINTER-F-L-COMP
               T3=R*AINTER-F-L-COMP
               ELSE
               T1=R*NOC(I-1)
               T3=R*NNC(I-1)
               ENDIF
            IT2=I+1
               IF(IT2 .GE. N) THEN
```

```
                T2=R*AINTER-F-R-COMP
                T4=R*AINTER-F-R-COMP
                ELSE
                T2=R*NOC(I+1)
                T4=R*NNC(I+1)
                ENDIF
            T5=(2-2*R)*NOC(I)
            RR=1/(2+2*R)
            T=(T1+T2+T3+T4+T5)*RR
            DIFF=(NNC(I)-T)/T
            NNC(I)=T
                IF (DIFF .LT. 0.0000000) THEN
                   DIFF=-1*DIFF
         ENDIF
                IF (DIFF .GT. ADIFF) THEN
                ADIFF = DIFF
                ENDIF
420         CONTINUE
                IF (ADIFF .LE. TOL) GOTO 230
410      CONTINUE
      WRITE (*,*) 'SOLUTION NOT CONVERGED AFTER', K,'ITERATIONS'
      GOTO 430
430   CONTINUE
      RETURN
      END

C  ************************************************************
C  This subroutine calculates the area under the curve next to the dissimilar
C  steel junction formed during heat treatment.
C  AREANEW is the total area under the curve.

      SUBROUTINE TOTAL-AREA (NN,NC,DXA,CALA,CALBE,AREAOLD,AREANEW)
      IMPLICIT DOUBLE PRECISION (A-H,O-Z)
      DOUBLE PRECISION NC(5000),AREA2,C1,C2,CM,DXA,CALA,CALBE
      DOUBLE PRECISION AREAOLD,AREANEW

      J=0
      AREANEW=0.0
      TOTAREA2=0.0
         DO 501 I=1,NN
         J=J+1
```

```
          C1=NC(I)
          C2=NC(I+1)
          CM=CALA
             IF (I .EQ. NN)THEN
             C2=CALBE
             ENDIF
          CALL SEG-AREA(C1,C2,CM,DXA,AREA2)
          TOTAREA2=TOTAREA2+AREA2
501       CONTINUE
       AREANEW=TOTAREA2-AREAOLD
       AREANEW=ABS(AREANEW)
          IF (AREANEW .LT. 0.00000000) THEN
          WRITE(*,*) 'TOTAL AREA IS NEGATIVE'
          ENDIF
       RETURN
       END

   C  ***************************************************************
   C  This subroutine is part of SUBROUTINE TOTAL-AREA.
   C  AREA is the area under the curve.
   C  C1 is the concentration of the first node to be analysed.
   C  C2 is the concentration of the second node, on the left of C1.
   C  CM is the matrix concentration, and is constant in this case.

       SUBROUTINE SEG-AREA(C1,C2,CM,DXA,AREA)
       IMPLICIT DOUBLE PRECISION (A-H,O-Z)

       AREA=0.0
          IF ((C1 .EQ. C2) .AND. (C2 .EQ. CM)) GOTO 600
          IF ((C1 .EQ. C2) .AND. (C1 .LT. CM)) THEN
          AREA=DXA*(CM-C1)
          GOTO 600
          ENDIF
          IF ((C1 .LT. C2) .AND. (C2 .LT. CM)) THEN
          AREA=DXA*(CM-C2) + 0.5*DXA*(C2-C1)
          GOTO 600
          ENDIF
          IF ((C1 .LT. C2) .AND. (C2 .EQ. CM)) THEN
          AREA=0.5*DXA*(C2-C1)
          GOTO 600
          ENDIF
```

```
          IF( (C2 .LT. C1) .AND. (C1 .LT. CM) )THEN
          AREA=DXA*(CM-C2) + 0.5*DXA*(C1-C2)
          GOTO 600
          ENDIF
          IF( (C2 .LT. C1) .AND. (C1 .EQ. CM) )THEN
          AREA= 0.5*DXA*(C1-C2)
          GOTO 600
          ENDIF
600     CONTINUE
        RETURN
        END

    C   ************************************************************
    C   This subroutine finds the node lying on the left-hand side of the moving
    C   carbide/matrix interface.

        SUBROUTINE CALCM (D20,DXA,M)
        IMPLICIT DOUBLE PRECISION (A-H,O-Z)
        DOUBLE PRECISION MR,D20,DXA,M
        INTEGER MI

        MR=D20/DXA
        MI=D20/DXA
        DIFF=MI-MR
           IF (DIFF.LE.0) THEN
           M=MI
           ENDIF
           IF (DIFF.GE.0) THEN
           M=MI-1
           ENDIF
        RETURN
        END

    C   ************************************************************
    C   This subroutine is used when the low-alloy side of a dissimilar joint is
    C   2¼Cr1Mo steel and so the re-precipitation of more stable carbides
    C   occur during ageing.  The number of nodes in the carbide phase NA remains
    C   the same; and VOLFRAC, DIMEN and CALCIF subroutines are called to
    C   recalculate the dimensions and interface concentrations in the block.

        SUBROUTINE CARBIDE-CHANGE(TEMP,DCARBIDEB,WFB,VFA0,VFB,
```

```
&    D20,D3,D60,DXA,L,NA,NDXA,N,NHCA,NEWNHCA,TOTDIS,CALA,
&    CBEB,AK,CALBE,CBEAL,MM,CAAL,OC)
  IMPLICIT DOUBLE PRECISION (A-H,O-Z)
  REAL DCARBIDEA,DCARBIDEB
  DOUBLE PRECISION TEMP,WFA,VFAO,VFB,D20,D3,D60,DXA,L,NA,NDXA,N
  DOUBLE PRECISION NHCA,NEWNHCA,TOTDIS,CALA,CBEB,AK,CALBE,CBEAL
  DOUBLE PRECISION MM,CAAL,OC

      IF (TEMP .LE. 873) THEN
      DCARBIDEA=3
      WFA=0.0088
      CAAL=8.78
      CALA=0.00022
      ENDIF
      IF (TEMP .EQ. 923) THEN
      DCARBIDEA=3
      WFA=0.0101
      CAAL=8.70
      CALA=0.00081
      ENDIF
      IF (TEMP .GE. 973) THEN
      DCARBIDEA=3
      WFA=0.0116
      CAAL=8.61
      CALA=0.00242
      ENDIF
  CALL VOLFRAC(DCARBIDEA,WFA,DCARBIDEB,WFB,VFAO,VFB)
  CALL DIMEN(D20,VFAO,VFB,D3,D60,DXA,TOTDIS,NA,NDXA,N,NHCA,NEWNHCA)
  D2=D20
  D30=D3
  TOTDIS=D20+D3
  WRITE (*,*) 'Distance from new carbide to the joint interface', D3
  CALL CALCIF (D3,CALA,D60,CBEB,AK,CALBE,CBEAL)
  WRITE(*,*) 'Carbon concentration at interface, low-alloy side',CALBE
  WRITE(*,*) 'Carbon concentration at interface, high-alloy side',CBEAL
  M=NA
  MM=M
  JI=1
  RETURN
  END
```